

MAGNETOM Flash

The Magazine of MR

Issue Number 1/2009
ISMRM Edition

SIEMENS

Clinical

Clinical Validation
of *syngo* ASL
Page 50

MRI in Inflammatory
Arthritis
Page 54

Case Report:
Rectum
Page 62

How-I-do-it

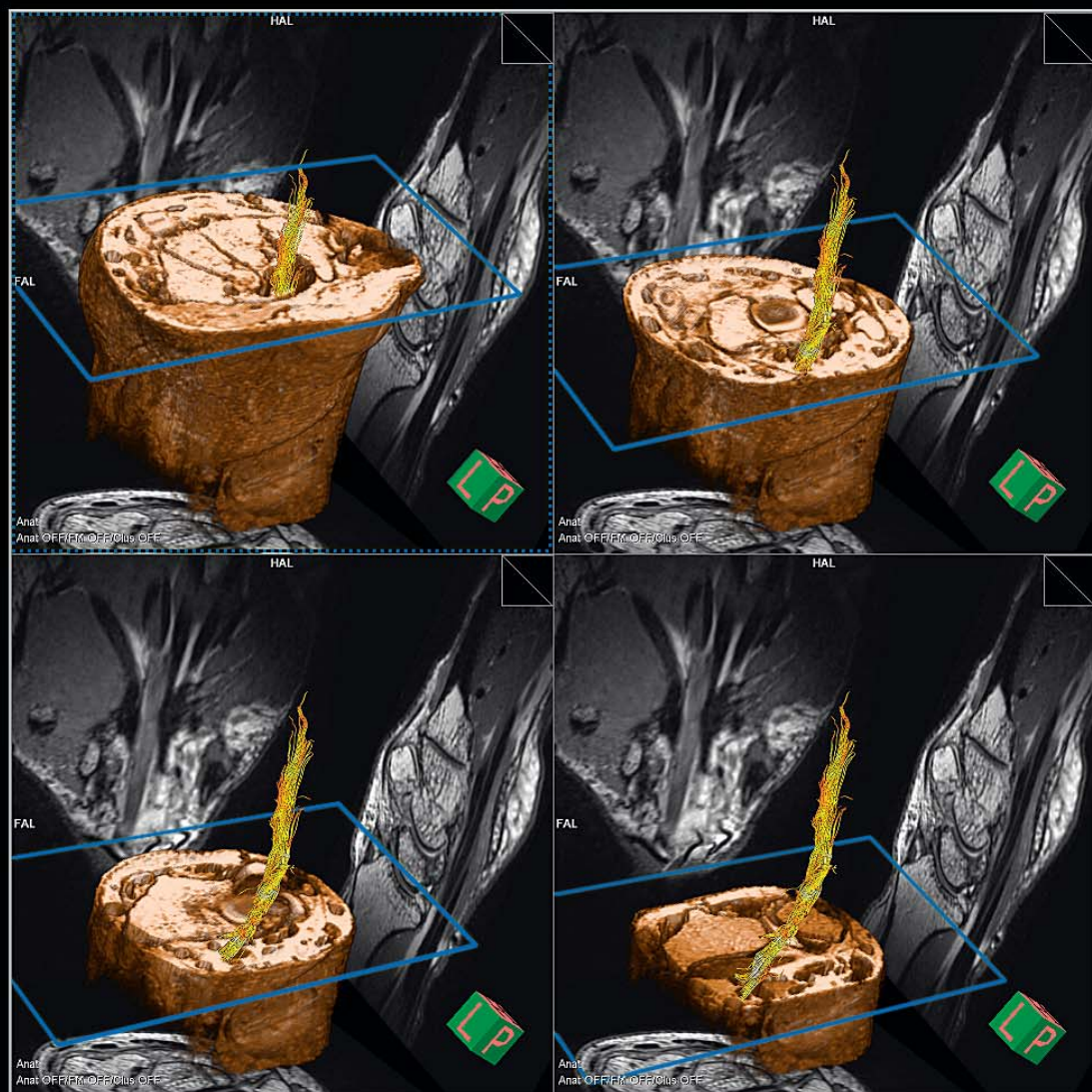
Pediatric Cardiovascular
MRI at 3T
Page 72

Technology

TrueFormTechnology
Page 114

Parallel Transmit
Technology
Page 124

Patient Applications Transfer Edit View Image Tools Scroll Evaluation System Options Help



Waiting for patient registration.



syngo DTI Wrist Postprocessing

40

Dr. Ioannis Panagiotelis



Dear MAGNETOM user,

Back in 2005 a Flash editorial predicted that by the end of 2008 3T MRI would emerge as a mainstream investment for all types of hospitals and not exclusively in university settings. Today, with approximately 800 Siemens 3T systems already sold in 46 different countries, it is clear that 3T MRI has more than met our expectations.

MAGNETOM Trio is currently the most popular system in academic and research settings. It has been installed in over 200 different universities and university hospitals worldwide. Indeed, several universities operate as many as 4 different Trio systems. MAGNETOM Trio remains the system of choice for cutting-edge neuroscience centres and any institute performing breakthrough MRI research.

Throughout the world there is discussion about rising healthcare costs and the ageing population. At Siemens we have responded to this challenge by providing products that will enable our customers to diagnose faster and with more accuracy and confidence. Our new product lines will be easier to operate, provide increased options for clinical use, be more patient-friendly and help increase

our customers' competitive edge and success in the clinical environment. MAGNETOM Verio was introduced last year in line with this strategy as yet another step forward in 3T. It has already succeeded in becoming the best seller at 3T. MAGNETOM Verio also offers future security, flexibility and utilization diversity to healthcare providers seeking the most secure investments against the current background of economic uncertainty. As a one-size fits-all kind of system it has become extremely popular.

The combination of 3T with a 70 cm bore and Tim technology unites in a single system most of the valuable experience we have gained over recent years with the introduction of MAGNETOM Espree and the MAGNETOM Trio in 2004 and 2005 respectively. With almost 35% of the adult population in the USA recognised clinically obese and with this trend of increasing obesity occurring elsewhere in the world, an open bore architecture becomes a necessity. MAGNETOM Verio has all the characteristics of a high-end device by providing, for example, strong gradients and advanced shim performance. It also boasts TrueForm Design, an innovation

aimed at reducing 3T-related image artifacts.

In this issue of MAGNETOM Flash we have tried to include as diverse a range of material as possible. An overview on using 3T in private practise is followed, for example, by case studies from most areas of radiology as well as from a variety of sources from around the world. Special articles cover subjects ranging from 3T in pediatrics to intraoperative applications. The technology section demonstrates results from elite academic sites using the new 32-channel coils, as well as detailed articles explaining how TrueForm actually works and what it does.

We hope you will enjoy reading about, and be inspired by, all this and more in this 3T special issue of MAGNETOM Flash.

Regards,

Dr. Ioannis Panagiotelis
Global Marketing Manager
Premium MRI

MAGNETOM Flash is part of Life, Siemens' unique customer care solution that helps you get the most from your investment. With its programs and services Life sharpens your skills so you can see optimal clinical value. It provides the support you need to maximize productivity and it assures that as technology changes, you will always be at the cutting edge.

The Editorial Team

We appreciate your comments.

Please contact us at magnetomworld.med@siemens.com



Matthias Lichy, M.D.
Editor in Chief



Antje Hellwich
Associate Editor



Dagmar Thomsik-Schröpfer,
Ph.D., MR Marketing-Products,
Erlangen, Germany



Okan Ekinci, M.D.
Center of Clinical Competence –
Cardiology
Erlangen, Germany



Heike Weh
Clinical Data Manager,
Erlangen, Germany



Bernhard Baden
Clinical Data Manager,
Erlangen, Germany



Ignacio Vallines, Ph.D.
Applications Manager,
Erlangen, Germany



Wellesley Were
MR Business Development
Manager
Australia and New Zealand



Milind Dhamankar, M.D.
Sr. Director, MR Product
Marketing, Malvern, USA



Michelle Kessler, US
Installed Base Manager,
Malvern, PA, USA

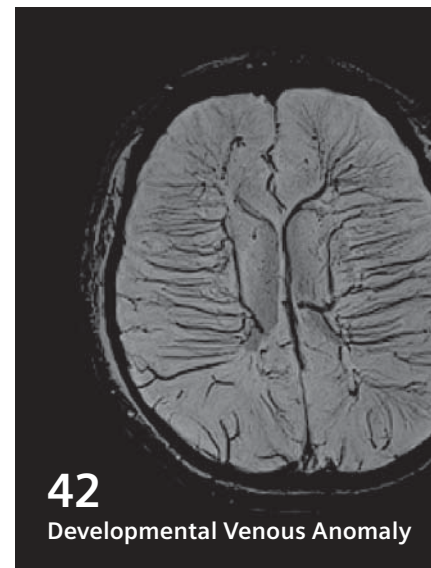
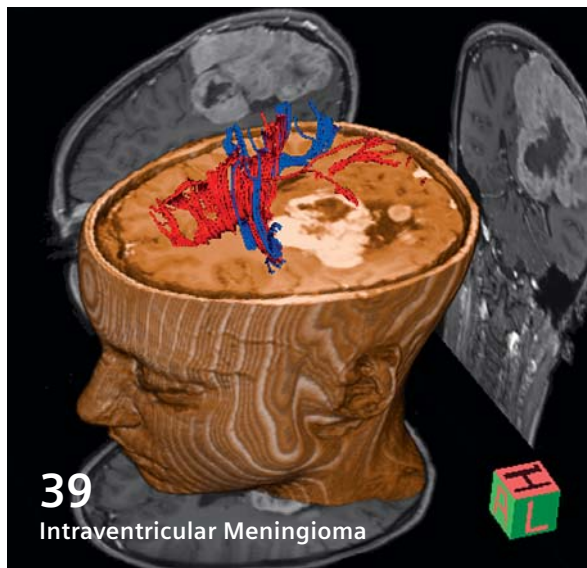


Gary R. McNeal, MS (BME)
Advanced Application Specialist,
Cardiovascular MR Imaging
Hoffman Estates, USA



Dr. Sunil Kumar S.L.
Senior Manager Applications,
Canada

Content



- 6** 3T MAGNETOM Verio in Clinical Routine
Markus Lentschig
- 22** MAGNETOM Verio – An Initial Indian Experience
Sumita Kundu, S. K. Sharma

Clinical Neurology

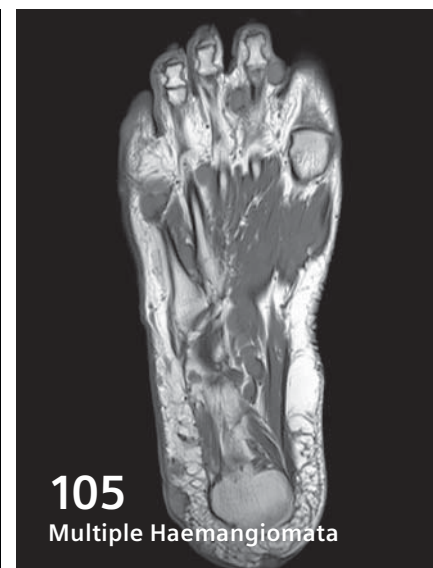
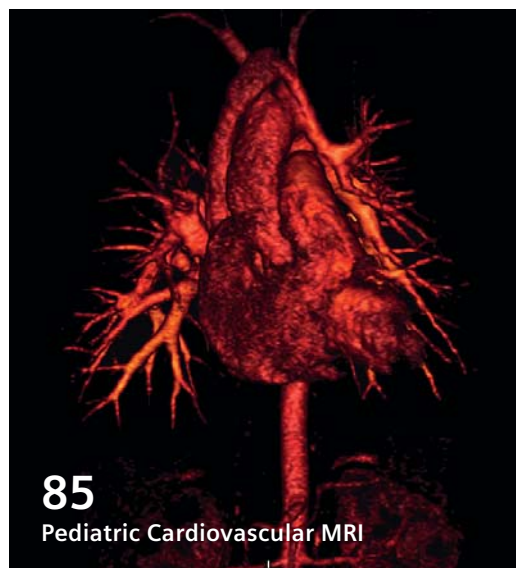
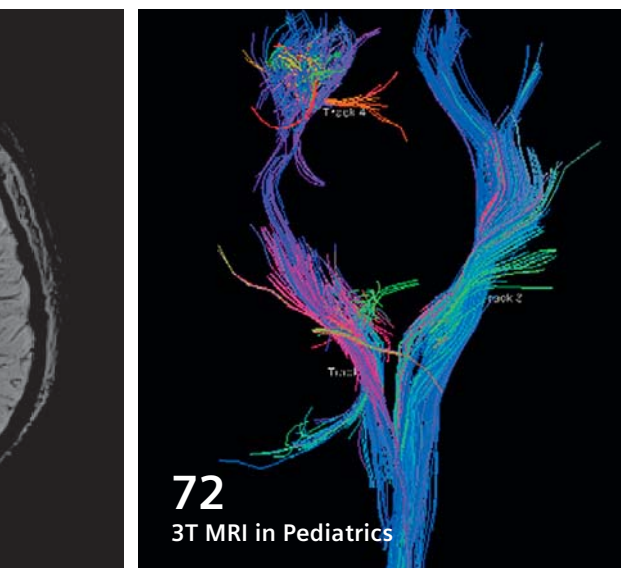
- 32** Case Report: Meningitis
Kirralie Lyford, Richard O'Sullivan
- 34** Case Report: Leptomeningeal Disease on Susceptibility-Weighted Imaging (syngo SWI)
Noelene Bergen, Nick Ferris
- 36** Case Report: DTI for Presurgical Evaluation in Case of Hippocampal and Mesial Sclerosis
Vicente Belloch
- 39** Case Report: Intraventricular Meningioma
Vicente Belloch
- 42** Case Report: Developmental Venous Anomaly
Masahiro Ida
- 44** Brain Spectroscopic Imaging at 3T with the 32-Channel Phased-Array Head Coil
Gregory Sorensen, et al.
- 50** Clinical Validation of Arterial Spin Labeling
Jessica A. Turner, et al.

Clinical Orthopedic Imaging

- 54** Magnetic Resonance Imaging in Inflammatory Arthritis
Marius Horger
- 60** Case Report: Right Hip and Hamstring
Kirralie Lyford, Richard O'Sullivan

Clinical Abdomen / Pelvis

- 62** Case Report: Rectum
Kirralie Lyford, Richard O'Sullivan
- 64** Case Report: Rectal Cancer Staging
Noelene Bergen, Nick Ferris



Clinical Women's Health

- 68** Case Report: MR Breast Imaging at 3 Tesla
Manfred Kontrus

Clinical Pediatric Imaging

- 72** 3T MRI in Pediatrics: Challenges and Clinical Applications
Charuta Dagia, Michael Ditchfield

Clinical → How I do it

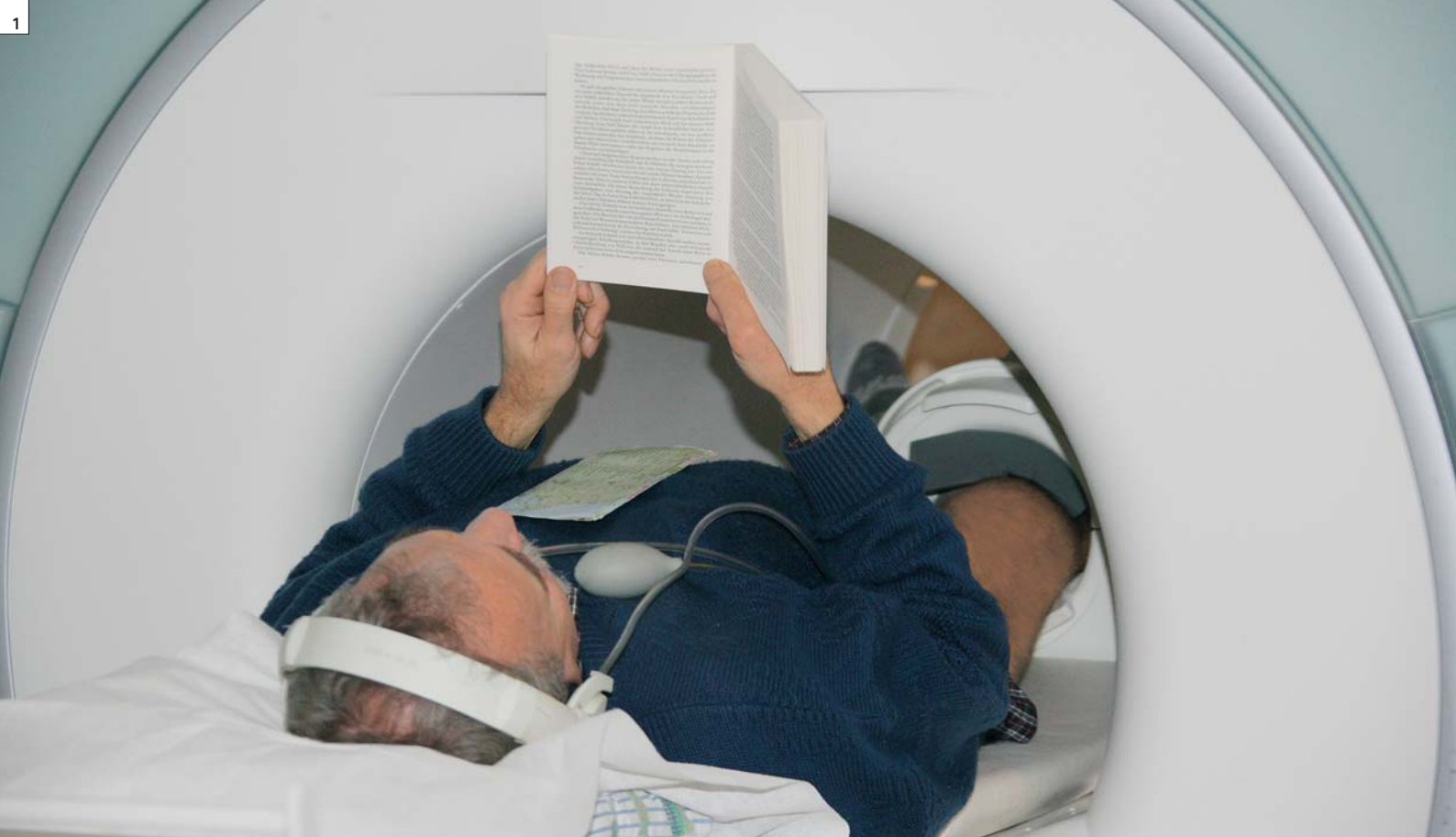
- 85** Pediatric Cardiovascular MR Imaging at 3T
Gary McNeal

Clinical Cardiovascular

- 102** Case Report: Thoracic Spine Angiogram
Kirralie Lyford, Richard O'Sullivan
- 105** Case Report: Multiple Haemangiomata
Noelene Bergen, Nick Ferris
- 107** Imaging of Carotid Atherosclerotic Plaque with 3T MRI Using Dedicated 4-Channel Surface Coils
Tobias Saam, et al.

Technology

- 114** TrueForm™ Design
Ioannis Panagiotelis, Mathias Blasche
- 120** TrueForm Retains the Spectral Integrity on the MAGNETOM Verio
Ravi Seethamraju, et al.
- 124** Parallel Transmit Technology for High Field MRI
Lawrence L. Wald, Elfar Adalsteinsson
- 136** Fast Clinical Protocols at 1.5T and 3T with Matrix and 32-Channel Head Coils
Thomas Benner
- 144** Large FOV Imaging at 3T with a 32-Channel Body Array Coil
Yutaka Natsuaki, Gerhard Laub
- 150** Improving High Resolution fMRI at 3T with the 32-Channel Head Array
Christina Triantafyllou, Lawrence L. Wald



1 MAGNETOM Verio's 70 cm bore.

3T MAGNETOM Verio in Clinical Routine

Markus Lentschig, M.D.

MR and PET/CT Imaging Center Bremen Mitte, Bremen, Germany

Introduction

The MR and PET/CT center operating within the Bremen-Mitte clinic – a maximum care hospital providing approx. 1,200 beds – was privatized in 1994 by Professor Terwey. It works in close cooperation with Siemens Healthcare. The current equipment park includes a 1.5T MAGNETOM Avanto (76/32, T-class) installed in August 2004, a 1.5T MAGNETOM Espree (76/18, I-class), installed as the first system in

Europe in December 2004, and a 3T MAGNETOM Verio (102/18) that became operational in January 2008.

The operators of the MR and PET/CT center Bremen-Mitte postponed the procurement of a 3 tesla MR system for many years. Since it was needed to provide both outpatient and inpatient radiology, the MR system had to be suitable for clinical routine. The higher magnetic field strength changes a number of phys-

ical effects as compared to 1.5 tesla systems and for many years, high-field magnetic resonance tomography (3 tesla) had been reserved for dedicated examinations, especially in the area of neuro radiology or orthopedics. While the signal-to-noise ratio (SNR) increases with a higher magnetic field, the resonance frequency, the T1 and T2* relaxation times, the RF exposition and, as a result, the energy transfer to the patient are

also affected. Similarly, the dielectric resonance frequencies are changed and this may have a negative effect on image quality. Taken together, these differences let us to conclude that a 3 tesla magnet was not suitable for routine clinical application. In addition, the RF-specific problem of increasing the specific absorption rate (SAR) – i.e. the energy absorbed in the body over time due to RF stimulation – is frequently a limiting factor especially with ultra fast imaging, narrowing the possibility of routine operation for 3T systems even further. Another factor was the considerably higher cost structures not only with respect to procuring but also to operating the system due to its higher energy and helium requirements. With the announcement of the new 3T MAGNETOM Verio systems and the accompanying technical changes, including the larger bore diameter of 70 cm and the shorter magnet length of 1.72 meters, we decided early on to procure the system as a replacement for the 1.5T MAGNETOM Symphony installed in 1997.

Installation

After dismantling the MAGNETOM Symphony and slightly modifying the RF-room (“3T fits in the footprint of 1.5T”), the system was delivered on January 8, 2008. The installation time was a total of 10 days. Because both physicians and employees were thoroughly familiar with the *syngo* user interface, MAGNETOM Verio was implemented in clinical routine in the afternoon of January 18, 2008, three days ahead of the planned start-up on January 21, 2008. The multifaceted sequence spectrum with its software pre-installed by Siemens allowed direct system implementation without large changes to the measurement sequences. The measurements corresponded in principle to the known sequences of the 1.5T systems MAGNETOM Avanto and MAGNETOM Espree. In parallel to routine

diagnostics, only the protocols needed to be fine-tuned in the coming weeks and months according to the special requirements of our institute.

Technical advantages of the Verio 3T systems

MAGNETOM Verio is an ultra light magnet with “zero helium boil-off”, which reduces the life-cycle costs. Considering the helium shortage of the past years, this is quite a bonus.

The magnetic field strength twice that of 1.5 tesla systems, increases the signal, essentially doubling the SNR. However, the higher magnetic field strength changes the relaxation times and makes for stronger susceptibility effects so that, depending on their influence, the real signal gain does not correspond to 100% for all measurements. The increase in SNR can be used to shorten the acquisition time as compared to 1.5T with the same spatial resolution or vice versa, to increase spatial resolution at the same acquisition time, that is, to improve the quality of the examination, for example, through improved detail display, higher resolution, thinner slices, or a higher matrix. During routine examinations we usually combine both effects, i.e. we use sequence protocols with higher resolution and tolerable acquisition times. As a result, we obtain higher diagnostic safety, higher patient comfort, and consequently higher system acceptance.

The quality of spectroscopy benefits from the 3 tesla technology which is routinely used in our institute for neurological questions (brain tumors, dementia diagnosis) or for prostate examinations (tumor diagnostics). Due to the larger chemical shift with 3 tesla, a considerably improved spectral resolution is obtained. In addition, applications such as diffusion imaging use the higher signal intensity, in particular diffusion tensor imaging (*syngo* DTI). Due to the increase in

susceptibility artifacts with increasing magnetic field strengths, the BOLD (Blood Oxygen-Level Dependent) contrast is also higher and functional imaging is improved. Similarly, “arterial spin labeling” (ASL) techniques can be performed with a noticeable gain in signal. The introduction of the so-called “TrueForm Design” – combining “TrueForm Magnet Design”, “TrueForm Gradient Design”, and “TrueForm RF Design” – supported the implementation of 3 tesla systems in clinical routines. The “TrueForm Magnet Design” follows the human body. It is therefore cylindrical and not oval, as in the past. The result is a more homogeneous magnetic field leading to fewer B_0 artifacts. By doubling the magnetic field strength, the proton resonance frequency also doubles and affects the RF technology, especially the dielectric effects. The resulting artifacts appear as inhomogeneous image brightness that could obscure pathological findings. Through three-dimensional adjustments or estimations of RF fields in the human body and the associated specific absorption rate, more homogeneous B_1 field distributions are obtained that reduce the artifacts. This means that fewer so-called “shark bites” are present. Also, there is less need for overlaps when performing examinations with a large field-of-view (FOV). As a result whole-body examinations can be performed with the MAGNETOM Verio.

In addition, changes and improvements in the sequence technology have minimized typical RF problems. Special attention should also be given to parallel imaging which accelerates almost all common imaging sequences because it does not change the contrast characteristics of the sequence on which it is based. As a result, acquisition times and subsequently the SAR can be reduced. By shortening the inter-echo times by a spe-

cific acceleration factor in parallel imaging, it is possible to reduce susceptibility artifacts which in turn diminish local distortions during, e.g., EPI (Echo Planar Imaging) examinations. The disadvantageous reduction of the SNR with parallel imaging is at least partially compensated for by the higher magnetic field strength. As a result, higher acceleration factors can be used as compared to 1.5 tesla systems, especially when using multi-channel transmit and receive coils, e.g. the 15-channel knee coil.

The SAR can be also reduced by pulse sequences with longer RF pulses, gradient echoes or hyper echoes. Another method are sequences with variable flip angles.

Expanding the magnet aperture to 70 cm and having a relatively short magnet of 1.72 m for 3 tesla increases patient acceptance and makes the system suitable for routine operations (Fig. 1). This was an essential decision criterion for us because we had already made such positive experiences with the MAGNETOM Espree, a system that uses a larger bore. Patients who are particularly claustrophobic or extremely adipose (weighing up to 250 kg) appreciate the larger bore enough to significantly reduce the administration of sedatives at our institute. The larger magnet aperture is also advantageous for patients with position-dependent pain by allowing them to be positioned with bent legs or on the side. A larger bore diameter is also highly suitable for examining the most varied orthopedic functions. In addition, the acquisition time can be shortened for anxious patients due to the higher signal intensity.

Again this increases patient acceptance

of these types of examinations.

The optimally linked magnet design, the RF pulses, the gradients, and the examination sequences resulted in the application of 3 tesla technology and thus MAGNETOM Verio in clinical routine diagnostics where it is readily tolerated by patients. With our examinations, SAR warnings did not appear more frequently on the monitors than with 1.5 tesla systems.

Another considerable advantage in routine examination is the Tim (Total imaging matrix) technology which we already use on both 1.5 tesla systems. The multi-coil concept and parallel imaging in combination with technical improvements, such as "scan@center", "AutoCoil Select", "Inline composing" or even "syngo Tim-CT", provide for considerably easier examination planning with almost no changes in patient positioning and coils. In addition, whole-body examinations for patients up to 198 cm in height are possible. Furthermore, the workflow was largely improved by facilitating planning of larger examination volumes or so-called "multi-station" examinations in different table positions as well as by providing easy to operate "Set-and-Go" protocols.

Tim Planning Suite

Technologists performing examinations at the Verio, find the workflow largely simplified and improved. Tim technology allows easy planning, especially for whole-body examinations, angiography or examination of the entire spine. For these "multi-station" examinations, the localizers of the different stations are already combined via Inline composing. This means that the technologists can

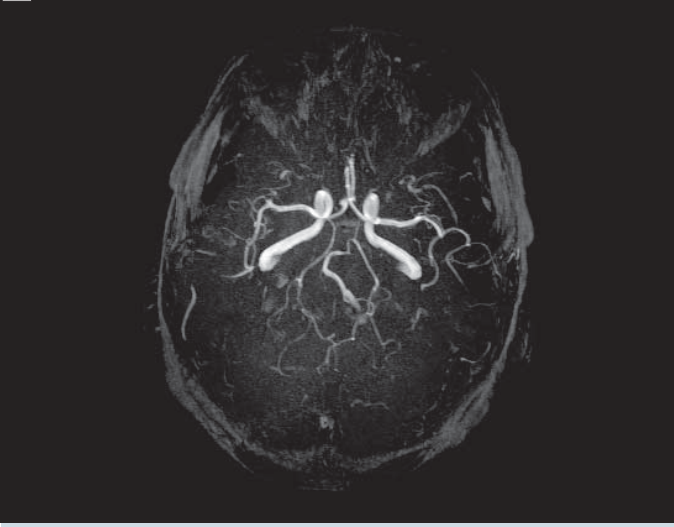
use the composed localizers and plan as well as perform the remaining course of the examination, making patient repositioning or coil changes unnecessary. To ensure the best possible magnetic field homogeneity, the existing "scan@center" technology guarantees that the measurement volume to be examined is always positioned in the magnet isocenter. At the same time, the necessary coils are detected and selected with "AutoCoil Select" which avoids any kind of error. The workflow is further improved by the ease of use of the "Set-and-Go" protocols, also leading to shorter examination times.

Tim Neuro Suite

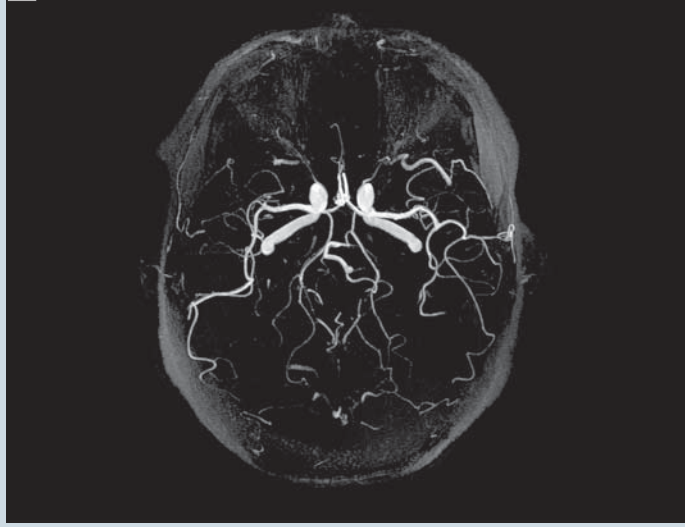
All neuro applications used with 1.5 tesla systems can be implemented using the 3T MAGNETOM Verio leading to significant quality improvements because the improved SNR can be usefully applied in a variety of ways.

The extension of the longitudinal relaxation rate of static tissue as compared to blood is advantageous for MR angiography at 3T. Due to saturation effects, greater suppression of the static tissue is obtained. Time-of-flight (TOF) angiographies can be performed with much higher resolutions, using the same or reduced examination times. As a result, intracranial arteries can be evaluated far into the periphery (Fig. 2). Furthermore, the *syngo* SWI sequences (susceptibility-weighted imaging) implemented with, e.g., blood diagnostics are more sensitive with MAGNETOM Verio than with 1.5 tesla systems due to higher susceptibility sensitivities that help detect the smallest blood deposits or calcifications (Fig. 3).

2A

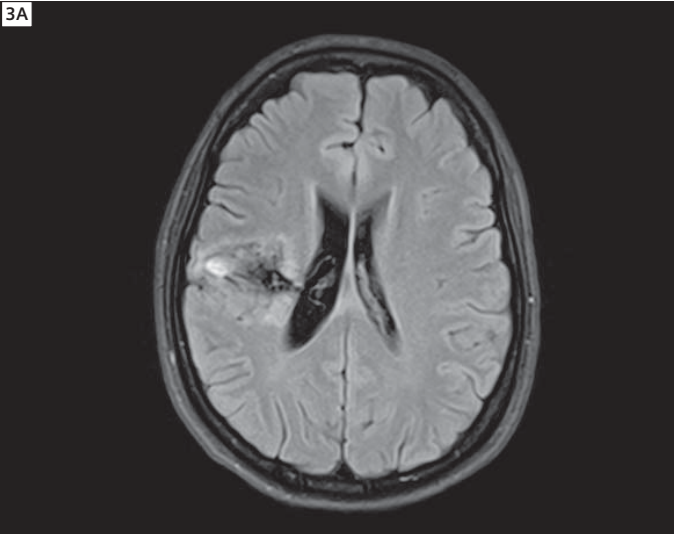


2B

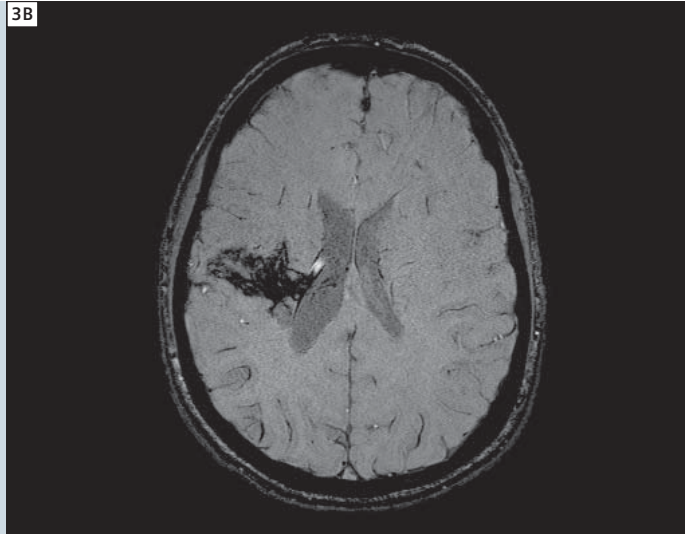


2 Time-of-flight (TOF) angiography of the intracranial arteries in the same patient. **A:** has been acquired on a 1.5T MAGNETOM Espree (matrix 192 x 384, FOV 167 x 200, TA 5:48 min). **B:** has been acquired on a 3T MAGNETOM Verio (matrix 662 x 768, FOV 181 x 200, TA 4:56 min).

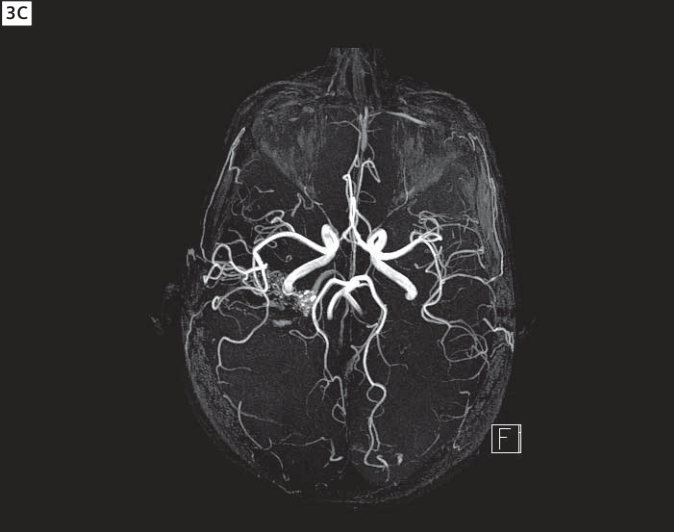
3A



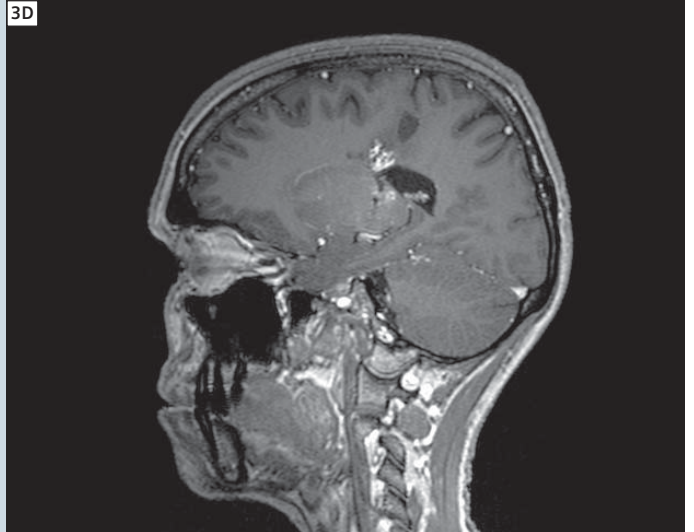
3B



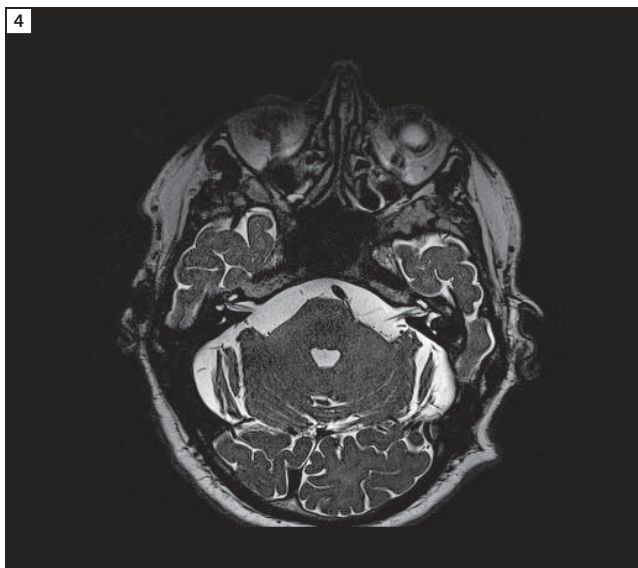
3C



3D



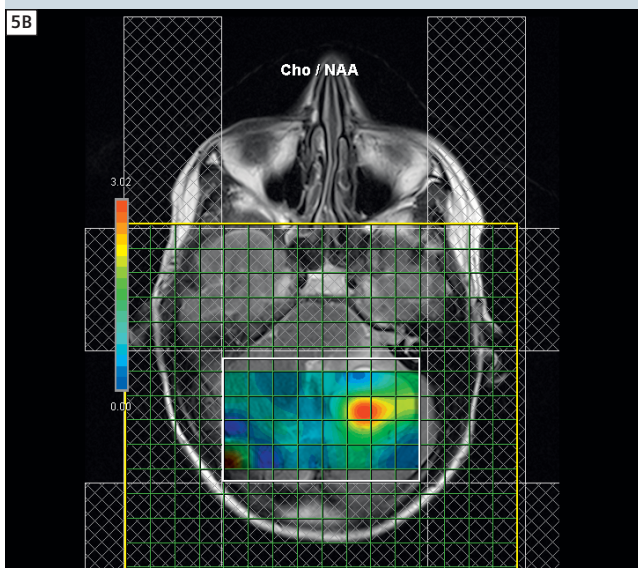
3 AV-Angioma. **A:** FLAIR, p2 9000/94/2500, matrix 388 x 512, FOV 230, TA 01:52 min. **B:** syngo SWI (susceptibility-weighted imaging) 3d p2 28/20, matrix 262 x 448, FOV 230, TA 03:25 min. **C:** Time-of-Flight p2, 22/3,9, matrix 662 x 768, FOV 200, TA 06:36 min. **D:** 3D FLASH p2 1900/2,5/900, matrix 492 x 512, FOV 250, TA 04:17 min.



4 T2-weighted SPACE 3D. Matrix 380 x 384, FOV 200 x 200, slice thickness 0.5 mm, TA 04:16 min.



5A Hemangioblastoma of the left cerebrum.



5B Chemical Shift Imaging (CSI) spectroscopy showing significantly increased Cholin and reduced N-Acetylaspartat in the tumor (increased Cholin/NAA – ratio).

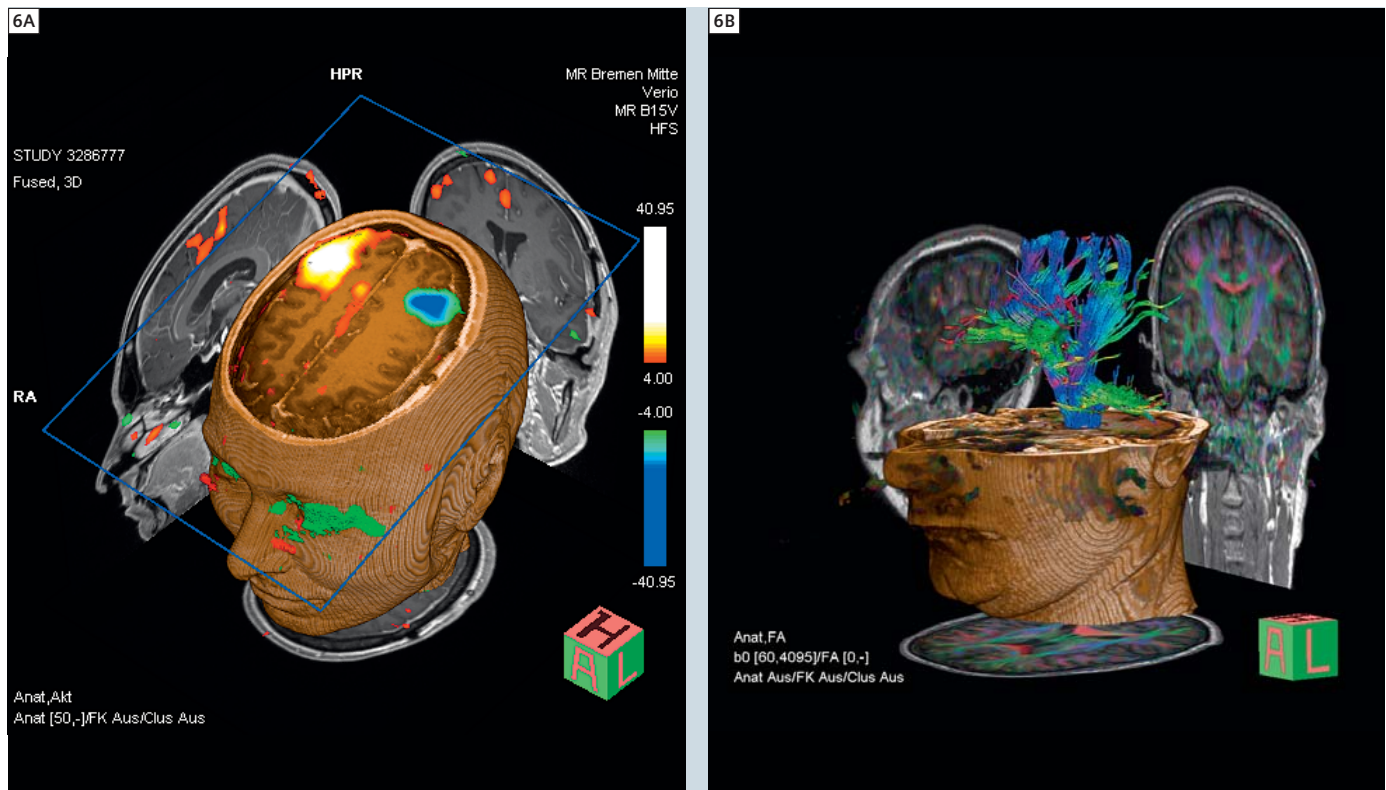
The quality of the *syngo* SPACE sequence was also greatly improved by using 3T technology. Examinations with isotropic voxels, including in the sub-millimeter range, are possible (Fig. 4), resulting in largely improved reconstructions in all planes.

Advanced neuro applications such as functional imaging (fMRI), spectroscopy or diffusion tensor imaging (*syngo* DTI) can also be implemented in routine application due to their continuously good image quality and easy workflow. Today, these examination methods are no longer reserved for just scientific centers. In tumor diagnostics as well as in the diagnosis of neurodegenerative diseases, our institute uses spectroscopy, mostly with CSI (chemical shift imaging) technology, as routine method or to obtain and evaluate additional information for differential diagnosis (Fig. 5). In addition to increasing the SNR, doubling the field strength also doubles the frequency differences of the various metabolites. This results in higher frequency resolution, a higher spectral resolution, and a sharper delineation of the spectral peaks. Especially in the primary diagnostics of malignant brain tumors, functional imaging (in routine examinations, only motor centers are displayed via finger tapping) and DTI measurements (e.g. for displaying the pyramidal tract and proof or exclusion of tumorous infiltration) are very helpful for the neurosurgeon (Fig. 6). Also the time involved for these measurements allows for execution even during primary diagnostics.

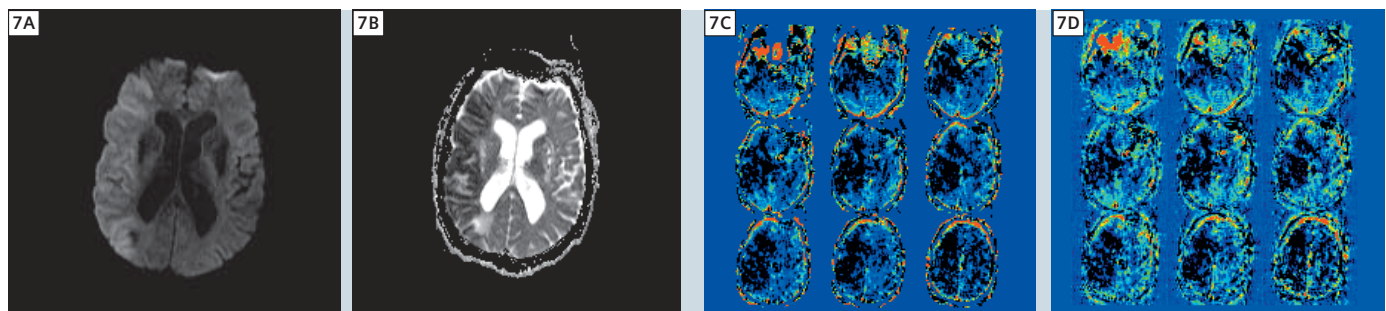
The BOLD contrast is based on the different susceptibilities of oxygenated (diamagnetic) and deoxygenated (paramagnetic) blood. In activated brain regions, the paramagnetic deoxygenated blood increases locally. Since the sensitivity of susceptibility rises with increasing field strength, this signal is stronger at 3 tesla than at 1.5 tesla.

The gain in signal with diffusion tensor imaging is as much as 50%.

As a product to be clinically applied, the MAGNETOM Verio provides for the first time the ASL technique (arterial spin labeling) for perfusion measurements, e.g. in the brain without the use of gad-



6 Functional MR imaging (fMRI). **A:** syngo DTI finger tapping experiment. **B:** Tractography of the pyramidal tract.



7 Acute occlusion of the right a. cerebri media. **A:** Hyperintense signal on the diffusion-weighted image. **B:** Corresponding signal loss on the ADC map. **C:** syngo ASL revealed a significantly lowered perfusion within the whole right a. cerebri media blood supply area and **D:** a significant reduction of the relative cerebral blood flow.

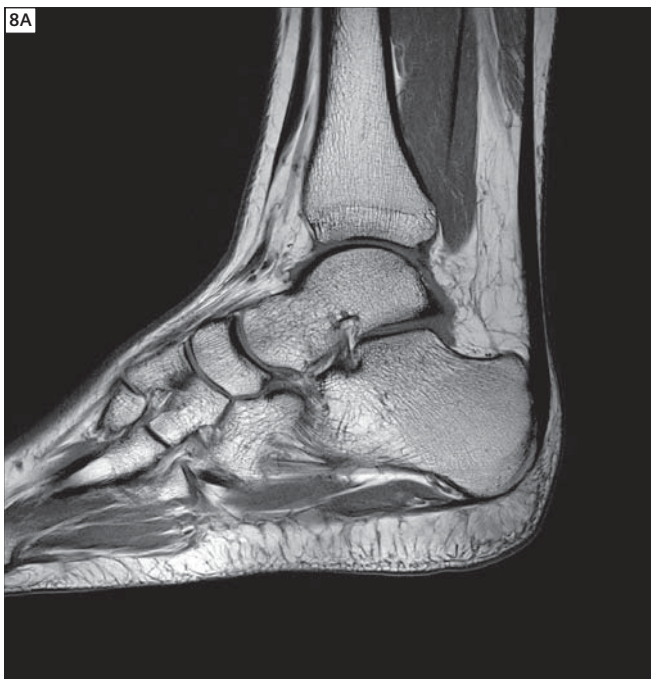
olinium-based contrast agents. This is especially advantageous for multi-morbid stroke patients with frequently limited or unclear renal functions while considering the current Nephrogenic Systemic Fibrosis (NSF) problem (Fig. 7). The ASL perfusion contrast increases due to the improved SNR and the T1 values at 3 tesla. The use of the Tim Planning Suite allows, for example, the examination

of the entire spine in a simple workflow. The individually acquired images in the different stages are automatically combined via Inline composing. Because the T1 relaxation time is extended by 30 to 50% at 3 tesla (versus 1.5 tesla), it clearly affects T1-weighted images. As compared to examinations at 1.5 tesla, T1 contrast of the spine (sagittal) is reduced at 3 tesla, which means that the contrast of the vertebral body is reduced as well.

Possible diagnostic misinterpretations are to be ruled out by supplementary STIR contrast measurements that are regularly taken for evaluating paravertebral structures.

Tim Ortho Suite

As compared to examinations with systems of lower field strengths, the improved quality of examinations with a 3T system is undisputed and also evident



8 Ankle, acquired using the 8-channel foot-ankle coil.
A: T1-weighted sagittal TSE, TR 1200 ms, TE 15 ms, matrix 717 x 896, FOV 180, SL 3.0 mm, TA 03:28 min.



B: T1-weighted coronal TSE, TR 1200 ms, TE 16 ms, matrix 571 x 1024, FOV 180, SL 3.0 mm, TA 03:29 min.

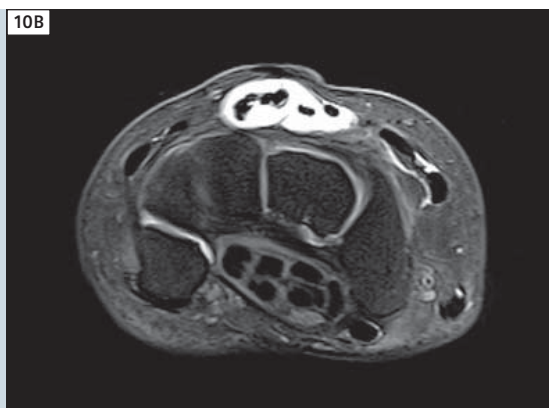
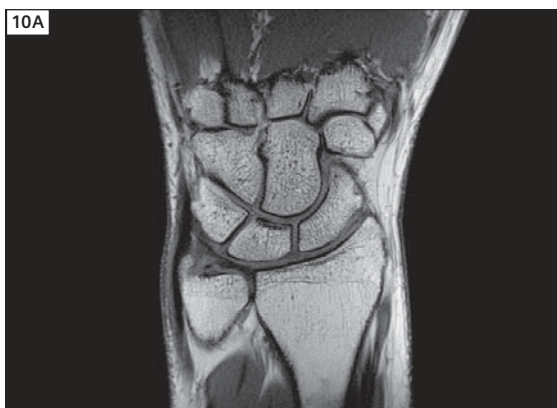
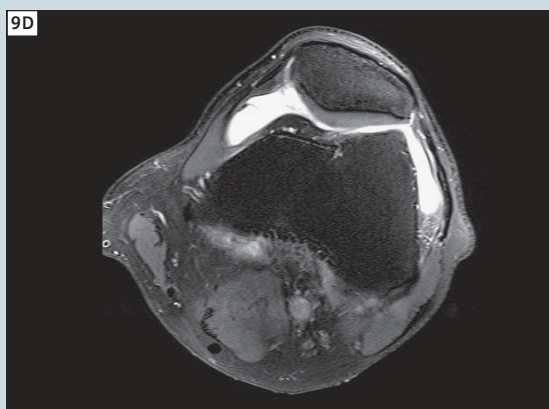
at the MAGNETOM Verio. In contrast to 1.5 tesla systems, spatial resolution can be increased at comparable examination times, allowing for examinations with a 1024 x 1024 matrix (Fig. 8) whereas images with an examination quality comparable to a 1.5T system are generated at considerably shorter acquisition times. A routine knee examination can be performed in 5 minutes (Fig. 9). At our institute, we usually combine the increase in resolution and the time-savings according to the purpose of the examination or the patient. Special coils, such as the 15-channel knee coil, the 8-channel wrist coil (Fig. 10) or the 8-channel foot and ankle coil, enable the use of parallel imaging with higher PAT factors. Again, these result in shorter measurement times and higher resolution.

Tim Cardio Suite

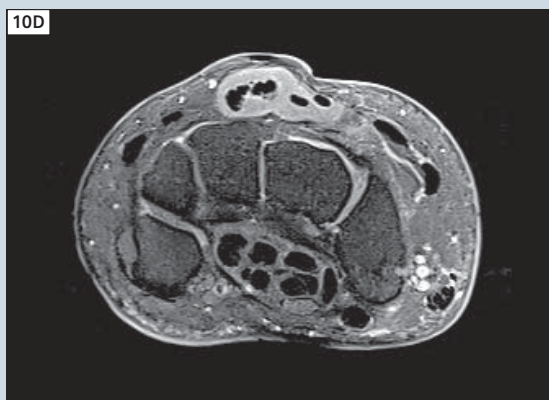
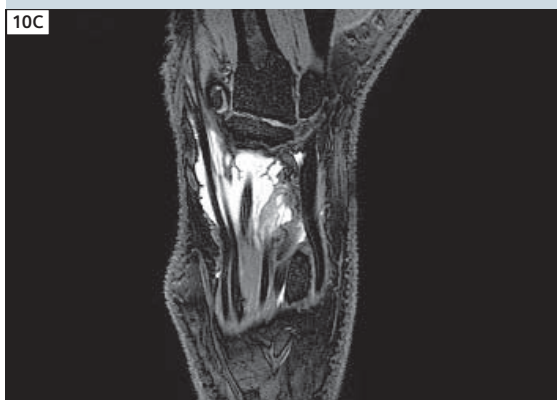
In cardio-vascular diagnostics too, MAGNETOM Verio offers advantages as compared to 1.5T systems. By doubling the field strength, the SNR is increased, especially with respect to morphological as well as functional or dynamic studies. Due to physical conditions, the sequences have to be in part adjusted to avoid 3T-specific artifacts. These include, for example, susceptibility effects that increase at 3 tesla, or "off-resonance" artifacts that reduce image quality as low-signal bands or ghosting artifacts. These banding artifacts typically occur, for example, when acquiring TrueFISP sequences used in cardio-vascular MR diagnostics for functional examinations. By using short repetition times as much as possible and special frequency adjustments, the artifacts are reduced or avoided. For frequency adjustments, an additional so-called "frequency scout" has to be

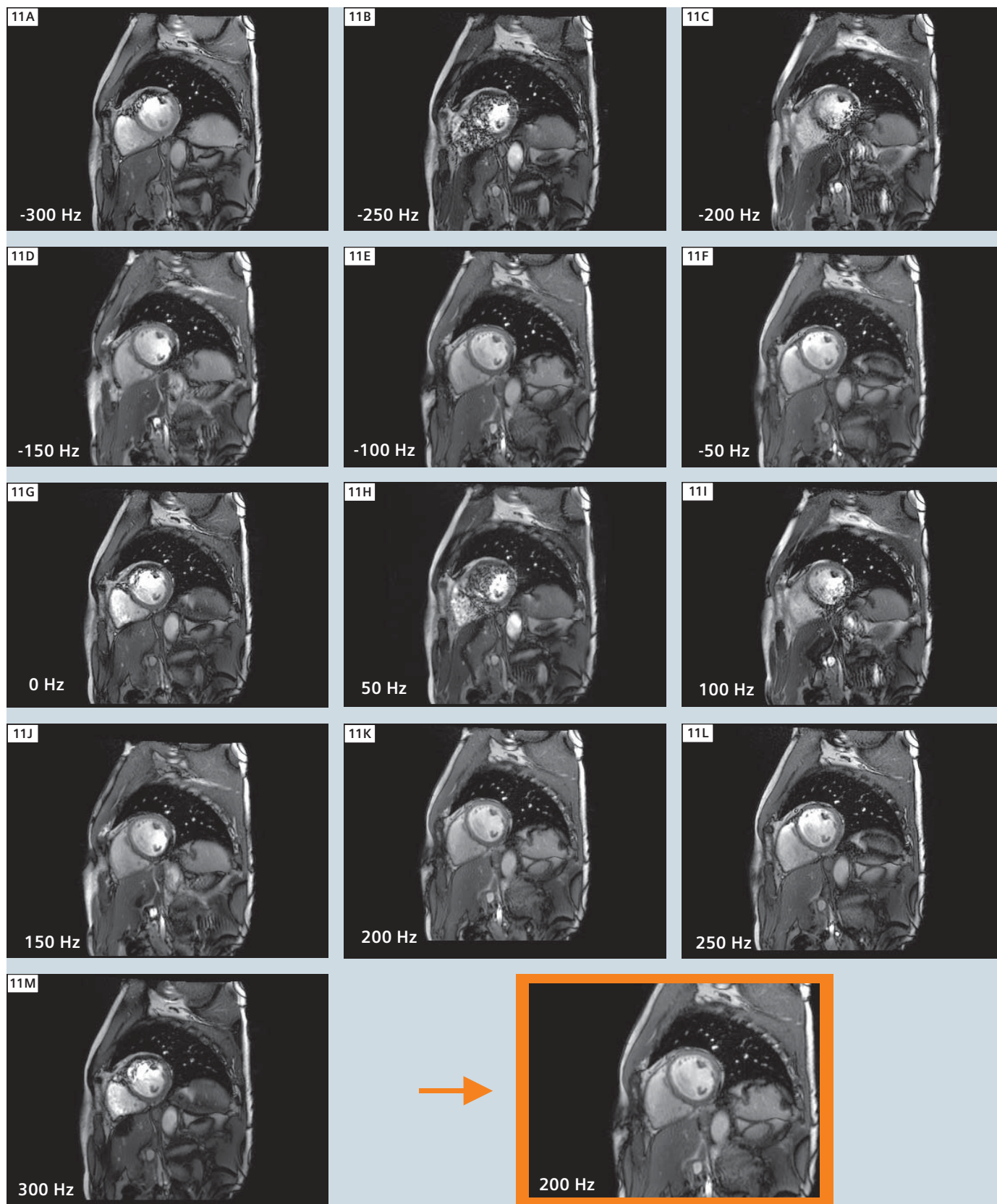


9 Chondromalacia.
A: T1-weighted sagittal TSE, TR 900 ms, TE 14 ms, matrix 464 x 640, FOV 180, SL 3.0 mm, TA 03:14 min.
B: Proton-Density-weighted sagittal image with fat saturation, TR 4500 ms, TE 35 ms, matrix 232 x 512, FOV 180, SL 3.0 mm, TA 0:58 min.
C: Proton-Density-weighted coronal image with fat saturation, TR 3460 ms, TE 35 ms, matrix 307 x 512, FOV 180, SL 3.0 mm, TA 01:23 min.
D: Proton-Density-weighted transversal image with fat saturation, TR 4080 ms, TE 41 ms, matrix 307 x 512, FOV 160, SL 3.0 mm, TA 01:50 min.



10 Ganglion of the extensor tendon.
A: T1-weighted coronal Turbo Spin Echo (TSE), TR 1180 ms, TE 16 ms, matrix 307 x 512, FOV 100, SL 1.5 mm, TA 03:13 min.
B: Proton-Density-weighted transversal image with fat saturation, TR 4400 ms, TE 38 ms, matrix 240 x 320, FOV 100, SL 3.0 mm, TA 01:59 min.
C: 3D DESS coronal, TR 16.5, TE 4.4, matrix 221 x 156, FOV 100, SL 0.4 mm, TA 04:17 min.
D: T1-weighted Turbo Spin Echo transversal with fat saturation, TR 1390 ms, TE 15 ms, matrix 230 x 384, FOV 100, SL 1.5 mm, TA 05:20 min.





11 Frequency scout, short axis. Acquisition with different frequencies. Banding artefacts are less prominent at a 200 Hz, therefore this frequency is used for the dynamic TrueFISP scan.

measured (duration approx. 30 s) to determine the frequency where banding artifacts are not present (Fig. 11). In the subsequent function measurement, the frequency determined is changed on the examination task card, reducing the artifacts.

For morphological sequences (T1, T2, T2 SPAIR), these adjustments are not necessary for tissue characterization and dynamic measurements. The improved SNR with MAGNETOM Verio noticeably increases the image quality, especially when reaching higher flip angles due to the use of parallel imaging. In this case, not only is the SNR increased, but so is the contrast-to-noise ratio (Fig. 12). The two high-resolution “whole heart” measurements for the three-dimensional display of the coronary arteries can also be generated with MAGNETOM Verio. However, in this case FLASH 3D techniques have to be applied that will result in a somewhat reduced tissue contrast because of the longer T1 time as compared to 1.5 tesla systems. To compensate for the reduced tissue contrast, “whole heart” measurements are high resolution images that allow for post-reconstruction adapted to the respective coronary artery (Fig. 13).

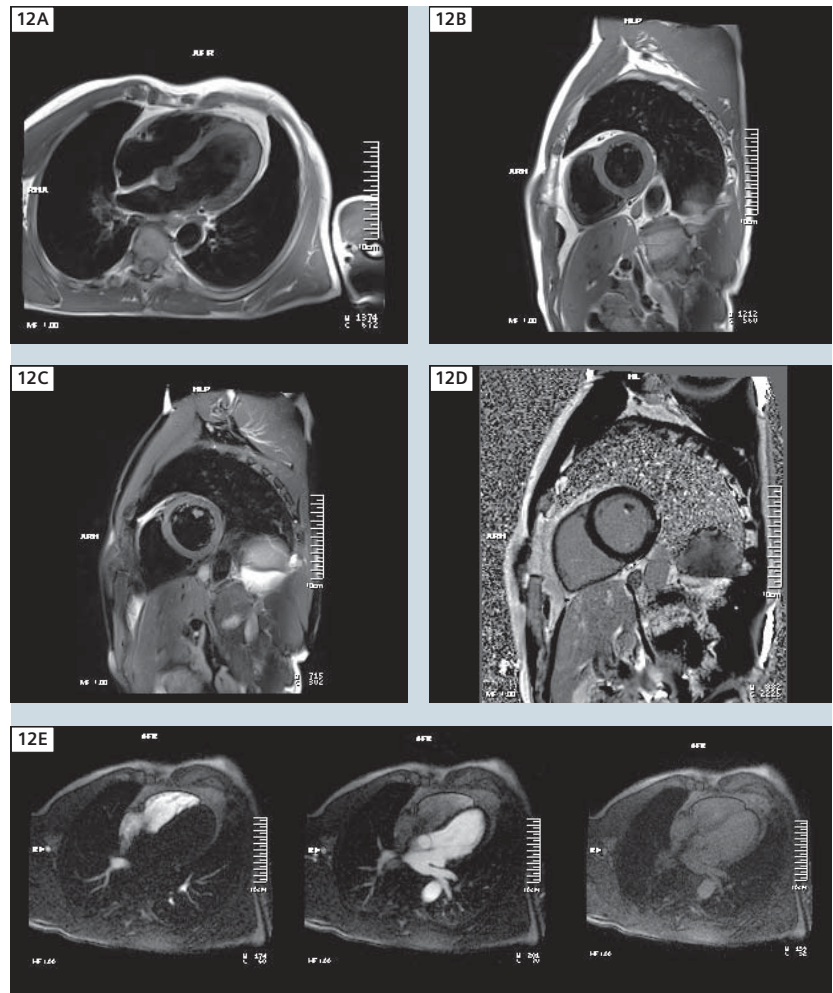
Tim Breast Suite

For detecting even small tumors in the breast, images with the highest possible spatial resolution have to be acquired within a short acquisition time while covering a large field-of-view. For anatomical displays, the higher SNR at 3 tesla is especially suitable for providing higher diagnostic safety.

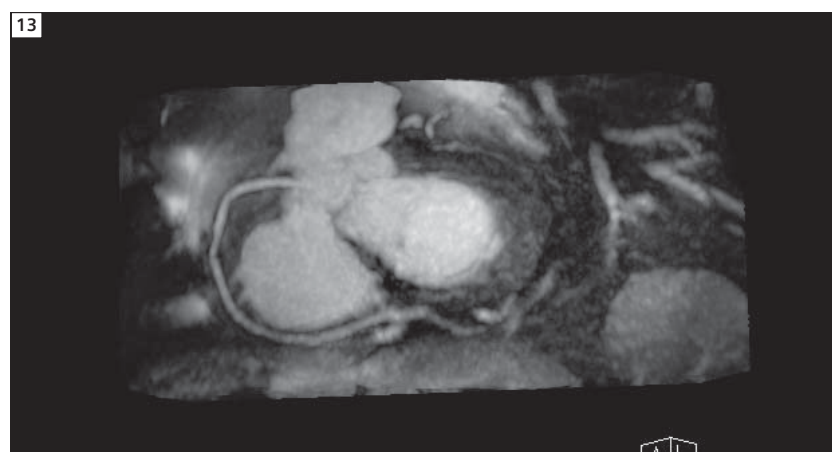
We also use the Verio with excellent results for MR mammography. With all measurements, we obtain a homogeneous fat suppression. The dynamic sequences are generated as 3D sequences with an effective slice thickness of 1 mm per 60 seconds acquisition time (Fig. 14). Subjectively, we reach a satisfactory signal increase in the images.

Tim Body Suite

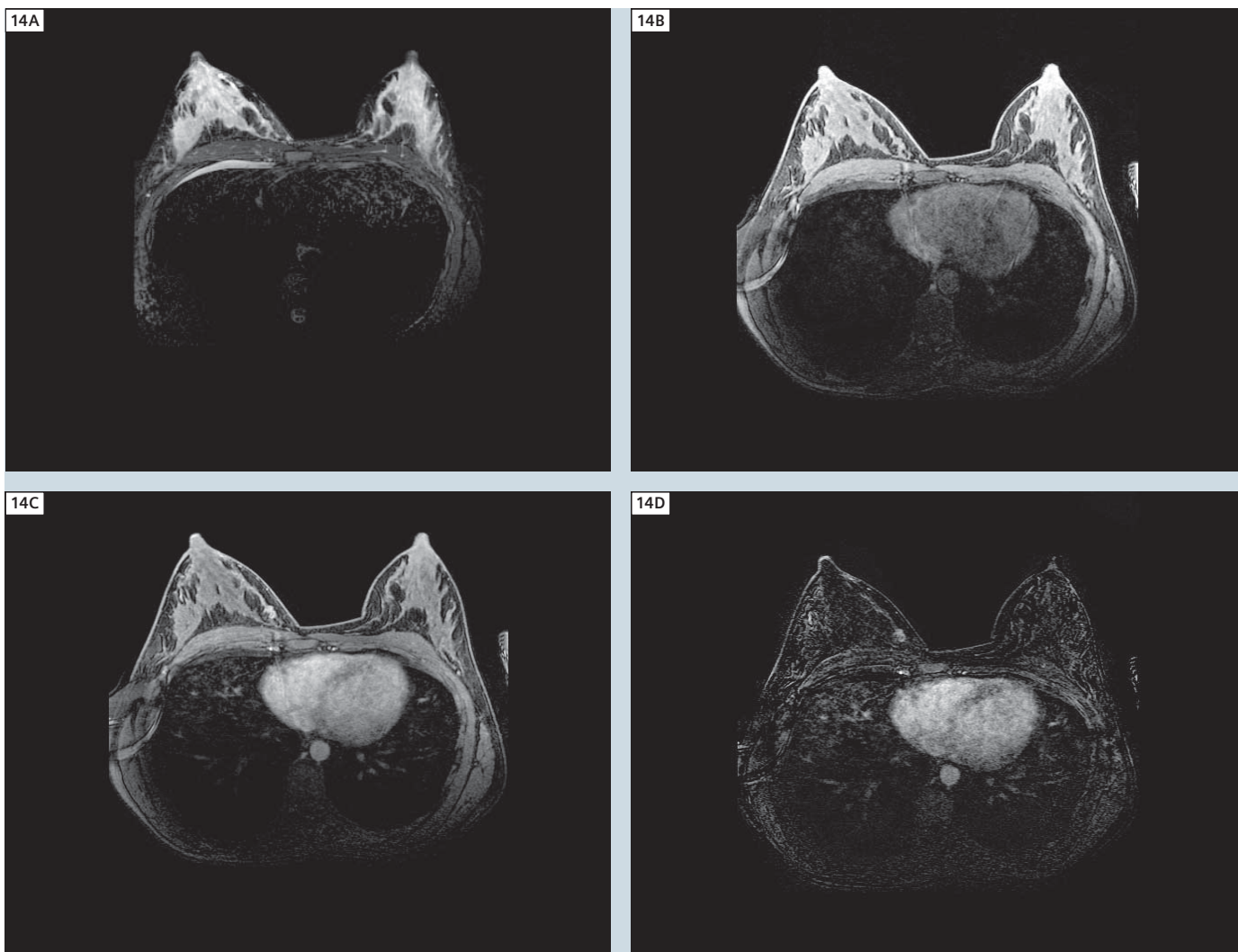
As in cardio-vascular diagnostics, imaging is negatively affected by the physiological respiratory motion and pulsation



12 Excellent signal-to-noise ratio of an examination with the MAGNETOM Verio
A: T1-weighted 4-chamber view B: T1-weighted short axis C: T2-weighted SPAIR short axis D: tissue characterisation E: dynamic scan.



13 Maximum Intensity Projection (MIP) of the right coronary artery. Whole heart measurement 3D FLASH TR 342 ms, TE 1.5 ms, 200 Hz, matrix 464 x 512, FOV 320, SL 0.9 mm, TA 05:31 min.

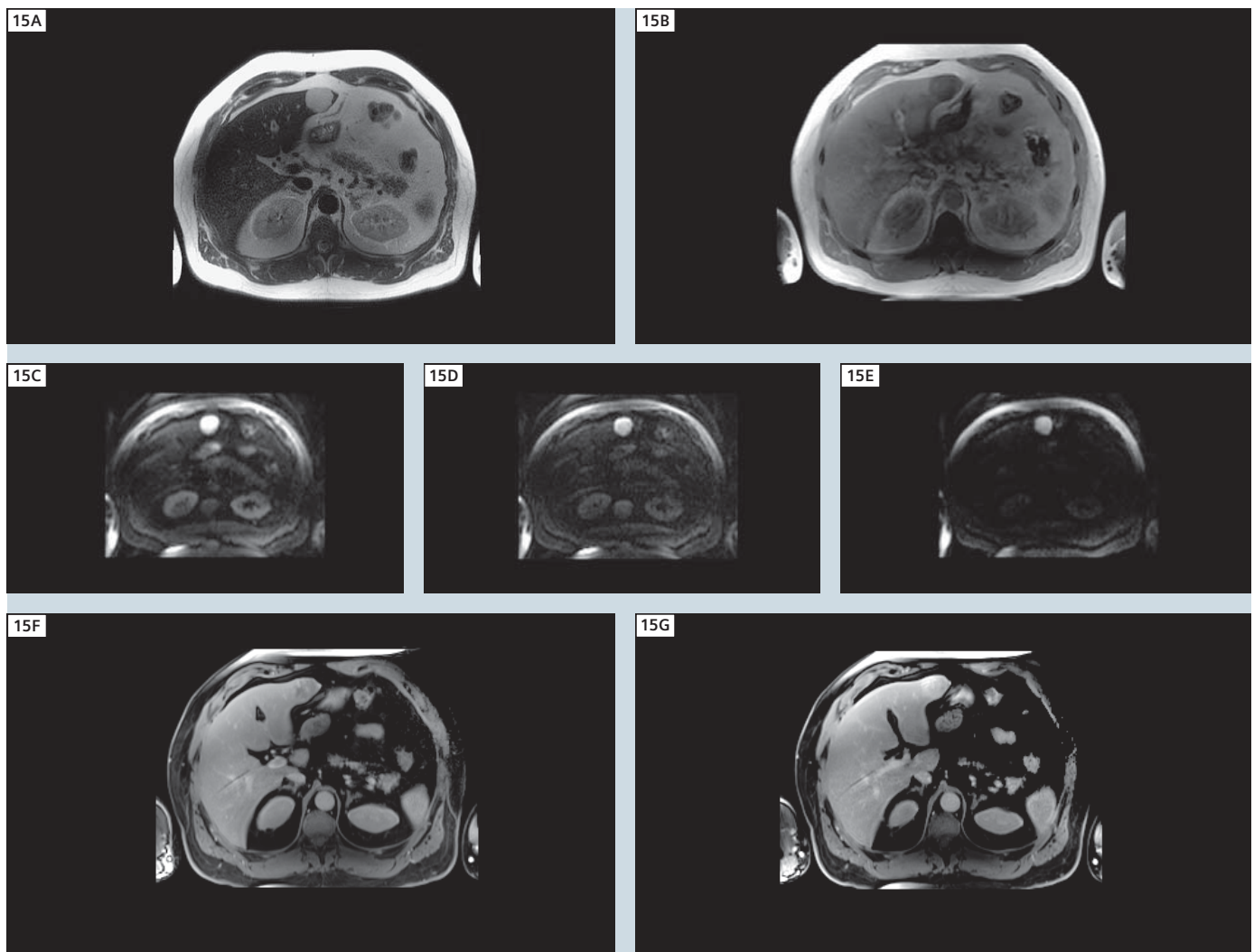


14 Ductal carcinoma within the right upper medial quadrant with local lymphangiosis carcinomatosa. **A:** TIRM, TR 4300 ms, TE 41 ms, TI 230 ms, matrix 314 x 320, FOV 313, SL 4.0 mm, TA 03:18 min. **B and C:** T1-weighted 3D FLASH p2, TR 4.5 ms, TE 1.6 ms, matrix 300 x 448, FOV 340, SL 1.0 mm, TA 01:00 min. **D:** Subtracted image.

of the vessels in abdominal diagnostics. Added to these are motion artifacts caused by gut mobility and increased susceptibility effects resulting from air in intestinal loops. To date, implementation of 3 tesla systems has been limited due to B_1 inhomogeneities caused by dielec-

tric effects. In part, these were signal changes limiting diagnostic findings, for example, in the left lobe of the liver. Additionally, due to the large field-of-view required for abdominal examinations, SAR limits were reached early so that examinations had to be performed

by increasing slice thickness or reducing the number of slices. These limited the implementation of routine diagnostics. Again, the optimally linked magnet design, the RF pulses, the gradients and the examination sequences for MAGNETOM Verio ensure that both the B_1 -inhomoge-



15 Haemangioma of the left liver lobe with signal intense visualization on A: HASTE image, low signal correlate on B T1-weighted f12d image and decreasing signal intensity on diffusion-weighted images (C–E; 50-300-600). F, G: Typical contrast behaviour after Gadolinium.

neities as well as the SAR problems, as described above, are noticeably reduced or avoided for abdominal diagnostics (Fig. 15). In case a mild form of B_1 inhomogeneities continues to be present with individual patients, additional B_1 filters can be implemented in the

measurement that increase acquisition times only slightly. Parallel imaging is gainfully employed in abdominal diagnostics as well, especially for shortening breathholds (Figs. 16, 17), which also contributes to improving the spatial resolution.

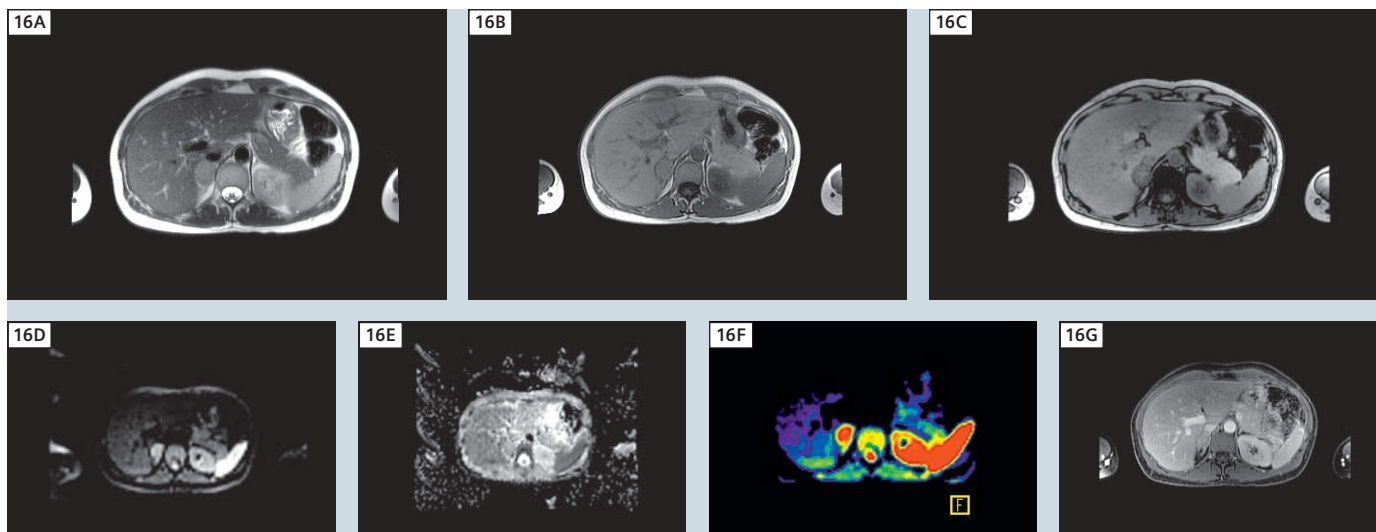
An examination including breathhold technique is not necessary for displaying pelvic organs. Therefore the higher SNR is used to increase spatial resolution, e.g. for the preoperative diagnostics of rectal cancer (Fig. 18) or other pathologies in the pelvis minor (Fig. 19),

including supplemental diffusion measurements. Also examinations that require a larger FOV, for example MR urography (Fig. 20), can be acquired.

Tim Angiography Suite

The positive effects of the longer T1 times at 3 tesla on time-of-flight (TOF) angiography have already been mentioned under the Tim Neuro Suite.

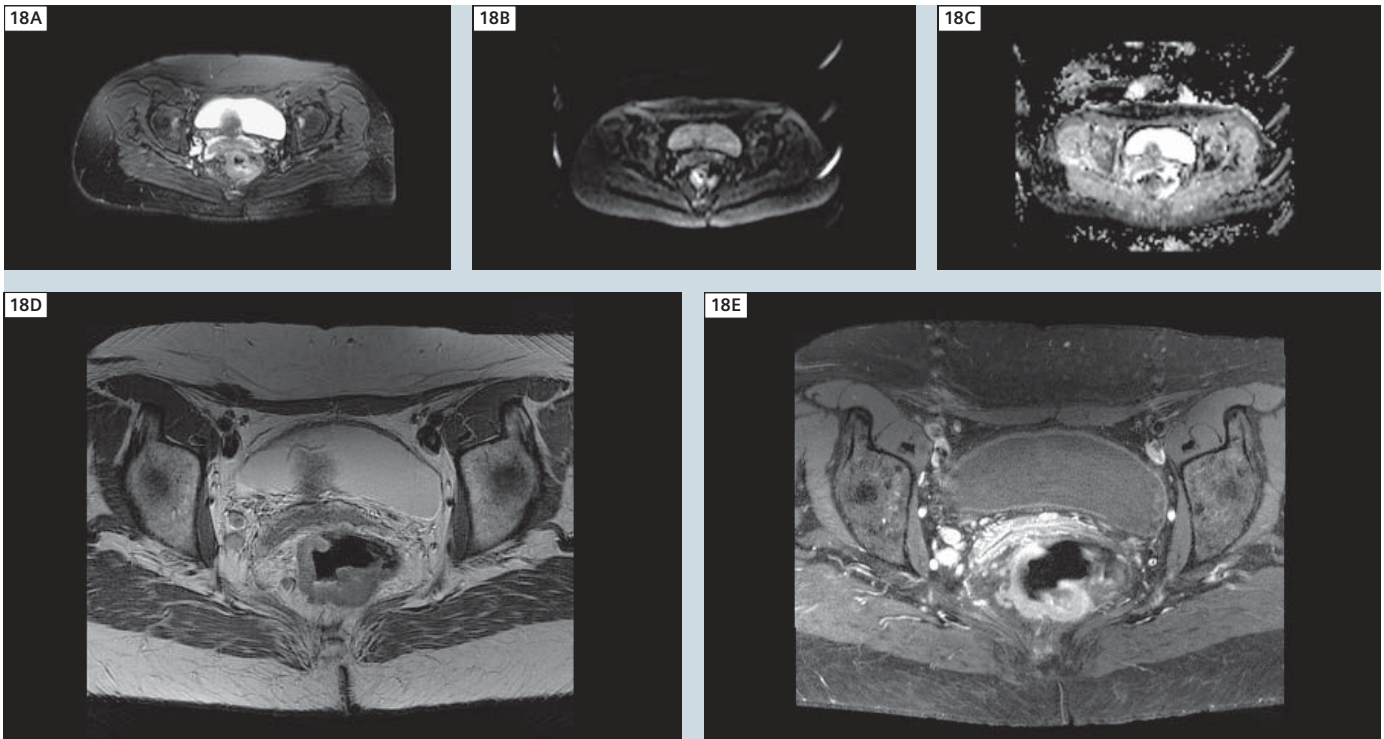
With the MAGNETOM Verio, it is possible to generate excellent high-resolution, temporal 4D studies. The same applies to pelvic-leg angiography and whole-body angiography which can be performed



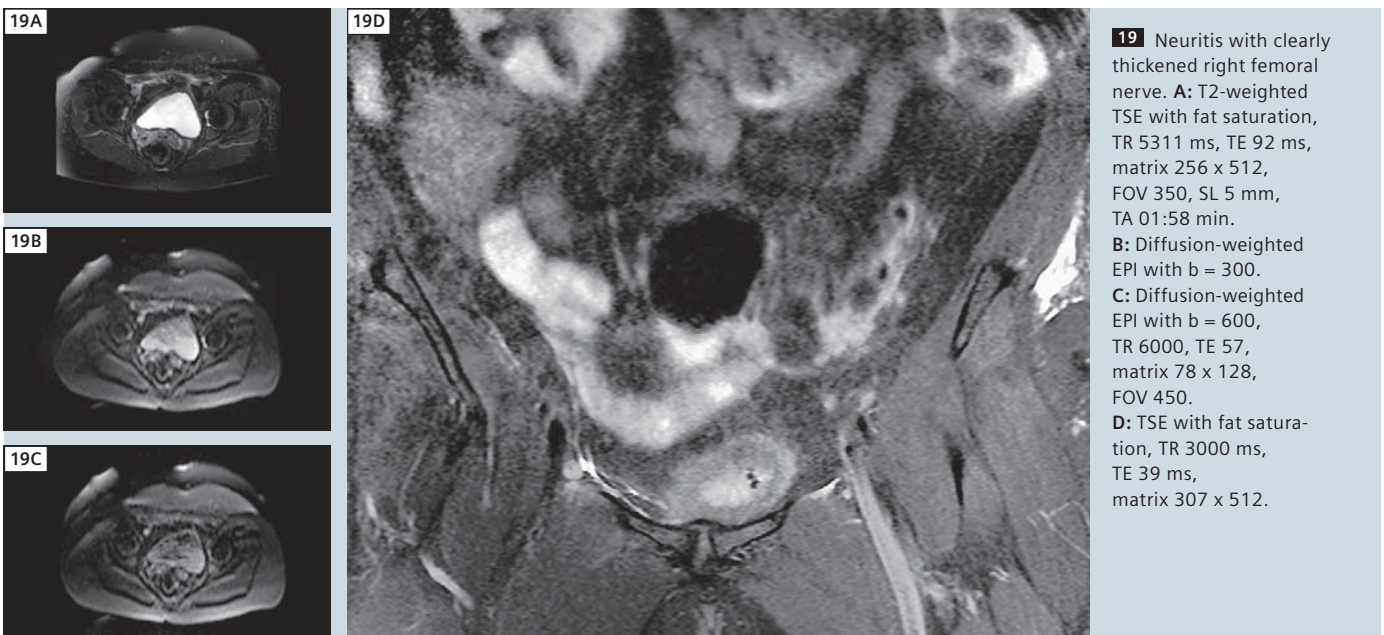
16 Carcinoma of the adrenal gland with **A**: moderate signal intense appearance on HASTE image, **B**: moderate hypointense signal correlate on T1-weighted fl2d inphase image. **C**: Without significant signal decay on opposed phase images and significant reduction of the diffusibility (signal intense on $b = 600$). **D**: Hypointense on corresponding ADC map. **F**: Color-coded, so-called PET-like image. **G**: Contrast enhancement within the lesion (VIBE).



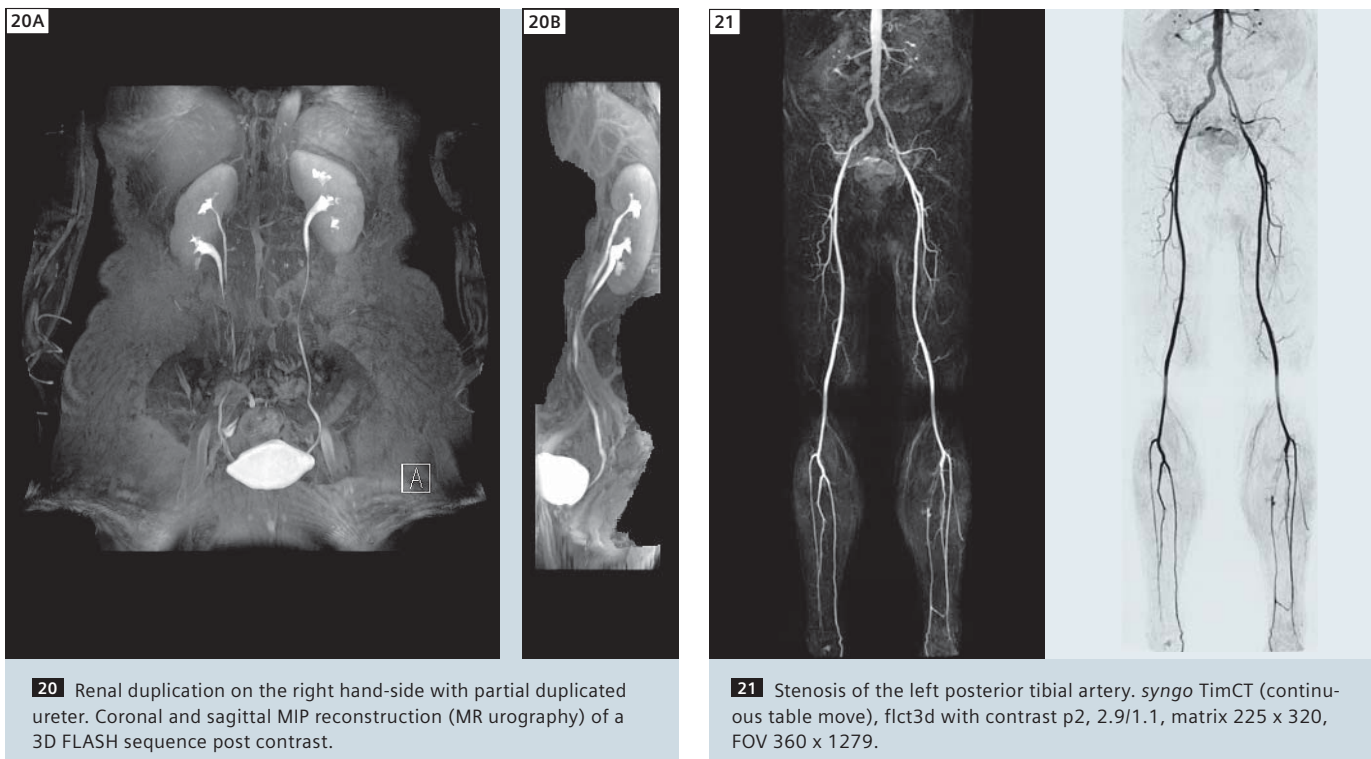
17 Autoimmune vasculitis with thromboses of the portal vein, stenoses of the subhepatic inferior caval vein and extensive collateralisation. **A**: HASTE image. **B**: syngo TWIST angiography with high temporal resolution. **C**: Coronal MIP of a VIBE sequence.



18 Rectal cancer. **A:** T2-weighted Turbo Spin Echo (TSE) p2, TR 4500 ms, TE 99 ms, matrix 176 x 512, FOV 400, SL 5 mm, TA 01:06 min. **B:** Diffusion-weighted Echo Planar Imaging (EPI) with $b = 600$, matrix 78 x 128, FOV 450. **C:** ADC map. **D:** T2-weighted TSE, TR 2500 ms, TE 59 ms, matrix 320 x 320, FOV 380, SL 3 mm, TA 04:40 min. **E:** Post-contrast T1-weighted TSE with fat saturation, TR 951 ms, TE 11 ms, matrix 346 x 384, SL 3 mm, TA 03:38 min.



19 Neuritis with clearly thickened right femoral nerve. **A:** T2-weighted TSE with fat saturation, TR 5311 ms, TE 92 ms, matrix 256 x 512, FOV 350, SL 5 mm, TA 01:58 min. **B:** Diffusion-weighted EPI with $b = 300$. **C:** Diffusion-weighted EPI with $b = 600$, TR 6000, TE 57, matrix 78 x 128, FOV 450. **D:** TSE with fat saturation, TR 3000 ms, TE 39 ms, matrix 307 x 512.



with Tim technology as a multi-station angiography or as a syngo TimCT examination with continuous table feed (Fig. 21). For deformities such as arterio-venous deformities, an ideal synergy exists between vessel-specific MR contrast agents (Vasovist) and a higher signal intensity at the Verio, making high-resolution MR angiography possible (Fig. 22).

Summary

After over a year's experience with the Siemens MAGNETOM Verio, we can recommend, without hesitation, the system's superb routine performance for all organs. This applies in particular to the user interface and system operation which are largely the same as those for 1.5 tesla systems. The sequence spectrum already included in the delivered software allows the Verio to be immediately put into clinical operation. The benefit of the higher signal-to-noise ratio available by doubling the field strength also allows for a considerably improved image quality even for older

3 tesla systems. This applies in particular to neurological examinations as well as joint diagnostics. The higher signal can be used to increase spatial resolution or to accelerate the examination as such (a combination of both under ideal circumstances).

Thanks to technical developments in the area of image data acquisition (e.g. parallel imaging) and the introduction of TrueForm magnet design, MAGNETOM Verio – in combination with an optimized coil technique and adjusted sequence design – enables the examination of body regions at 3 tesla that were previously limited and prevents or greatly reduces known B_0 and B_1 artifacts. This is particularly true for examinations of the abdomen and the pelvis, as well as whole-body examinations. The SAR problem was also positively influenced.

In conclusion, we are dealing with an MR system that has the potential of a "workhorse" in the private radiology practice. As a result, 3T technology is no longer reserved just for scientific or

university-associated centers. The Verio is equally favored by patients, technologists and physicians even though one problem occurs regularly: We have to expand our patient information and explain to a large number of patients why it is not necessary to clarify every question with the MAGNETOM Verio. There are also two other existing 1.5 tesla systems, MAGNETOM Avanto and MAGNETOM Espree which can be used for this purpose.

References

- 1 Baudendistel K.T et al. (2004) Klinische MRT bei 3 Tesla: Aktueller Stand. Radiologe 44:11–18.
- 2 Bernstein MA et al. (2001) High-resolution intracranial and cervical MRA at 3.0 T: technical considerations an initial experience. Magn Res Med 46:955–962.



22 Arterio-venous malformation of the lower right extremity. **A:** Arterial phase, **B:** venous phase. *syngo* TimCT (continuous table move) with contrast p2, 2,9/1,1, matrix 225 x 320, FOV 360 x 1279.

- 3 Frayne R et al. (2003) Magnetic Resonance imaging at 3.0 Tesla: challenges and advantages in clinical neurological imaging. *Invest Radiol* 38:385–402.
- 4 Kangarlu A et al. (2004) Klinische Hoch- und Ultrahochfeld-MR und ihre Wechselwirkung mit biologischen Systemen. *Radiologe* 44:19–30.
- 5 Kuhl CK et al. (2008) Whole-body high-field-strength (3.0-T) MR imaging in clinical practice. Part I. Technical considerations and clinical applications. *Radiology* 246:675–696.
- 6 Kuhl CK et al. (2008) Whole-body high-field-strength (3.0-T) MR imaging in clinical practice. Part II. Technical considerations and clinical applications. *Radiology* 247:16–35.
- 7 Schmitt et al. (2004) 3 Telsa-MRT: Der Erfolg höherer Feldstärken. *Radiologe* 44:31–48.

Contact

Markus G. Lentschig, M.D.
MR and PET/CT Imaging Center Bremen
Mitte
Sankt-Juergen-Str. 1
28177 Bremen
Germany
www.mr-bremen.de



Dr. Markus Lentschig (back row, right) and his team.

MAGNETOM Verio – An Initial Indian Experience

Dr. Sumita Kundu, M.D., DMRD; Dr. S. K. Sharma M.D.

Consultant Radiologists, EKO MRI Centre, Kolkata, India

Introduction

The MR unit of our institute, EKO MRI Centre, was established in 1992 with a 1 Tesla System. A 1.5 Tesla unit was subsequently added in response to increasing patient load and demand for MRI. When we found it necessary to further enhance our services we replaced the 1 Tesla unit with a 3 Tesla MRI. MAGNETOM Verio with its unique equation of 70 cm + 3T + Tim (Total imaging matrix) was our unanimous choice. One of the main features that helped us decide in favour of MAGNETOM Verio is its wide bore (70 cm) which was unthinkable in the 3T MRI segment. In the past few months we have had several instances where we have benefited from this wide bore system. Not only were we able to accommodate more obese patients, but also patients with deformities, which prevented

them from lying straight in the bore. Patients with conditions like ankylosing spondylosis; kyphosis etc. could be comfortably positioned for scanning. In fact we have been able to scan patients even in semi-reclining position with good image quality. Several patients who have been claustrophobic in other MRI scanners were more compliant in the Verio and rarely has there been an instance of abandoning the scan due to patient discomfort.

The Tim technology complimented with iPAT (Integrated Parallel Acquisition Technique) has enabled us to significantly cut down our scan time and increase patient throughput. This has facilitated us to perform whole-body metastasis screening with a reasonable scan time, which in itself is an advantage as many of these patients, particularly those with

skeletal metastasis, are in pain and not able to tolerate long scan times.

We have used the MAGNETOM Verio to scan patients from head to toe. The high signal-to-noise ratio (SNR) of 3T MRI with a wide bore magnet along with Tim technology has certainly made MR scanning easier for us and more comfortable for our patients. We have been able to achieve excellent results in musculoskeletal, neuro and body MRI and have faced no problems in scanning patients of various age groups and physical habitus. The following are examples of patients who have been part of our initial interesting experience on the MAGNETOM Verio system.

Case 1: Villous Adenoma

Patient history

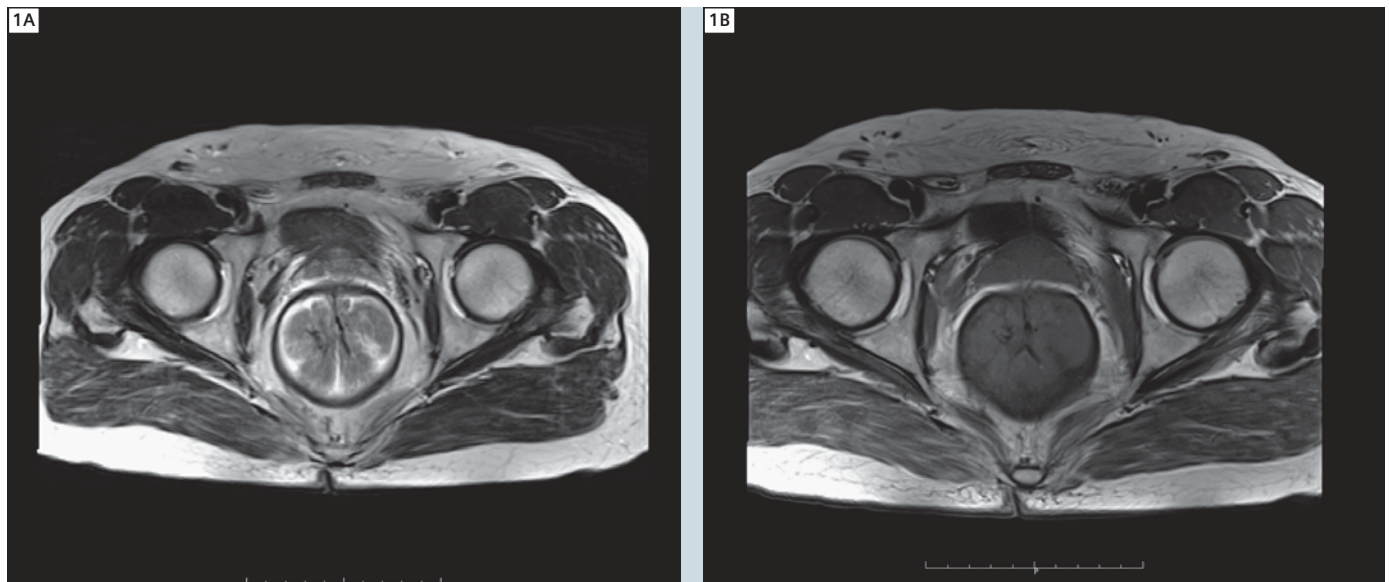
A 61-year-old male presented with a history of intermittent bleeding per rectum and mucoid stool since 3 years. Per rectal examination was suggestive of a large polypoid mass at the anterior wall of the rectum with unknown upper

extent. There is a history of polypectomy in the anal region about 12 years back.

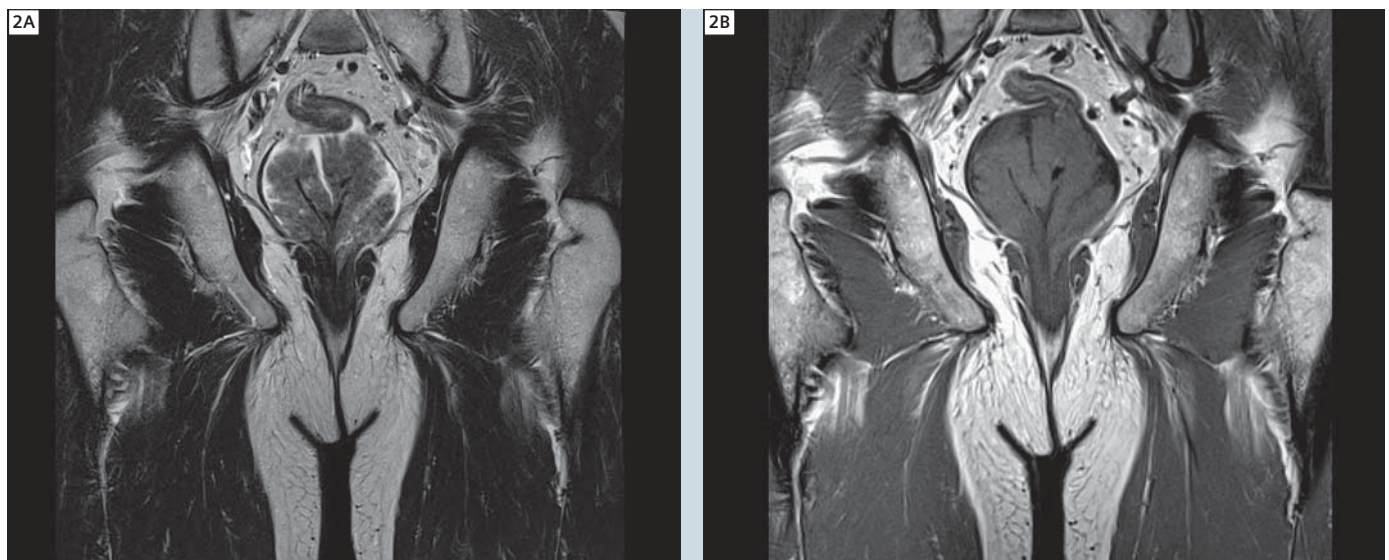
Image findings

The rectum is distended and shows a well defined space occupying lesion (SOL)

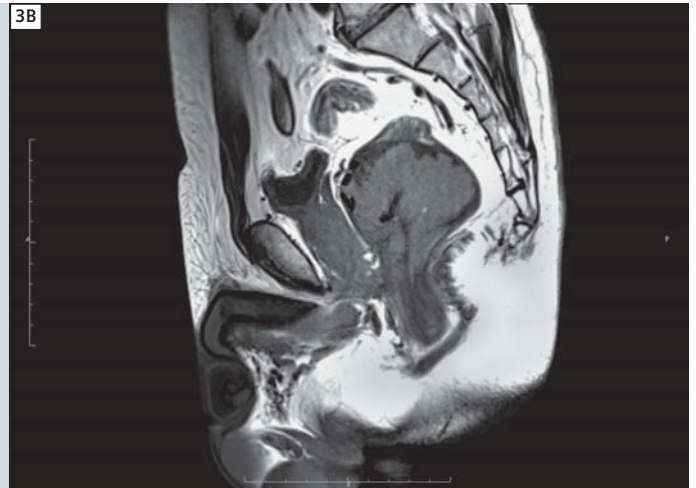
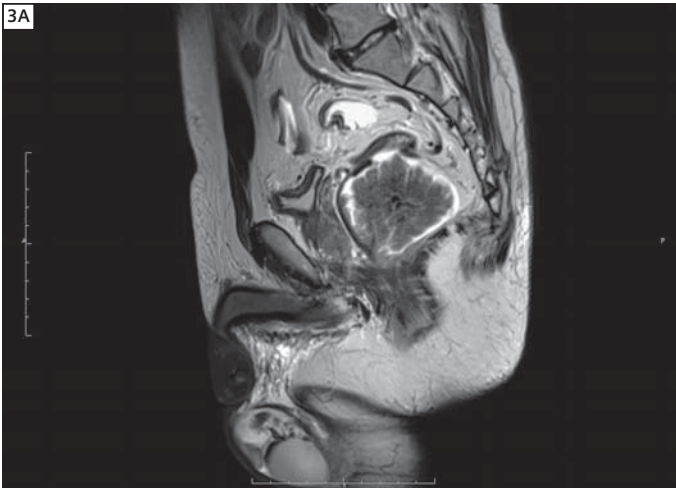
with frond-like projections from a central core. The SOL shows hypointense signal in T1 and T2-weighted images while the central core is markedly hypointense in T2-weighted images with enhancement in the contrast enhanced study. The



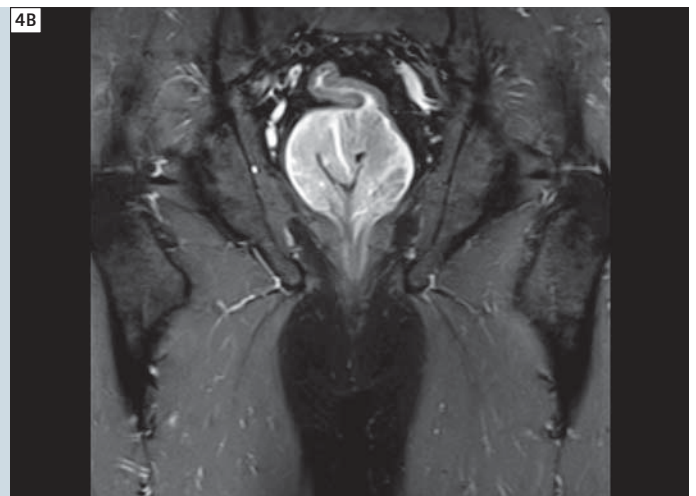
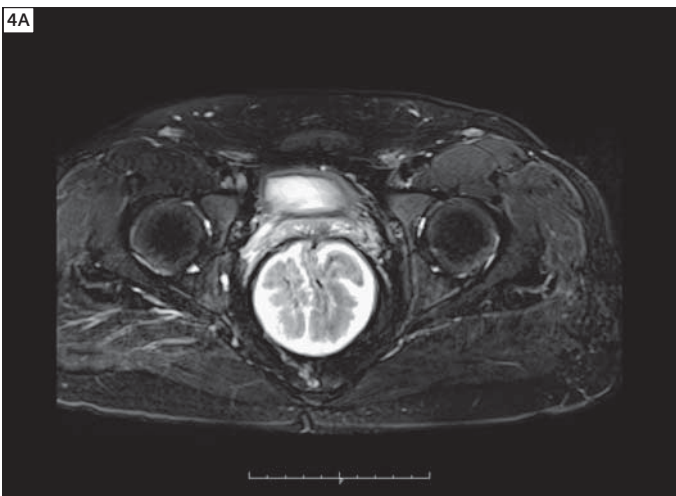
1 A: T2-weighted axial image. Distended rectum, hypointense mass with hypointense branching core surrounded by fluid content. B: T1-weighted axial image, showing hypointense mass.



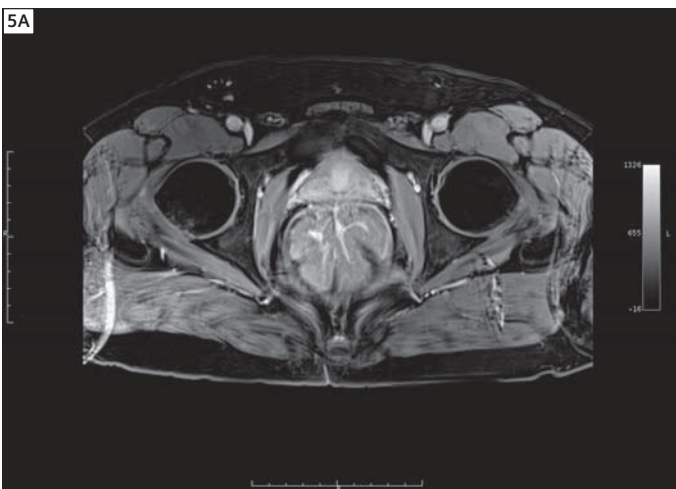
2 A: T2-weighted coronal image. Frond like projections of the mass seen. B: T1-weighted coronal image.



3 A: T2-weighted sagittal image. Anterior rectal wall thickened, mass attached just above the anorectal junction. B: T1-weighted sagittal image.



4 A: Fat suppressed T2-weighted axial image. No intramural extension of the mass. Anterior attachment can be clearly seen. B: Coronal STIR image.



5 A: Contrast enhanced T1-weighted axial image. Fairly intense enhancing central branching core. B: Contrast enhanced T1-weighted coronal image. The enhancing nature of the mass is well appreciated, mass clearly delineated from the rectal wall.

remaining part of the SOL shows mild enhancement and is surrounded by fluid. The SOL measures 7.0 cm in AP, 6.7 cm in transverse and 6.2 cm in cranio-caudal axes and appears to be attached to the anterior wall just above the anorectal junction. The rectal wall adjacent to the base of the lesion anteriorly is thickened and shows tortuous flow voids.

Remaining parts of the anorectal region do not show any significant abnormality. No evidence of peri-rectal or pelvic lymph node enlargement is seen. Fat planes around the rectum are preserved and no extra-luminal invasion of the rectal mass is noted.

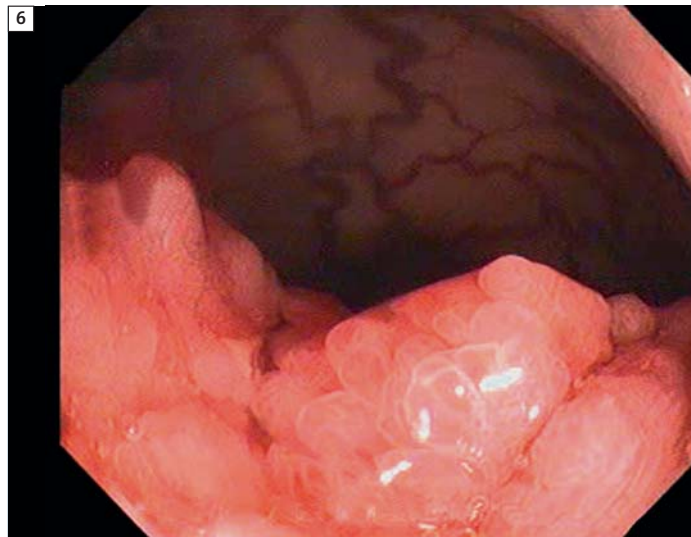
Urinary bladder does not show any intraluminal mass.

Prostate shows normal size, shape and parenchymal signals.

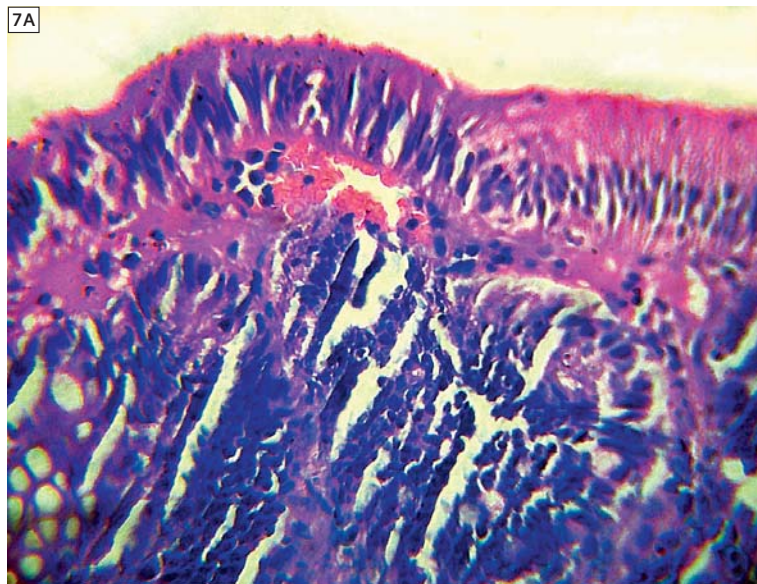
Visualised muscles and bones do not show any significant abnormality.

Impression

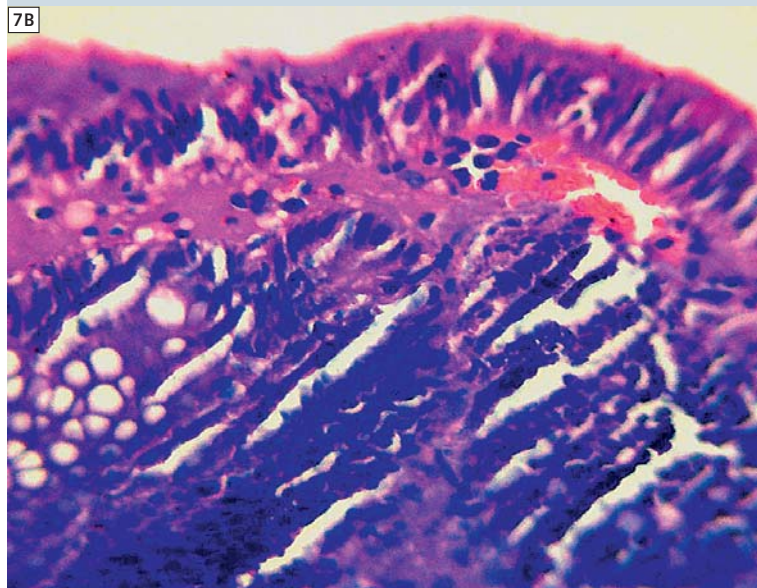
The findings are suggestive of a mass in the rectum with signal characteristics, morphology and enhancement pattern consistent with a villous adenoma. It appears to be attached to the anterior rectal wall just above the anorectal junction and shows increased vascularity in the region of its base. No evidence of perirectal invasion or enlarged lymph nodes is noted.



6 Colonoscopy. Polypoid mass 3 cm from the anal verge extending up to 10 cm, compromising the lumen.



7 Histopathology: Villous structure with vascular branching core.



Villous has pseudo stratified lining without atypia.

Diagnosis:
Villous
Adenoma.

Case 2: Internal Carotid Artery Dissection

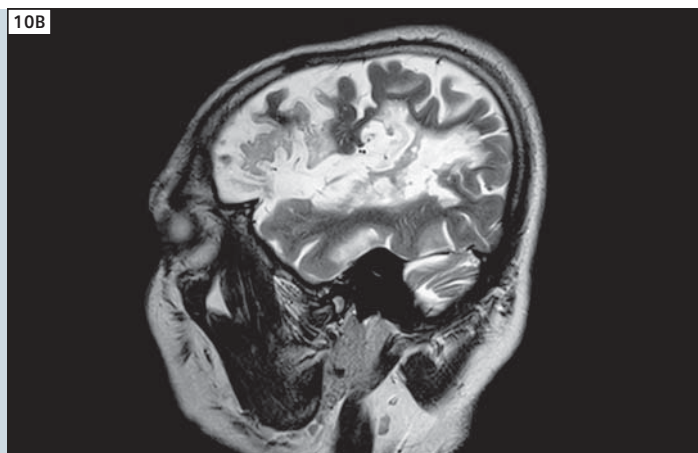
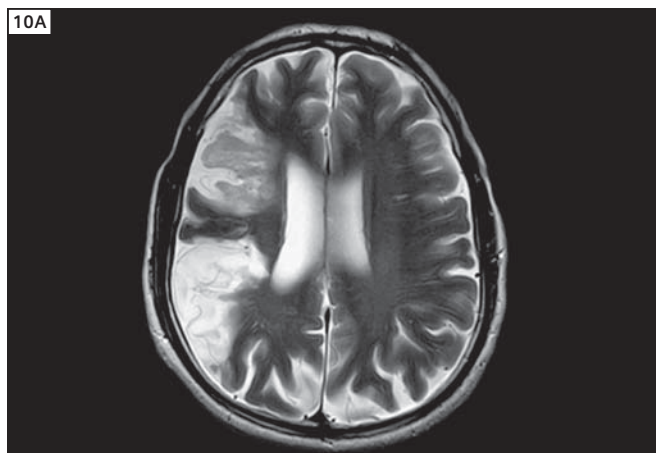
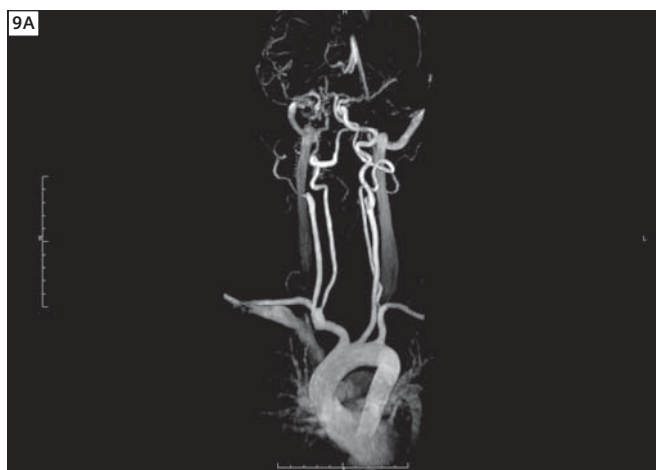
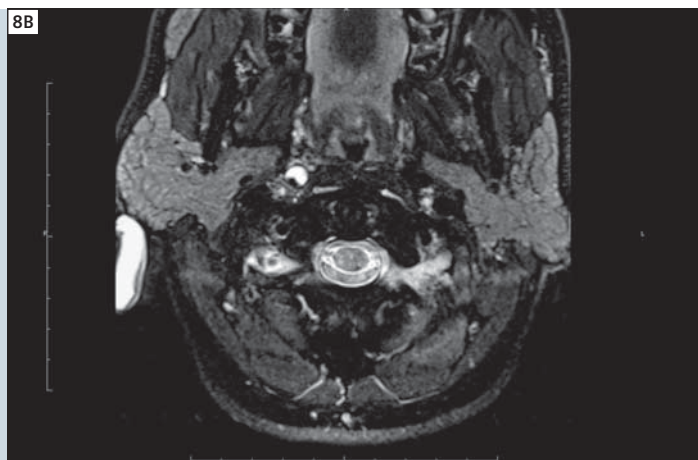
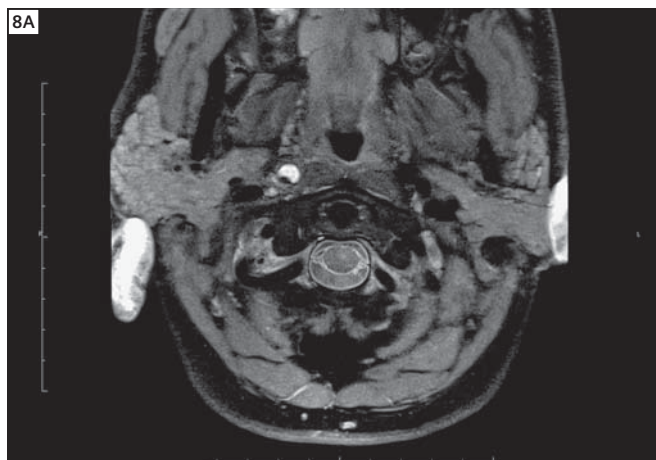
Patient history

A 52-year-old male presented with a history of acute onset of hemiparesis and severe headache. There is no history of Hypertension or Trauma.

Image findings

Brain: There is a large hyperintense area in frontal, parietal, temporal and insular regions of the right cerebral hemisphere and in the right basal ganglia in FLAIR

and TSE T2-weighted images with hypointensity in the T1-weighted images. There are areas of restricted diffusion in this lesion. Left parasellar region is nor-



mal but there is loss of flow void in right internal carotid artery (ICA) in the cavernous part and carotid canal.

MR Angiogram of the neck: Right com-

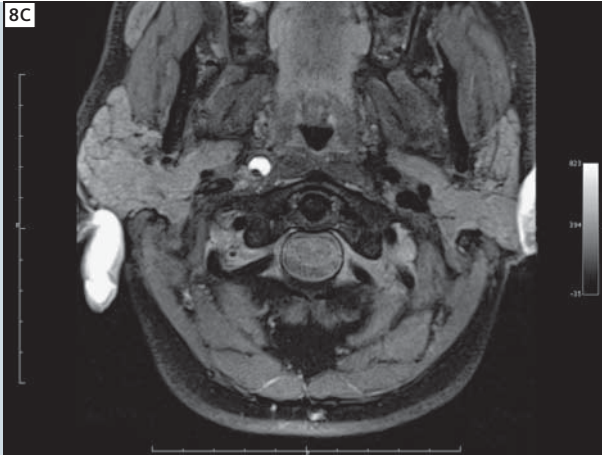
mon carotid artery shows normal flow signal, origin, course, calibre and bifurcation but there is loss of normal flow signal and luminal enhancement of the

right internal carotid artery about 0.8 cm distal to its origin. T1, T2 and proton density-weighted axial images in this region show an ovoid, eccentric hyperintensity with thin hypointense strands within it and a small area of hypointensity in its postero-lateral aspect. Enhancement is seen in the lumen of the intracranial part of the right internal carotid artery in contrast enhanced angiogram with luminal narrowing. Right common carotid artery shows normal flow void in T1-weighted transverse images.

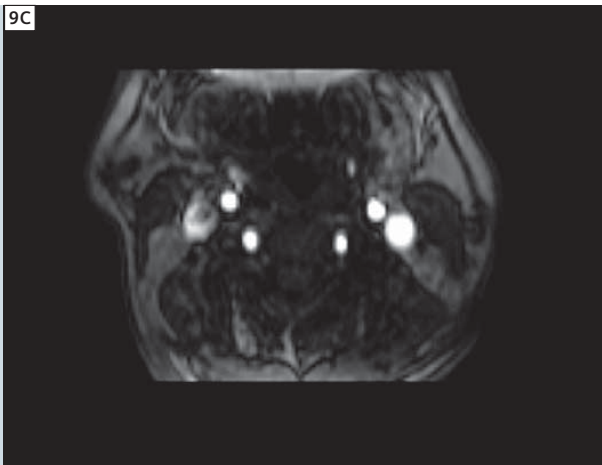
Left common carotid artery, intracranial and extracranial parts of left internal carotid artery show normal flow void and luminal enhancement with normal course, calibre, flow signal and bifurcation. Extracranial and intracranial parts of both vertebral and visualized parts of external carotid arteries also show normal appearance.

Impression

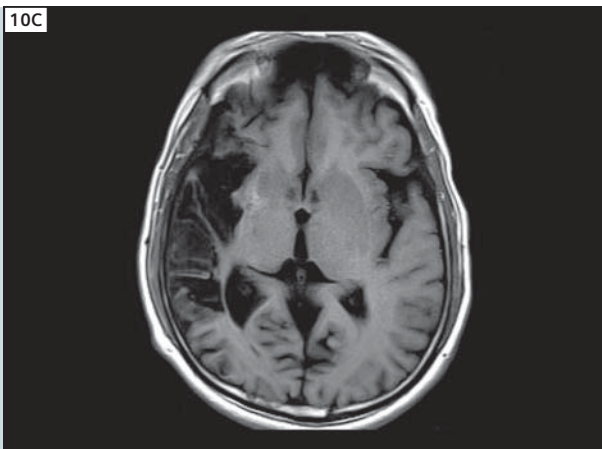
The findings are suggestive of right internal carotid dissection with eccentric intramural haematoma just beyond the proximal extracranial part of right internal carotid artery. There is loss of flow in the right internal carotid artery beyond the dissection up to the intracranial part with a large acute to subacute infarction in right middle cerebral artery territory, involving the frontal, parietal, temporal, insular and basal ganglia regions. Empty sella turcica is noted.



8 Ovoid eccentric hyperintensity in the right internal carotid artery (ICA).
A, B: Proton-Density-weighted transversal image with fat saturation.
C: T2-weighted transversal image with fat saturation.



9 **A, B:** Contrast enhanced MR Angiography (ceMRA) of the neck. Note the loss of flow in the right ICA.
C: Transversal ceMRA.



10 Follow-up scan of the brain.
A, B: T2-weighted transversal and coronal image showing the infarct.
C: T1-weighted FLAIR image showing the infarct in the MCA (Middle Cerebral Artery) territory.

Case 3: Ankylosing Spondylosis

Patient history

A 46-year-old female presented with a history of neck pain radiating to the left shoulder for the last 2 years and low back pain radiating to left lower limb for the last 3 years. She has a stooped gait and was advised MRI of cervical and lumbosacral spine. She was refused at other MRI scanners as she was unable to lie down straight in the magnet due to her kyphosis and her inability to extend her left lower limb.

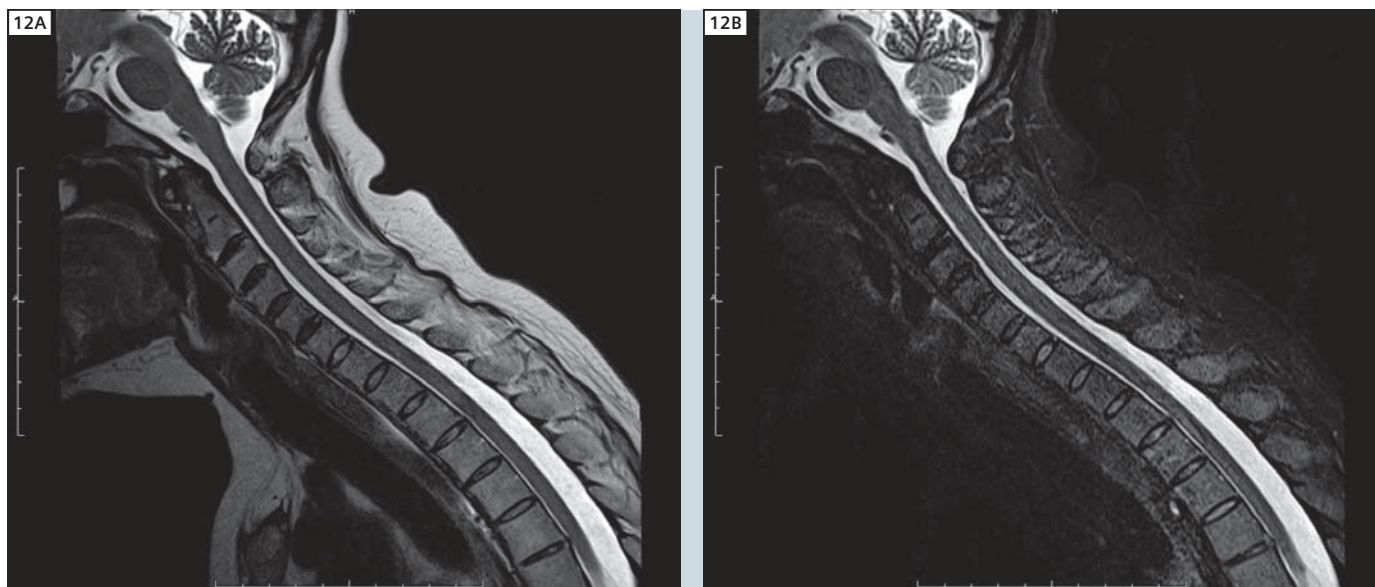
Image findings

Cervical spine: There are mild degenerative changes in the endplates of cervical vertebrae with focal areas of fatty marrow change. There appears to be forward bending of the spine but cervical vertebrae otherwise show normal height and alignment. Intervertebral discs show normal height with evidence of dessication at C4–C5 and C5–C6 levels.

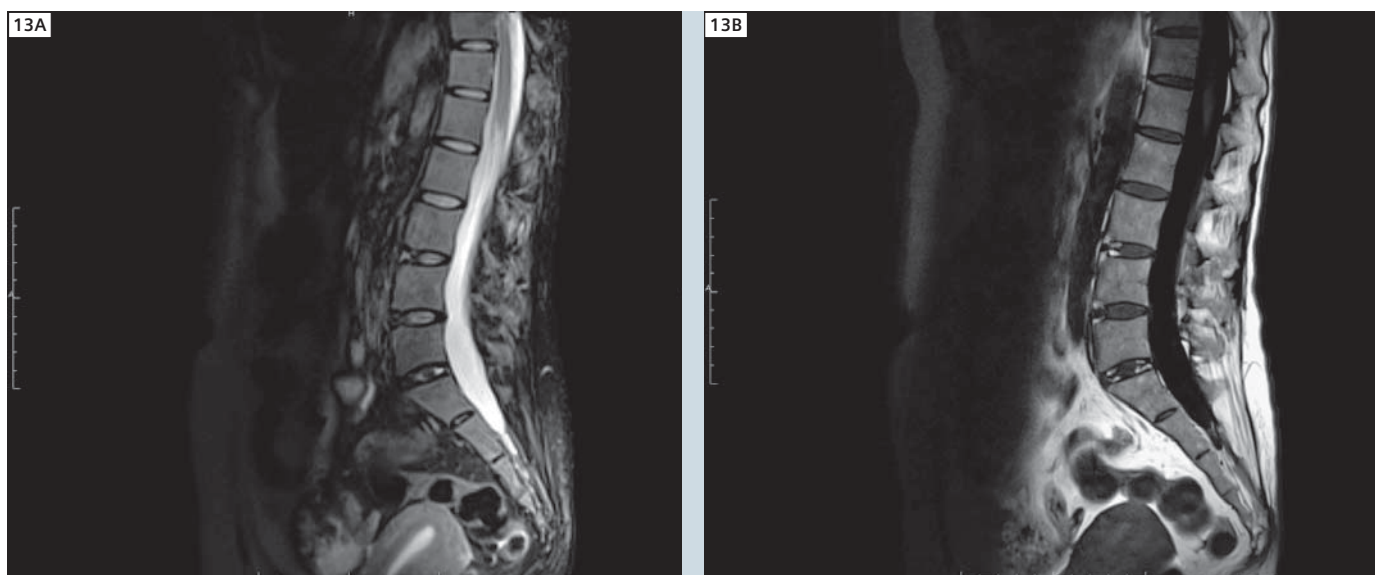
Lumbosacral spine: L5 vertebra is completely sacralized and degenerative changes are noted in the endplates of lumbar vertebrae and facet joints. Height, alignment and marrow signals of the visualised lumbosacral vertebrae are otherwise normal but subarticular fatty marrow change is seen in both sacro-iliac joints in some regions. Small area of marrow oedema is also noted in



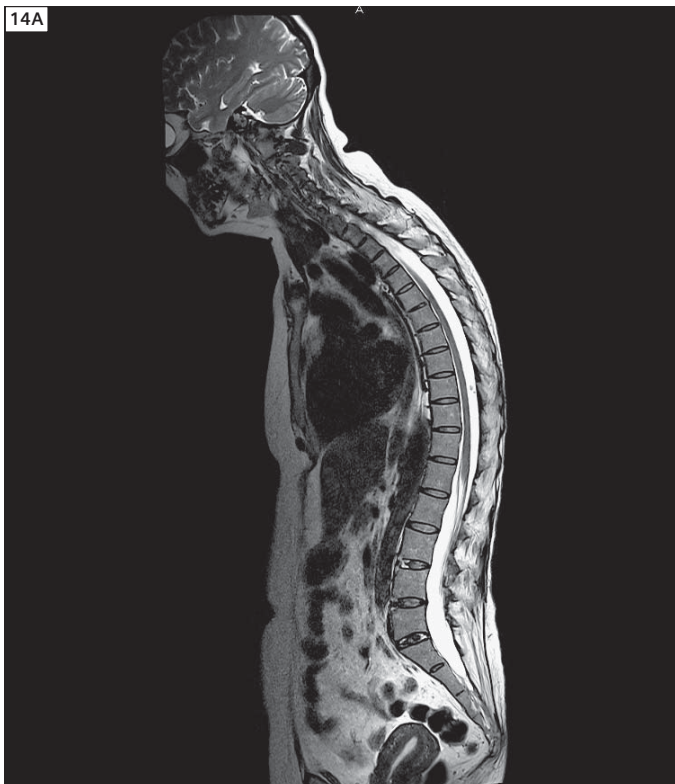
11 The patient is unable to extend her left lower limb, but may be positioned comfortably in the 70 cm bore of the MAGNETOM Verio.



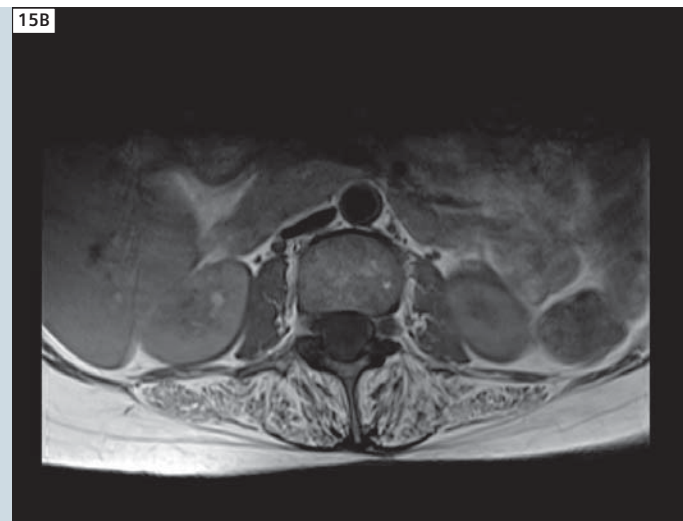
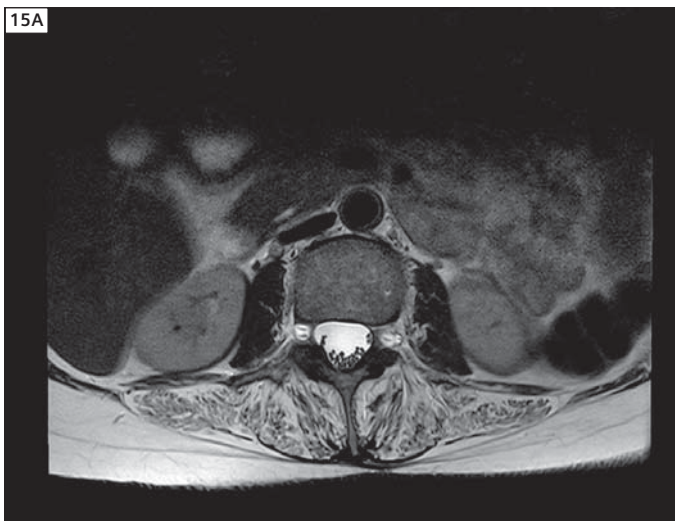
12 Degenerative changes. **A:** T2-weighted sagittal image. **B:** T2-weighted sagittal TIRM DarkFluid image.



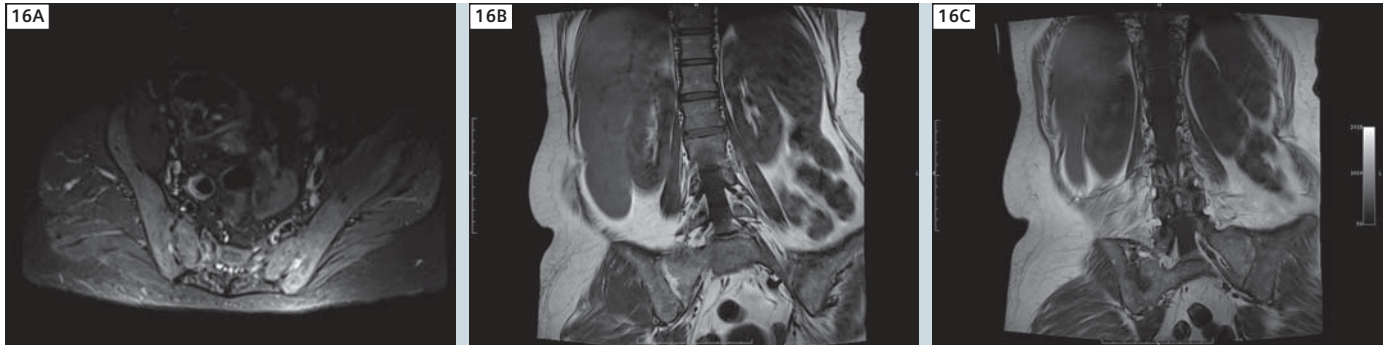
13 T2 and T1-weighted sagittal images show calcification of discs.



14 T2-weighted sagittal whole spine image. Kyphosis, sacralization of L5 vertebra with calcification of the lumbar discs.



15 T2 and T1-weighted axial images showing squaring of vertebra.



16 A: T2-weighted TIRM image showing bilateral sacroiliitis. B, C: T1-weighted coronal images showing bilateral sacroiliitis.

iliac aspect of left sacro-iliac joint with oedema in the joint space.

Lumbar inter-vertebral discs show evidence of dessication with calcification at L2–L3, L3–L4 and L4–L5 levels.

Impression

The findings are suggestive of degenerative changes in the cervical and lumbar spine with sacralisation of L5, calcification of lumbar discs and bilateral chronic sacroiliitis with bony ankylosis favouring an inflammatory arthropathy like ankylosing spondylosis. No evidence of compression on the cord or nerve roots is seen though a mild posterior disc bulge at L3–L4 is noted.

Contact

Dr. Sumita Kundu, M.D., DMRD
Consultant Radiologist
EKO MRI Centre
54 J L Nehru Road
Kolkata – 700071
India
Phone +91 33 2282 8105
enquiry@ekoxray.com



Dr. S. K. Sharma and Dr. Sumita Kundu

Case Report: Meningitis

Kirralie Lyford; Richard O'Sullivan, M.D.

Primary Health, The Epworth MRI Department, Richmond, Victoria, Australia

Sequence details

Multiplanar T1, T2 and fat suppressed T2-weighted images were acquired together with multiplanar post Gadolinium enhanced T1-weighted images. The images were acquired on our 3T MAGNETOM Verio.

Image findings

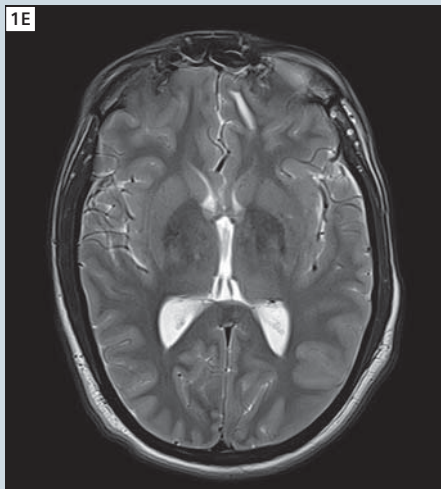
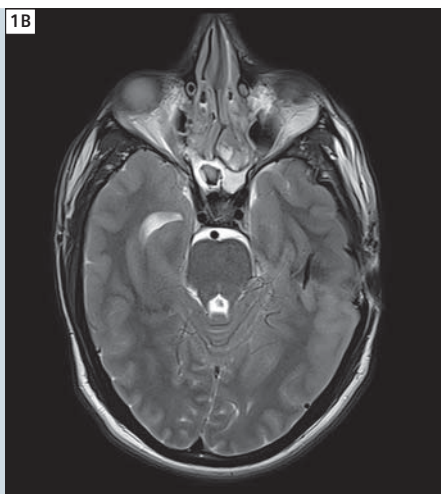
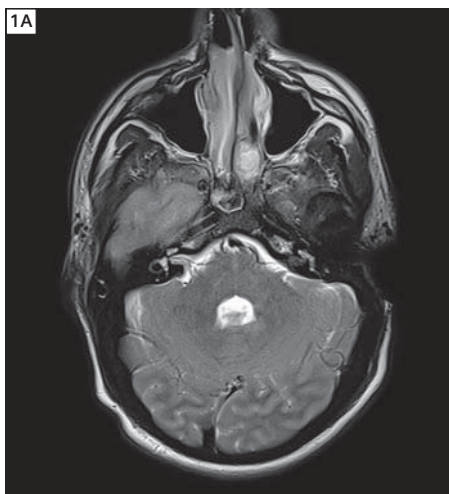
Midline is central. There is ventriculomegaly involving the lateral and third ventricles with subtle subependymal spread of CSF and sulci effacement

consistent with hydrocephalus. There is a defect in the floor of the left anterior cranial fossa with a 3.5 x 0.8 cm encephalocele that extends inferiorly to the nasopharynx. Peripherally enhancing 2 x 1 cm meningocele is seen extending inferiorly posterior to the hard palate. This meningocele contains complex fluid suspicious for infection / meningitis. Extensive mucosal thickening is seen in the remaining paranasal sinuses. In addition there is a band of oedema in

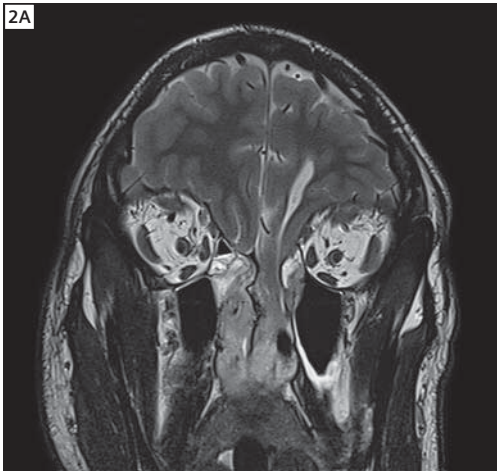
the anteroinferior left frontal lobe but no enhancing intra-axial mass is seen. No other abnormality is demonstrated in the remaining brain.

Conclusion

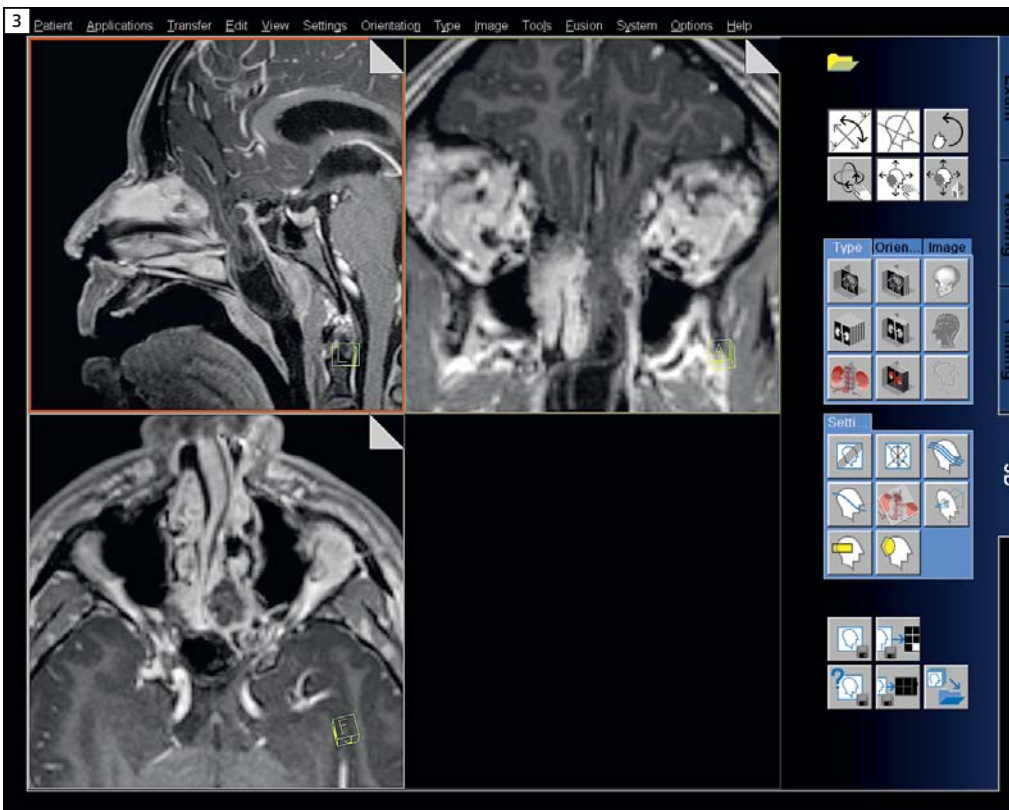
Left anterior cranial fossa bony defect is seen, through this passes a 3 x 1 cm left frontal encephalocele with meningocele extending more inferiorly. This extends to the posterior margin of the hard palate. CSF within the meningocele has peri-



1 Transversal T2-weighted TSE, demonstrating a defect in the floor of the left cranial anterior fossa: TR 3500 ms, TE 92 ms, slice thickness 3 mm, FOV 180 x 180 mm, matrix 314 x 448.



2 Coronal T2-weighted TSE; the encephalocele is well delineated, extending to the nasopharynx: TR 2600 ms, TE 101 ms, slice thickness 2 mm, FOV 180 x 180 mm, matrix 314 x 448.



3 Thin-slice multiplanar reconstruction of post-contrast 3D T1-weighted MPRAGE examination; peripheral contrast-enhancement of the meningocele and complex fluid contents are suspicious for infection / meningitis.



Dr. Richard O'Sullivan and Kirralie Lyford.

peripheral type enhancement, strongly suspicious for meningitis at this site. There is minor oedema on the anterior/inferior left frontal lobe but no enhancing intracranial abscess is identified. This is associated with extensive mucosal thickening throughout the ethmoid sinuses and to a lesser extent in the sphenoid and maxillary antra. There is mild hydrocephalus with widespread sulcal effacement, ventriculomegaly and subtle subependymal spread of CSF.

Contact

Kirralie Lyford
Epworth Hospital
MRI Department
88 Bridge Road Richmond
Melbourne, Victoria, 3121
Australia
kirralie.lyford@symbionhealth.com

Case Report: Leptomeningeal Disease on Susceptibility-Weighted Imaging (*syngo* SWI)

Noelene Bergen; Nick Ferris, M.D.

Dept. of Diagnostic Radiology, Peter MacCallum Cancer Center, Melbourne, Australia

Patient history

A 41-year-old female, of caucasian descent, with known metastatic melanoma, presented with new onset of left trigeminal nerve symptoms (left facial sensory abnormalities) and diplopia. Spinal leptomeningeal tumor deposits had been demonstrated at MRI 2 weeks earlier, at the C5 and lumbo-sacral levels, though the CSF was not examined at that time. The only CSF examination at our institution was performed

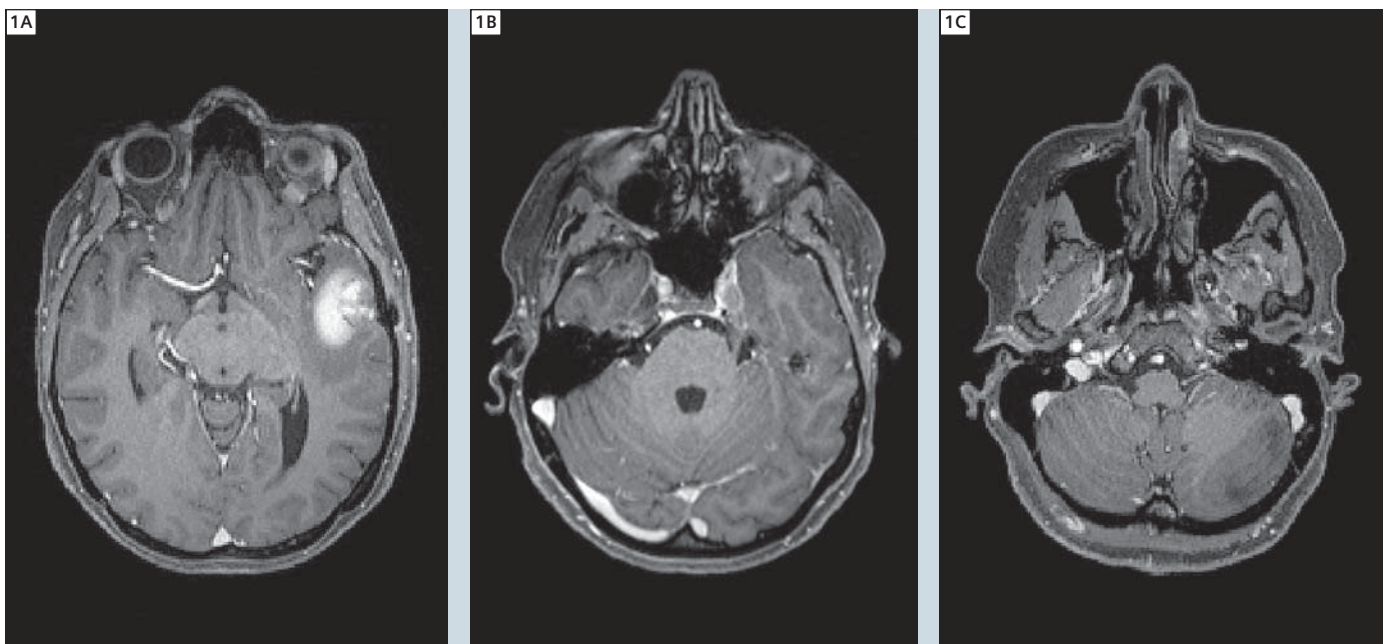
9 months earlier, and was negative at that time.

Sequence details

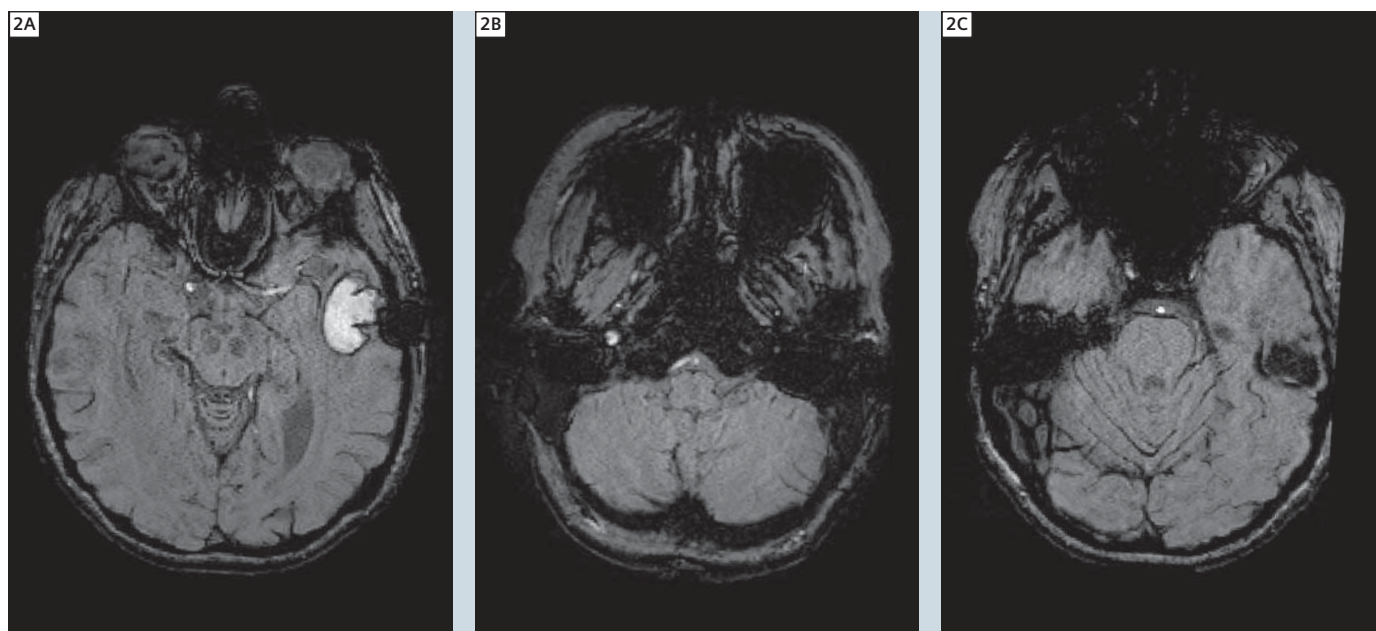
We used *syngo* SWI with the following parameters:
TR 27 ms, TE 20 ms, bandwidth 120 Hz/pixel, slice thickness 2 mm with a 0.4 mm gap, matrix 256 x 182, 1 average. Scan time was 2:48 min.

Image findings

T1-weighted images demonstrated evidence of a haemorrhage from a known pre-existing metastasis in the left temporal lobe, with a new T1 hyperintense collection seen medial to a heterogeneous mass laterally in the left temporal lobe; only part of this underlying mass was shown to enhance (Fig. 1A). Post-contrast images demonstrated a weakly-enhancing mass filling Meckel's cave on the left, engulfing the branches



1 Post-contrast T1-weighted MRI (A) demonstrating haemorrhage in the left temporal lobe. (B) showing the left trigeminal nerve lesion. (C) demonstrates the weakly contrast-enhancing mass of the Meckel's cave.



2 Susceptibility-weighted MRI – syngo SWI.

of the left trigeminal nerve (Fig. 1B). There was also questionable enhancement on the surface of the medulla (Fig. 1C).

Susceptibility-weighted images (*syngo* SWI) showed the expected hypointense rim around the left temporal hematoma (Fig. 2A), with a defect at the site of rupture of the underlying metastasis into the haematoma. Of note, SWI did not show abnormal signal on the cortical surface of the left temporal lobe, and no SWI or FLAIR signal abnormality was seen in adjacent subarachnoid spaces. SWI also showed a thin layer of marked signal loss on the surface of the medulla

(Fig. 2A), and in multiple cerebellar sulci superiorly (Fig. 2B). In context, this was strongly suspicious for leptomeningeal tumor deposits. The differential diagnosis includes superficial siderosis (secondary to repeated subarachnoid haemorrhages from vascular anomalies), normal neuromelanin (in those with heavily pigmented skin), and neurocutaneous melanosis (usually in young children). Others [1] have noted that T2*-weighted imaging may significantly improve the detection of cerebral melanoma metastases.

¹ Gaviani P et al AJNR 27:605-8, 2006.

Contact

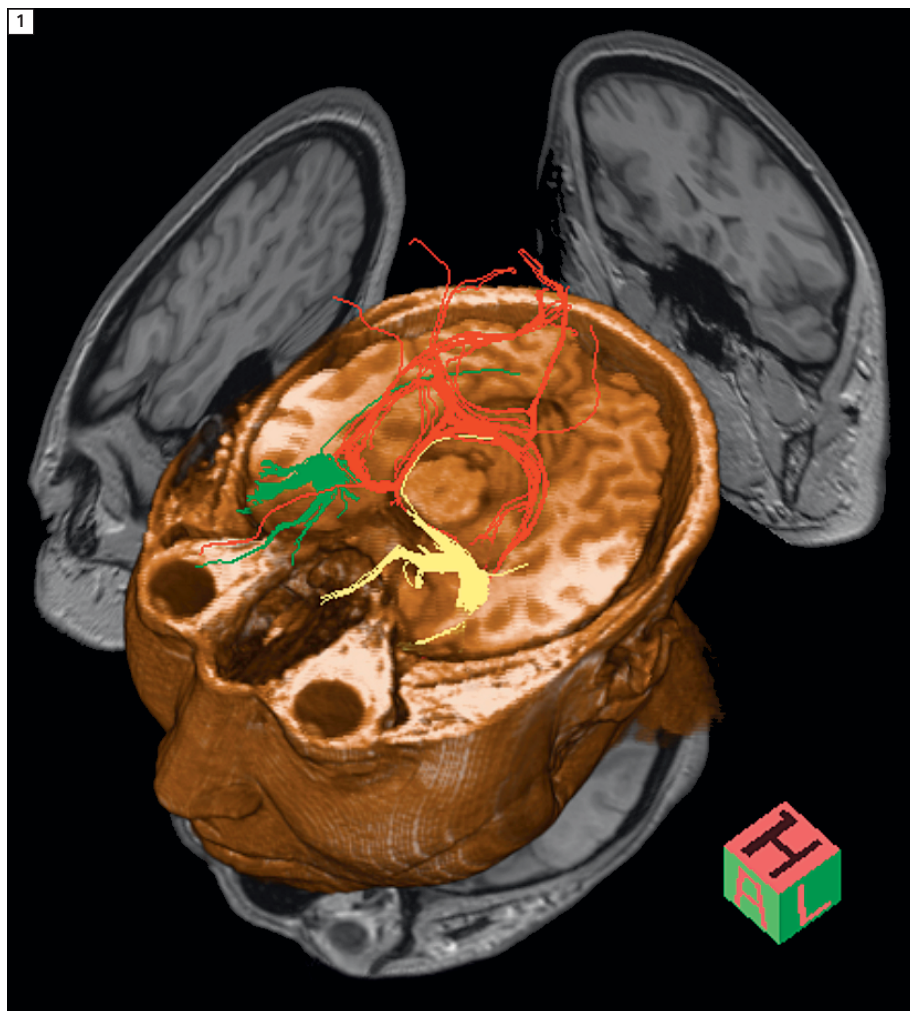
Noelene Bergen
Department of Diagnostic Radiology
Peter MacCallum Cancer Center
St Andrew's Place
East Melbourne
Victoria 3002
Australia
noelene.bergen@petermac.org

Case Report:

DTI for Presurgical Evaluation in Case of Hippocampal and Mesial Sclerosis

Vicente Belloch, M.D.

Clínica ERESA, Sección RM, ERESA-Hospital La Fe, Valencia, Spain



1 Tractography of uncinate fasciculus (left yellow, right green and fimbria of the hippocampi red). The uncinate fasciculus, the temporal stem and the fimbria of the hippocampus of the left hemisphere are recognized in its normal anatomic topography, and showed for comparison with the same structures at the right hemisphere.

Patient history

A 34-year-old female presented with a 15-year history of partial complex seizures with occasional generalization, and clinical diagnosis of left temporal drug-resistant epilepsy. Evaluated at the Video EEG Unit, the left temporal origin of the seizures is confirmed. A conventional 1.5T MRI study, performed at another institution, shows a subtle hyperintensity in the left hippocampus on T2-weighted TSE and FLAIR sequences. With a diagnosis of mesial sclerosis, the patient is proposed to a surgical treatment for her disease at our institution.

Sequence details

All images were acquired at our 3 Tesla MAGNETOM Trio, A Tim System (software version syngo MR B15) with the standard 12-channel Head Matrix coil.

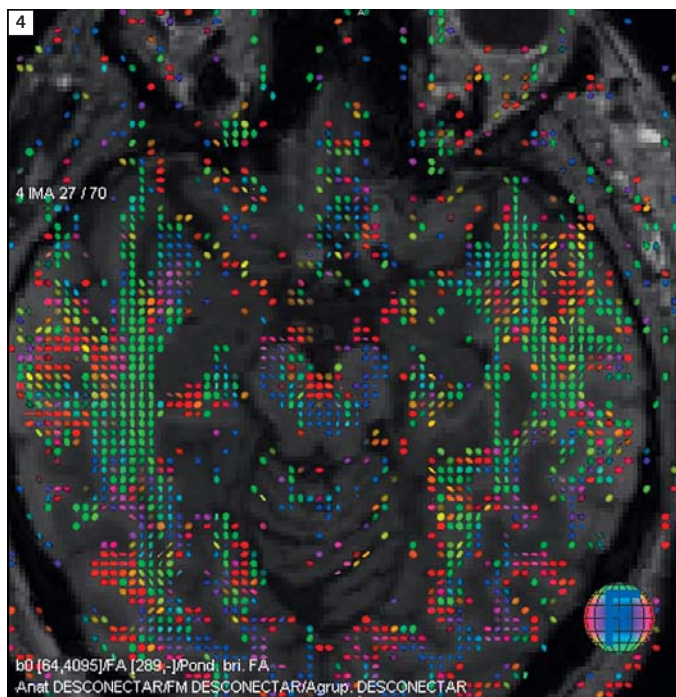
- Single shot Echo Planar Imaging (EPI) Diffusion Tensor Imaging (syngo DTI) with the following parameters:
TR/TE = 10.100/102 ms, FOV = 250 x 250 mm, averages = 2, matrix 128 x 128, resulting voxel size = (2.0 x 2.0 x 2.0) mm³, 30 non-collinear directions, b-values 0, 1000 s/mm² acquisition time: 11:05 min.
- T1-weighted 3D MPRAGE with the following parameters:
TR/TE 19/4.9 ms; FOV: 250 x 250; matrix 256 x 256; resulting voxel size = (1.0 x 1.0 x 1.0) mm³, acquisition time: 5:49 min.



2 Tractography of uncinatus fasciculus (left yellow, right green). To achieve the goal of the temporal epilepsy surgery (hippocampectomy and fronto-temporal disconnection), it is important to confirm the location of the uncinatus fasciculus and temporal stem. A subtle loss of fibers in the frontal component of the left uncinatus fasciculus is also appreciated.



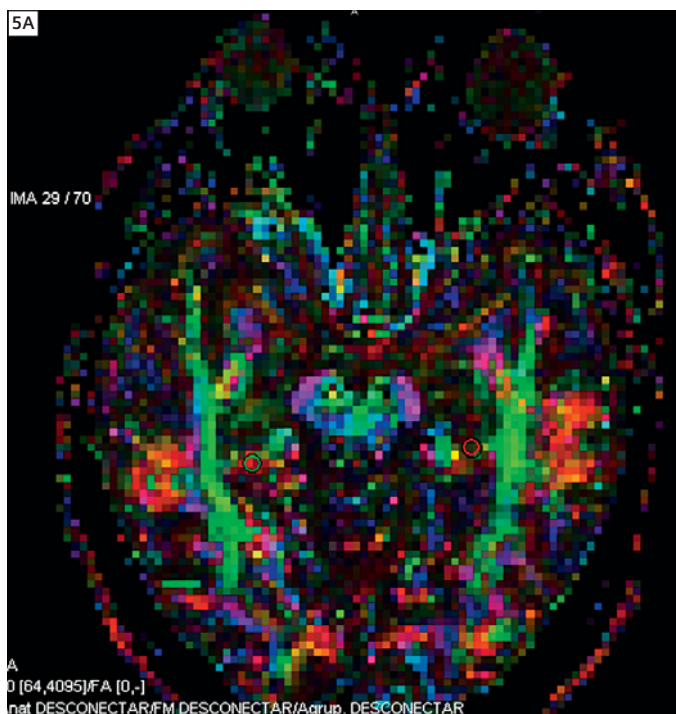
3 Tractography of the left uncinatus fasciculus (yellow) and fimbria of the left hippocampus (red). Lateral projection. The tracts connected to the amygdala-hippocampus complex are shown (fornix, cingulate and uncinatus).



4 Glyph texture ("smarties") of a colored Fractional Anisotropy (FA) DTI T1-weighted anatomical slice at the hippocampi level of the temporal lobes. A clear asymmetry is shown in the location and orientation of the Eigenvectors between the hippocampi. At the left hippocampus the diffusion vectors are sparser and randomly oriented compared to the right hippocampus.

Conclusion

Based on the findings, the patient was treated by an anterior temporal Ojemann lobectomy. Pathology confirmed the left hippocampal and mesial sclerosis. Currently the patient is free of seizures. In conclusion, DTI tractography from an isotropic acquisition combined with 3D T1-weighted "neuronavigator" sequence are currently performed at our institution for the evaluation of patients and candidates for epilepsy surgery. In this case, the ROI analysis of DTI confirmed the diagnosis of mesial sclerosis. Tractography guides the neurosurgeon to recognize the temporal stem and connections of amygdalohippocampal complex, and has helped to performed less extensive and aggressive surgical resections.



5 (A, B) Region-of-Interest (ROI) analysis of the hippocampus. There is loss of FA and increase of ADC in the left hippocampus compared to the right; these findings are very suggestive of left temporal mesial sclerosis.

Contact

Vicente Belloch, M.D.
Chief Radiologist and Scientific Director,
ERESA.
Professor at the Universidad Jaime I de
Castellón.
ERESA-Hospital La Fe
Valencia, Spain
vbelloch@eresa.com

5B

ID	FA		FA		ADC	
	Tamaño	Est	Tamaño	Est	Tamaño	Est
1	308.0	36.8	285.5	70.0	828.7	48.3
	3 / 262	352	6 / 177	381	3 / 761	871
2	435.0	75.9	482.0	101.4	680.0	55.1
	4 / 385	566	6 / 385	654	4 / 605	740

Case Report:

Intraventricular Meningioma

Vicente Belloch, M.D.

Clínica ERESA, Sección RM, ERESA-Hospital La Fe, Valencia, Spain

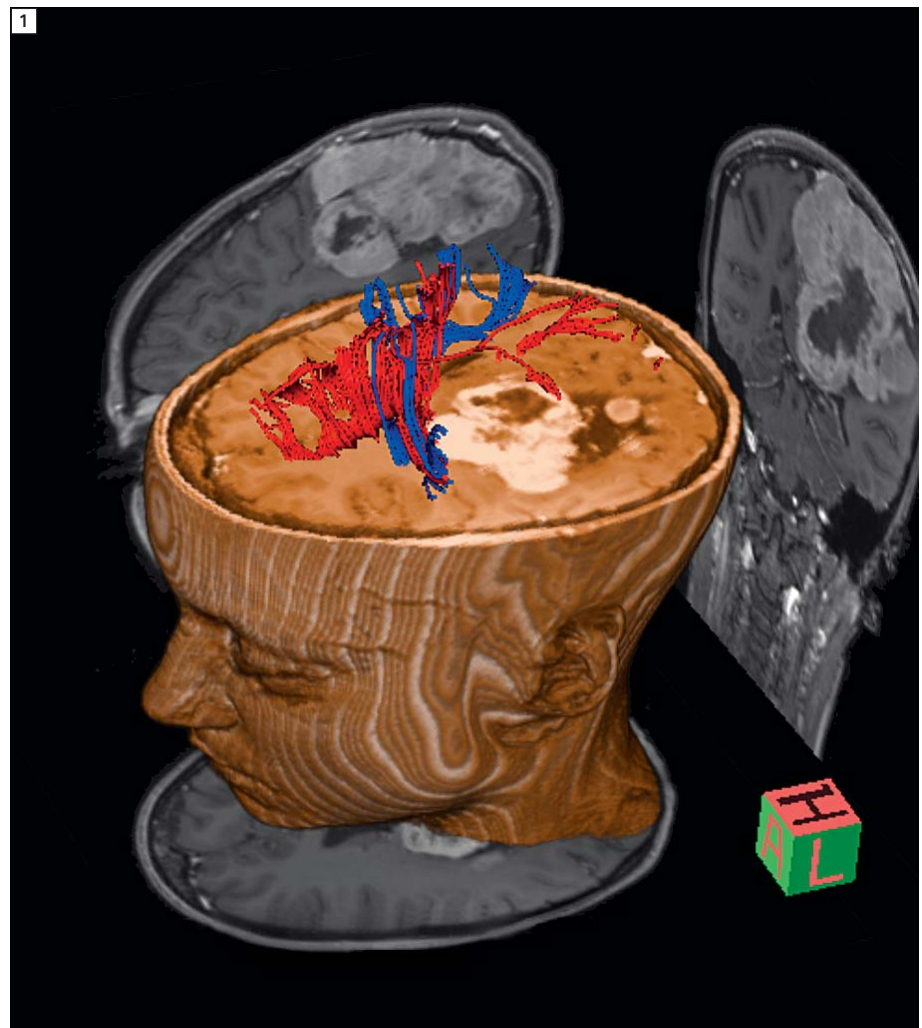
Patient history

A 19-year-old female patient without previous history of epilepsy presented with a tonic-clonic seizure. At another institution with CT and MRI, an intense enhancing mass displacing the left hemisphere anteriorly has been diagnosed. The dimensions of the lesion make it difficult to assess if the lesion is intra or extra-axial. Differential diagnosis between oligodendroglioma and intraventricular meningioma has been suggested and the patient has been sent to our institution for surgical treatment of the lesion.

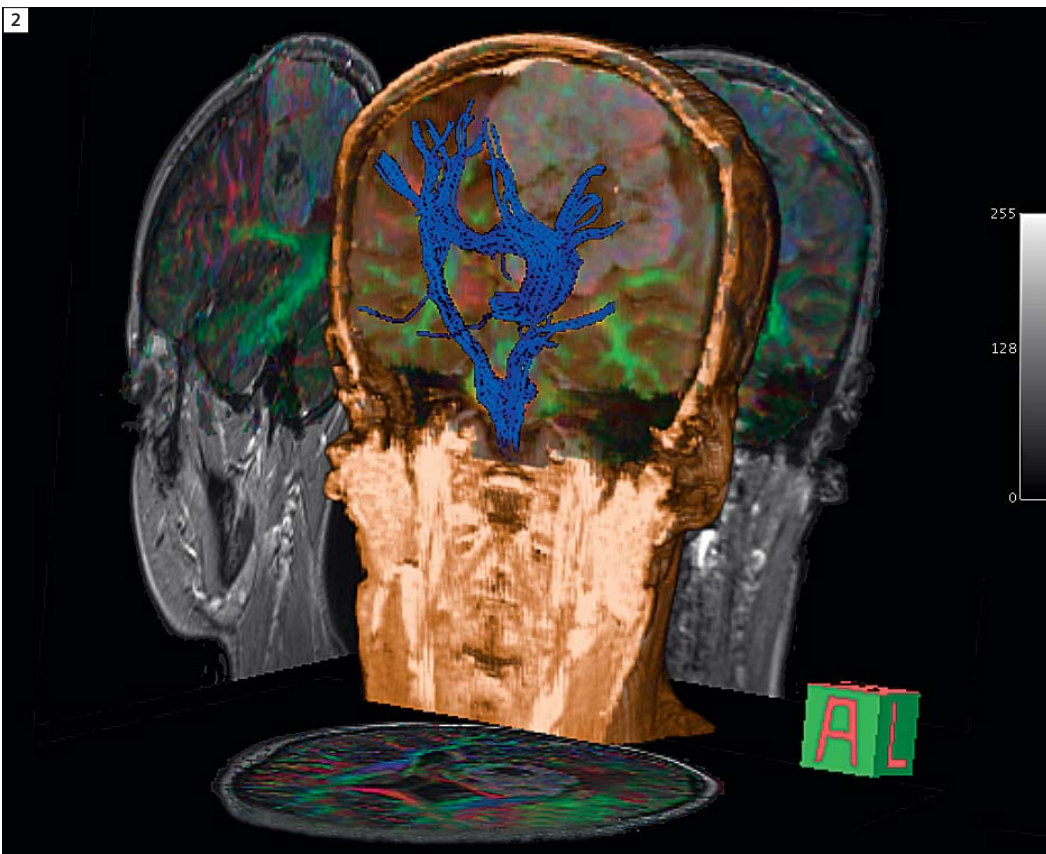
Sequence details

Images were acquired at 3Tesla (MAGNETOM Trio, A Tim System) using the standard Head Matrix coil and software version *syngo* MR B15.

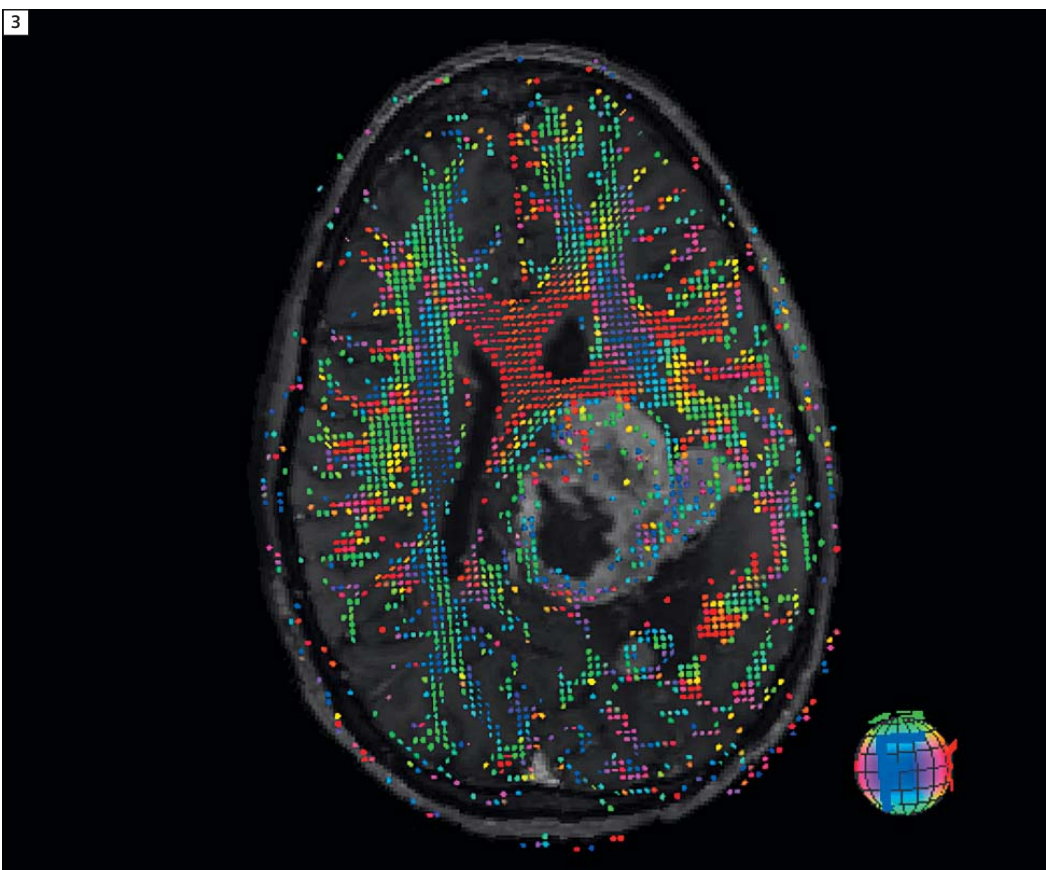
- Single shot Echo Planar Imaging (EPI) Diffusion Tensor Imaging (*syngo* DTI). TR 10.100 ms, TE 102 ms, FOV 250 mm, 2 averages, matrix 128 x 128, 70 contiguous axial slices, voxel = 2.0 x 2.0 x 2.0 mm, 30 non-collinear directions with $b = 1000 \text{ s/mm}^2$ and one acquisition without diffusion encoding. Acquisition time: 11:05 min.
- T1-weighted 3D MPRAGE. TR 19 ms, TE 4,9 ms, FOV 250 x 250, matrix 256 x 256, 160 contiguous sagittal slices, voxel = 1.0 x 1.0 x 1.0 mm. Post gadolinium injection Gd-DTPA. Acquisition time: 5:49 min.



1 Tractography of corpus callosum and internal capsule of both hemispheres (red corpus callosum, blue internal capsule): superior oblique view at the level of corona radiata, showing how the enhancing mass displaces anteriorly the left projections of corpus callosum and left internal capsule.

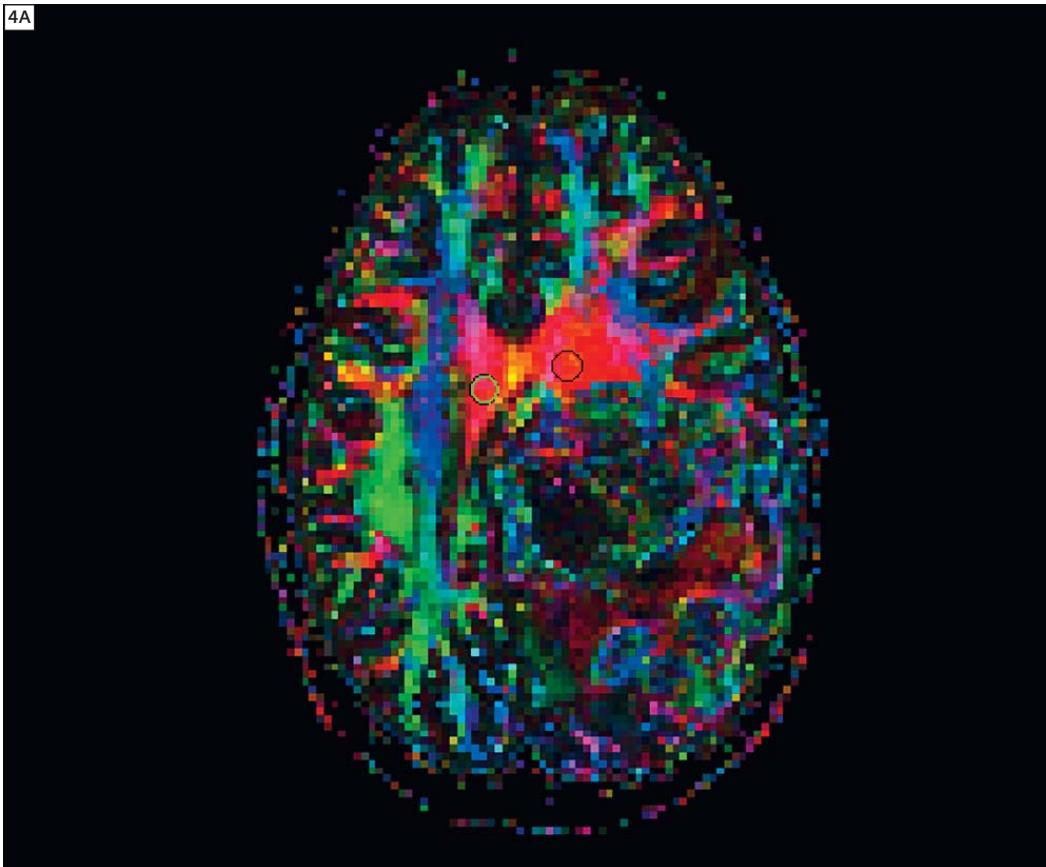


2 Tractography of internal capsule (blue): Front oblique view showing the anterior displacement and angulation of the tracts of the left internal capsule. A fused image, consisting of a contrast-enhanced T1-weighted and colored FA image is shown with the tractography.



3 Glyph texture ("smarties") of a colored FA DTI-T1-weighted anatomic slice at the corona radiate: Anterior displacement of body and splenium of corpus callosum, and left corona radiata is shown, but no asymmetry of orientation and number of Eigenvectors is seen between both hemispheres, indicating that the tumor displaces but not infiltrates the white matter, suggesting a benign histology.

4A



4 (A, B) Region-of-Interest (ROI) analysis of corpus callosum: no significant differences are seen between the values of FA and ADC between left and right hemicorpus, indicating that the tumor displaces but not infiltrates the white matter, suggesting a benign histology.

4B

ID	FA			TraceW			ADC		
	Media aritmética	DesEst	Tamaño	Media aritmética	DesEst	Tamaño	Media aritmética	DesEst	Tamaño
1	859.9	83.8	12 / 761 / 990	119.4	8.6	12 / 96 / 126	729.2	175.7	12 / 446 / 1055
2	925.1	37.9	8 / 872 / 978	110.6	5.0	8 / 104 / 120	817.3	87.3	8 / 651 / 944

Conclusion

Surgery determined that the lesion was extra-axial, and pathology indicated that it was a meningothelial (typical) left atrium intraventricular meningioma. DTI study guided the neurosurgeon to preserve the internal capsule, corona radiata of left hemisphere and posterior part of the body and splenium of corpus callosum. The patient was discharged with no motor or other deficits.

Contact

Vicente Belloch, M.D.
Chief Radiologist and
Scientific Director, ERESA.
Professor at the
Universidad Jaime I de Castellón
ERESA-Hospital La-Fe
Valencia
Spain
vbelloch@eresa.com

Case Report:

Developmental Venous Anomaly

Masahiro Ida, M.D.

Department of Radiology, Tokyo Metropolitan Ebara Hospital, Tokyo, Japan

Patient history

39-year-old female patient with developmental venous anomaly.

Image findings

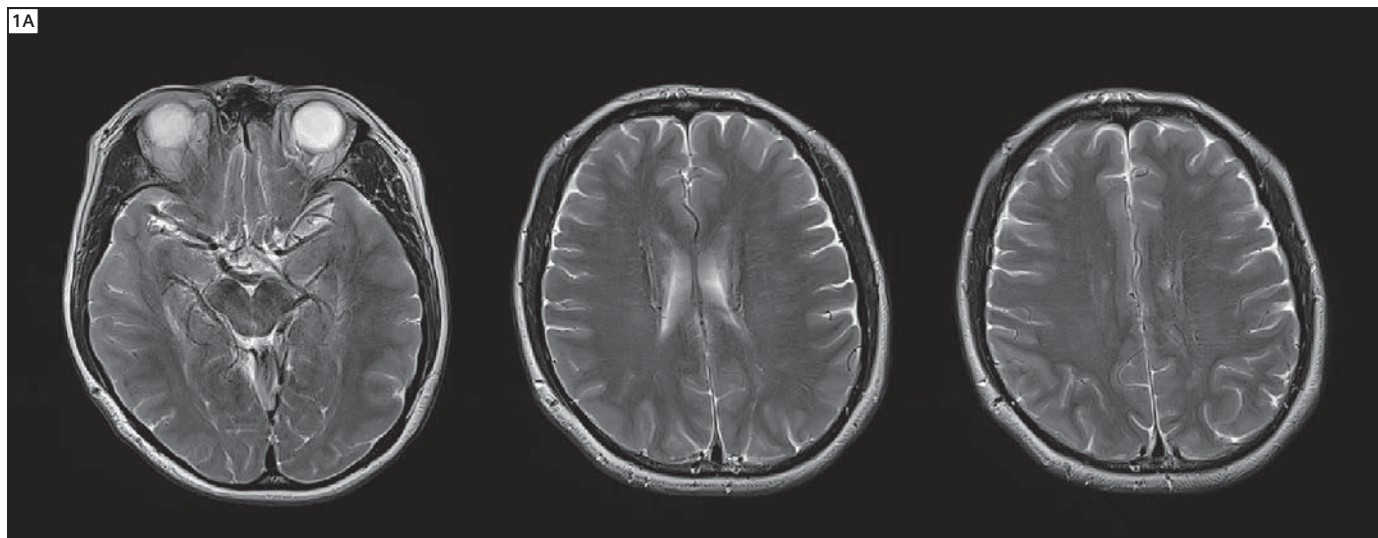
Axial T2-weighted Turbo Spin Echo (TSE) image reveals slightly enlarged subependymal veins along the ventricular lining and linear hyperintensities along the medullary vessels perpendicular to a long axis of the lateral ventricles. Susceptibility-weighted image (*syngo* SWI) acquired with a 32-channel head coil at 3T (MAGNETOM Trio, A Tim System) reveals diffusely prominent deep

medullary and collector veins draining into the subependymal veins. These veins can be well delineated from the surrounding brain tissue by their signal loss on *syngo* SWI; this is a clear advantage to conventional T2-weighted TSE imaging (Figs. 1A–1C).

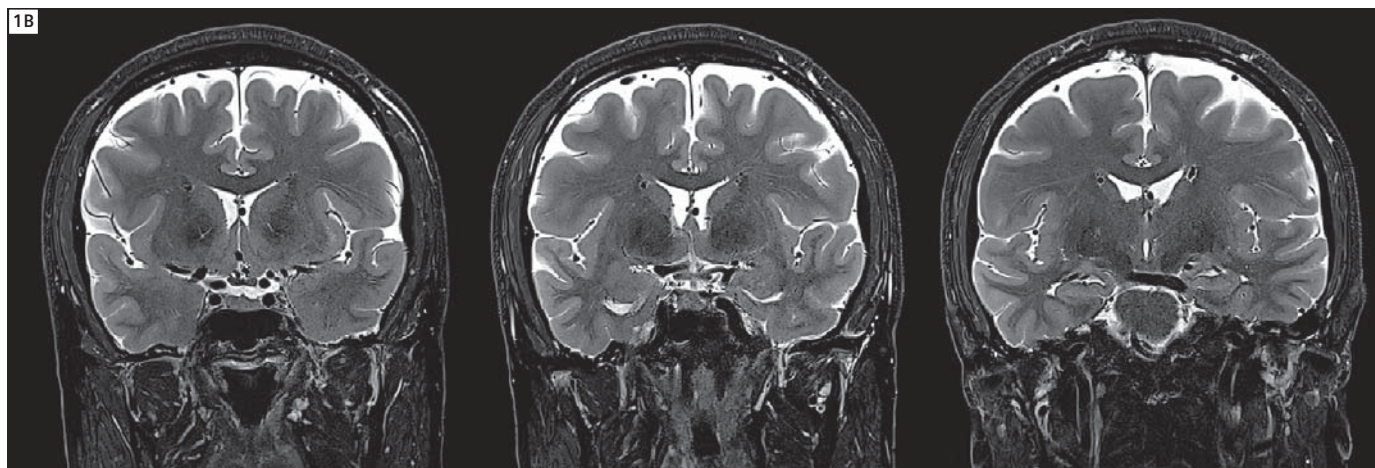
The *syngo* SWI findings are also concordant to the postcontrast 3D T1-weighted images, also demonstrating strongly enhancing umbrella-like medullary and collector veins. These findings are consistent with developmental venous anomaly (DVA).

Contact

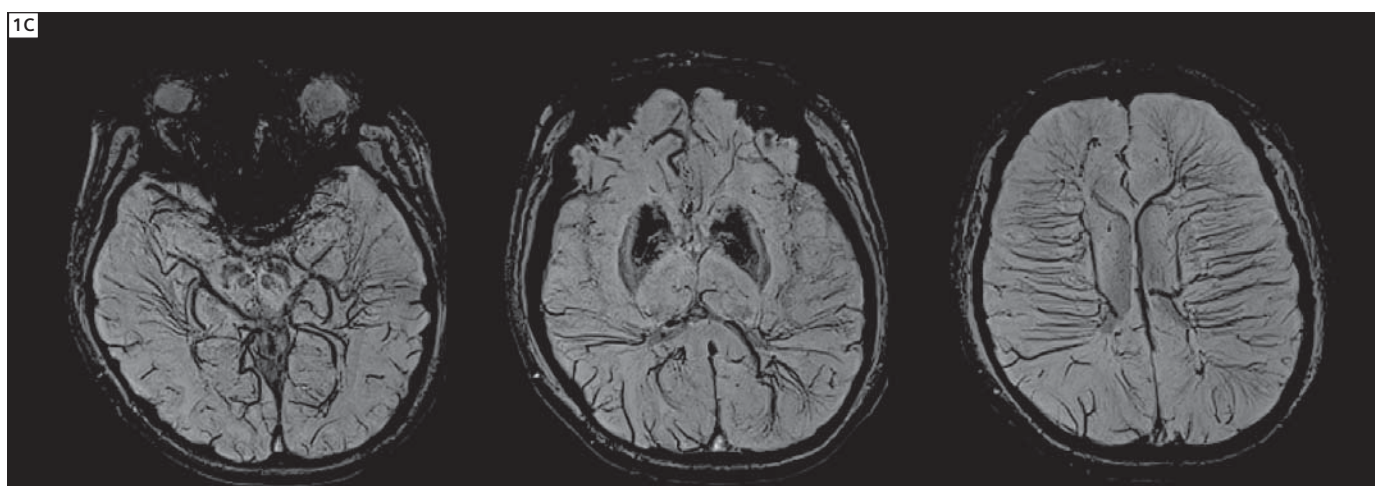
Masahiro Ida, M.D.
Department of Radiology
Tokyo Metropolitan Ebara Hospital
4–5–10 Higahsi-Yukigaya, Ota-ku,
Tokyo 145–0065
Japan
rxb00500@gmail.com



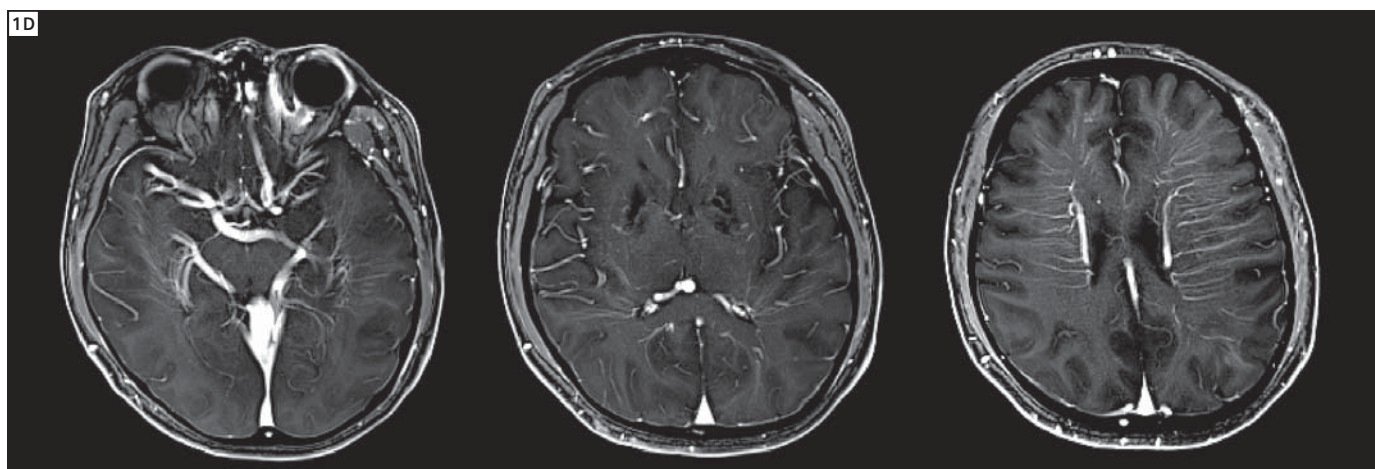
1A Transversal T2-weighted TSE images acquired with the 32-channel head coil at 3T. Slice thickness 5 mm, TR 4500 ms, TE 98 ms, BW 180 Hz/px, PAT factor 2, turbo factor 11, FOV 199 x 220 mm, matrix 371 x 512, total acquisition time: 2:32 min.



1B Corresponding fat-suppressed (SPAIR) coronal T2-weighted TSE images. Slice thickness 2 mm, TR 4000, TE 72 ms, BW 205 Hz/px, PAT factor 3, turbo factor 9, FOV 200 x 200 mm, matrix 410 x 512, 2 averages, acquisition time: 6:32 min.



1C Transversal thin MinIP (slice thickness 9.6 mm) susceptibility-weighted image (*syngo* SWI). Original slice thickness 1.2 mm, TR 28 ms, TE 20 ms, BW 120 Hz/px, PAT factor 3, turbo factor 10, FOV 230 x 230 mm, matrix 320 x 320, acquisition time: 6:01 min.



1D Axial thin MPR (slice thickness 5 mm) of contrast-enhanced 3D T1-weighted FLASH imaging. Original slice thickness 1 mm, TR 12 ms, TE 6.2 ms, BW 340 Hz/px, PAT factor 4, FOV 220 x 220 mm, matrix 320 x 320, acquisition time: 2:54 min.

Case Report:

Brain Spectroscopic Imaging at 3T with the 32-Channel Phased-Array Head Coil

Ovidiu C. Andronesi¹; Dominique Jennings¹; Nouha Salibi²; A. Gregory Sorensen¹

¹Athinoula A. Martinos Center for Biomedical Imaging, Department of Radiology, Massachusetts General Hospital, Boston, MA, USA

²Siemens Medical Solutions USA, Charlestown, MA, USA

Introduction

The newly developed 32-channel phased-array head coil [1, 2] has shown clear advantages for high resolution imaging, functional MRI (fMRI), perfusion and diffusion imaging of brain [3]. Known for its low intrinsic sensitivity, MR spectroscopic imaging (MRSI, also named chemical shift imaging or CSI [4]) is an obvious application that can benefit from the increased signal-to-noise ratio (SNR) provided by the 32-channel technology. Increased SNR will improve the current performance and reliability of MRSI, which will help in the realization of its full clinical potential. MRSI can study a wealth of in vivo metabolic processes that are complementary to the information derived from water imaging. However, obtaining clinically beneficial MRSI data is challenged by the much lower metabolite concentration compared to water, which in turn often imposes long scanning times. Here we present brain MRSI data from a volunteer and from a brain tumor patient acquired at 3T with the standard 12-channel Head Matrix coil and with the recently released 32-channel phased-array head coil. The SNR of the

32-channel coil can be flexibly traded for reduced scan time and/or increased resolution of MRSI, or it can be used to improve the accuracy and reliability of spectral data.

Methods

All measurements were conducted on the same whole body 3T scanner (MAGNETOM Trio, A Tim System, Siemens, Erlangen) using similar MRSI/MRI protocols. One healthy volunteer and one high-grade glioma patient were studied after informed consent approved by IRB protocols at our institution. For both subjects, one high resolution 3D structural scan (0.9 mm isotropic) was acquired with a multi-echo MPRAGE (MEMPRAGE) [5, 6] sequence (TR = 2.5 s, TI = 1.2 s, TE1/TE2/TE3/TE4 = 1.59/3.19/4.79/6.39 ms, FA = 7°, NA = 1) to identify the anatomy and position the volume of interest (VOI) for the CSI measurement. In the case of the glioma patient a single dose of Gd-DTPA (Magnevist) was bolus injected before the MEMPRAGE. In order to ensure the same CSI slice prescription when changing coils, an AutoAlign scout [7] was run

prior to the spectroscopy measurement. The 2D CSI slice position was approximately at the same level from the skull base for the volunteer and for the patient. In both subjects the VOI could be positioned roughly in the center of the reference MEMPRAGE image. The hybrid 2D CSI protocol consisted of a PRESS [8] pre-selected VOI surrounded by 8 outer volume saturation bands (OVS) [9, 10] placed around the skull for lipid suppression. The WET (Water Enhanced Through T1 Effects) [1] method was used for water suppression (30 Hz bandwidth). Acquisition parameters were common for both subjects: FOV of 200 x 200 x 15 mm³, VOI 80 x 80 x 15 mm³, weighted elliptical phase encoding (16 x 16 matrix size yielding a voxel size of 12.5 x 12.5 x 15 mm³), TR = 1.5 s, TE = 30 ms, NA = 4 (TA = 7:12 min), 1250 Hz bandwidth and 1024 points for the time-domain. In addition, in the volunteer case two more 2D CSI data sets were recorded when using the 32-channel coil: 1) having the same resolution (16 x 16 matrix) and NA = 2 (TA = 4:45 min), and 2) increasing the resolution (20 x 20 matrix) and NA = 1 (TA = 6:26 min).

During data processing the data were interpolated to a 32 x 32 matrix. Processing included: k-space Fourier transformation and a spatial 50 Hz Hanning filter, subtraction of the residual water signal, time domain 1 Hz exponential apodization, zero filling to 2048 points, Fourier transformation of the time domain signals, frequency shift correction as well as phase correction and baseline correction. Data were quantified either with the fitting routine from *syngo* MR B15A or exported to jMRUI3.0 software [12] and fitted using the AMARES algorithm with soft constraints [13]. Shimming of the unsuppressed water signal from the VOI was performed with each coil until similar T2* (45 ms) and linewidth (9 Hz) values were obtained for both subjects to achieve similar spectral quality. However, in the case of the 32-channel coil convergence towards the optimal shim was slower and the shim values were higher suggesting either a slight increase in the distortion of the main magnetic field homogeneity (possibly due to the more compact geometry compared to the 12-channel coil), or an influence on the shimming algorithm of the less uniform receive profile for the 32-channel coil.

Volunteer results

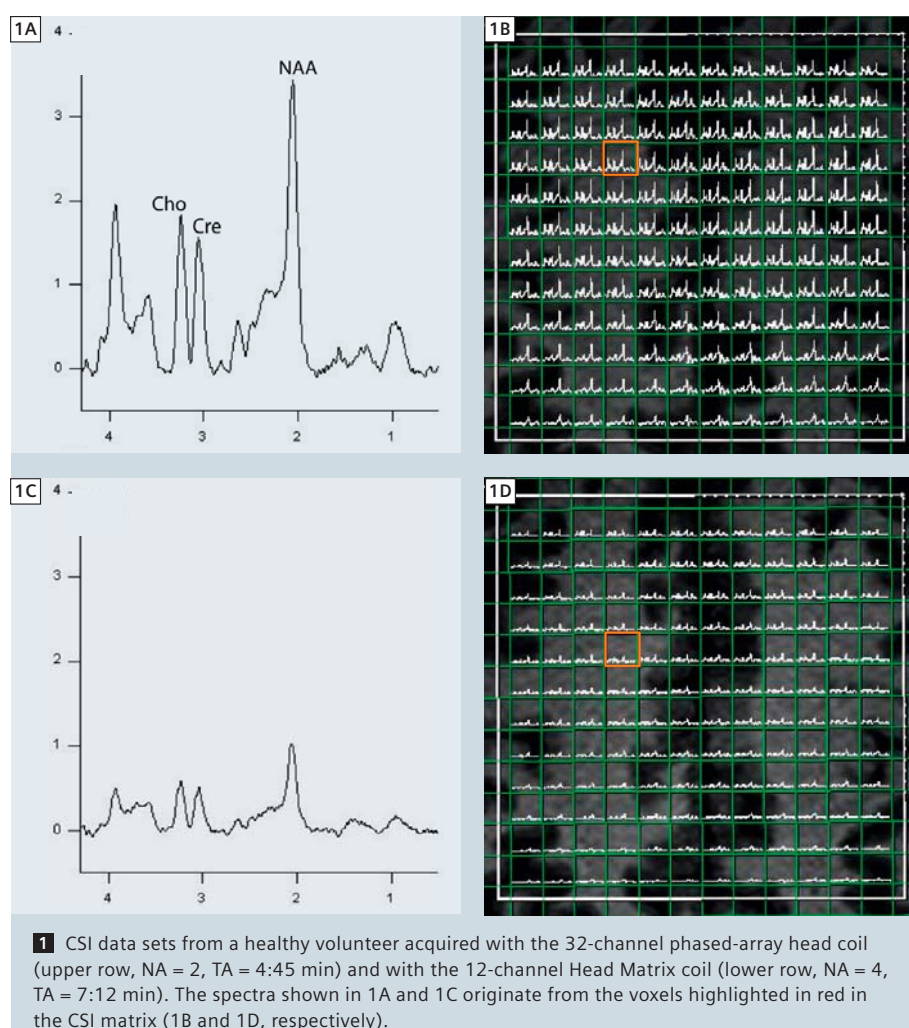
The need for averaging due to low SNR represents one of the main reasons for the increased scanning times in MRSI. To demonstrate the SNR gain of the 32-channel coil and how this can be traded to reduce scan time and/or increase resolution, three different protocols were compared on an adult (40 years age) healthy volunteer:

- 1) NA = 4, 16 x 16 weighted elliptical phase encode matrix (TA = 7:12 min);
- 2) NA = 2, 16 x 16 weighted elliptical phase encode matrix (TA = 4:45 min);
- 3) NA = 1, 20 x 20 weighted elliptical

phase encode matrix (TA = 6:26 min). The reference scan obtained with the 12-channel Head Matrix coil was acquired using the first protocol and the parameters described in the methods section.

Protocols 1 and 2 produced similar SNR with the 32-channel coil, resulting in an average gain of 3–4 times across all voxels and all metabolites compared to the reference CSI acquired with the 12-channel Head Matrix coil. A some-

what smaller SNR gain of 2–3 folds was obtained with protocol 3. Figure 1 shows examples of the 2D-CSI data acquired following protocol 2 for 32-channel coils (Figs. 1A, B) and protocol 1 for 12-channel Head Matrix (Figs. 1C, D). The spectra are scaled to the same intensity (vertical axis) and frequency (horizontal axis) ranges. Enlarged views of spectra from the voxels highlighted in red are shown in figures 1A and 1C.

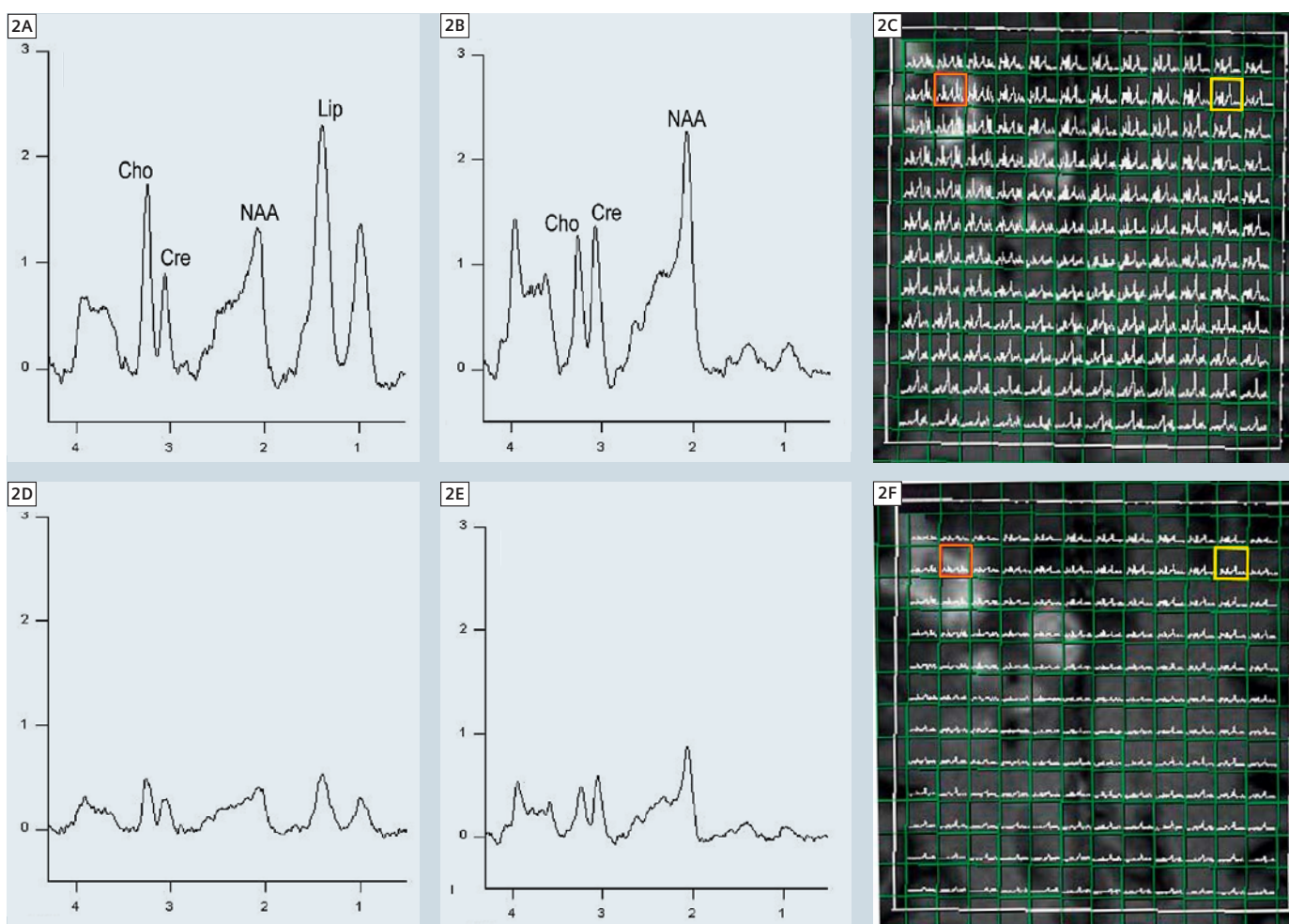


Patient results

One young patient (24 years age) with a recurrent high-grade glioma enrolled in a phase II study of a new antiangiogenic drug was imaged with structural, perfusion and diffusion-weighted imaging [14] which were followed by 2D CSI. All data were obtained within the same visit after 1 day of treatment. All the necessary data were first collected using the 32-channel coil. After switching to the 12-channel coil only the AAscout,

MEMPRAGE and the CSI protocols were repeated, adding in total an extra 15 minutes to the scan time, including the time needed for changing coils. No extra Gd-DTPA dose was injected. For consistency with the previous visits, the 2D CSI measurement with the 32-channel coil was performed with the protocol 1 (NA = 4, TA = 7:12 min). The same protocol was also employed with the 12-channel Head Matrix coil.

The patient results of Figure 2 demonstrate a 3–4 fold increase in SNR with the 32-channel coil, which is similar to the increase in SNR observed in the volunteer data. The spectra are scaled to the same intensity and frequency range. The data in the upper (lower) row are obtained with the 32(12)-channel coil. Examples of tumor (Figs. 2A, D) and healthy (Figs. 2B, E) brain spectra are shown from the highlighted voxels (red

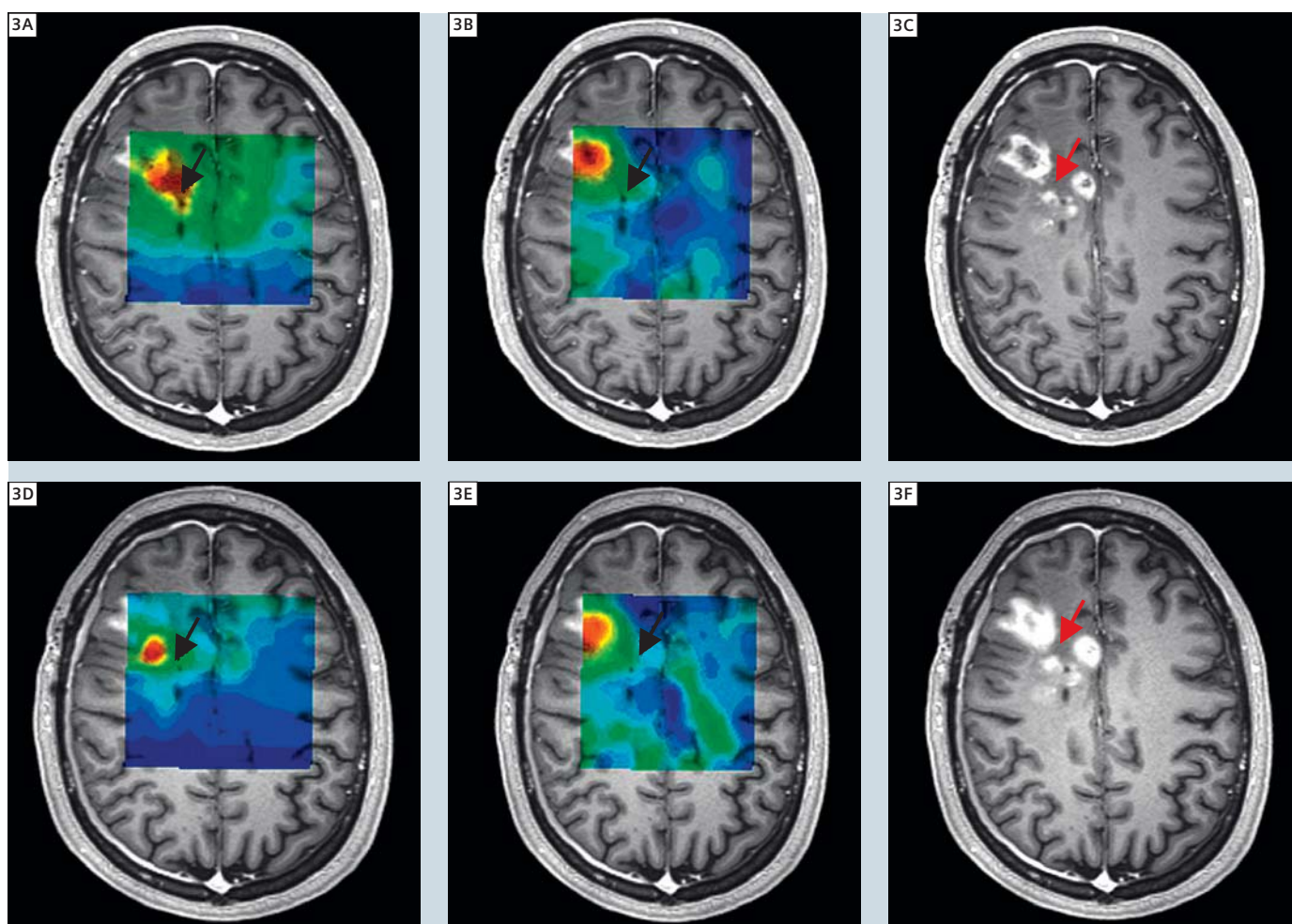


2 CSI data sets from a high-grade glioma patient acquired with the 32-channel phased-array head coil (2A–C) and with the 12-channel Head Matrix coil (2D–F). The same protocol with TR = 1.5 s, TE = 30 ms, NA = 4, TA = 7:12 min was employed. Tumor spectra are shown in 2A and 2D, originating from the red highlighted voxels (2C and 2F, respectively). Spectra of the healthy contra-lateral side are presented in 2B and 2E (yellow voxels in 2C and 2F, respectively).

and yellow, respectively) in the corresponding 2D CSI data matrix (Figs. 2C, F). A large contribution from lipid signal is found in the tumor. The particular position of the tumor in the anterior part of the VOI reduces the possibility of contamination with lipid signal from the skull due to the direction of the chemical shift error displacement from posterior to anterior (i.e. posterior voxels are more likely to be contaminated with lipid

signal from skull). A close inspection of the voxels inside and outside the VOI reveals reduced lipid signals outside the VOI. The highest lipid signals are within the lesion; it was concluded that a lipid metabolite map can be reliably computed as demonstrated in figures 3B and 3E. As evident from spectra of Figs. 2A and D the tumor is characterized also by decreased NAA and increased Cho levels, confirming together with the

lipids findings a high-grade glioma [15, 16]. A Cho/NAA map was calculated and overlaid on the Gd-DTPA enhanced image. Figure 3 shows the corresponding Cho/NAA maps (Figs. 3A, D), lipid maps (Figs. 3B, E) and post-Gd MEMPRAGE reference image (Figs. 3C, F), where the upper (lower) row data are obtained with the 32(12)-channel coil.



3 Metabolite maps and Gd-DTPA enhanced images for a high-grade glioma patient obtained using the 32-channel phased-array head coil (upper row) and the 12-channel Head Matrix coil (lower row). Cho/NAA maps are computed in 3A, D and lipid maps in 3B, E. The black arrows (3A, B, D, E) indicate areas where the 32-channel coil detects changes more reliable than the 12-channel coil. The red arrows (3C, F) point to the region of decreased intensity among the three main Gd enhancing lesions.

The maps obtained with the 32-channel phased-array head coil (Figs. 3A, B) have a better coverage of the extent of the lesion probed by the Gd image (Fig. 3C) as indicated by the black arrows. Interestingly the lipid map (Fig. 3B) overlaps well over the largest Gd enhancing lesion, while the increase of Cho/NAA ratio (Fig. 3A) seems to be more confined to the space among the three main Gd enhancing lesions, which corresponds to a region of reduced intensity in the MEMPRAGE image (Figs. 3C, F, red arrows) as compared to the contra-lateral normal side. However the extent of the Cho/NAA is better defined than the region of reduced intensity, possibly pointing to the most active part of the tumor that needs to be followed during the course of the treatment.

Conclusion

Data obtained from a healthy volunteer and from a patient with glioma indicate that CSI measurements with the 32-channel phased-array head coil can reduce by half the acquisition time (number of averages) while maintaining a 3–4 times gain in SNR compared to the 12-channel Head Matrix coil. SNR gain is also possible when simultaneously increasing the spatial resolution (with a larger phase encoding matrix) and reducing the scan time (number of averages).

Clinical benefits are demonstrated in the patient data, which show that possible hot spots of the tumors can be more reliably identified. Metabolite maps of the 32-channel coil conform better to the Gd enhancing lesions and the peritumoral regions.

The advantages reported here with the use of a 32-channel coil in the evaluation of tumors are also relevant to other brain spectroscopy applications including stroke, psychiatric or neurodegenerative diseases. The improved SNR and reliability, and the shorter scan times are likely to increase the clinical use of MR spectroscopy. They will also have considerable impact on the development of functional (dynamic) MR spectroscopy

[17] and its clinical applications. Besides reducing scan times, increasing resolution and improving accuracy, innovative ideas could utilize image encoding with the geometry of large phased arrays coils [1]; latter could then improve the chemical shift displacement error that still hampers MRSI signal localization using slice selective excitation and gradient encoding.

Acknowledgements

I would like to thank Michael Hamm and Josef Pfeuffer from Siemens Medical Solutions USA Inc. for their assistance during this project.

References

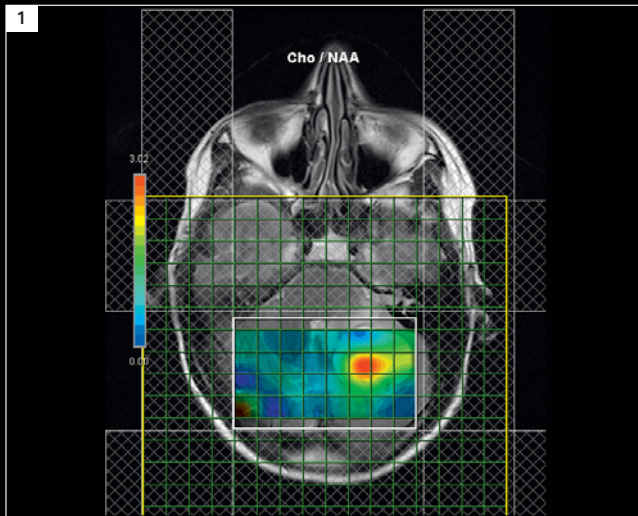
- Wald LL, Wiggins G. Highly parallel detection for MRI. *MAGNETOM Flash* 2008;38(1):34–44.
- Stapf J. 32-Channel phased-array head coil. *MAGNETOM Flash* 2008;38(1):45.
- Runge VM. 32-Channel head coil imaging at 3T. *Case Reports from Scott and White Clinic and Hospital. MAGNETOM Flash* 2008;39(2):38–42.
- Brown TR, Kincaid BM, Ugurbil K. NMR Chemical-Shift Imaging in 3 Dimensions. *Proceedings of the National Academy of Sciences of the United States of America-Biological Sciences* 1982;79(11):3523–3526.
- Mugler JP, Brookeman JR. 3-Dimensional Magnetization-Prepared Rapid Gradient-Echo Imaging (3D MPRAGE). *Magnetic Resonance in Medicine* 1990;15(1):152–157.
- van der Kouwe AJW, Benner T, Salat DH, Fischl B. Brain morphometry with multiecho MPRAGE. *Neuroimage* 2008;40(2):559–569.
- van der Kouwe AJW, Benner T, Fischl B, et al. On-line automatic slice positioning for brain MR imaging. *Neuroimage* 2005;27(1):222–230.
- Bottomley PA. Spatial Localization in NMR-Spectroscopy In vivo. *Annals of the New York Academy of Sciences* 1987;508:333–348.
- Moonen CTW, Sobering G, Vanzijl PCM, Gillen J, Vonkienlin M, Bizzi A. Proton Spectroscopic Imaging of Human Brain. *Journal of Magnetic Resonance* 1992;98(3):556–575.
- Duyn JH, Gillen J, Sobering G, Vanzijl PCM, Moonen CTW. Multisection Proton MR Spectroscopic Imaging of the Brain. *Radiology* 1993;188(1):277–282.
- Ogg RJ, Kingsley PB, Taylor JS. WET, a T-1-Insensitive and B-1-Insensitive Water-Suppression Method for in-Vivo Localized H-1-NMR Spectroscopy. *Journal of Magnetic Resonance Series B* 1994;104(1):1–10.
- Naressi A, Couturier C, Devos JM, et al. Java-based graphical user interface for the MRUI quantitation package. *Magnetic Resonance Materials in Physics Biology and Medicine* 2001;12(2–3):141–152.
- Vanhamme L, van den Boogaart A, Van Huffel S. Improved method for accurate and efficient quantification of MRS data with use of prior knowledge. *Journal of Magnetic Resonance* 1997;129(1):35–43.
- Batchelor TT, Sorensen AG, di Tomaso E, et al. AZD2171, a pan-VEGF receptor tyrosine kinase inhibitor, normalizes tumor vasculature and alleviates edema in glioblastoma patients. *Cancer Cell* 2007;11(1):83–95.
- Griffin JL, Shockcor JP. Metabolic profiles of cancer cells. *Nature Reviews Cancer* 2004;4(7):551–561.
- Hakumaki JM, Poptani H, Sandmair AM, Yla-Herttuala S, Kauppinen RA. H-1 MRS detects poly-unsaturated fatty acid accumulation during gene therapy of glioma: Implications for the in vivo detection of apoptosis. *Nature Medicine* 1999;5(11):1323–1327.
- Ross B, Lin A, Harris K, Bhattacharya P, Schweinsburg B. Clinical experience with C-13 MRS in vivo. *Nmr in Biomedicine* 2003;16(6–7):358–369.

Contact

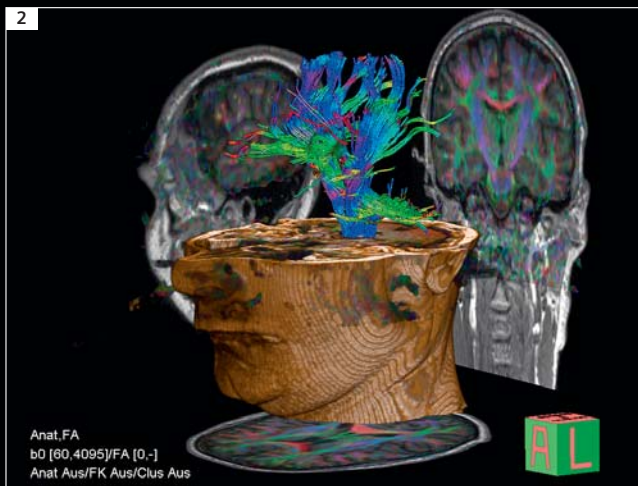
Ovidiu C. Andronesi
Athinoula A. Martinos Center
for Biomedical Imaging
Department of Radiology
Massachusetts General Hospital
Boston, MA, 02114
USA
ovidiu@nmr.harvard.edu

Try them on your system

Trial licenses for most of the applications featured in this issue of MAGNETOM Flash are available free of charge for a period of 90 days: Please contact your local Siemens representative for system requirements and ordering details.



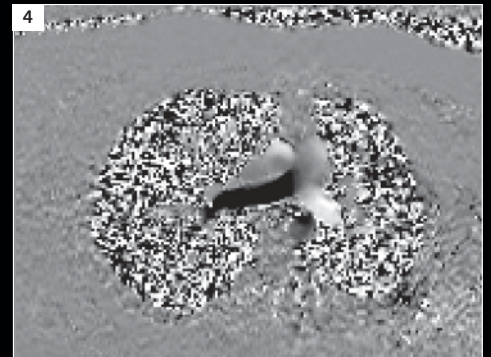
1 Chemical Shift Imaging (CSI) spectroscopy (page 10)



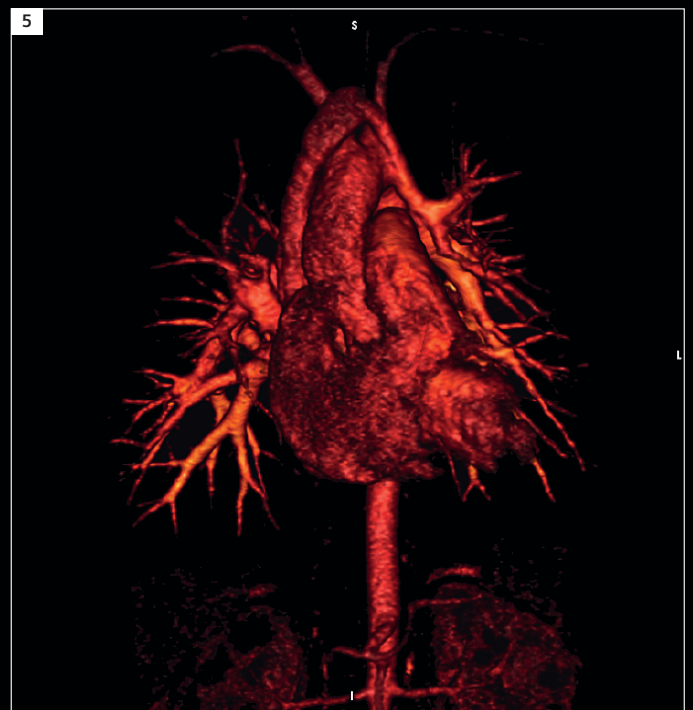
2 syngo DTI Tractography (page 11)



3 syngo SWI (page 43)



4 Argus Flow, flow quantification (page 88)



5 3D VRT – Volume Rendering Technique (page 98)



6 syngo TWIST (page 106)

Case Report: Clinical Validation of Arterial Spin Labeling

Jessica A. Turner; Sumiko Abe; Liv MacMillan; Jerod Rasmussen; Steven G. Potkin

Brain Imaging Center, University of California, Irvine, CA, USA

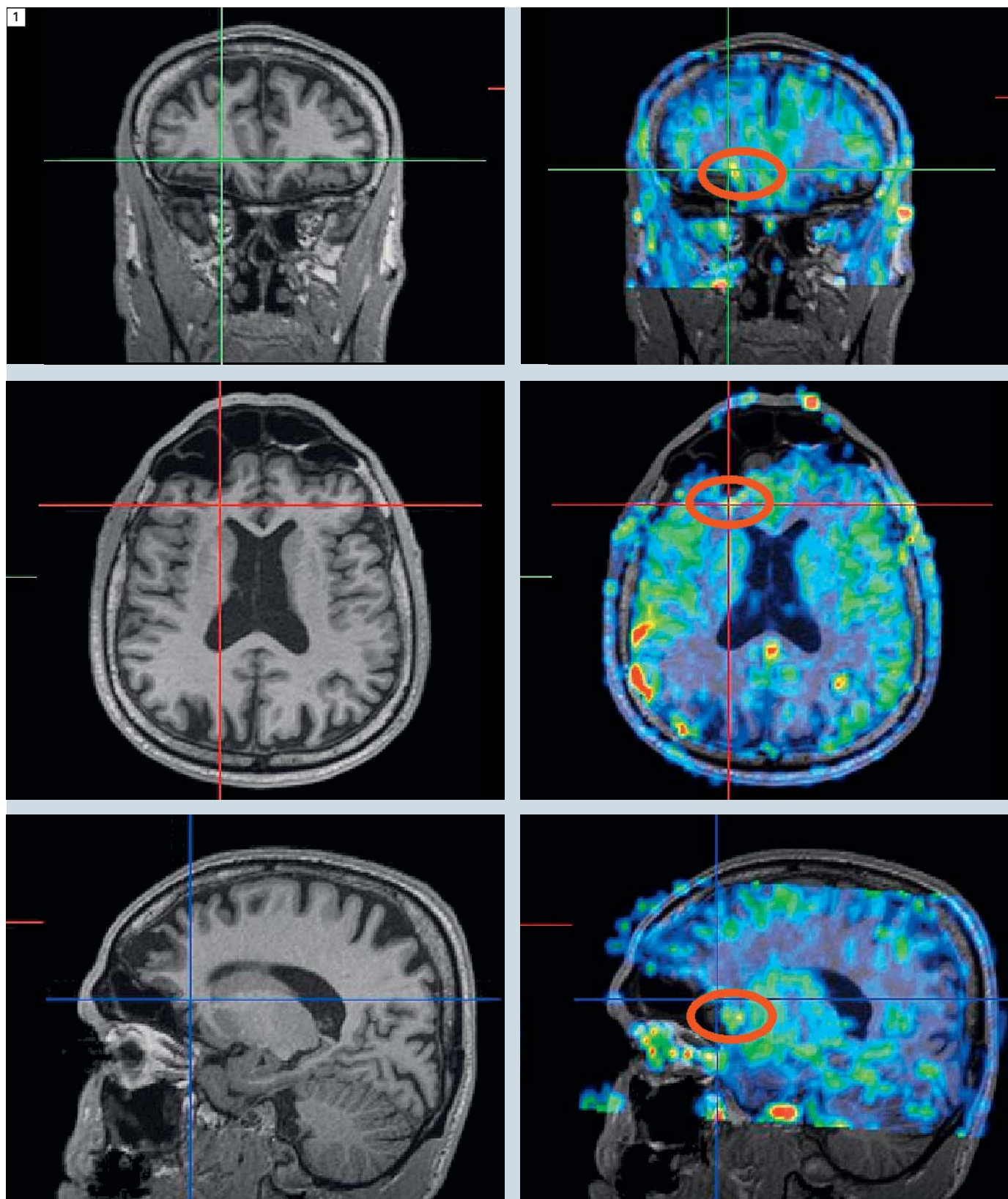
Introduction

Arterial spin labeling (ASL) magnetic resonance imaging methods are perfusion-based imaging techniques; they provide quantitative measures of capillary blood flow rCBF (regional cerebral blood flow), in units of ml/100 g/min. Like positron emission tomography and certain other imaging methods, ASL measures can be either absolute (measuring overall flow), or relative (measuring changes in flow). However, ASL does not require injection of radioactive tracers or contrast agent, since it depends on the endogenous tracer of the spin-tagged blood. This allows it to be used in many clinical populations, and to be used repeatedly over shorter periods of time without any side effects observed with other exogenous tracer based methods. The basis of ASL is to use an appropriate RF pulse to tag all the blood in a particular location with a particular magnetization, i.e. an inversion (hence spin labeling). As the blood perfuses from the tagging location into the rest of the brain, the tagged blood changes the magnetization characteristics of the area, and thus can be measured [1]. ASL has been used successfully to measure blood flow in cardiovascular disorders and brain tumors [2–6]. Areas of high perfusion around a tumor, for example, can indicate where the growth is occurring most rapidly [7]. ASL can identify signs of stenosis which can be very difficult to otherwise identify non-invasively in the clinic [8]. These

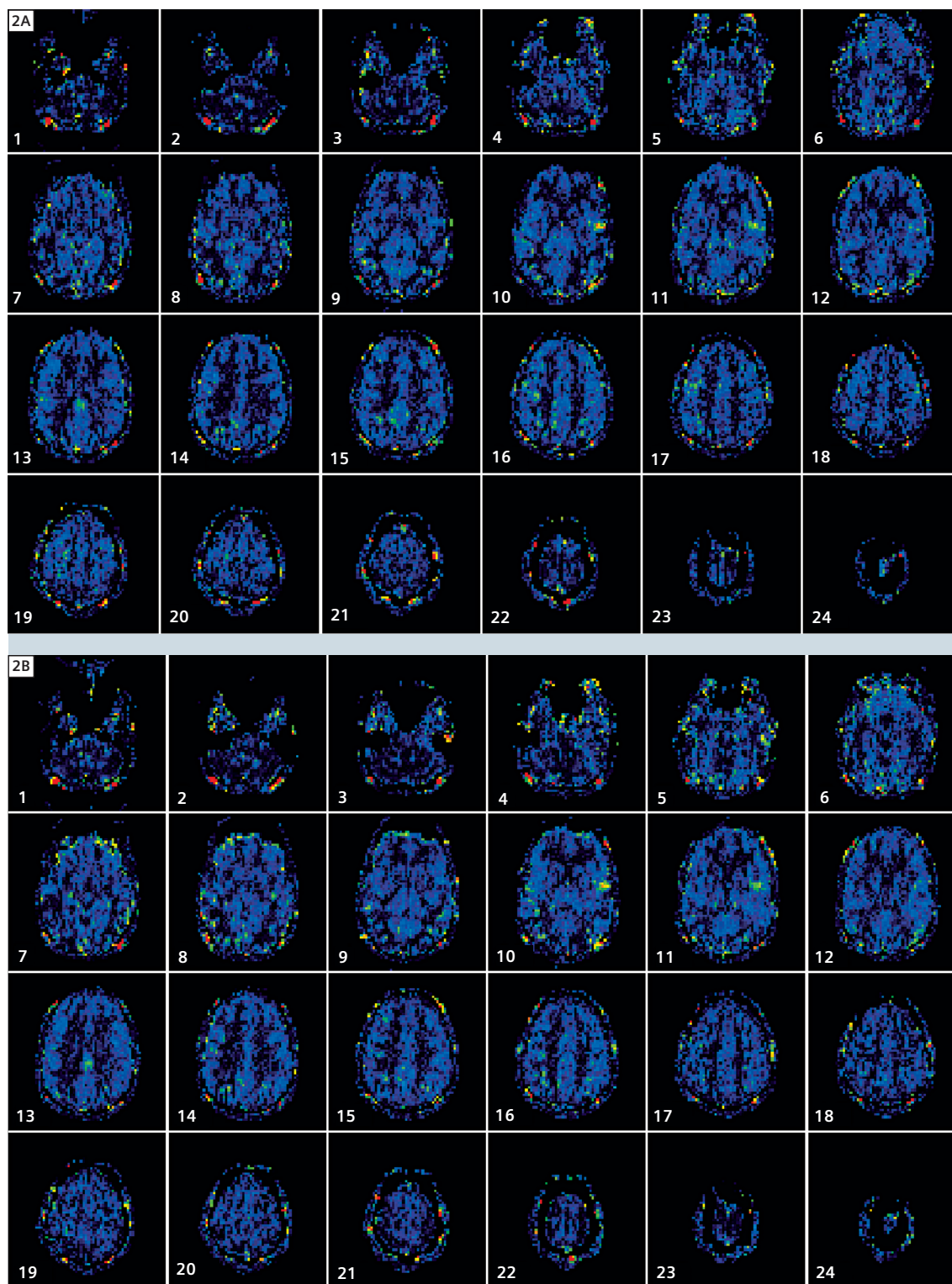
disorders which stem from structural changes closely involved with the cardiovascular system are obvious candidates for a study using ASL. Here we would like to demonstrate how ASL can be useful in clinical settings. The following protocol (referred to as “FBIRN-ASL protocol”) was used: FAIR QUIPSSII as pulsed ASL method, TI2 = 1600 ms, TI1 = 600 ms; TR = 4 s, TE = 12 ms; flip angle 90 degrees; 24 slices, 4 mm thick, 1 mm gap. P >> A phase encoding; 220 mm FOV, base resolution 64, phase partial Fourier 6/8, ascending slice order, AC–PC aligned. Fat saturation was turned on; the coil combine mode was sum of squares. The bandwidth was 2368 Hz/Px, echo spacing 0.49. We collected 105 measurements, which included an M0 reference scan. All studies were conducted using the 12-channel Siemens product Head Matrix coil. 3D PACE was used for real-time prospective motion correction.

Case 1

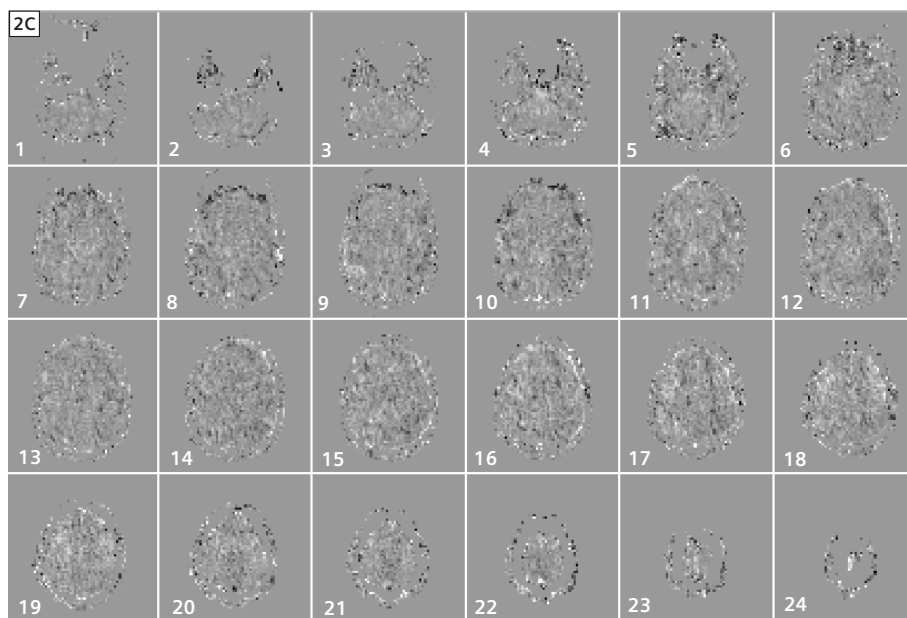
The subject is a 47-year-old male, who has been schizophrenic for 31 years, currently on antipsychotics and sleep aids. He had a self-report of a head injury at age 3 requiring both stitches and surgery, and another concussion with hospitalization in his teens. His schizophrenic symptoms are stable on his current medications. The head injury is not the current cause for treatment. The subject received T1- and T2-weighted anatomic scans, and an ASL scan using the FBIRN settings. The MRIs were reviewed by a radiologist to determine whether the internal brain damage required any current attention, and it was determined that it did not. The rCBF measures from the entire brain, from gray matter and from areas near the damage were measured for comparison both in their means and their variability. The T1 and T2-weighted images clearly showed areas of damage in the frontal lobes, with multiple fluid filled cysts, and dilation of the posterior sulci. There was no dilatation of the left frontal horn of the ventricles, which frequently is associated with atrophy, so general atrophy was not noted. The ASL images showed the expected distortion from the frontal cysts. The rCBF measures both globally and from the entire grey matter of the subject were in general quite low, 45–47 ml/100 g/min (as compared to 58 ml/100 g/min for similarly aged healthy males, using a 1.5T multi-slice CASL method, in Parkes et al. (2004).) Areas near the cysts showed a higher variability in rCBF than did the overall grey matter measures.



1 rCBF measurement around the area of brain damage. Left row is the anatomical scan and the right row shows the ASL rCBF measurement fused to the anatomical scan. The rCBF of the area around the brain damage is found to be higher.



2A, B Representative images from the experiment. **(2A)** rCBF images when eyes open and **(2B)** when closed.

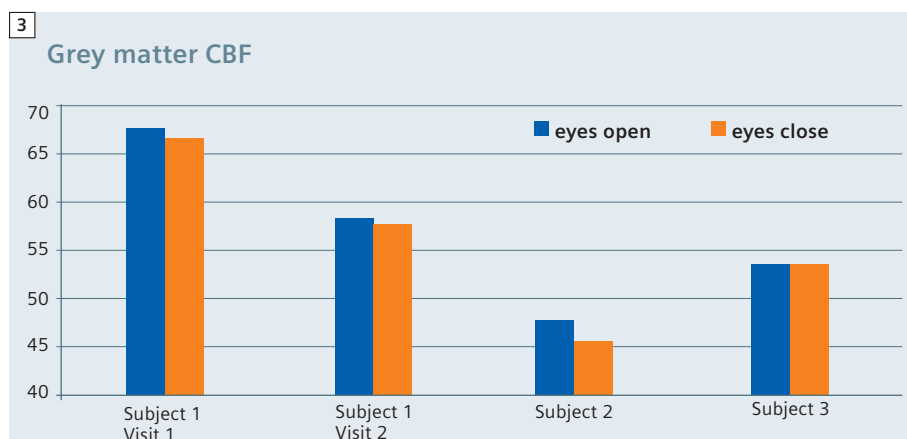


2C Difference images between eyes closed and eyes open.

Case 2

Three healthy subjects (ages 22 to 62) were scanned twice each in the FBIRN-ASL setting, once with eyes open and once with eyes closed. One subject was scanned twice in each condition. No motion correction was included during the scan.

Various rCBF measures were summarized from the rCBF images in each condition. The difference image (rCBF with eyes open – rCBF with eyes closed) was calculated for each subject. Head movement over the 105 image volumes was also measured in the two conditions. Overall, ASL flow within the grey matter mask increases very slightly with the eyes open. In three of the four cases, head movement was greater when the subject's eyes were closed.



3 Grey matter rCBF [ml/100 g/min]. There is a consistent decrease in grey matter CBF when the eyes are closed.

Contact

Jessica A. Turner, Ph.D.
Project Manager, FBIRN
(www.nbirn.net)
Department of Psychiatry and
Human Behavior
University of California
Irvine, CA, 92617
USA
Phone: +1(949) 824-3331
Fax: +1(949) 824-3324
turnerj@uci.edu

References

- 1 Detre, J. A., Leigh, J. S., Williams, D. S., & Koretsky, A. P. (1992). Perfusion imaging. *Magn Reson Med*, 23(1), 37–45.
- 2 Deibler, A. R., Pollock, J. M., Kraft, R. A., Tan, H., Burdette, J. H., & Maldjian, J. A. (2008a). Arterial spin-labeling in routine clinical practice, part 2: Hypoperfusion patterns. *AJNR Am J Neuroradiol*.
- 3 Deibler, A. R., Pollock, J. M., Kraft, R. A., Tan, H., Burdette, J. H., & Maldjian, J. A. (2008b). Arterial spin-labeling in routine clinical practice, part 3: Hyperperfusion patterns. *AJNR Am J Neuroradiol*.
- 4 Noguchi, T., Yoshiura, T., Hiwatashi, A., Togao, O., Yamashita, K., Nagao, E., et al. (2008). Perfusion imaging of brain tumors using arterial spin-labeling: Correlation with histopathologic vascular density. *AJNR Am J Neuroradiol*, 29(4), 688–693.
- 5 Tourdias, T., Rodrigo, S., Oppenheim, C., Naggara, O., Varlet, P., Amoussa, S., et al. (2008). Pulsed arterial spin labeling applications in brain tumors: Practical review. *J Neuroradiol*, 35(2), 79–89.
- 6 Wolf, R. L., & Detre, J. A. (2007). Clinical neuroimaging using arterial spin-labeled perfusion magnetic resonance imaging. *Neurotherapeutics*, 4(3), 346–359.
- 7 Bartsch, A. J., Homola, G., Biller, A., Solymosi, L., & Bendszus, M. (2006). Diagnostic functional mri: Illustrated clinical applications and decision-making. *J Magn Reson Imaging*, 23(6), 921–932.
- 8 Detre, J. A., Samuels, O. B., Alsop, D. C., Gonzalez-At, J. B., Kasner, S. E., & Raps, E. C. (1999). Noninvasive magnetic resonance imaging evaluation of cerebral blood flow with acetazolamide challenge in patients with cerebrovascular stenosis. *J Magn Reson Imaging*, 10(5), 870–875.

Case Report:

Magnet Resonance Imaging in Inflammatory Arthritis

Marius Horger, M.D.

University Hospital Tübingen, Dept. of Diagnostic and Interventional Radiology, Tuebingen, Germany

Introduction

Magnetic Resonance Imaging (MRI) has advanced to the most accurate imaging modality in the diagnosis and response monitoring of inflammatory arthritis. Unlike conventional X-ray technique, MRI delivers information concerning both morphologic changes of the involved joint and pathophysiologic data with respect to the degree of synovial membrane and/or bone and juxta-articular inflammation. Furthermore, the excellent resolution and the high tissue contrast enable not only assessment of inflammatory activity, but also differentiation between the different types of arthritis disorders.

Hence, this short case series should help understand some of the most important benefits of the use of MRI. Early detection of inflammatory activity and onset of bone destruction, irrespective of the underlying arthritis type, remain major goals in the diagnosis. Established technologies (e.g. dynamic contrast enhanced MRI) and newer technologies (e.g. *syngo* ASL Arterial Spin Labeling) make even quantification of inflammation-related synovial perfusion practicable in the routine diagnosis. The latter delivers this information even without the use of intravenous contrast. Finally, MRI also helps to better understand the pathomechanisms responsible for disease progression.

Sequence details

The MR imaging protocol consisted of the following:

Axial T1-weighted 2D spin-echo

sequence: Repetition time (TR) 863 ms; echo time (TE) 12 ms; slice thickness (SL) 2 mm; bandwidth (BW) 195 Hz/px; matrix 320 x 204; in-plane resolution (IPR) 0.4 x 0.3 mm; averages (AVR), 2; acquisition time (TA) 4:10 min, coronal T1-weighted 2D spin-echo sequence (TR, 570 ms; TE, 12 ms; SL, 1.5 mm; BW, 195Hz/px; matrix, 320x232; IPR, 0.4 x 0.3 mm; AVR, 2; TA, 5:11 min.)

Coronal T2-weighted 2D fast spin-echo sequence with spectral fat-saturation: TR 7210 ms; TE 81 ms; echo train length (ETL) 15; SL 1.5 mm; BW, 180 Hz/px; matrix 320 x 320; IPR 0.4 x 0.3 mm; AVR 4; TA 5:58 min.

3D DESS (dual-echo steady state): TR 21.6 ms; TE 6.8 ms; ETL 15; BW 180 Hz/px; matrix 256 x 256; resolution 0.6 x 0.6 x 0.6 mm; AVR 2; TA 7:12 min.

3D FLASH (fast low angle shot), a spoiled gradient-echo sequence with spectral fat saturation for dynamic MR imaging: TR 3.95 ms; TE 1.45 ms; resolution 0.6 x 0.6 x 0.8 mm; BW 350 Hz/px; 32 slices per slab; slice partial Fourier 6/8; flip angle 20°; IPR 0.4 x 0.3 mm; AVR 2; TA 13 s.

Axial T1-weighted spin-echo sequence with spectral fat saturation for post-contrast imaging: TR 798 ms; TE 12 ms; SL 1.5 mm; no gap; BW 195 Hz/px; matrix 320 x 2042; IPR 0.7 x 0.6 mm; AVR 2; TA 5:31min.

Case 1

Late rheumatoid arthritis (RA)

Patient history

A 48-year-old female patient with known rheumatoid arthritis presented with progressive swelling of the metacarpophalangeal joints. The patient was known to be in compliant and indolent and had discontinued therapy one year ago. On conventional radiographs of the hands (not shown), newly occurred intraosseous cysts were diagnosed, additionally to the typical erosions in the bare area of the metacarpal bones.

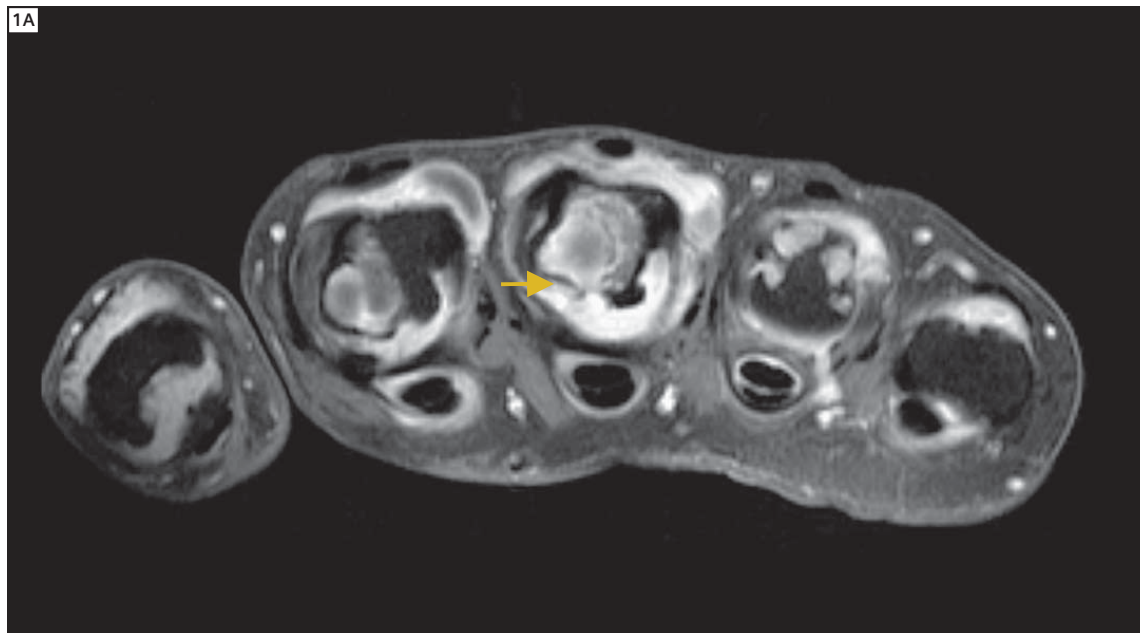
Image findings

High-resolution MRI of both hands using a dedicated hand coil and a 3T magnetic field (Siemens MAGNETOM Trio) revealed typical signs of elevated intraarticular pressure due to overproduction of joint effusion by the inflamed synovia. Due to the excellent image resolution (in plane resolution, 0.3 x 0.4 mm) and contrast and the use of a thin slice protocol (1.5 mm), interruption of cortical bone (arrow) along the metacarpal heads is well depicted on axial fat-saturated T1-weighted post-gadolinium image, demonstrating continuity of the joint cavity with the intraosseous cysts (Fig. 1A). Note enhancement of both articular synovia and metacarpal cystic

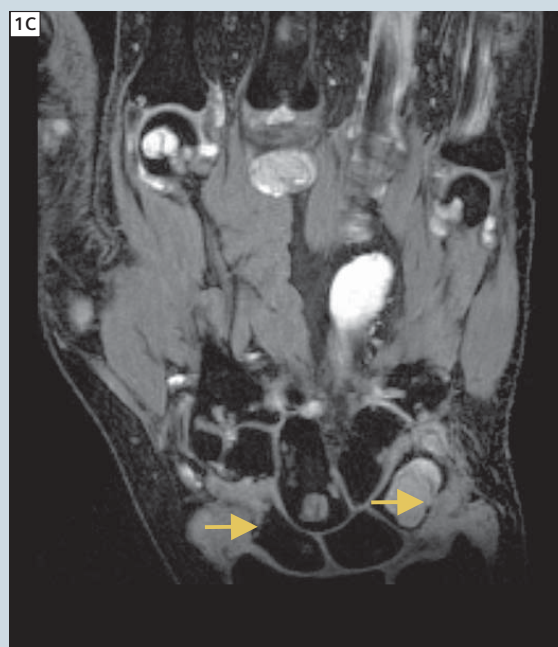
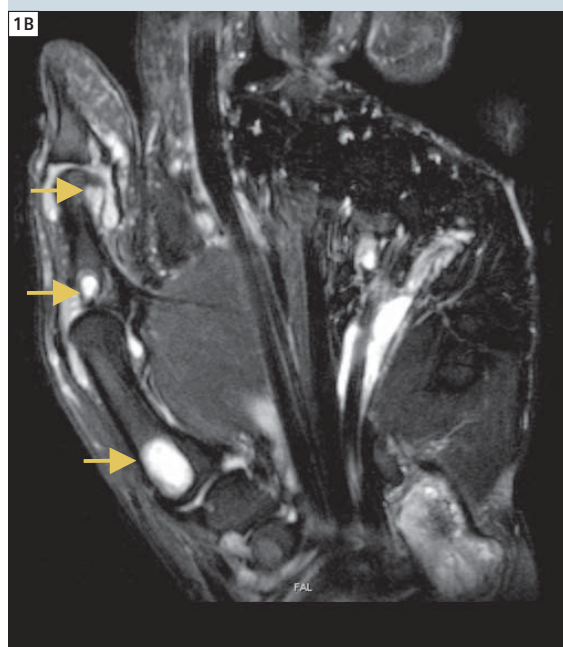
lesion representing extension of articular active pannus into the bony canal. There is only a small amount of effusion in the joint space and in the adjacent involved metacarpal bones II and III. Note also tenosynovitis of the flexor tendon sheaths.

In the other hand, coronal fat-saturated T2-weighted image (Fig. 1B) and coronal DESS image (Fig. 1C) both show the pathways of arousal of intraosseous cysts at sites where the cortical bone has become permeative. Note volar disten-

sion of articular synovial membrane in the interphalangeal joint of the 1st finger denoting overpressure and the accompanying intraosseous cysts (arrows). On the fat-saturated T2-weighted image, differentiation of articular fluid from



1A Axial fat-saturated T1-weighted post-gadolinium image, demonstrating continuity of the joint cavity with the intraosseous cysts.



1B, C B: Contralateral hand to Fig. 1A, coronal fat-saturated T2-weighted image C: Contralateral hand to Fig. 1A, coronal DESS image.

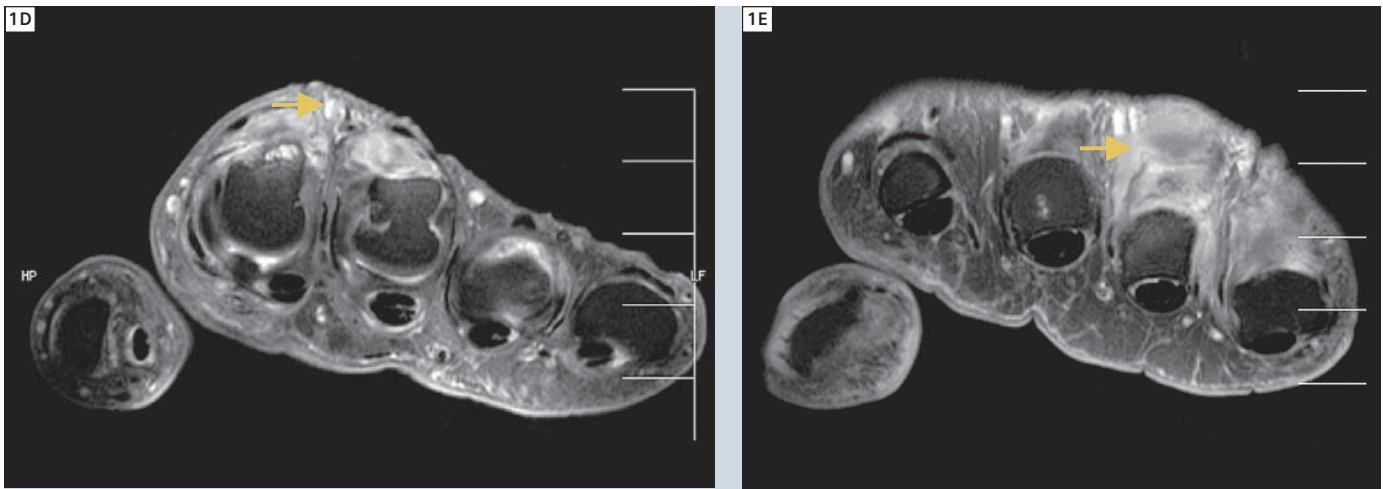
active pannus is not possible. However, on the coronal DESS image synovial proliferation shows lower signal compared to intraarticular effusion. Fig. 1D shows extra-synovial inflammation on the dorsal side of the hand over the metacarpophalangeal joints. Note distension of articular capsule with disruption and formation of fistula (arrow, Fig. 1D) and

pseudocyst, (Fig. 1E) both known decompression forms of inflamed joints occurring especially in untreated patients. Due to the high resolution synovial thickening can be delineated excellently also on the non-enhanced T1-weighted image (Fig. 1F).

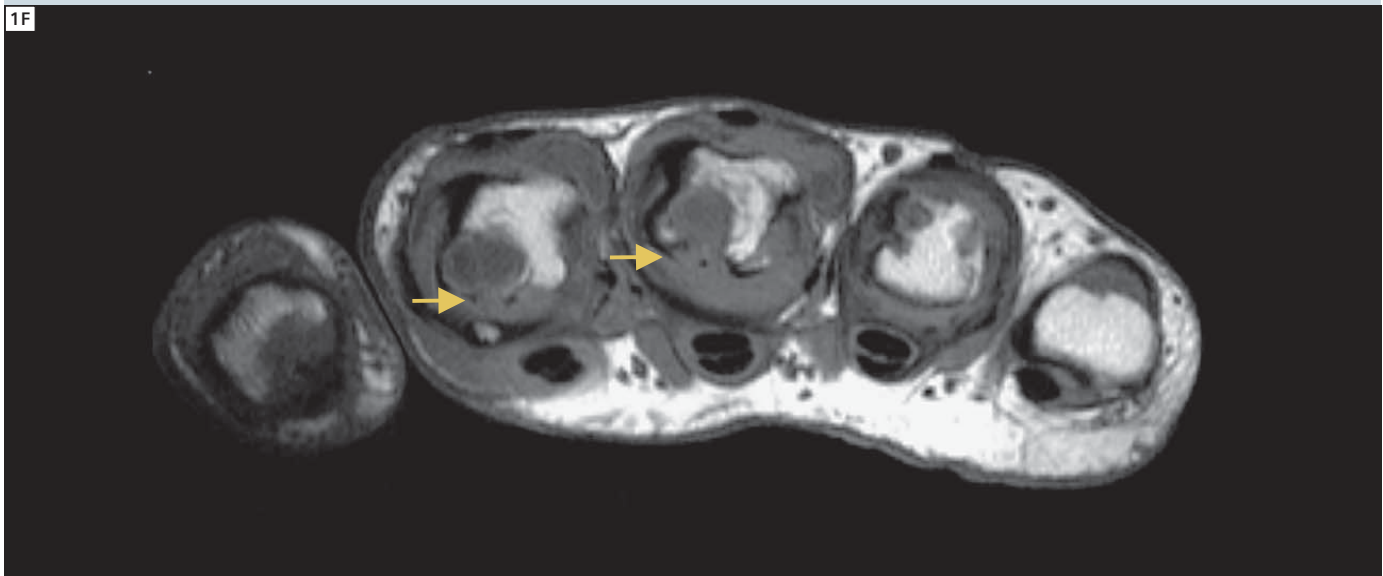
Case 2 Psoriatic arthritis (PsA)

Patient history

A 64-year-old male patient with known psoriatic arthritis (PsA) presented with progressive exercise-induced joint pain and swelling involving all hand joints, despite ongoing immunosuppressive therapy.



1D, E Axial fat-saturated T1-weighted post-gadolinium image, demonstrating extra-synovial inflammation.



1F Axial non-enhanced T1-weighted image; synovial thickening can be delineated excellently due to the high resolution.

Image findings

On conventional radiographs of the hands (Fig. 2A), juxta-articular osteopenia, joint space narrowing with osteophyte formation (bony proliferation) was diagnosed in the wrist joint, intercarpal joint as well as to a lesser degree also in all other hand joints. Fusiforme swelling of the fingers was also noticed presumed to represent polydactylia.

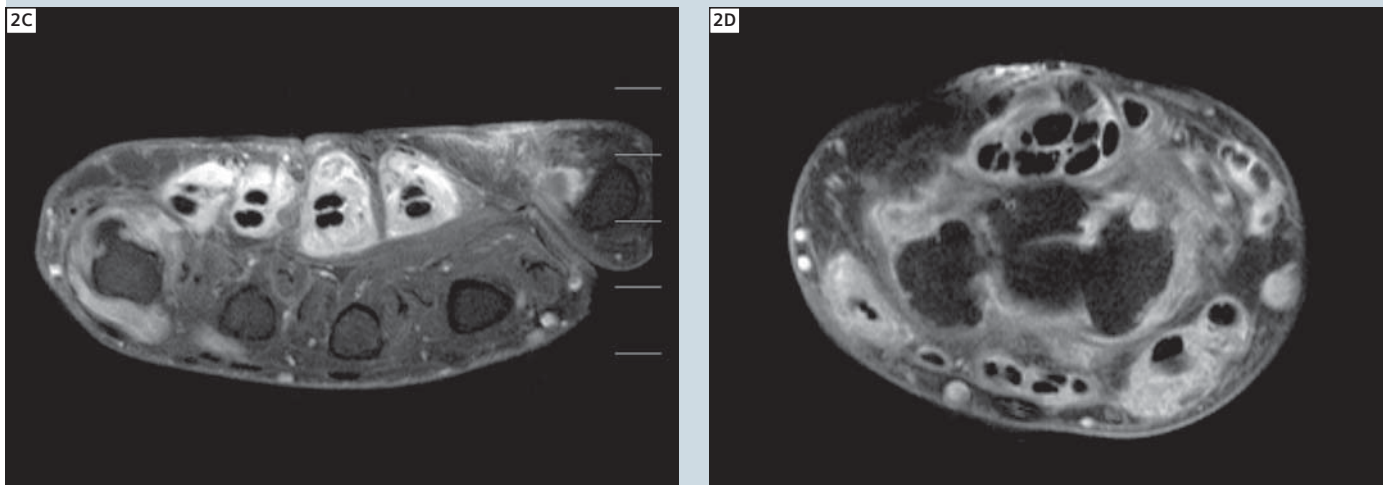
High-resolution MRI of both hands using

a dedicated hand coil and a 3T magnetic field (Siemens MAGNETOM Trio) revealed severe erosions in all joints, particularly in the wrist and the metacarpophalangeal joints (Fig. 2B). Note also tendon tear on the radial side of the wrist joint (arrow). Fig. 2C shows strong inflammation and thickening of the flexor tendon sheaths along the metacarpal bones. Note destruction of the Vth metacarpal head

which differs in its morphology from the classical erosion by rheumatoid arthritis. The latter lacks new bone formation and is mainly localized at the so-called bare area. At the level of the wrist, the destructive character of this inflammatory arthritis becomes more evident. Note also the strong synovial hypertrophy of both extensor and flexor tendon sheaths (Fig. 2D).



2A, B A: Conventional radiograph of the hand; juxta-articular osteopenia and joint space narrowing with osteophyte formation (bony proliferation) and fusiforme swelling of the fingers are present. B: Coronal DESS image visualizing severe erosion in all joints.



2C, D Axial fat-saturated T1-weighted post-gadolinium images.

Case 3

Systemic lupus erythematoses (SLE)-induced arthritis

This case compiles images of three different patients suffering from systemic lupus erythematoses (SLE) and complaining about joint pain. In the 1st patient, conventional X-ray of the hand did not disclose any pathologic findings (Fig. 3A). Axial fat-saturated T1-weighted post-gadolinium image however, shows strong synovial thickening and enhancement involving all joints, but in particular the metacarpophalangeal (MCP) joints (Fig. 3B). Note also extra-synovial extension of inflammation and accompanying tenosynovitis. The latter represents a frequent image finding in SLE-patients. There is no erosion at the level of MCP joints. At the 3rd metacarpal head, partial average volume simulated the presence of a prelesion which was not confirmed in the coronal plane.

In the second patient, a child* with SLE-associated arthritis, coronal DESS image demonstrates incomplete ossification of the carpal bones and open growth plates of the long bones (Fig. 3C). There is also small erosion in the capitate bone which represents an unusual finding for SLE-arthritis.

Nevertheless, axial fat-saturated post-gadolinium image at the level of the basis of the MCP demonstrates further erosions (arrow) and also strong enhancement in the thickened synovial membrane (Fig. 3D).

In the third patient with SLE, focal erosion of the 3rd metacarpal head (arrow) is nicely depicted on axial non-enhanced T1-weighted image (Fig. 3E). There is also thickening of the articular synovia. However, it is only the use of intrave-

nous contrast material that allows appreciation of inflammatory activity of such findings. On the corresponding axial fat-saturated post-gadolinium image, mild enhancement is seen in the synovial membrane of the 3rd and 4th MCP, but none in the intraosseous pannus of the 2nd MCP (Fig. 3F). This finding is compatible with inactive pannus.

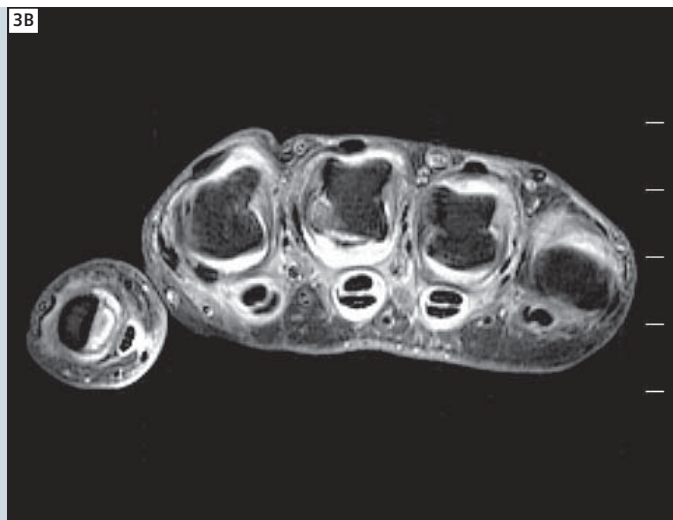
*The safety of imaging fetuses / infants has not been established.

Contact

Prof. Dr. Marius Horger
Department of Radiology
University Hospital of Tuebingen,
Hoppe-Seyler-Straße 6
72076 Tuebingen
Germany
marius.horger@med.uni-tuebingen.de



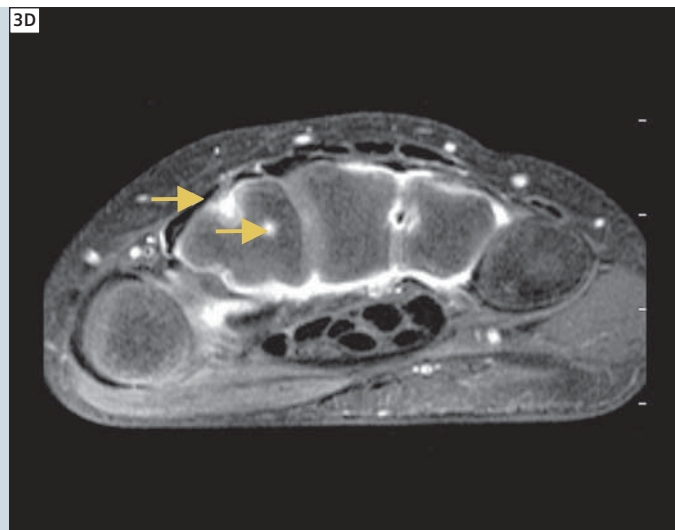
3A Conventional radiograph of the hand; no pathologic findings are disclosed.



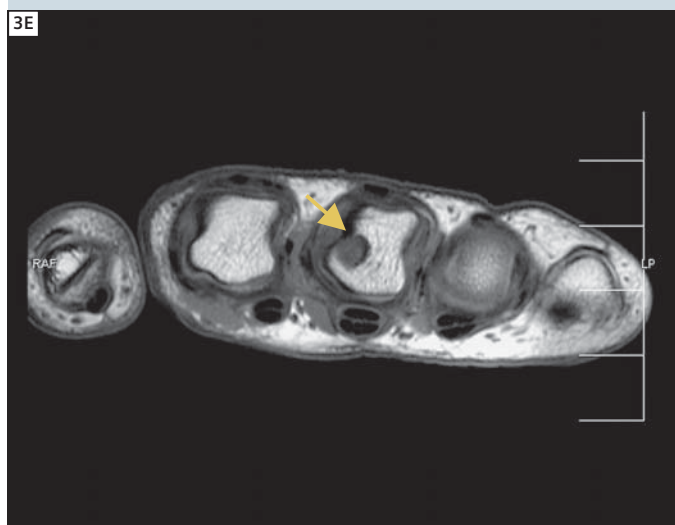
3B Axial fat-saturated T1-weighted post-gadolinium image; strong synovial thickening and enhancement involving of all joints are present.



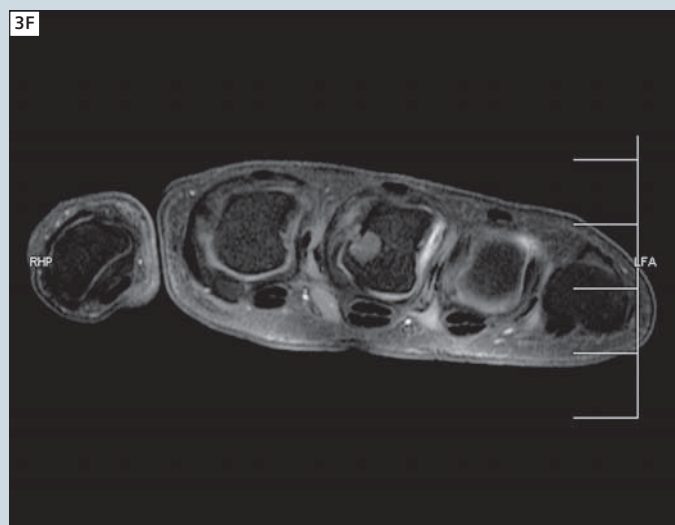
3C Coronal DESS image showing incomplete ossification of the carpal bones and open growth plates of the long bones.



3D Axial fat-saturated T1-weighted post-gadolinium image showing erosions and also strong enhancement in the thickened synovial membrane.



3E Axial non-enhanced T1-weighted image; a focal erosion of the 3rd metacarpal head is delineated in detail.



3F Axial fat-saturated T1-weighted post-gadolinium image.

Case Report:

Right Hip and Hamstring

Kirralie Lyford; Richard O'Sullivan, M.D.

Primary Health, The Epworth MRI Department, Richmond, Victoria, Australia



1 Coronal T2-weighted TIRM demonstrating large haematoma within the muscle belly of the semimembranosus and adductor magnus; note also the diffuse oedema.

Sequence details

Multiplanar T1, proton density and fat suppressed T2-weighted images were acquired of the right hamstring from origin to insertion. The images were acquired on our 3T MAGNETOM Verio.

Image findings

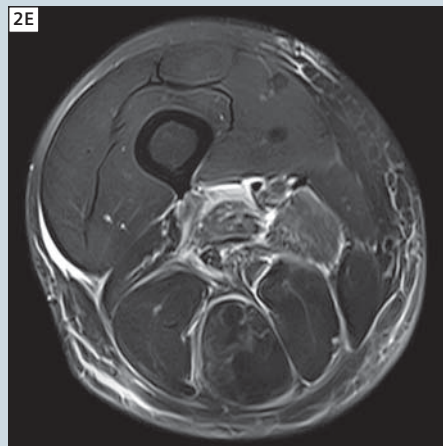
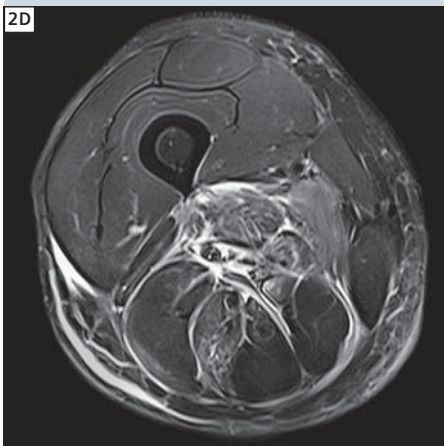
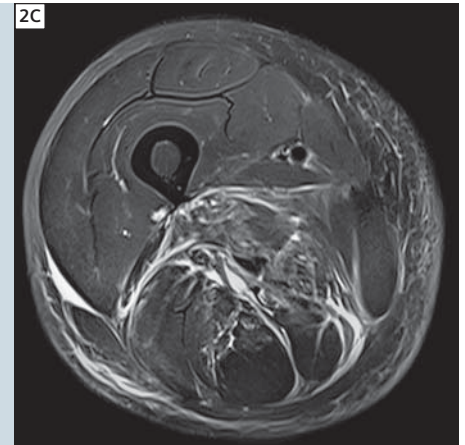
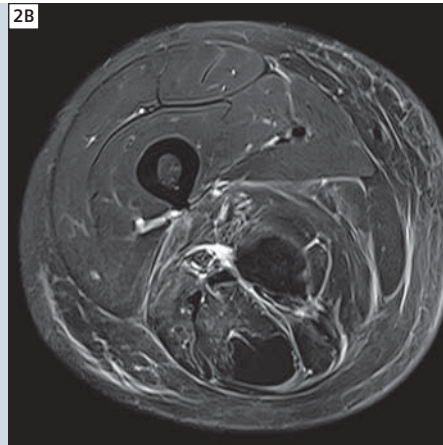
The ischial tuberosity is within normal limits. The hamstring tendon origin is intact. Beginning approximately 6 cm below the insertion there is focal discontinuity and irregularity of the biceps femoris tendon over approx. 1.5 cm. This is associated with extensive oedema in the adjacent muscle belly over at least 7 x 6 cm. Inferior to this level the tendon of the long head of biceps is within normal limits. Diffuse oedema is also demonstrated in the lower 25 cm of the short head of biceps. There is no muscle fiber discontinuity and the distal long head of biceps demonstrates only minor muscle oedema. In addition, approx. 5 cm inferior to the ischial tuberosity there is a large (15 x 6 x 7 cm) haematoma on the anterior margin of the semimembranosus tendon extending into the muscle belly of the semimembranosus. This is associated with diffuse oedema in the adjacent semimembranosus muscle belly. Diffuse oedema with preservation of muscle architecture is also seen over approx. 15 cm of the semitendinosus muscle belly in the mid thigh. The distal insertion of the biceps, semimembranosus and semitendinosus are all within normal limits. Extensive oedema is demonstrated in the soft tissues.

Conclusion

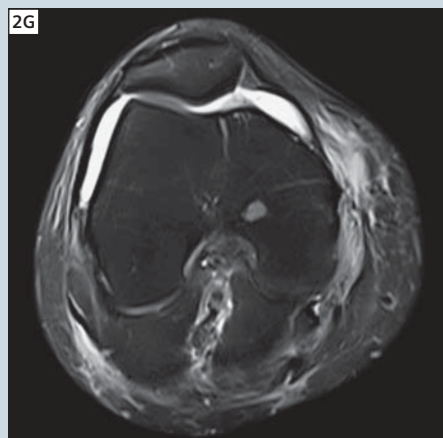
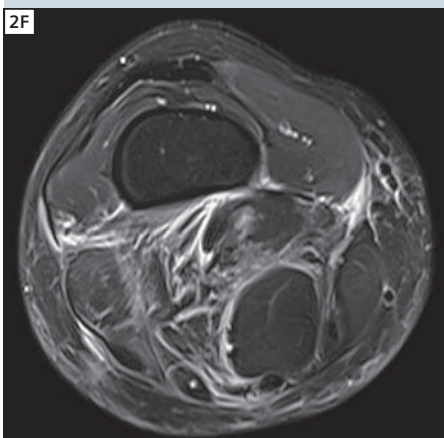
1. Intact hamstring tendon origin.
2. Beginning approx. 6 cm from the ischial tuberosity there is high grade partial / near complete tear of the biceps femoris tendon associated with Grade I injury to the adjacent muscle belly. The tendon reconstitutes distally and there is diffuse oedema throughout the muscle belly of the short head of biceps without focal discontinuity.
3. Approx. 5 cm inferior to the ischial tuberosity there is a large (7 x 15 cm) haematoma within the muscle belly of the semimembranosus, likely extending into the interfascial plane between the semimembranosus and adductor magnus. The tendon remains intact and there is diffuse oedema throughout the adjacent adductor magnus and semimembranosus muscle belly. The appearances are consistent with Grade II tear of the semimembranosus.
4. Diffuse oedema is seen over at least 20 cm of the semitendinosus muscle belly in the mid thigh consistent with Grade I injury.

Contact

Kirralie Lyford
Epworth Hospital
MRI Department
88 Bridge Road Richmond
Melbourne, Victoria, 3121
Australia
kirralie.lyford@sybionhealth.com



2 Transversal small FOV T2-weighted TSE with SPAIR fat suppression of the right upper leg. Images are sorted in craniocaudal slice orientation (A–G).



Case Report: Rectum

Kirralie Lyford; Richard O'Sullivan, M.D.

Primary Health, The Epworth MRI Department, Richmond, Victoria, Australia

Patient history

In this 34-year-old female patient suffering from Cohn's disease, a complex anal fistula is seen, communicating with the skin, the bowel and a large presacral collection. The patient was referred to our institution to evaluate the exact extension of the complex fistula and for further evaluation of therapeutic procedures.

Sequence details

Multiplanar T2, fat suppressed T2 and post contrast enhanced fat suppressed T1-weighted images were acquired using our 3T MAGNETOM Verio system with the integrated spine and a body-phased array coil.

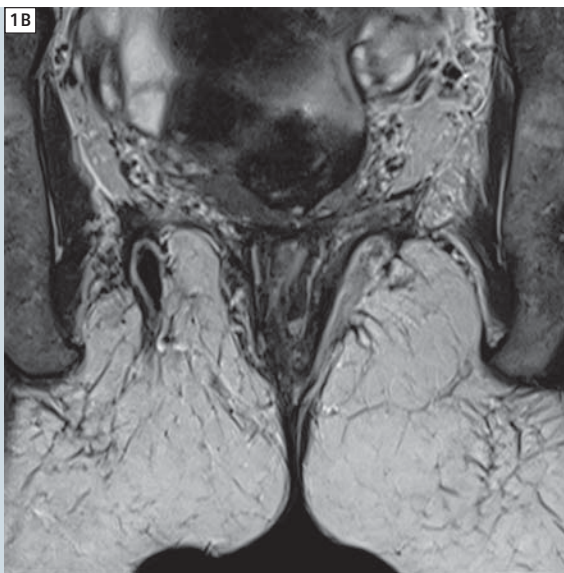
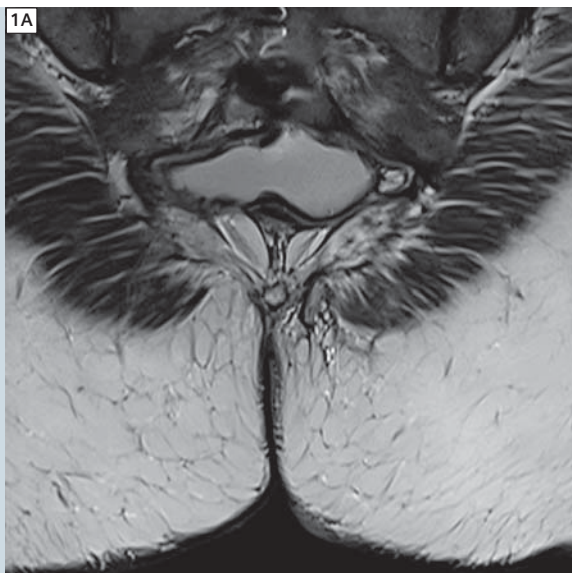
Image findings

A fistula is demonstrated on the left beginning at the 12 o'clock position immediately anterior to the rectum. Seton is demonstrated in-situ and this extends superiorly into the left ischio-rectal foss, extending into an ischio-rectal abscess (measuring 5 cm in anterior-posterior dimension). There is a blind ending situs extending anteriorly in to the left obturator internus and posteriorly to end up being medial to the gluteus maximus in the midline. This also communicates with the bowel approximately 3 cm above the anal verge at 3 o'clock position and communicates with a large (6 x 1.5 cm diameter) presacral collection. There is a second sinus tract that is

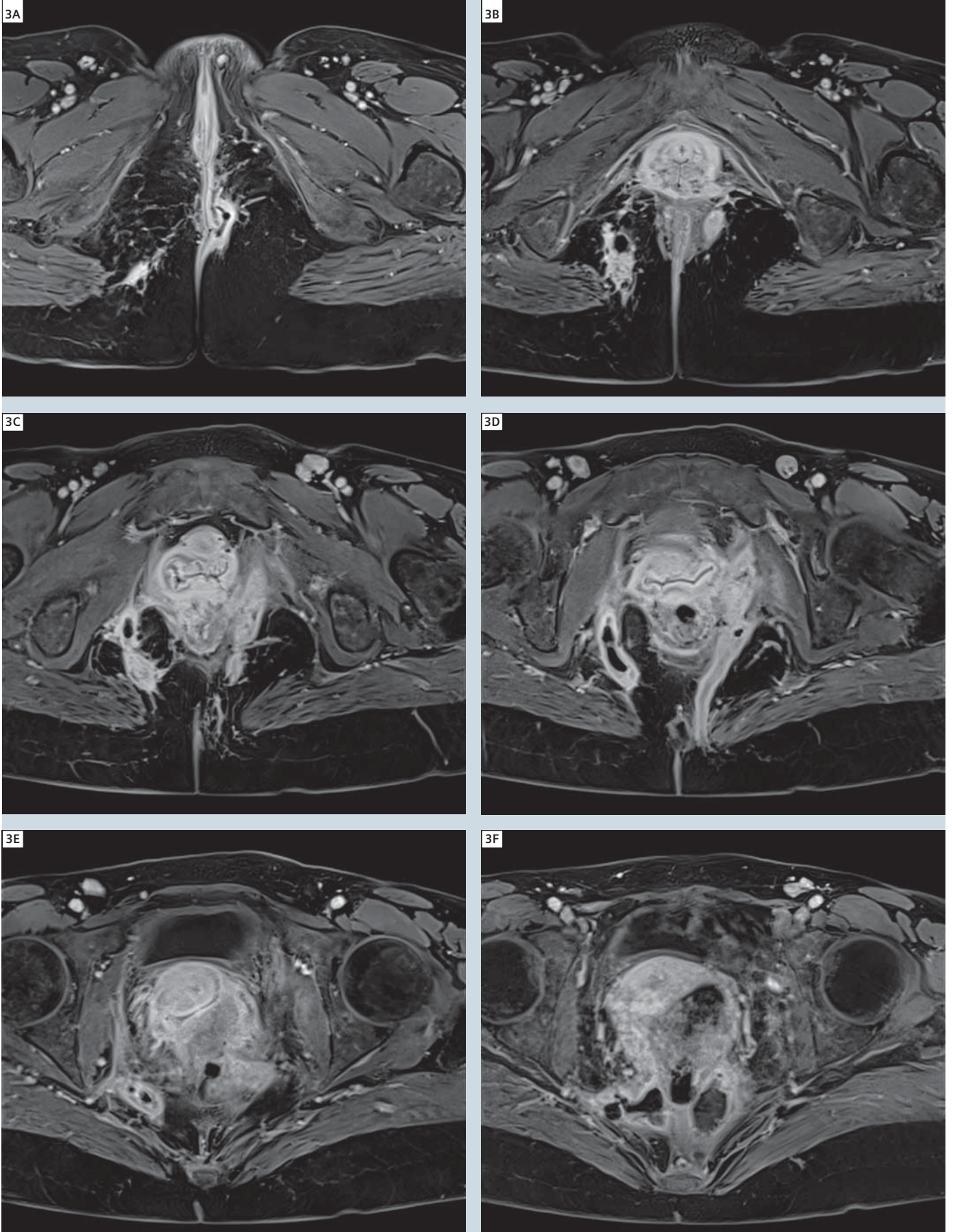
filled with air in the right ischio-rectal fossa with extension towards the skin and is also communicating with the large presacral collection. No definite vaginal fistula is seen. There is no definite osteomyelitis but there is diffuse oedema in the left gluteus maximus and left obturator internus.

Contact

Kirralie Lyford
Epworth Hospital
MRI Department
88 Bridge Road Richmond
Melbourne, Victoria, 3121
Australia
kirralie.lyford@symbionhealth.com



1 Coronal
T2-weighted
Turbo Spin Echo:
TR 4522 ms,
TE 101 ms,
slice thickness
3 mm,
FOV 170 x 170 mm²,
matrix 256 x 320.



3 Transversal contrast enhanced 3D T1-weighted VIBE with fat suppression (SPAIR): TR 3.9 ms, TE 1.9 ms, slice thickness 2.5 mm, FOV = 245 x 245 mm², matrix 320 x 320.

Case Report:

Rectal Cancer Staging

Noelene Bergen; Nick Ferris, M.D.

Peter MacCallum Cancer Centre, Department of Diagnostic Radiology, Melbourne, Australia

Patient history

The 71-year-old male presented with a 4 months history of diarrhoea, mild faecal incontinence and no per rectal (PR) bleeding. A proctoscope and a detailed examination under anesthesia (EUA) demonstrated tumor 7 cm from anal verge with no obstruction. Liver metastases had been identified on a CT scan performed elsewhere. Both the primary rectal tumor and the liver underwent MRI examination – the primary for formal anatomical staging, and the liver for assessment of the resectability, or otherwise, of the presumed metastases. The rectal tumor was staged as T3 N0 M0, with extension through the margin of the mesorectal fascia on the left indicating a high risk of local recurrence after surgical excision.

Technique

Our rectal cancer protocol involves sagittal, axial and coronal T2-weighted Turbo Spin Echo (TSE) sequences of the pelvis.

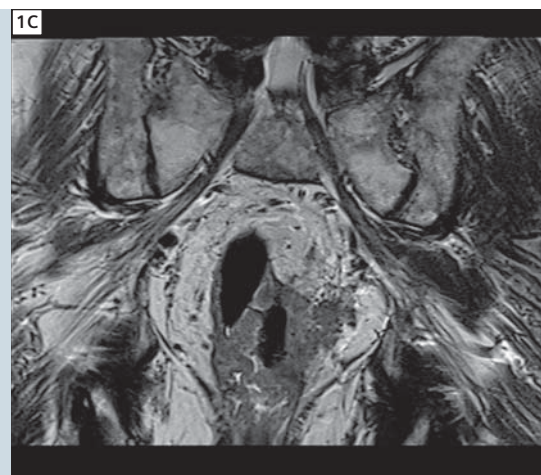
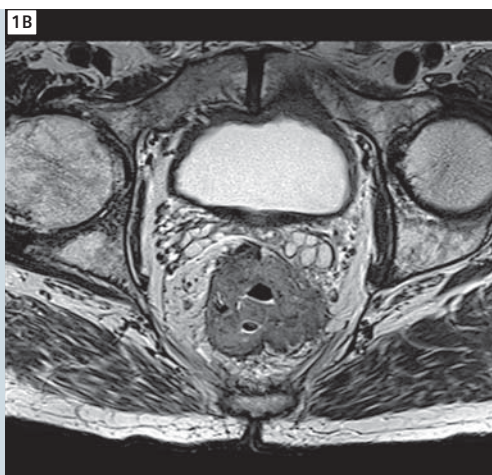
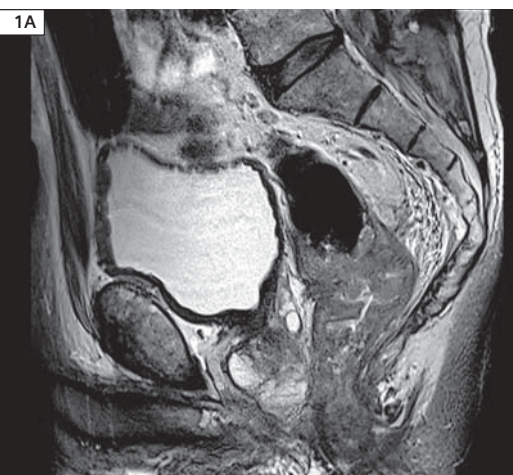
The sagittal series are performed with a field-of-view (FOV) of 200 x 200. TR in the 4000 ms range and TE 90 ms with a resolution of 384 x 307. Scan time is 3 minutes.

We perform 2 series of T2 axials. The first is throughout the whole lesser pelvis at a slice thickness of 4 mm and 1.5 mm gap. The resolution is 320 x 240 at a FOV of 260 mm for this series. This gives 30 slices under 2 minutes. We then perform a higher resolution axial series through the lesion and angled at right angles to the bowel wall. This is to get the lesion in profile and better visualise

local extension into the mesorectal fat. This sequence is performed at a FOV of 200 mm and slice thickness of between 2.5 and 3 mm with 0.3 mm gap.

Resolution is 384 x 307. This is acquired in 3 minutes 20 seconds.

The coronal series is performed with a FOV of 220 mm and a slice thickness of 4 mm with a gap of 1.0 mm and a resolution of 384 x 284 in 3 minutes. In this case the tumor demonstrates frank T3 tumor extension into the mesorectal fat on the left, with the tumor extension reaching and transgressing through the mesorectal fascia. The tumor has not yet reached the left pelvic side wall, although it involves at least one of the left internal iliac vessels. Along the left anterior lateral aspect, the



1 High-resolution T2-weighted TSE sequences used for local staging of rectal cancer. The tumor as well as all relevant anatomical structures for T-staging are visualized in detail including the mesorectal fascia. Slice orientation **1A** sagittal, **1B** transversal, **1C** coronal angulation).

tumor extends to about the left seminal vesicle although no definite evidence of tumor extension into the seminal vesicle has been seen.

If the tumor does extend into seminal vesicles it would be a T4a tumor. There were multiple suspicious nodes visualised indicating at least T3D disease. The MRI examination of the liver was enhanced by use of gadoxetate (Primovist), a contrast agent approximately 50 % of which is taken up by hepatocytes, and later excreted into the bile. The use of this agent increases the liver:lesion contrast ratio in images obtained more than 15 minutes after contrast injection, and hence increases sensitivity for non-hepatocytic lesions, such as metastases.

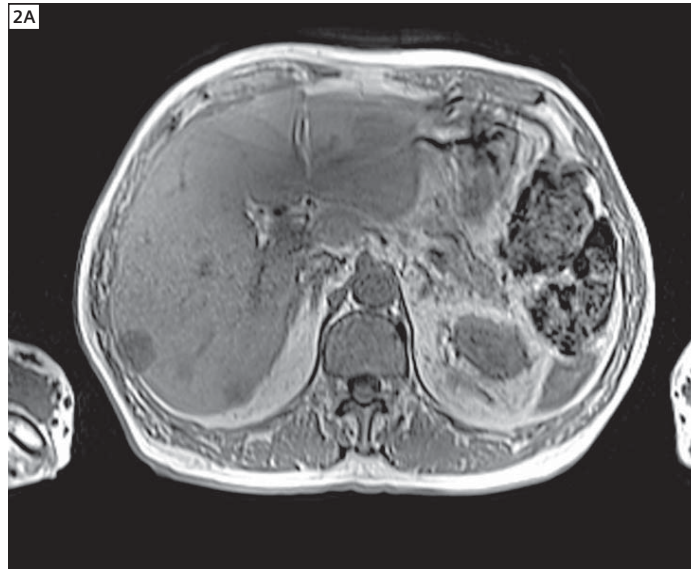
Technique

A 3D gradient echo technique, VIBE, was used for the contrast-enhanced images, allowing thin sections and rapid coverage of the whole liver during each of the phases of contrast enhancement. Enhancement can be made more conspicuous by the use of inline subtraction of a pre-contrast mask image.

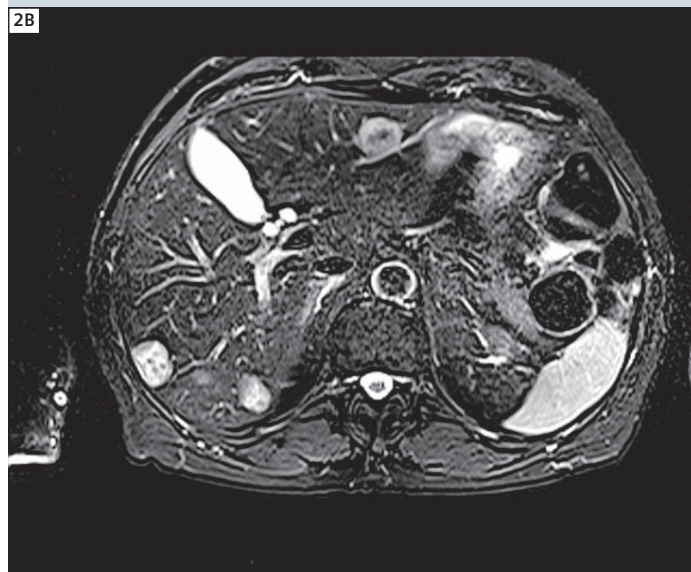
For the T1-weighted VIBE in and out of phase breath-hold we used a FOV 300 x 400, 2 mm no gap. The TE used was 2.5 ms and TR 5.5 ms. This is a 21 second breath-hold for 192 images.

The next sequence was a T2-weighted TSE respiratory triggered with fat sat. This was with a FOV of 285 x 380 and 168 x 320 resolution. The time for this acquisition is approximately 2 minutes. For the T1-weighted VIBE fat-sat breath-hold we use a FOV of 300 x 400, 2 mm no gap. The TR is 4 ms TE 1.4 ms at a resolution of 168 x 32.

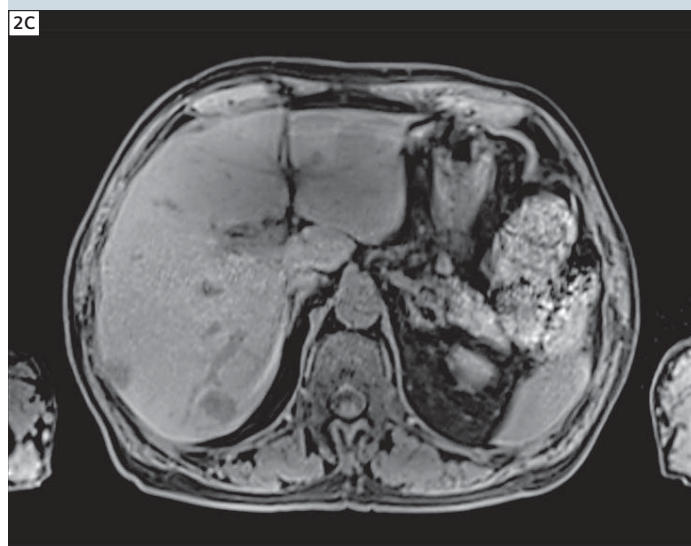
Liver metastases from colorectal carcinomas are typically hypointense, relative to normal liver, on T1-weighted images, and mildly hyperintense on T2-weighted, fat-suppressed images. In the arterial phase of contrast enhancement, these lesions show irregular marginal enhancement, which becomes indistinguishable from the rest of the normal liver parenchyma in the venous and interstitial phases.



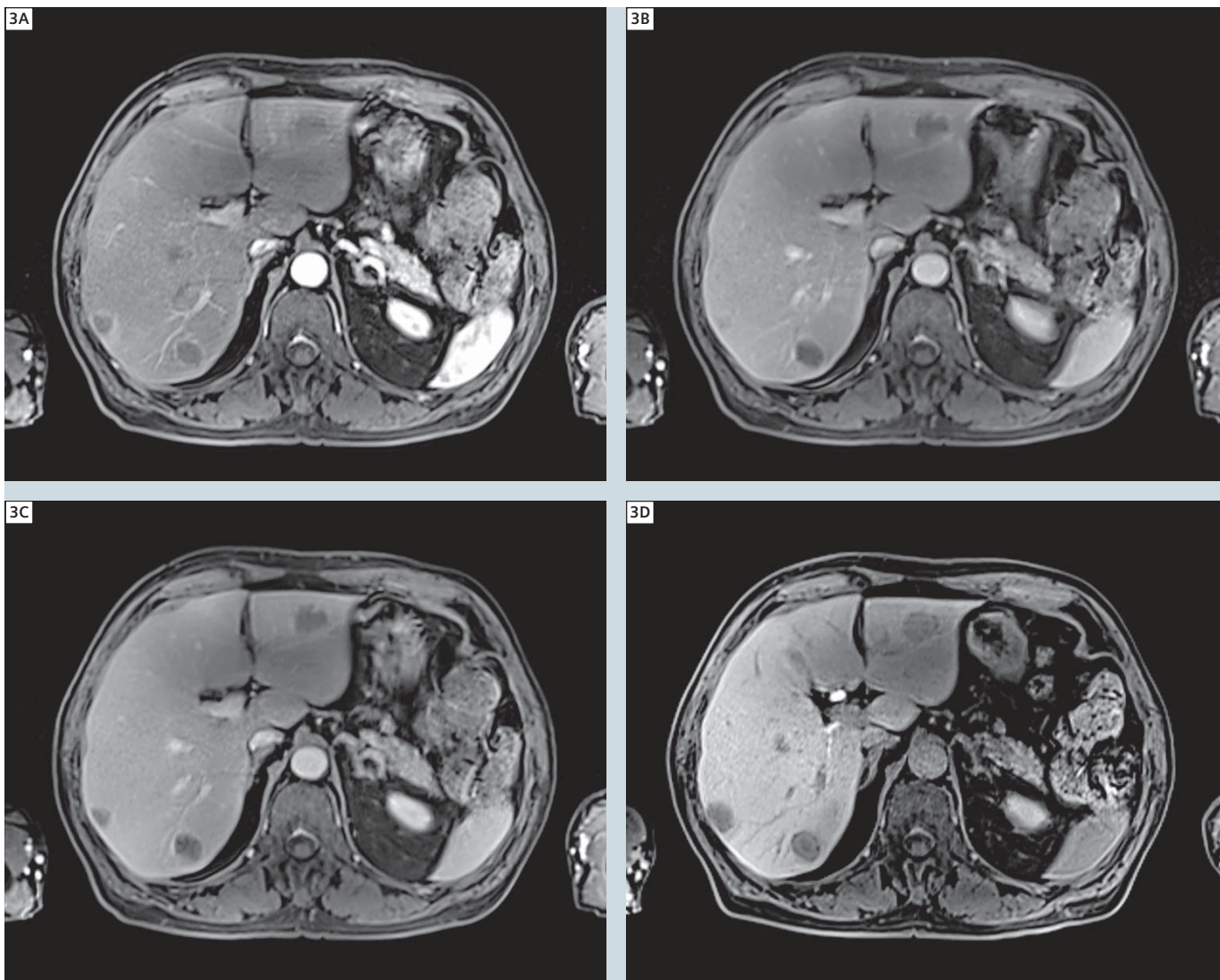
2 Native MR sequences used for M-staging of liver metastases. **2A** T1-weighted VIBE in and out of phase (in phase is shown).



2B T2-weighted TSE with respiratory gating (PACE).



2C Native T1-weighted 3D GRE (VIBE used also for Inline subtraction as a pre-contrast mask image).



3 Dynamic liver MRI (T1-weighted 3D VIBE) shows multiple liver lesions with pathognomonic enhancement patterns of rectal carcinoma metastases: **3A** arterial phase, **3B** and **3C** portal-venous phase, **3D** equilibrium phase

In this case, the delayed post-contrast images were obtained at 40 minutes after contrast injection. Delayed images show parenchymal enhancement due to hepatocyte uptake of gadoxetate, but no enhancement of non-hepatocytic lesions such as metastases. Enhancement of the bile, due to hepatocyte excretion of the contrast agent will also be apparent. Six lesions with the MRI characteristics of liver metastases were identified, lying superiorly near the margin between segments 7 and 8 (Fig. 4B), more centrally in segment 7 (Fig. 4A), in segment 6 (three lesions – Fig. 4D), and in seg-

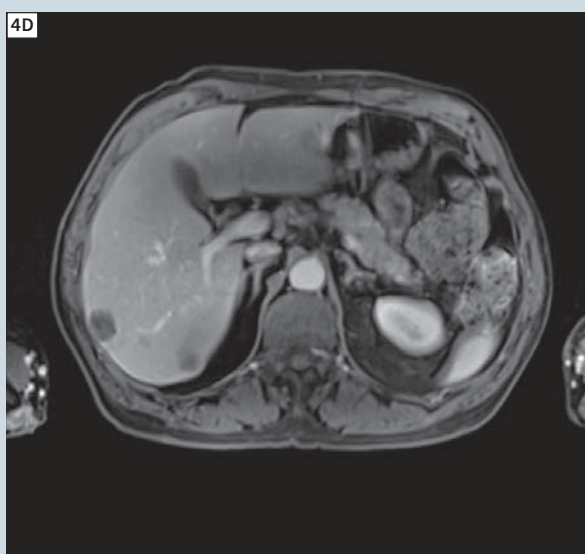
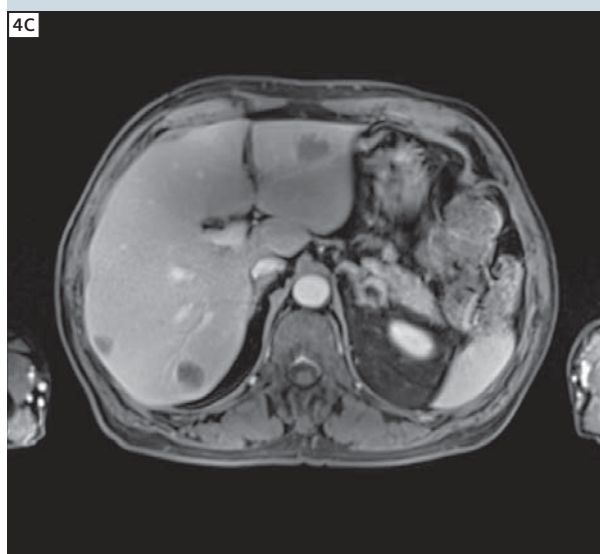
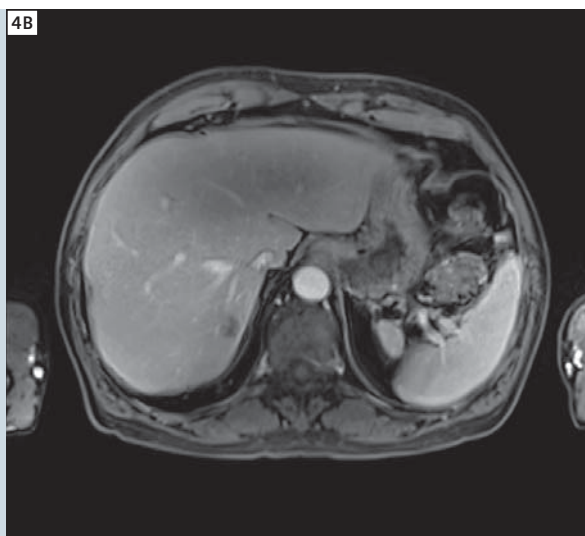
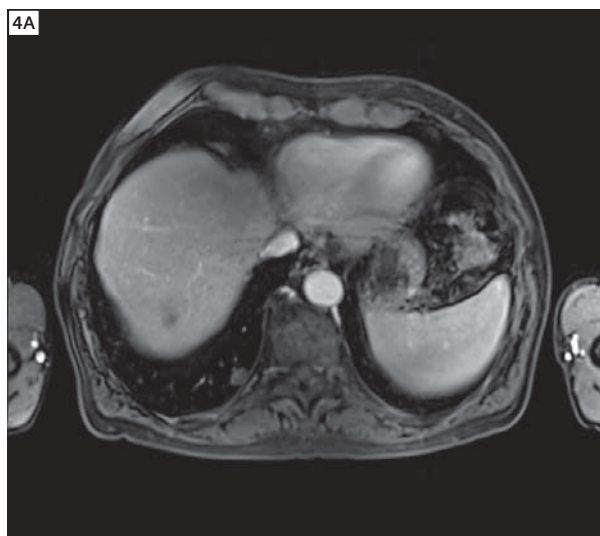
ment 3 (Fig. 4C).

A small hypointense lesion in segment 8 (Fig. 5) shows no arterial phase enhancement, and is thought incidental (it was not identified in the thicker-section T2-weighted images).

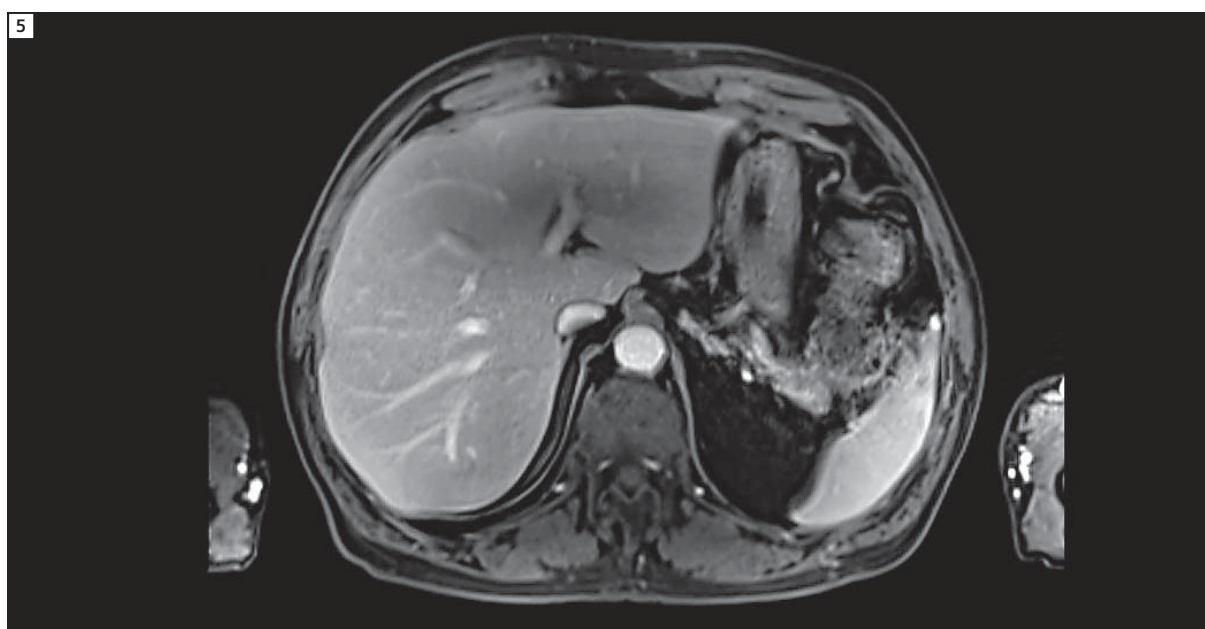
Note was also made of the presence of several small, rounded masses in the right lung (e.g. Fig. 4A), indicating the presence of lung metastases as well as liver metastases. This, and the presence of liver lesions in both right and left lobes, argued against resection of the liver lesions with curative intent.

Contact

Noelene Bergen
Department of Diagnostic Radiology
Peter MacCallum Cancer Center
St Andrew's Place
East Melbourne
Victoria 3002
Australia
noelene.bergen@petermac.org



4 Dynamic liver MRI (T1-weighted 3D VIBE) demonstrates a multi-focal spread of the rectal cancer within both lobes of the liver (sorted in craniocaudal slice orientation).



5 Hypointense lesion in segment 8 without correlation on T2-weighted MRI.

Case Report: MR Breast Imaging at 3T Invasive Lobular Carcinoma (ILC) and Complicated Cyst

Manfred Kontrus, M.D.

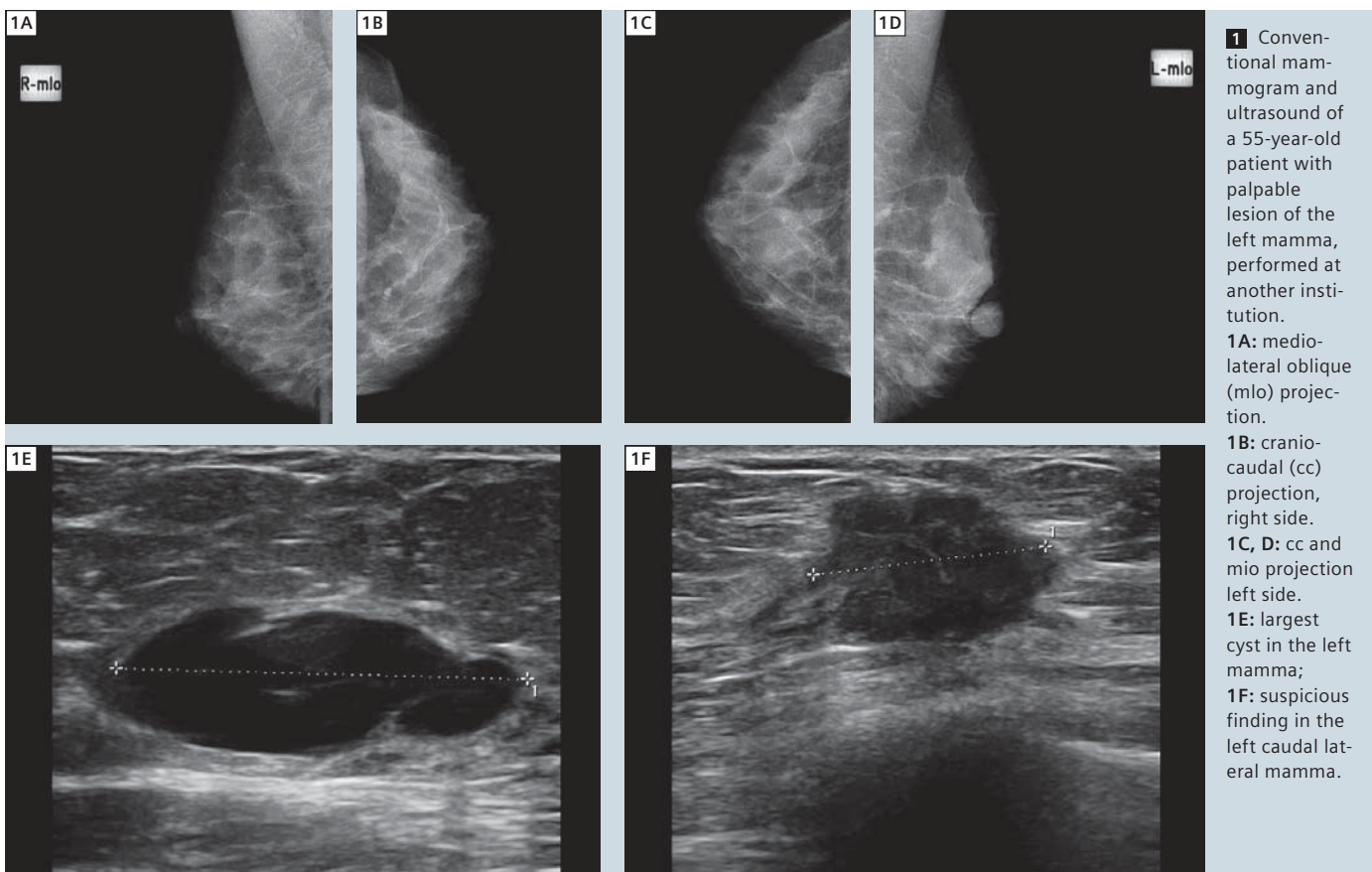
Private Clinic Villach, Radiology Department, Villach-Warmbad, Austria

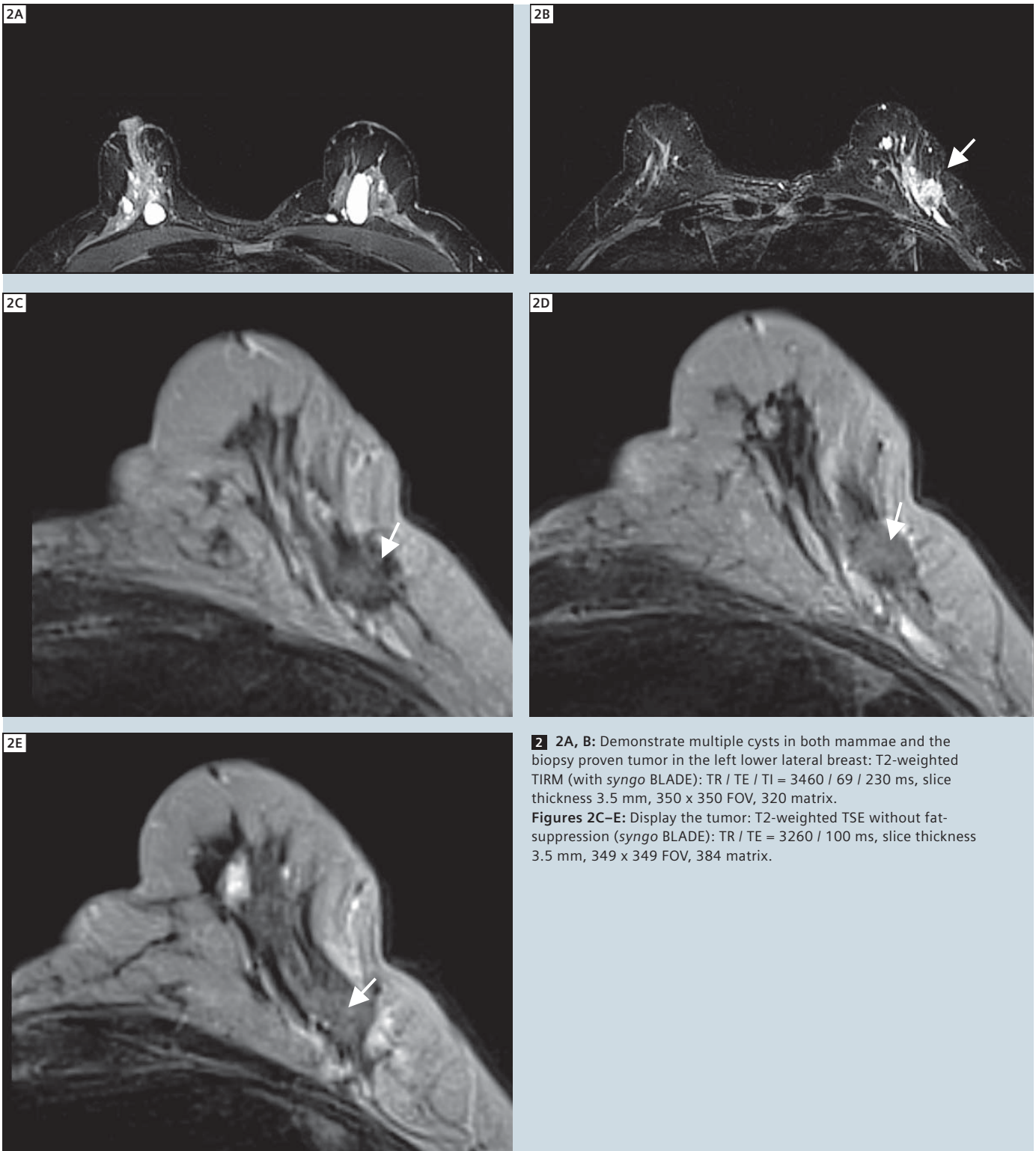
Patient history

A 54-year-old patient consulted her gynecologist because of a palpable mass in the left lateral breast. While a conventional mammogram, performed at an other institution, was not conclusive (Figs. 1A–D), ultrasound revealed multiple cystic lesions in both mammae

(largest cyst in the left mamma shown in Fig. 1E). A hypoechogenic lesion with irregular shape was detected in the left lateral caudal quadrant with a maximum diameter of approximate 2 cm. Because of its features on ultrasound, this lesion was suspected to be potentially malig-

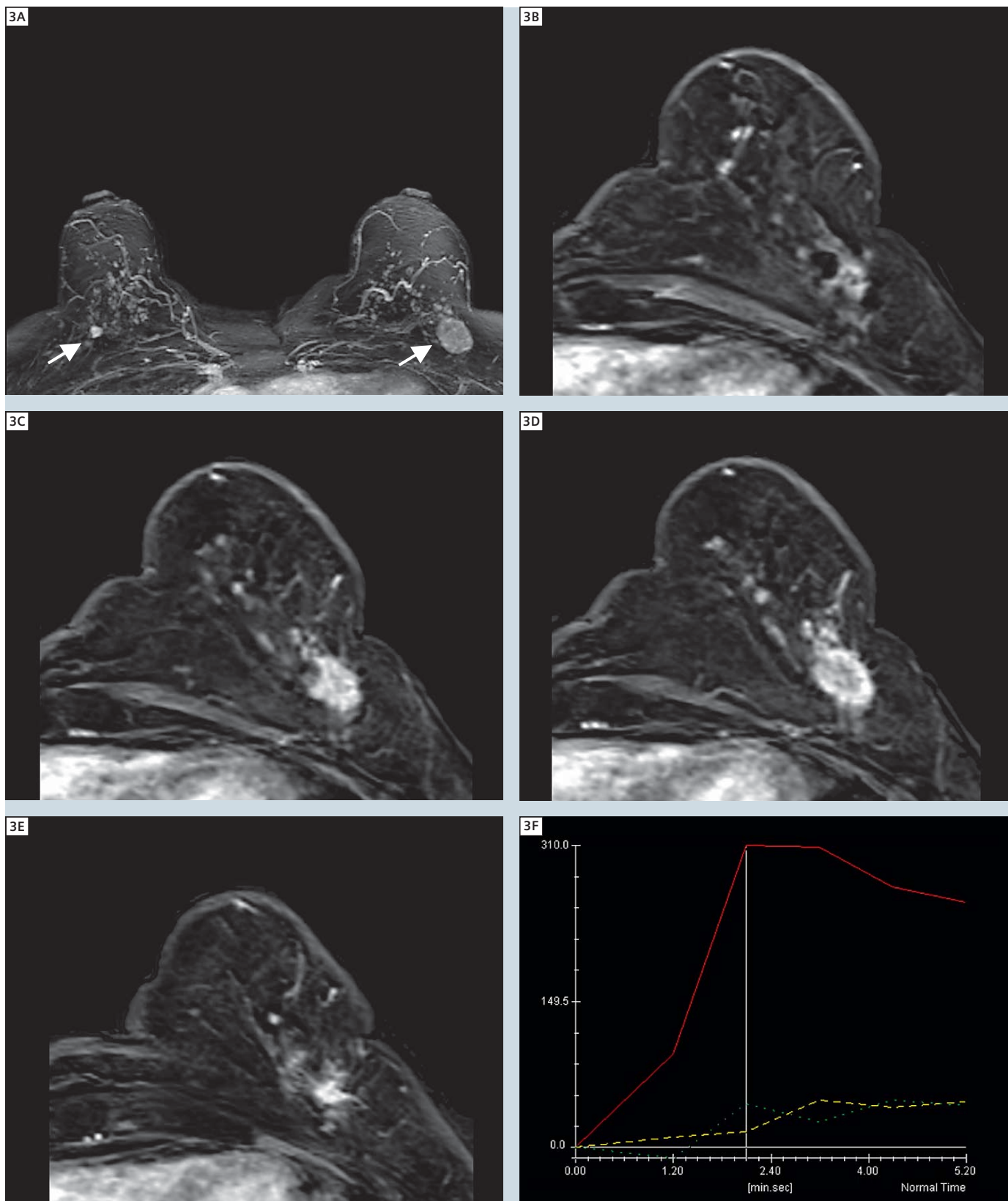
nant (BI-RADS 5). An ultrasound-guided biopsy was performed. Based on histopathology, an invasive lobular carcinoma (ILC) was diagnosed. The patient was then referred to our institution for pre-operative evaluation and exclusion of multifocal disease.



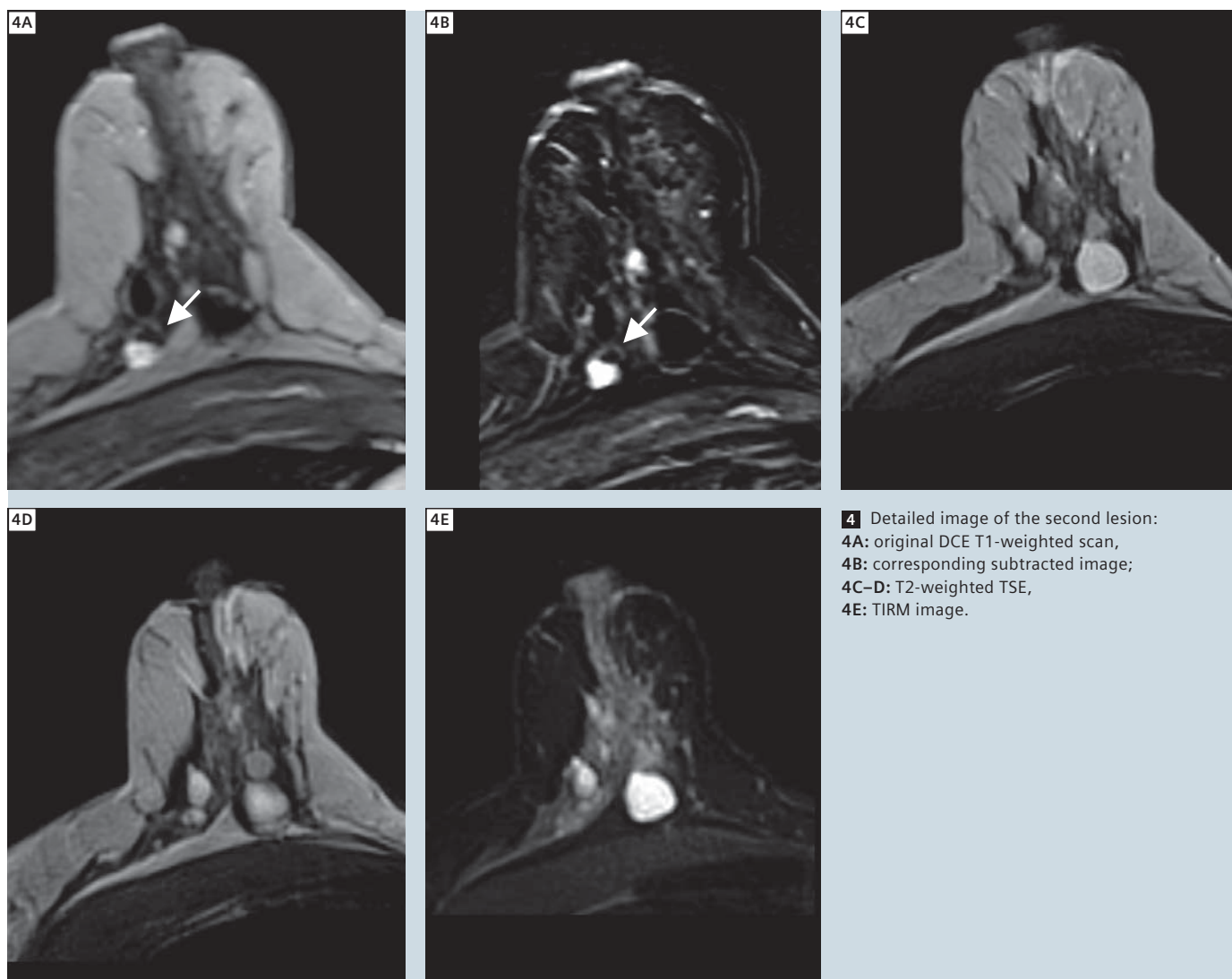


2 **2A, B:** Demonstrate multiple cysts in both mammae and the biopsy proven tumor in the left lower lateral breast: T2-weighted TIRM (with syngo BLADE): TR / TE / TI = 3460 / 69 / 230 ms, slice thickness 3.5 mm, 350 x 350 FOV, 320 matrix.

Figures 2C–E: Display the tumor: T2-weighted TSE without fat-suppression (syngo BLADE): TR / TE = 3260 / 100 ms, slice thickness 3.5 mm, 349 x 349 FOV, 384 matrix.



3 Figure 3A: MIP based on DCE T1w (3D FLASH) showing the tumor (arrow left breast) and a second suspicious lesion on the contralateral side (arrow). Figures 3B–E: Show the lesion in detail. Figure 3F: Corresponding signal-intensity time curves (red line region-of-interest within tumor lesion). (3D FLASH parameters: TR / TE = 6.09 / 2.45 ms, slice thickness 1.5 mm, 340 x 340 FOV, 314 x 448 matrix).



4 Detailed image of the second lesion:
4A: original DCE T1-weighted scan,
4B: corresponding subtracted image;
4C–D: T2-weighted TSE,
4E: TIRM image.

Sequence details

All images were acquired using our 3T MAGNETOM Verio and a seven-channel breast coil. The image protocol included T2-weighted TSE with and without fat-saturation, acquired with the *syngo* BLADE k-space sampling scheme to reduce motion artefacts and the routinely applied dynamic 3D T1-weighted FLASH (DCE T1w) scan, including automatically generated subtraction and MIP reconstructions.

Conclusion

In concordance with the ultrasound examination, large cysts are present (Fig. 2A). The biopsy-proven ILC in the left lower lateral mamma is clearly

outlined on T2-weighted TIRM images (arrow in Fig. 2B) and T2-weighted TSE by its space occupying character and destruction of the architecture of the breast (Figs. 2C–E); DCE T1w scans show typical pattern of a malignant lesion (Figs. 3B, E); the corresponding signal-intensity time curve showed a fast increase, followed by a wash-out (red curve in Fig. 3F). However, DCE T1w revealed an additional focus with similar DCE T1w kinetics on the contralateral side with a maximal diameter of 0.6 cm, which was therefore classified as BI-RADS 4. With the given set-up in our institution, a direct MRI-guided biopsy of the lesion was not possible and therefore

a further correlation with ultrasound and an ultrasound-guided biopsy were performed. Based on these results, this lesion was then classified as a complicated cyst (BI-RADS 3) and a preservative surgery of the left mamma was performed. Postoperative follow-up was unsuspecting.

Contact

Dr. Manfred Kontrus
 Private Clinic Villach
 Dept. of Radiology
 Dr. Walter Hochsteiner Str. 4
 9504 Villach-Warmbad
 Austria
manfred.kontrus@privatklinik-villach.at

3T MRI in Pediatrics: Challenges and Clinical Applications

Charuta Dagia; Michael Ditchfield, M.D.

Department of Medical Imaging, The Royal Children's Hospital & Murdoch Children's Research Institute Melbourne, Australia

Reprinted from European Journal of Radiology, 68 (2008) 309–319, with permission from Elsevier.

1. Introduction

The primary reason for increasing the magnetic field strength in magnetic resonance imaging (MRI) is to take advantage of the linear relationship between field strength and the signal-to-noise ratio (SNR). By increasing the signal that is obtained in MRI there is improvement in either the spatial or temporal resolution or both [1–4]. In pediatrics* there are a number of unique challenges which improved spatial and/or temporal resolution assist in overcoming. The challenges of high field MRI remain relevant in the pediatric setting. These include the altered T1 contrast, artefacts and safety issues, including specific absorption rate (SAR). These challenges also create opportunities with improvement in MR angiography (MRA), arterial spin labeling (*syngo* ASL), functional MRI (fMRI), susceptibility-weighted imaging (*syngo* SWI), and MR spectroscopy (MRS), all of which have distinctive applications in pediatrics.

This review will try to address basic considerations for pediatric 3T MR imaging, list the frequent and potential future applications, and discuss the challenges and restrictions.

2. What are the challenges of imaging children?

The four main challenges in imaging children are: (1) anatomical challenges, (2) developmental issues, (3) physiological challenges and (4) behavioural challenges.

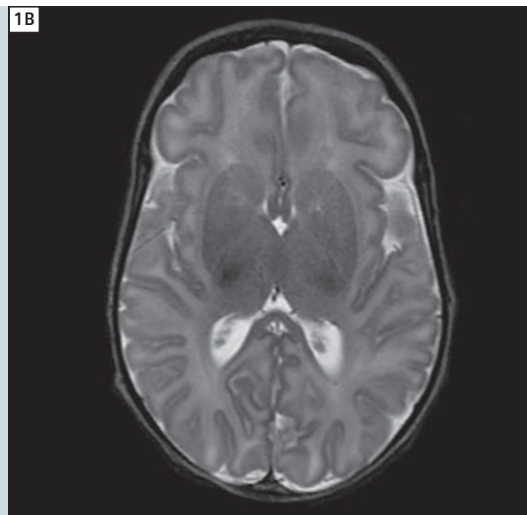
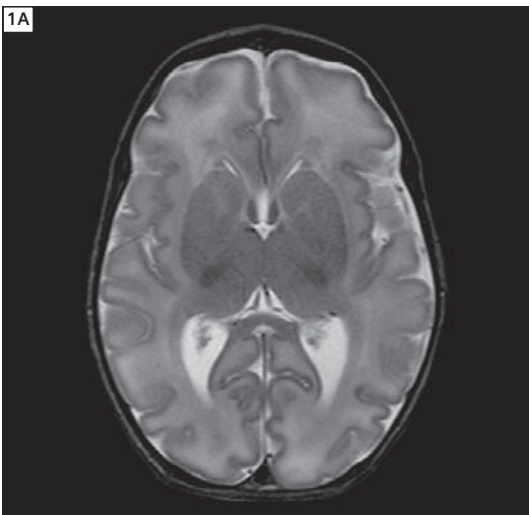
2.1. Anatomical challenges

In children, normal structures are smaller than in adults. However, we often forget how small they are compared to the average adult. An average term neonate weighs 3.5 kg, with brain 25% of the adult size [5]. A premature neonate at 24 weeks gestation may weigh as little as 0.5 kg, with a very small brain. Other anatomical structures that we image such as the inner ear, cranial nerves,

brachial plexus, biliary tree, peripheral joints and blood vessels are very small in children. The improved SNR at higher field strength allows the acquisition of thinner slices and improved spatial detail of these structures.

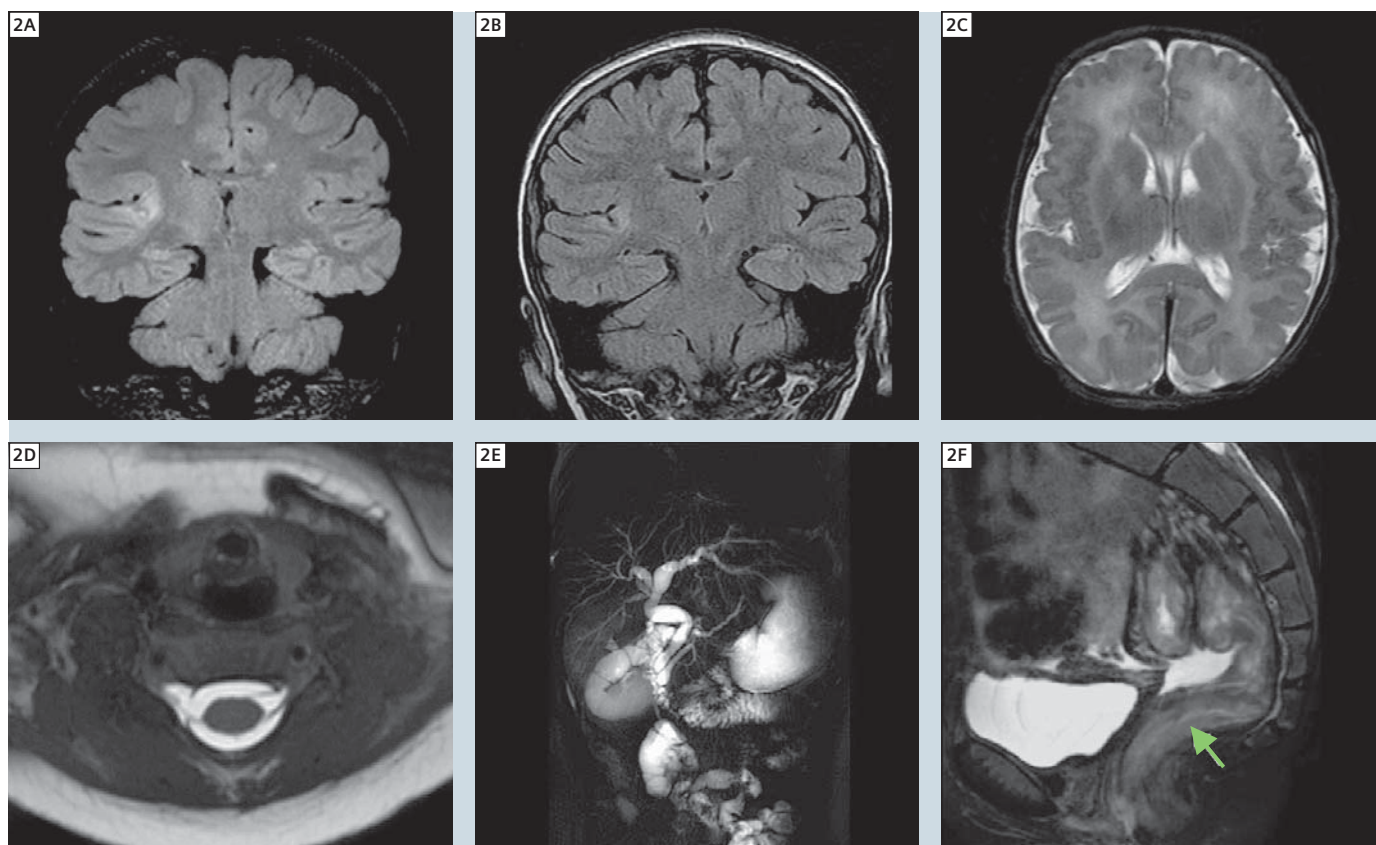
2.2. Developmental issues

With development and maturation, in addition to growth, there are changes in the appearance of many structures. This is especially true for the brain, bones and cartilage. The brain sulcation and myelination of the white matter tracts develop rapidly in the neonatal period, the changes being more dramatic in the premature (Fig. 1A and B). In the joints, with maturation there is conversion of the epiphyseal and apophyseal cartilage to bone. These changes are better visualised with improved spatial resolution as the structures involved are often small and the changes subtle.



1 Axial T2 images from serial 3T MRI brain studies of a premature infant (34 weeks gestation) obtained 7 days (**A**) and 6 weeks (**B**) after birth demonstrate temporal maturation of the sulcal pattern, and progressive myelination in the posterior limbs of internal capsules and ventro-lateral thalami.

*The safety of imaging fetuses / infants has not been established.



2 Histologically confirmed cortical dysplasia: coronal T2 FLAIR images from MRI brain study performed at 3T (**A**) demonstrates ill-defined increased signal in the right insular cortex and adjacent white matter, much better appreciated than on (**B**) the earlier study performed at 1.5T, (**C**) axial T2 image of a term neonate with polymicrogyria, (**D**) axial T2 TrueFISP MRI of the cervical spine in a 3-month-old infant demonstrates avulsed right C6 ventral nerve root and traumatic pseudo-meningocele due to obstetric brachial plexus palsy, (**E**) MRCP of a patient with a choledochocoele and (**F**) sagittal T2 TSE images demonstrate recto-sigmoid wall oedema and thickening due to inflammatory bowel disease.

2.3. Physiological challenges

In children the blood flow, pulse and respiratory rates are considerably faster. The normal heart rate in a neonate can be as high as 140/min, and the respiratory rate up to 40/min. Children are also unable to hold their breath satisfactorily until they are about 8 years of age [6]. These parameters are significant for cardiac, chest and abdominal imaging and benefit from the shorter scan times as a result of the improved temporal resolution.

2.4. Behavioural challenges

One of the greatest challenges in children is getting them to cooperate adequately for a diagnostic MRI study. Younger children usually require sedation or general anaesthesia for a successful scan. This involves some inherent risk, requires specialised staff, MR compatible anaesthetic and monitoring equipment. It is also

slow and expensive [7]. The need for anaesthesia can be reduced by the use of bean bags, timing the scan with feeds and sleeping, education and practice sessions with dedicated educational play therapy staff, MRI toys and where possible a practice MRI unit [6]. The chance of these succeeding is greater if the scan times are shorter which can be achieved at higher field strength due to the improved temporal resolution.

3. How good is 3T at imaging children?

3.1. Can it do the basics?

With continuing hardware advances such as the availability of dedicated receiver coils, new pulse sequences and parallel imaging techniques, the 3T MRI unit can be used for imaging of all the organ sys-

tems evaluated on the 1.5T system [3,8]. Many pediatric MRI applications benefit from the increased signal at 3T (Fig. 2A–F; Table 1). Others, involving anatomic regions such as the heart, chest and abdomen are inherently prone to 3T artefacts, which must be controlled – these are discussed later in the article.

3.2. Is the SNR doubled?

The primary benefit of imaging at high field strength is the increased SNR. This is a direct consequence of the increase in MR signal resulting from greater number of protons aligned with the main magnetic field [2]. The signal increases four-fold when going from 1.5 to 3T. However, the noise is also doubled. So theoretically, the SNR should increase two-fold at 3T, when compared to 1.5T. However, this assumes fully relaxed T1

conditions and a constant bandwidth and flip angle [9].

The observed SNR gain is influenced by numerous factors including receiver coil design, B_0 and B_1 field homogeneity and radiofrequency (RF) flip angle limitations governed by increased RF power deposition [10]. In practice, in controlling for chemical shift, susceptibility and SAR at 3T, the bandwidth is usually increased and the flip angle reduced. In addition, at 3T the relaxation times are altered, and the T1 of tissues is longer [11,12]. If the TR is kept constant, there will be a reduction in SNR. Increasing the TR to compensate for the longer T1 will increase the acquisition time [2].

Therefore, the signal-to-noise gain is always less, (typically 1.7–1.8-fold), and this gain varies for different tissues [10,13].

3.3. How fast?

The improvement in SNR can be used to reduce the scan time. However, as discussed above, the observed SNR gain is less than two-fold, so it is not possible to image at twice the speed. Nevertheless, imaging is faster at 3T. In our practice this has not allowed us to reduce the need for general anaesthesia routinely at 3T. In isolated instances, however, this has been possible. However, it has allowed us to perform sequences more

routinely than is possible at 1.5T, due to the inherently longer scan times. This has been particularly true for MR spectroscopy (MRS) [2], whole body MRI and diffusion-weighted imaging (*syngo* DWI), including diffusion tensor imaging (*syngo* DTI) and 3D imaging, including 3D dynamic vascular imaging – these are discussed in detail later.

3.4. What resolution can be achieved?

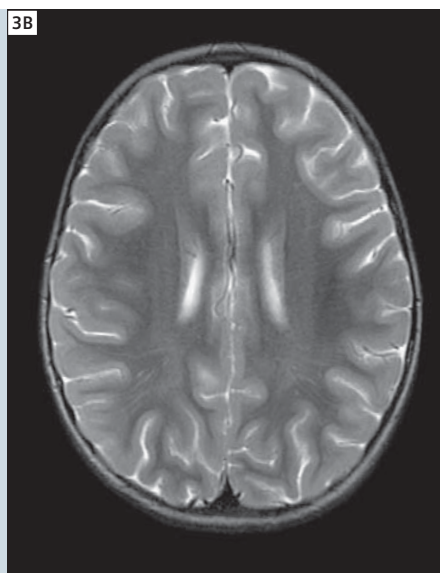
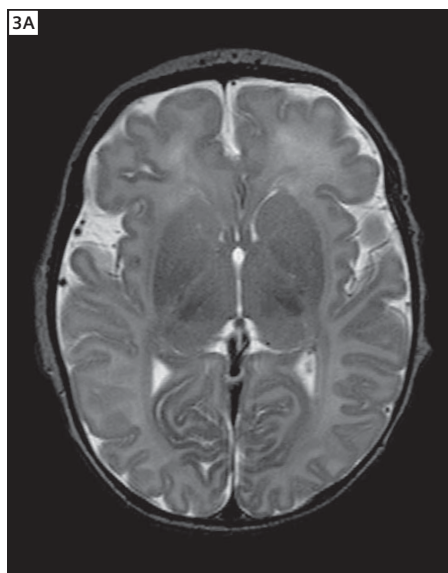
The SNR gain can also be used to increase spatial resolution. This has improved the imaging quality of small structures in children (Table 1). We have also been able to diagnose subtle abnormalities, which were earlier missed at

Table 1: Pediatric applications that benefit from the improved spatial and temporal resolution.

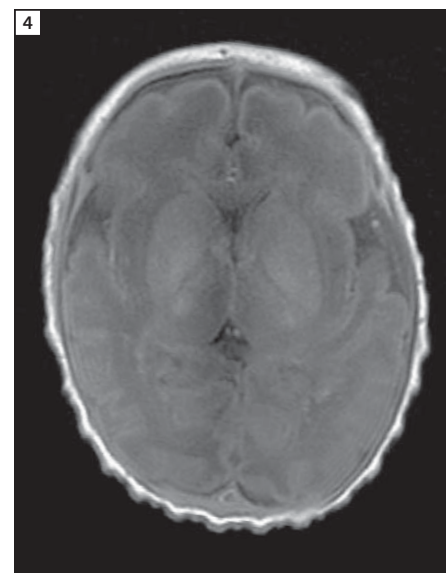
	Application	Examples of specific diseases
Neonate	All structures	
Nervous system	Brain Inner ear Cranial nerves Brachial plexus	Cortical dysplasia, migrational abnormalities Congenital sensory neural hearing loss Neuritis, e.g. bells palsy Birth trauma
Abdomen	Biliary tree	Sclerosing cholangitis, post liver transplant assessment
Musculoskeletal system	Small joints Polyarthropathy	Post reduction of dislocated hips in DDH, pre operative congenital deformity correction Haemophilia
MR angiography	Vasculitis Vascular malformations Congenital heart disease	Takayasu's arteritis, Moya Moya, Kawasaki disease Characterising type of vascular malformation Pulmonary arterial and aortic abnormalities, anomalous pulmonary venous return
Whole body MRI	Neoplasia Bone infarction Multifocal diseases Osteoporosis (compression fractures)	Neuroblastoma, lymphoma, leukaemia, ewings sarcoma Sickle cell disease, post chemotherapy and steroid therapy Chronic recurrent multifocal osteomyelitis, polymyositis Metabolic bone disease, steroid therapy

Table 2: How the opportunities of high field MRI can be applied in different organ systems.

Opportunity	Central nervous system	Musculoskeletal system	Cardiovascular system
SNR	Improved DWI, DTI, fMRI	Small joints, cartilage structure	Improved temporal resolution
Longer T1	Improved MRA	Improved MRA	Improved MRA, ASL, myocardial tagging
Susceptibility	Improved fMRI, SWI	Improved detection of calcification	Potential BOLD imaging
Chemical shift	Improved MRS	Improved MRS and fat saturation	Potential MRS



3 Axial T2 TSE MRI brain images obtained at 3T: the claustrum (**A**) is well demonstrated in this term neonate, (**B**) the perivascular spaces are routinely visualised at 3T.



4 Axial T1 image from MRI brain study of a neonate. The image contrast is less due to the prolonged T1 time, and the high water content of non-myelinated white matter.

1.5T (Fig. 2A and B). As with the differences in image contrast when compared to 1.5T, it is also important to familiarise oneself with the normal structures that are routinely visualised at 3T, e.g. the claustrum and multiple perivascular spaces on brain studies (Fig. 3A and B).

4. What are the challenges and opportunities at 3T?

The improved signal at 3T confers indisputable advantages. However, further improvements with newer sequences and dedicated coils for imaging neonates and premature infants are routinely required to realise the full potential of 3T. In addition, the increased energy deposition raises important safety concerns. The primary challenges are due to longer T1 relaxation times, the effect on T2 and T2*, and the greater chemical shift. Each of these factors play a different role depending on the region studied, and also create opportunities in the form of important clinical applications as discussed below and in Table 2. T1 or the longitudinal relaxation time varies for different tissues; but is generally longer at higher field strength for a specific tissue type. The T1 times of

different tissues increase to varying degrees (Table 3). For instance, the T1 relaxation time of brain parenchyma is increased by up to 40% when compared to imaging at 1.5T. Other tissues with significant magnetisation transfer also demonstrate increments of 20–40%, whereas for cerebrospinal fluid, the change is negligible (Table 3). For some tissues the T1 is even higher, for example an increase of up to 73% is reported for the kidneys [3].

4.1.1. Challenges due to longer T1

The increase in tissue T1 time will usually cause a decrease in image SNR [3]. In addition, the T1 values of different tissues tend to become more uniform at higher field strengths [14–16], with the result that the T1 images show less contrast between tissues. The pulse sequence parameters used at 1.5T require modification when applying to 3T [17]. These adaptations help minimise the intrinsic 3T image contrast losses. Knowledge of T1 values of different tissues at 3T will help select TR, TE, flip angle and inversion time to optimise image contrast [2] (Tables 3 and 4). The longer relaxation times affect T1 imaging of the neonatal brain. The neonatal brain inherently

has high water content, especially in the white matter, making grey–white differentiation difficult. This is compounded at 3T due to the decreased T1 contrast (Fig. 4). It is less of a problem in older children, after myelination is complete. The decreased grey–white contrast can be improved by appropriate use of TR, TE and flip angle and the use of sequences such as T1 FLAIR.

4.1.2. Advantages of longer T1

- a) MRA: The longer T1 relaxation times allow better background suppression for MRA techniques, with a larger signal difference, or greater contrast, between blood vessels and the surrounding tissues [17]. This improves vessel visualisation both with time of flight (ToF) (Fig. 5) and contrast enhanced MRA (ceMRA). With ceMRA, the signal difference between blood and unenhanced tissue is further increased as the relaxivity of paramagnetic MR contrast agents is only slightly reduced at 3T [17]. Improved MRA has reduced the need for conventional angiography at our institution.
- b) Post contrast imaging: For post contrast imaging in general, the improved contrast resolution at 3T and the rela-

Table 3: Increase in T1 times of different tissues at 3T vs. 1.5T [4, 8, 27, 32, 33]

Tissue type	% T1 increase	Examples of tissue T1 times (ms)	
		at 1.5T	at 3T
Brain – grey matter	Up to 62%	960	1331
Brain – white matter	Up to 42%	700	832
CSF	Negligible change	Negligible change	Negligible change
Myocardium	43%	1030	1471
Blood	34%	1200	1500
Bone marrow	30%	290–550	370–590
Skeletal muscle	Up to 40%	860–1130	900–1420
Cartilage	10%	1020–1060	1170–1240
Synovial fluid	27%	2850	3620
Fat	20%	290–340	370–380
Liver	Up to 41%	493	641
Spleen	20%	790	950
Kidney	73%	652	774

tively less marked change in the relaxivity of paramagnetic contrast agents when compared to the surrounding parenchyma can permit a reduction

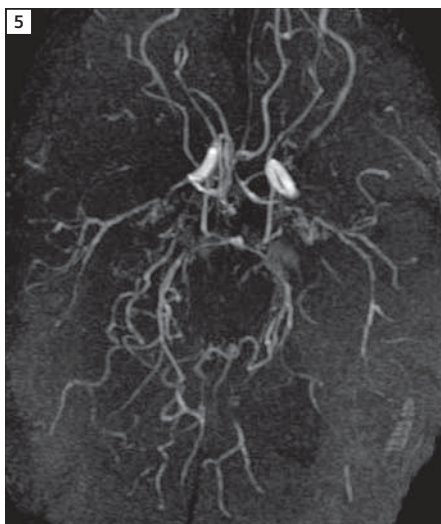
of gadolinium doses and potentially enable earlier detection of inflammatory and neoplastic diseases [18–20].

c) Arterial spin labelling: ASL enables perfusion imaging without contrast and is potentially a very useful technique in children. Blood is labelled magnetically and then followed into the brain. At 3T the label lasts longer due to the longer T1 tissue relaxation times [21] and there is a potential three-fold increase in the SNR with this technique. In addition, the rate of blood flow is faster in children so that the label can also pass further through the vascular bed before fading. ASL has enormous potential in vasculitic conditions such as Moya Moya disease. Moya Moya disease manifests with progressive irregularity, stenoses and obliteration of intracranial arteries and neo-vascularisation by collaterals that have a 'puff-of-smoke' appearance on angiography (Fig. 5). Treatment is surgical creation of burr-holes to promote collateral formation via intra- to extracranial anastomoses.

The timing of surgery is important to ensure the best possible outcome as collateralisation is optimal in the presence of a degree of tissue ischaemia, but delay can result in stroke. Serial imaging is used for assessment of the intra-cranial vasculature. ASL potentially has an important role in identifying parenchyma that is at risk of ischaemia, and to determine the optimal timing of surgery.

4.1.3. Effect on T2 and T2*

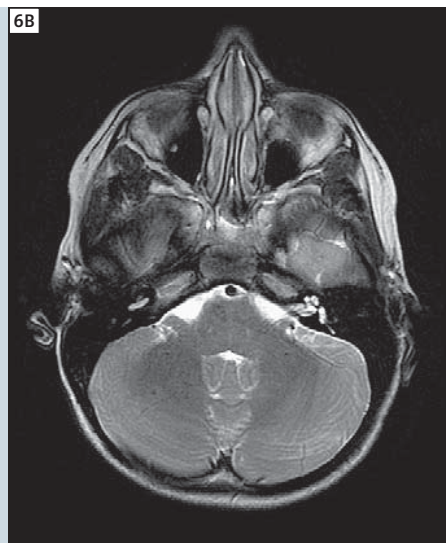
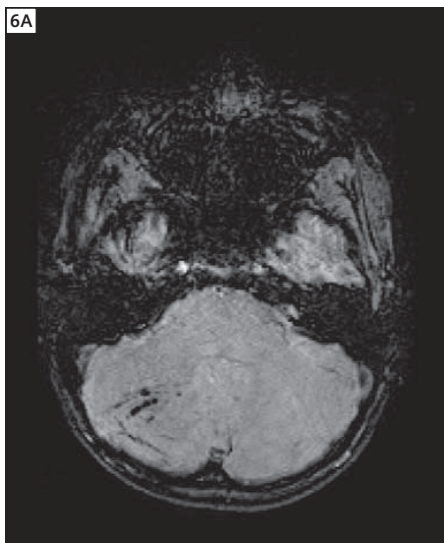
Tissue T2 values tend to decrease with field strength. However, tissue contrast on T2 images is not as significantly affected as T1 images [8]. Some recent reports suggest up to 10% decrease in T2 relaxation times at 3T, compared to 1.5T [16, 22, 23]. This further reduces the SNR gain for long TE sequences [17]. T2* decay, on the other hand, is considerably shorter at 3T due to microscopic field inhomogeneities which increase linearly with field strength.



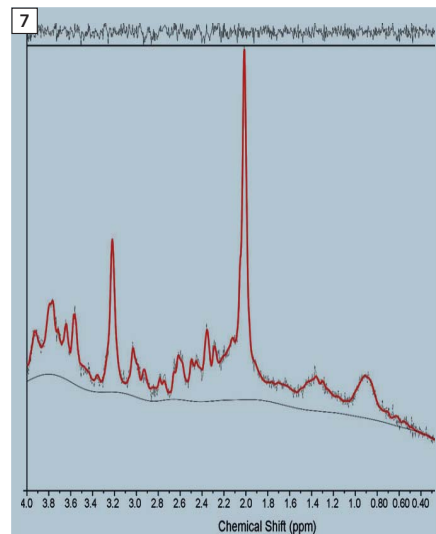
5 MoyaMoya disease. MIP of time-of-flight MR brain angiogram demonstrates marked irregularity, narrowing of several vessels of the circle of Willis, with collateral neovascularisation.

Table 4: Adapting (1.5T) parameters to circumvent important 3T specific challenges.

	Effect	Compensation	Effect of compensation (trade off)
↑T1 value	↓T1 tissue contrast	Increasing TR Parallel imaging techniques IR or MT sequences	↑Scan time ↓SNR
↓T2* values	Change T2* contrast	↓TE	↓SNR
↑Chemical shift	Artefact at fat–soft-tissue interfaces and MRS mis-registration	Doubling the readout bandwidth ↓FOV Fat suppression ↓Voxel Size	↓SNR, permits ↑, number of slices acquired for given TR ↓SNR Allows imaging at low readout bandwidth, SNR remains high
↑SAR	↑Body temperature	SAR monitor (legal limits) Special RF pulses ↓FOV Longer sequence duration ↓Flip angle ↓Number of slices Longer TR	↓SNR
↑Magnetic susceptibility	Image distortion, dark bands	Frequency encode parallel to long axis of implant Remove cause ↓Voxel size ↓Slice thickness ↓TE ↑Receiver bandwidth ↑Spatial resolution ↑ETL (TSE better than SE) Parallel imaging Shimming GRE sequence most affected	↓SNR ↓SNR ↑SAR ↓SNR
B ₁ inhomogeneity	Bright central region, signal loss	B ₁ insensitive (Adiabatic) pulses Shimming Dielectric pads	
↑Signal	↑Flow artefact	Saturation band Phase encode direction other than AP Gradient moment nulling Cardiac gating	



6 (A) Foci of profound signal loss due to haemosiderin on the susceptibility-weighted image on follow-up MRI brain study after trauma (B) these are only identified in retrospect on the axial T2 images.



7 3T proton MRS (TE 30 PRESS) from the parietal white matter of a child with guanidinoacetate methyltransferase (GAMT) deficiency demonstrating a dramatic reduction in the creatine peak.

4.1.4. T2* related artefacts or susceptibility artefacts

The susceptibility effect is a materials' tendency to distort the applied magnetic field, and increases linearly with field strength. It occurs at air, bone or soft-tissue interfaces; and can cause areas of signal loss, inhomogeneous fat saturation and geometric distortion [24] (Figs. 6A and 8D). It is commonly seen near the paranasal sinuses in brain imaging, due to bowel gas in abdominal imaging, and with metallic implants, especially dental hardware in teenage children. The effect can be quite marked at 3T and was initially considered a major limitation to the clinical utility of high field MRI. The detrimental effect of susceptibility from macroscopic structures can be controlled at 3T by a number of techniques. The cause should be removed if possible. Appropriate shimming directly reduces field inhomogeneity. Decreasing the voxel size and TE and increasing the bandwidth can reduce this artefact, but with a concomitant decrease in SNR. Parallel imaging also reduces susceptibility, with a reduction in SNR [2] (Table 4). This decrease is adequately compensated by the increased signal at 3T.

4.1.5. T2* applications

The increased susceptibility at 3T has a number of advantages:

- Functional MRI: fMRI** relies on the ability to detect the blood deoxyhaemoglobin levels (BOLD effect), a T2* dependent technique. The greater susceptibility at high field strengths produces increased sensitivity for fMRI. fMRI has important applications in pediatric neuroimaging, especially in the preoperative assessment of children with intractable epilepsy and brain tumors, to minimise the resection of functional parenchyma.
- Susceptibility-weighted imaging:** The increased susceptibility at 3T increases the sensitivity to haemorrhage and calcification, which is exploited with *syngo* SWI. *syngo* SWI is very sensitive in identifying haemorrhagic foci in the brain (Fig. 6A and B). Specific pediatric applications include non-accidental injury, birth trauma and diffuse axonal injury due to vehicular accidents. Calcification is also easier to detect and is useful for characterising masses such as dysembryoplastic neuroepithelial tumors.

SWI is also useful in children with haemosiderosis. Abnormal tissue iron depo-

sition at an early age is most commonly due to recurrent transfusions in thalassemia major. Myocardial iron deposition can be fatal due to arrhythmias and cardiomyopathy. This is prevented by judicious use of chelating agents, which have significant side-effects. Imaging at 3T can potentially increase the sensitivity for myocardial and liver iron quantification. This is useful to guide therapy – specifically, to optimise the dose of chelating agents and the timing of initiation of therapy.

4.2. Chemical shift

The chemical shift effect is increased two-fold at 3T compared to 1.5T [8, 25], and can result in pronounced artefacts, however, it can also be exploited for MRS.

4.2.1. Chemical shift artefact

Chemical shift artefact is caused by spatial mis-registration of fat and water, and causes a dark band at fat–soft tissue interfaces. It causes problems with MRS (discussed in detail later) and in abdominal imaging, where it can obscure subtle bowel wall changes in early inflammatory disease. This artefact is controlled by doubling the bandwidth [8, 26], or by decreasing the FOV [26]. Both of these

reduce SNR ($\text{SNR} \propto 1/\sqrt{\text{BW}}$), however, this loss is adequately compensated for by the increased signal at 3T [26]. The artefact can also be reduced by fat saturation, decreasing the voxel size and altering the TE.

4.2.2. MR spectroscopy

In the pediatric setting MRS is performed as a problem-solving tool, to answer specific questions. It is important for the work up of metabolic disorders. With significant overlap in the presentation of different conditions, MRS provides valuable information for the individual patient when considered in the appropriate clinical context. It can be diagnostic in certain entities, such as creatine deficiency syndromes (Fig. 7), useful to indicate disease activity, as in Leigh's disease and also to monitor response to treatment. It is also helpful to characterise space-occupying lesions and to determine the extent of infiltrative spread (Fig. 8). In neonates and pre term infants, MRS is performed for assessment of biochemical changes with brain maturation related to location and development, in order to detect brain injury (Fig. 9), and to distinguish hypoxic insults from metabolic/neurodegenerative conditions.

4.2.3. MRS: 3T advantages

Greater chemical shift is the basis of improvement in MRS at 3T, with increased frequency spread of individual peaks resulting in improved metabolite identification. In addition, the amount of signal derived from each metabolite is increased, so the metabolite peaks are easier to differentiate from background noise. The increased signal also enables faster acquisition times [8] which makes it more realistic in children, and especially neonates, who may not tolerate a longer sequence. The voxel size can also be reduced both with single voxel and multi voxel MRS, reducing the likelihood of contamination from subcutaneous/retro orbital fat in peripherally located lesions.

4.2.4. MRS: 3T challenges

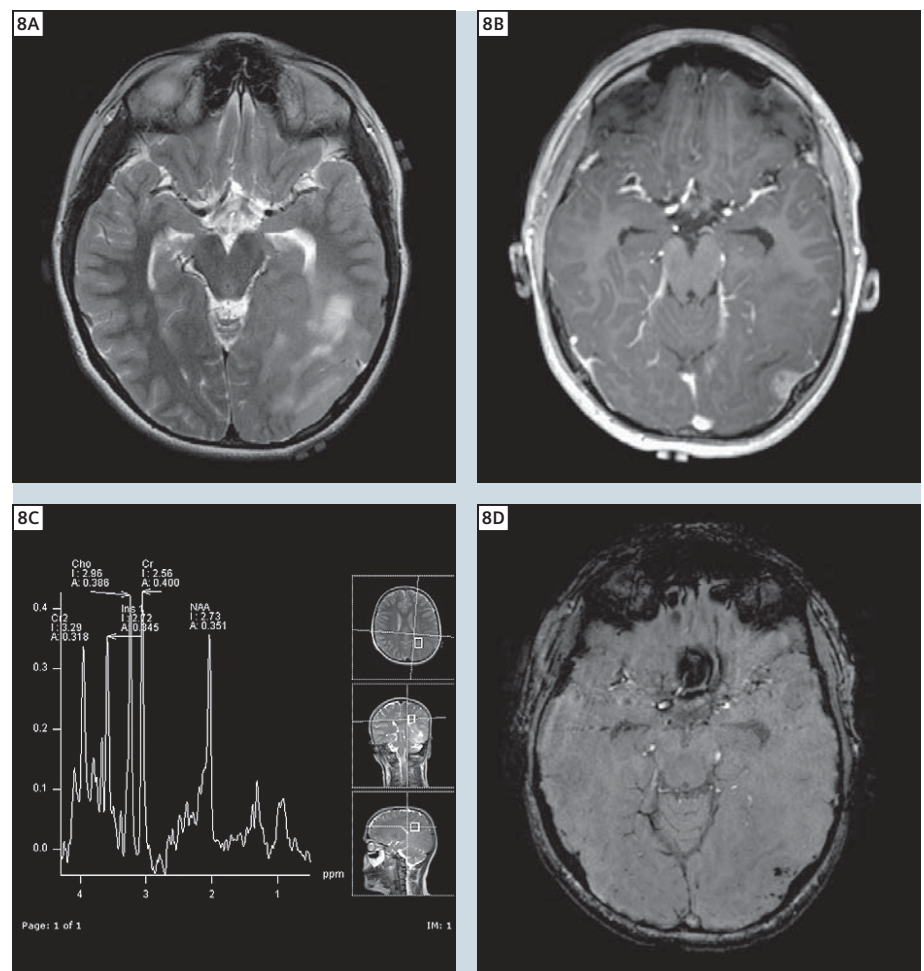
Performing MRS at high field strength has quite a few advantages – but at the same time, there are several issues to

consider when applying the 1.5T parameters and experience at 3T. The increased chemical shift also causes specific constraints for 3T MRS, whether using single or multi voxel techniques. Specifically, problems with misregistration (which results in poor lactate inversion at 3T, discussed later); and artefacts from increased susceptibility near bony structures, air sinuses and soft-tissue interfaces [25] are more pronounced than at 1.5T.

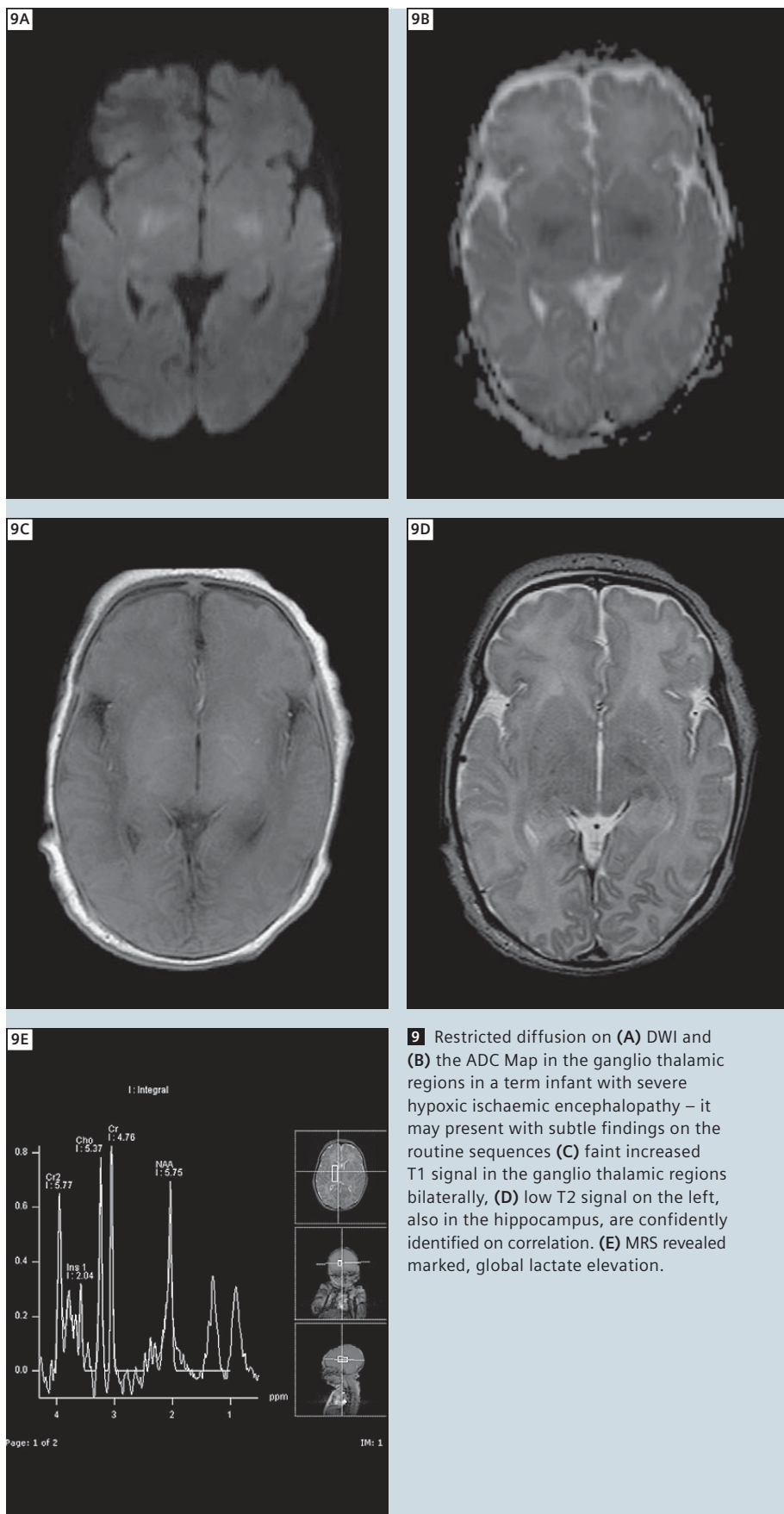
The greatest gain in SNR occurs at MRS using short TE – the latter is also the most useful in the assessment of metabolic diseases, as it is possible to detect metabolites with short T2 relaxation

times, and there is little need for T2 correction. However, the general disadvantages of short TEMRS are also relevant at 3T, i.e., the overlap of lipid and lactate peaks, and distortion of the baseline due to the effect of eddy currents [27]. Hence, spectra are usually obtained at two TE values.

3T MRS at intermediate TE suffers from variable lactate inversion, which complicates the distinction of lactate from lipids – an important consideration, especially in the neonatal period as an additional sign of hypoxia. At long TE MRS the signal benefit at 3T compared to 1.5T becomes negligible [27] and the baseline is smoother, which limits detection



8 Glioblastoma Multiforme: Axial images from MRI brain study performed for right homonymous hemianopia demonstrate (A) gyral thickening, ill-defined increased T2 signal and indistinct grey-white differentiation in the left parieto-occipital region. (B) Cortically based enhancement (C) MR spectroscopy demonstrates marked elevation of choline away from the small central enhancing area – this is useful to delineate tumor extent, and distinguish infiltrative spread from peri lesional oedema. (D) Foci of signal dropout from blood degradation products. Note the skull base susceptibility artefact.



9 Restricted diffusion on (A) DWI and (B) the ADC Map in the ganglio thalamic regions in a term infant with severe hypoxic ischaemic encephalopathy – it may present with subtle findings on the routine sequences (C) faint increased T1 signal in the ganglio thalamic regions bilaterally, (D) low T2 signal on the left, also in the hippocampus, are confidently identified on correlation. (E) MRS revealed marked, global lactate elevation.

of smaller metabolite peaks. However, in the hypoxic setting, it is the preferred second acquisition as lipids in the voxel are neutralised, and confident assessment of lactate levels is possible.

4.3. B₁ inhomogeneity

B₁ inhomogeneity produces regions of reduced signal in the centre of the imaged object. This effect is caused by a combination of (A) variable and reduced RF penetration depth as the magnetic field strength increases and (B) dielectric tissue properties cause resonance phenomena that appear as standing waves when half the wavelength is in the order of the object size.

This is an important 3T artifact, is unpredictable and depends on the body shape and organ size. It is less of a problem in smaller children, as the tissue depth for RF penetration is less and the organ size smaller. It can affect abdominal MR images of older children. Appropriate shimming is helpful to move these dark bands away from the region of interest. Dielectric pads can help with this artifact and newer B₁ insensitive (Adiabatic) pulses have been developed with the latest MRI machines.

4.4. Safety issues

4.4.1. Specific absorption rate

SAR reduction is a very important factor that permits the clinical use of 3T MRI. It is a measure of the amount of energy deposited by an RF field in a given mass of tissue, and is constrained by FDA guidelines. As the power required for excitation increases with increasing frequency (and thus field strength); the SAR increases with field strength. This is according to the formula $SAR \propto B_0^2$ [10]. Therefore, using equivalent parameters, there is a four-fold increase in SAR at 3T compared to 1.5T.

The SAR increase is greater in fast spin echo sequences due to the multiple refocussing pulses and with RF intense pulse sequences such as FLAIR [25]. It also increases with gradient echo sequences that have a very short TR (e.g. TrueFISP). SAR is related to the flip angle according to the formula $SAR \propto (\text{flip angle})^2$ [2]. Fast contrast

enhanced 3D angiography using a high flip angle; and fully rephased gradient echo techniques which yield optimum signal at high flip angle excitation with short TR easily reach SAR limits at 3T. The SAR can be reduced by using special RF coil designs such as transmit/receive array coils, by reducing the number of slices, by having a delay between sequences, or by the use of parallel imaging techniques. The choice of sequence can also reduce SAR, by using a smaller flip angle or echo train length, or an increased bandwidth or TE. However, reducing the flip angle or increasing the bandwidth alters tissue contrast. Specialised RF pulses that vary the flip angle throughout the sequence (e.g. hyperecho [28]) can reduce the SAR by up to four-fold (Table 4).

SAR potentially can create issues with temperature control, especially in neonates. They are kept wrapped in the scanner to keep them warm, however, the greater energy deposition has the potential to further increase body heat. Temperature monitoring (either skin or rectal) is therefore useful, but requires MR compatible probes. Although this is a potential issue at 3T, in practice it has not been anymore problematic when compared to scanning at 1.5T.

4.5. Specific applications that benefit from high field strength: whole body MRI, DWI & DTI and 3D imaging

The reduced scan times enable wider coverage while maintaining adequate SNR, and these advantages make whole body MRI and *syngo* DTI feasible at 3T.

4.6. Whole body MRI

There is an inherent advantage of the smaller patient size in pediatric whole body MR imaging, as the total number of acquisitions required is less than for adults. Whole body MRI in children is primarily used for oncologic screening to assess the skeletal spread [14], by obtaining overlapping STIR coronal sections (Fig. 10). An estimate of the total tumor burden, including soft-tissue involvement can be performed. It has a role in pediatric haematologic malignancies such as leukaemia and lymphoma

[29], round cell tumors especially neuroblastoma, and skeletal tumors such as Ewings sarcoma [30]. Myelofibrosis, and also the response to therapy can be assessed. Non-oncologic applications include multifocal muscle disease, screening the osteoporotic skeleton for fractures, multiple bone infarcts, assessment of total body fat stores or whole body MR angiography (e.g. Takayasu's arteritis) [31].

4.6.1. Diffusion weighted (DWI) and diffusion tensor imaging (DTI)

The improved SNR at 3T means that higher B values ($>1000 \text{ s/mm}^2$), thinner slices and imaging in a greater number of directions are possible, thereby improving DWI. Magnetic susceptibility artefact is more pronounced with EPI, and may be a problem with DWI at higher field strengths [32], especially with dental braces that are common in older children. This can be controlled – to an extent – with volume shimming, parallel imaging techniques, and bandwidth adjustment.

In the neonatal period, *syngo* DWI is very important for the assessment of hypoxic ischaemic encephalopathy, as it may present with subtle findings on the routine sequences (Fig. 9). It is also useful in the context of pediatric stroke, including vasculitis and sickle cell disease; also with traumatic brain injury and demyelinating disorders.

The benefit of DTI, when compared to conventional DWI, is the capability to determine white matter fibre orientation within collimated bundles – this directional information is displayed using 2D directionally encoded color anisotropy images or by 3D fibre tractography (Fig. 11). Also, qualitative measures derived from DTI, i.e., mean diffusivity and fractional anisotropy (FA) are rotationally invariant, and thus, in theory, not affected by changed head position or fibre orientation.

DTI is becoming increasingly important in the preoperative assessment of patients with brain tumors. Relationship of the mass with important white matter tracts can be demonstrated, and thus assist the surgeon in preserving func-

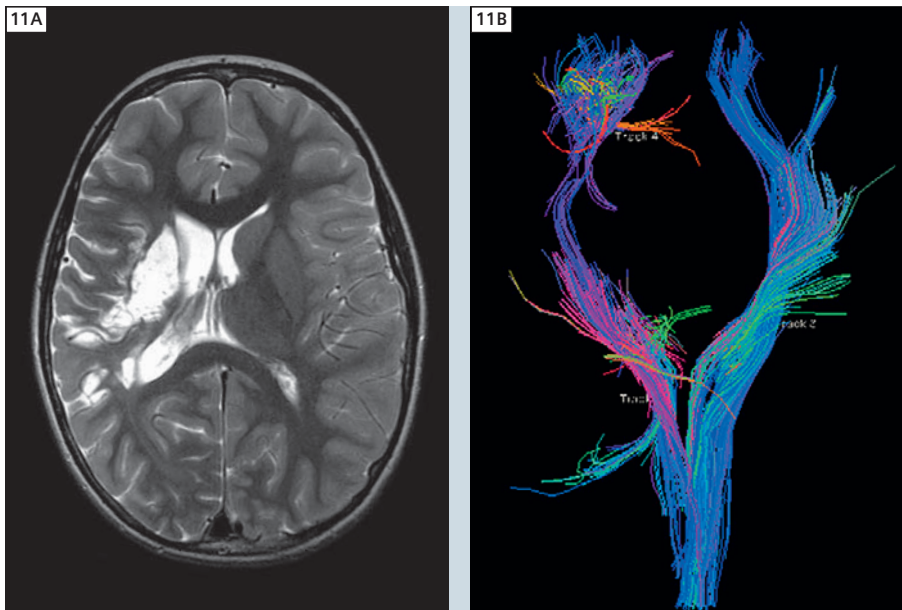


10 Coronal T2 STIR whole body MRI for metastatic neuroblastoma.

tion, while maximising lesion resection. With further advances, tractography can potentially enable more comprehensive assessment of other neural tract or pathway specific conditions, such as post delivery brachial plexus injuries; and aberrant connectivity in structural brain malformations.

4.7. 3D imaging and 3D dynamic MRA

The greater SNR enables faster acquisition of 3D data sets which are now routinely performed in our practice at 3T,



11 Sequela of right middle cerebral artery embolic occlusion secondary to traumatic internal carotid artery dissection. (A) Axial T2 image demonstrates cystic encephalomalacia and volume loss (B) disruption of the major white matter tracts (color coded) as depicted by tractography.

especially for post contrast imaging. Dynamic 3D imaging has also become practical with applications such as TWIST which enables sub-second time sequential 3D imaging. We have used this technique to evaluate the flow through complex vascular malformations, for planning treatment.

4.8. Challenging high field regions: cardiac and spinal imaging

There are definite advantages in having greater SNR for cardiac and spinal imaging, however, both regions have several high field issues, which come together to make these areas particularly challenging.

4.8.1. Cardiac imaging at 3T

The major indications for pediatric cardiac MR imaging are for assessment of ventricular function, the major vessels and post-operative anatomy in the context of congenital heart disease. However, all types of pathology including coronary artery abnormalities, cardiomyopathy, infiltrative disorders and cardiac tumors are imaged.

3T cardiac MRI has potential for improved coronary artery evaluation, and delayed

enhancement imaging in conditions such as cardiomyopathy and assessment for arrhythmogenic right ventricular dysplasia – these may be SNR-limited at lower field strengths.

Steady state free precession (TrueFISP) imaging, is very important in cardiac MRI at 1.5T. For the best TrueFISP imaging the TR is kept as short as possible (<4 ms), the flip angle as high and uniform as possible (all of which increase the SAR), and the magnetic field must be homogeneous (which is challenging at 3T). At 1.5T, the TrueFISP sequence is already at the SAR limit and to reduce the SAR at 3T, the flip angle must be reduced. This makes the blood pool darker and reduces the contrast between the blood pool SNR.

B_1 inhomogeneity artefact, susceptibility artefact and off resonance effects tend not to be a significant problem with cardiac imaging at 1.5T, however, occur unpredictably and can be severe at 3T [33]. Field inhomogeneity can be controlled by tight shimming and frequency correction.

Application of parallel imaging techniques may increase the clinical utility of 3T cardiac MRI. Higher acceleration

factors enable smaller acquisition windows, and support segmented acquisition schemes, an advantage for the higher heart rates of pediatric patients. Also, the energy deposition can be reduced due to fewer phase-encoding steps [33]. Improved MRA at 3T is very useful in the assessment of the major arteries and veins which are very important in children with congenital heart disease. This is particularly true of the pulmonary arteries, which commonly require assessment in the neonatal period.

4.8.2. Spine imaging

T1 imaging of the spinal cord is difficult at 3T. T1 prolongation results in reduced contrast between the grey and white-matter. This is accentuated in pediatric imaging due to the increased water content of neural tissue, especially before myelination is complete. In addition, CSF signal intensity at 3T is greater than at 1.5T which means there is reduced contrast between the spinal cord/conus and the surrounding CSF.

Gradient sequences such as T1 FLAIR may lessen the problems associated with T1 lengthening, with the potential of optimum contrast at 3T, at normal as well as abnormal tissue interfaces [26]. Studies comparing post-contrast T1 spin echo and gradient images have yielded equivocal results with regard to lesion conspicuity and detection – this may be overcome by acquiring one of each, in different planes [26]. In addition, CSF flow artefacts increase with higher field strength, due to the increased signal and spatial misregistration. The highly pulsatile CSF flow in children can cause a severe artefact which can obscure important pathology, such as leptomeningeal tumour spread. Gradient moment nulling may prove to be useful for CSF flow compensation [11]. Cardiac gating may also be used to overcome these effects [9].

5. Conclusion

3T MRI is being increasingly performed for clinical purposes. The signal increases four-fold when compared to imaging at 1.5T, and can translate to an observed SNR gain of 1.7–1.8. The increased SNR

is a significant advantage in pediatrics – improved spatial and temporal resolution assist in overcoming the major anatomic, physiologic and behavioural challenges of imaging children. Rapid changes with development and maturation can also be better assessed.

The challenges inherent to imaging at high field strength remain pertinent – important among these are the altered T1 contrast, artefacts and safety issues, especially SAR. These necessitate modification of the imaging protocols used at 1.5T. Ongoing physicist input, and technical support is essential. Hardware advances especially improved gradients, dedicated coils and sequences are very useful in this regard. The above mentioned challenges also create opportunities at 3T, with improvement in MRA, *syngo* ASL, *syngo* SWI, fMRI and MRS – all of which have distinctive applications in pediatrics. The SNR gain can be used as a trade-off, when compensating for the altered relaxation times and 3T specific artefacts.

3T MRI has the potential to image all the systems in pediatrics. Optimising the parameters with due consideration to specific pediatric features, such as the increased water content of non myelinated brain, is essential. Some 3T artefacts inherent to specific anatomic regions, like the dielectric effects encountered in adult abdominal imaging, are less problematic in pediatrics due the smaller size. On the other hand, the neonatal brain and pediatric spine are difficult to image at 3T. Several factors also limit cardiac imaging at present. Further improvements in coil technology and newer sequences may help overcome the challenges that remain.

Contact

Michael Ditchfield, M.D.
The Royal Children's Hospital
Femington Road, Parkville
Viktoria, Australia, 3052
michael.ditchfield@rch.org.au

References

- 1 Akisik FM, Sandrasegaran K, Aisen A, et al. Abdominal MR imaging at 3.0 T. *Radiographics* 2007;27(5):1433–44.
- 2 Barth MM, Smith MP, Pedrosa I, et al. Body MR imaging at 3.0 T: understanding the opportunities and challenges. *Radiographics* 2007; 27(5):1445–64.
- 3 Soher BJ, Dale BM, Merkle EM. A review of MR Physics: 3T versus 1.5T. *Magn Reson Imag Clin N Am* 2007;15(3):277–90.
- 4 Zimmerman RA, Bilaniuk LT, Pollock AN, et al. 3.0 T versus 1.5T. *Paediatr Brain Imag* 2006; 16(2):229–39.
- 5 Kliegman RM, Behrman RE, Jenson HB, et al. *Nelson Textbook of Pediatrics*. 18th ed. Saunders; 2008. p. 41.
- 6 Hallowell LM, Stewart SE, de Amorim e Silva CT, et al., Reviewing the process of preparing children for MRI. *Pediatr Radiol*. 2008;38(3):271–79.
- 7 Stokowski LA. Ensuring safety for infants undergoing magnetic resonance imaging. *Adv Neonatal Care* 2005;5(1):14–27.
- 8 Schick F. Whole-body MRI at high field: technical limits and clinical potential. *Eur Radiol* 2005;15(5):946–59.
- 9 Gonen O, Gruber S, Li BS, et al. Multi-voxel 3D proton spectroscopy in the Brain at 1.5T versus 3.0 T: signal-to-noise ratio and resolution comparison. *AJNR Am J Neuroradiol* 2001;22:1727–31.
- 10 Wen H, Denison TJ, Singerman RW, et al. The intrinsic signal-to-noise ratio in human cardiac imaging at 1.5, 3 and 4 T. *J Magn Reson* 1997; 125(1): 65–71.
- 11 Barker PB, Hearshen DO, Boska MD. Single-voxel proton MRS of the human brain at 1.5T and 3.0 T. *Magn Reson Med* 2001;45:765–9.
- 12 Thulborn KR. Clinical rationale for very-high-field (3.0 Tesla) functional magnetic resonance imaging. *Topics Magn Reson Imag* 1999;10(1):37–50.
- 13 Merkle EM, Dale BM. Abdominal MRI at 3.0 T: the basics revisited. *AJR Am J Roentgenol* 2006; 186(6):1524–32.
- 14 Michaeli S, Garwood M, Zhu XH, et al. Proton T2 relaxation study of water, N-acetylaspartate, and creatine in human brain using Hahn and Carr-Purcell spin echoes at 4 T and 7 T. *Magn Reson Med* 2002;47(4):629–33.
- 15 Ethofer T, Mader I, Seeger U, et al. Comparison of longitudinal metabolite relaxation times in different regions of the human brain at 1.5 and 3Tesla. *Magn Reson Med* 2003;50(6):1296–301.
- 16 de Bezelaire CMJ, Duhamel GD, Rofsky NM, et al. MR imaging relaxation times of abdominal and pelvic tissues measured in vivo at 3.0 T: preliminary results. *Radiology* 2004;230:652–9.
- 17 Bernstein MA, Huston III J, Lin C, et al. High-resolution intracranial and cervical MRA at 3.0 T: technical considerations and initial experience. *Magn Reson Med* 2001;46(5):955–62.
- 18 Bernstein MA, Huston III J, Ward HA. Imaging artifacts at 3.0 T. *J Magn Reson Imag* 2006; 24(4):735–46.
- 19 Fernandez-Seara MA, Wehrli FW. Postprocessing technique to correct for background gradients in image-based R*2 measurements. *Magn Reson Med* 2000;44(3):358–66.
- 20 Wood M, Hardy P. Proton relaxation enhancement. *J Magn Reson Imag* 1993;3:149–56.
- 21 Martirosian P, Klose U, Mader I, et al. FAIR True-FISP perfusion imaging of the kidneys. *Magn Reson Med* 2004;51(2):353–61.
- 22 Gold G, Han E, Stainsby J, et al. Musculoskeletal MRI at 3.0 T: relaxation times and image contrast. *AJR Am J Roentgenol* 2004;183:343–51.
- 23 Stanisz G, Odorobina E, Pun J, et al. T1, T2 relaxation and magnetisation transfer in tissue at 3T. *Magn Reson Med* 2005;54(3):507–12.
- 24 Tin Ging Ma H. Local experience of MR imaging with 3T (TRIO) equipped with TIM. *Biomed Imag Interv J* 2007;3(1):12–39.
- 25 Bronson J. High-field MRI: is it time for 3T? *Imag Econ* 2004. Available via http://www.imaging-economics.com/issues/articles/2004-02_04.asp.
- 26 Shapiro MD. MR imaging of the spine at 3T. *Magn Reson Imag Clin N Am* 2006;14(1):97–108.
- 27 Kim J-h, Chang K-H, Na DG, et al. 3T 1H-MR spectroscopy in grading of cerebral gliomas: comparison of short and intermediate echo time sequences. *AJNR Am J Neuroradiol* 2006;27:1412–8.
- 28 Hennig J, Scheffler K. Hyperechoes. *Magn Reson Med* 2001;46:6–12.
- 29 Iizuka-Mikami M, Nagai K, Yoshida K, et al. Detection of bone marrow and extramedullary involvement in patients with non-Hodgkin's lymphoma by whole-body MRI: comparison with bone and 67 Ga scintigraphies. *Eur Radiol* 2004;14(6):1074–81.
- 30 Mazumdar A, Siegel MJ, Narra V, et al. Whole body fast inversion recovery MR imaging of small cell neoplasms in pediatric patients: a pilot study. *AJR* 2002;179:1261–6.
- 31 Laffan EE, O'Connor R, Ryan SP, et al. Whole-body magnetic resonance imaging: a useful additional sequence in pediatric imaging. *Pediatr Radiol* 2004;34(6):472–80.
- 32 Phalke VM, Gujar S, Quint DJ. Comparison of 3.0 T versus 1.5T MR: imaging of the spine. *Neuroimag Clin N Am* 2006;16(2):241–8.
- 33 Nael K, Fenchel M. Cardiac MR imaging: new advances and role of 3T. *Magn Reson Imag Clin N Am* 2007;15(3):291–300.

Don't miss the talks of experienced and renowned experts covering a broad range of MRI imaging

Jörg Barkhausen, M.D.
University Hospital Essen

Dynamic 3D MRA – Clinical Concepts
(syngo TWIST)



John A. Detre, M.D.
University of Pennsylvania

Clinical Applications of Arterial Spin Labeling
(syngo ASL)



Tammie L. S. Benzinger, M.D., Ph.D.
Washington University School of Medicine

Clinical Applications of Diffusion-Tensor Imaging
(syngo DTI)



John F. Nelson, M.D.
Battlefield Imaging

Breast Cancer Management –
Cross Modality Approach



John A. Carrino, M.D., M.P.H.
Johns Hopkins University, School of Medicine

MRI in Sports Medicine



Visit us at
www.siemens.com/magnetom-world
Go to
Education > e-trainings & Presentations

Pediatric Cardiovascular MR Imaging at 3T

Gary McNeal

Clinical Application Specialist, Siemens Medical Solutions USA, Inc., Hoffman Estates, IL, USA

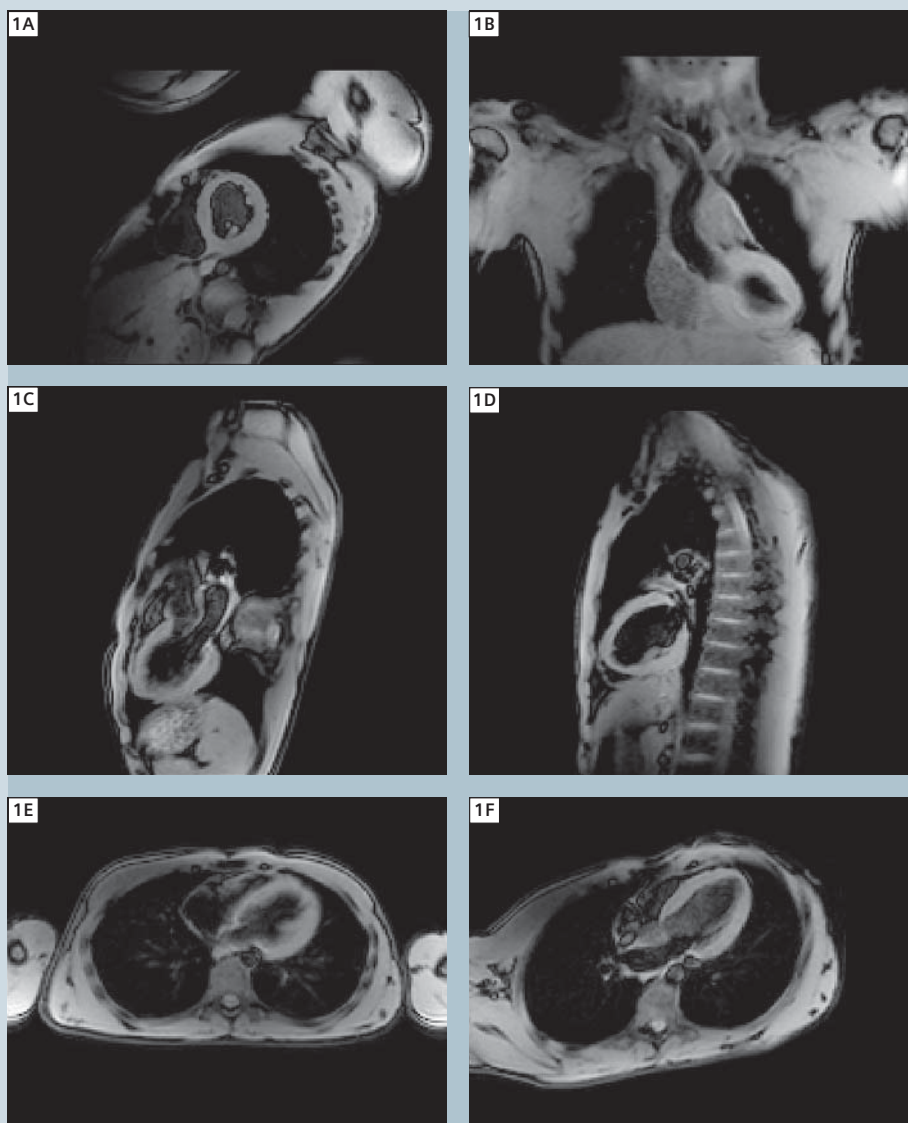
Introduction

Cardiovascular MR imaging of pediatric patients, especially those with congenital disease, is currently performed predominantly at major pediatric medical centers with both the high-end equipment and the specialized clinical expertise for these challenging exams. Most of these centers currently utilize 1.5T field-strength due to its wide-spread availability and due to the common perception that 3T field-strength poses too many technical challenges.

The basic challenges of imaging pediatric patients are mainly due to their higher heart rates and their smaller anatomic structures, as compared to adult patients. The additional challenges of imaging these patients at higher field-strength are due to the higher heat deposition (SAR) and increased T1 values of tissues, as compared to 1.5T imaging. This article demonstrates and discusses methods to overcome these challenges using the Siemens MAGNETOM family of 3T systems, namely the MAGNETOM Trio, A Tim System and the MAGNETOM Verio.

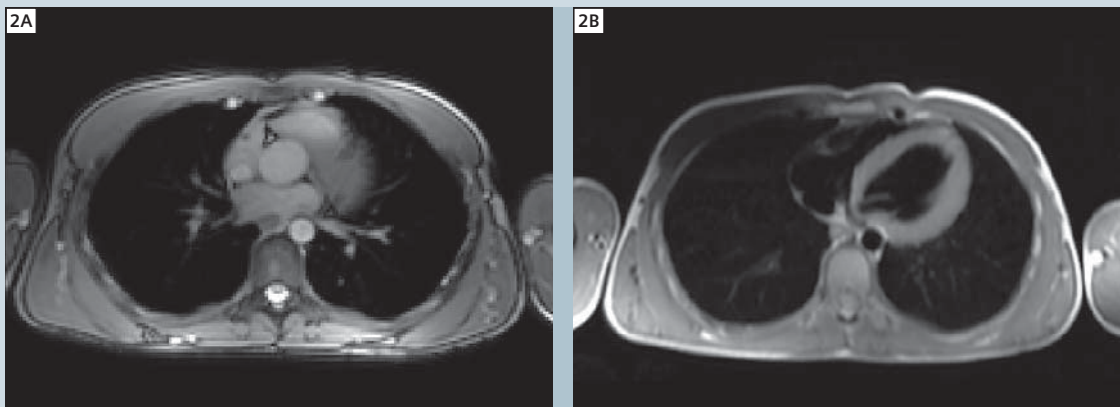
Methods

Ten pediatric patients ranging in age from 2 months* to 17 years were scanned on either a Tim Trio or a Verio system using standard commercially-available software and techniques. Standard pulse sequences and sequence parameter (syngo MR B15) were used in all cases. Pulse sequence parameters were optimized in each case to accommodate the patient's heart rate, body size, and level

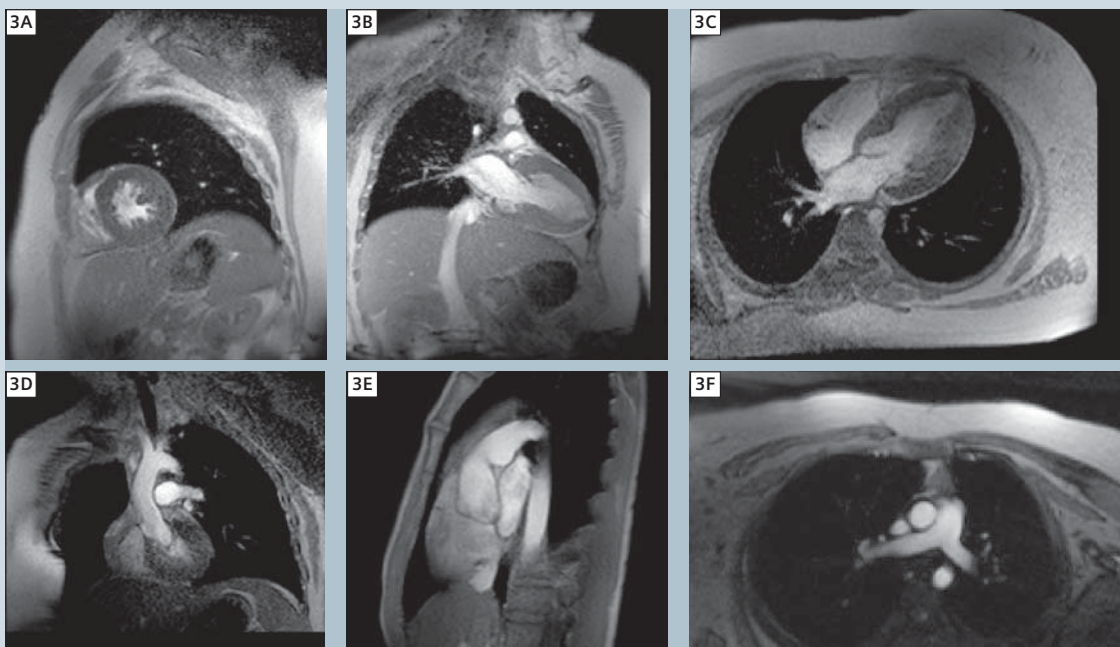


1 14-year-old male, single-shot dark-blood TurboFLASH, orthogonal and oblique localizers, triggered on every second heart beat, FOV 400 mm, 192 matrix, 7 mm slice, free-breathing, MAGNETOM Verio. (Courtesy of Children's Mercy Hospital, Kansas City, USA.)

*The safety of imaging fetuses/infants has not been established.



2 14-year-old male, single-shot bright-blood TrueFISP triggered on every single heart beat (A), single-shot dark-blood HASTE triggered on every second heart beat (B), FOV 360 mm, 192 matrix, 8 mm slice, free-breathing, MAGNETOM Verio. (Courtesy of Children's Mercy Hospital, Kansas City, USA.)



3 11-year-old female, GRE cine in short axis, 2-chamber and 4-chamber long axes, coronal, sagittal, and transverse views, FOV 360 mm, 224 matrix, 6 mm slice, breath-hold, MAGNETOM Verio. (Courtesy of Children's Mercy Hospital, Kansas City, USA.)

of sedation. Each exam was conducted within approximately 1-hour time-frame. Depending upon the clinical scenario, some patients received conscious sedation while others received general anesthesia.

At 1.5T field-strength the orthogonal and oblique localizers are typically performed with a single-shot bright-blood TrueFISP technique. However, at 3T field-strength these localizers are typically performed with a single-shot dark blood TurboFLASH technique due to its relative insensitivity to susceptibility artifacts, off-resonance artifacts, and heat deposition as compared to TrueFISP. Due to the dark-blood preparation pulse, this technique requires that the data is

acquired on every second heart beat, or every third heart beat in cases of extremely fast heart rates. This technique is also insensitive to patient breathing because it is a single-shot acquisition. A common strategy for imaging pediatric patients is to perform transverse stacks of single-shot bright-blood TrueFISP and single-shot dark-blood HASTE images to completely survey the entire heart and great vessels. These are typically slightly thinner slices than the localizers, with zero or minimal gap to assure that nothing is missed in the survey. TrueFISP is triggered to the diastolic segment of every single heart beat, whereas HASTE is triggered to the diastolic segment of every second (or third)

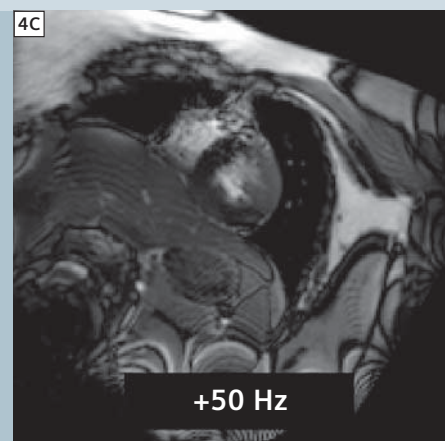
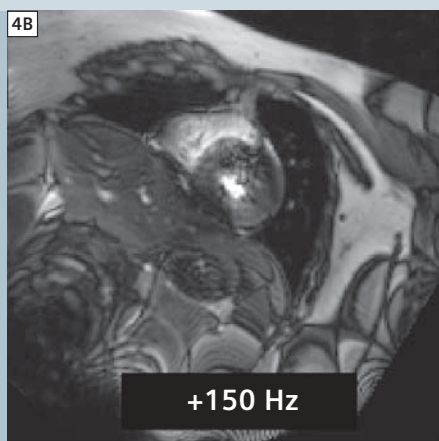
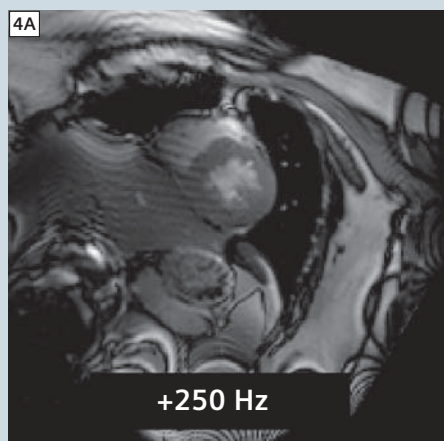
heart beat, and both techniques are insensitive to patient breathing. Gradient-echo (GRE) techniques are typically used for cine imaging at 3T because they are less sensitive to susceptibility artifacts, off-resonance artifacts, and heat deposition (SAR) than TrueFISP techniques. Pediatric cine imaging is performed in the standard short axis and long axis views of the heart, and often includes orthogonal views as well. Cine images are typically acquired with 1 signal average during a patient breath-hold, but can alternatively be acquired with 3–4 averages during free-breathing if the patient is sedated (as with the sagittal and transverse images in Fig. 3).

If one cares to invest some additional time to perform Frequency Scout scans in each view (approx 1 minute/view), one can use the TrueFISP technique for cine imaging instead of the GRE technique. Each Frequency Scout scan is performed in a single breath-hold and allows the selection of an optimal offset frequency to be used with a TrueFISP cine in the same view. Using an optimized offset frequency for TrueFISP does significantly reduce, and often eliminate, those pesky susceptibility artifacts and off-resonance artifacts. Frequency Scout results in a series of images, all with different offset frequencies – you

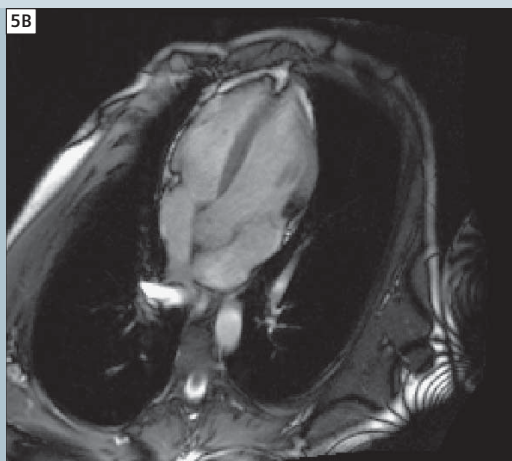
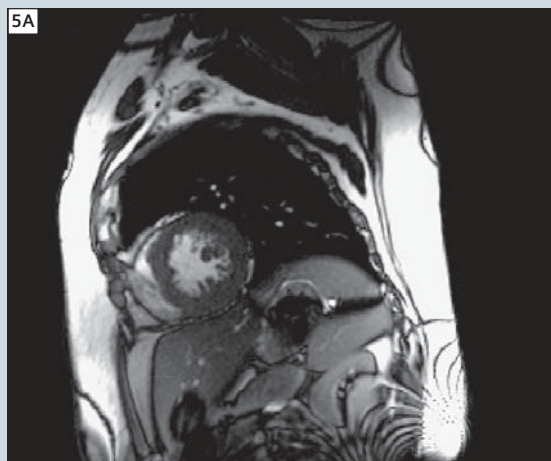
simply look at the image, select the one with the least amount of artifacts in the heart, and use its offset frequency in your subsequent TrueFISP cines in the same view.

TrueFISP images should ideally be acquired with maximal flip angle (90°) in order to maximize image contrast. At 1.5T it is common to use flip angles greater than 75° , but at 3T it is common to use much lower flip angles due to its inherently higher heat deposition (SAR), thereby compromising image contrast. To obtain the highest possible flip angle at 3T, one may increase the SAR limit to a higher level (FIRST LEVEL) and reduce

the RF pulse duration from (FAST) to (NORMAL) in the Sequence / Part 2 taskcard. This may increase the flip angle by as much as 10° – 15° , thereby improving the TrueFISP image contrast. By optimizing both the offset frequency and the flip angle, one can obtain quite good results with TrueFISP cine at 3T. Congenital disease is the most common indication for MR imaging of pediatric patients. Phase-contrast flow quantification methods play a huge role in pre-surgical and post-surgical assessment of these patients, particularly in cases involving vascular stenoses, coarctations, baffles, and abnormal valves. Flow



4 11-year-old female, Frequency Scout in the short axis view, offset frequency +250 Hz has least artifacts in the heart, FOV 400 mm, 192 matrix, 6 mm slice, breath-hold, MAGNETOM Verio. (Courtesy of Children's Mercy Hospital, Kansas City, USA.)



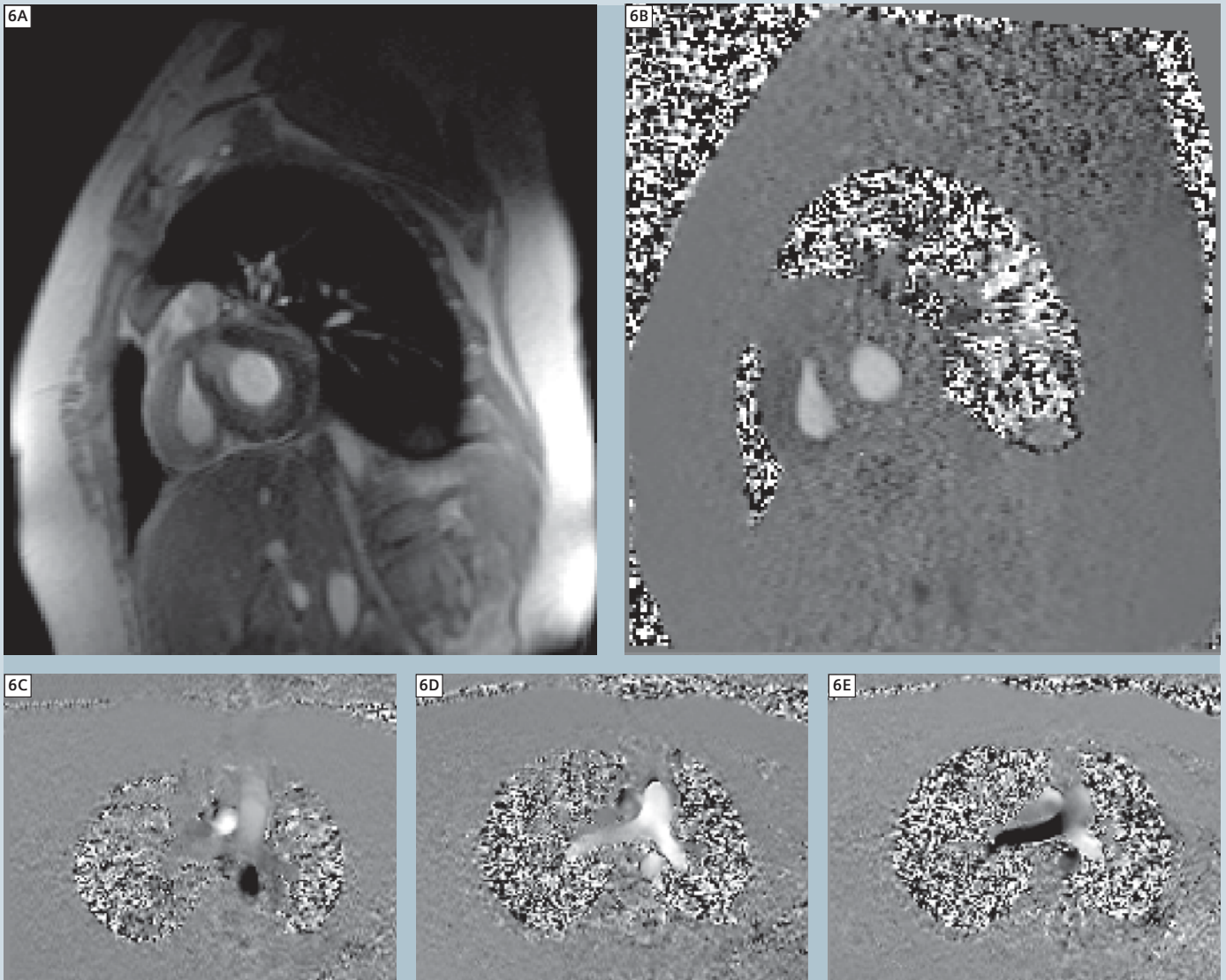
5 11-year-old female, TrueFISP cine in short axis and long axis views, optimized offset frequency and optimized flip angle, FOV 360 mm, 256 matrix, 6 mm slice, breath-hold, MAGNETOM Verio. (Courtesy of Children's Mercy Hospital, Kansas City, USA.)

imaging at 3T provides a significant signal-to-noise (SNR) advantage over 1.5T, and there are no discernable disadvantages at 3T. The SNR advantage may be used to improve spatial resolution, resulting in even better image quality at

3T in the same imaging time as 1.5T. This is quite an advantage in the setting of pediatric patients, where smaller FOV's and thinner slices are typically used to improve spatial resolution. Additionally, higher temporal resolution in

pediatric imaging is accomplished by reducing the number of k-space lines per cardiac phase (SEGMENTS) in order to reduce the TR as the heart rate is increased.

Three miscellaneous techniques

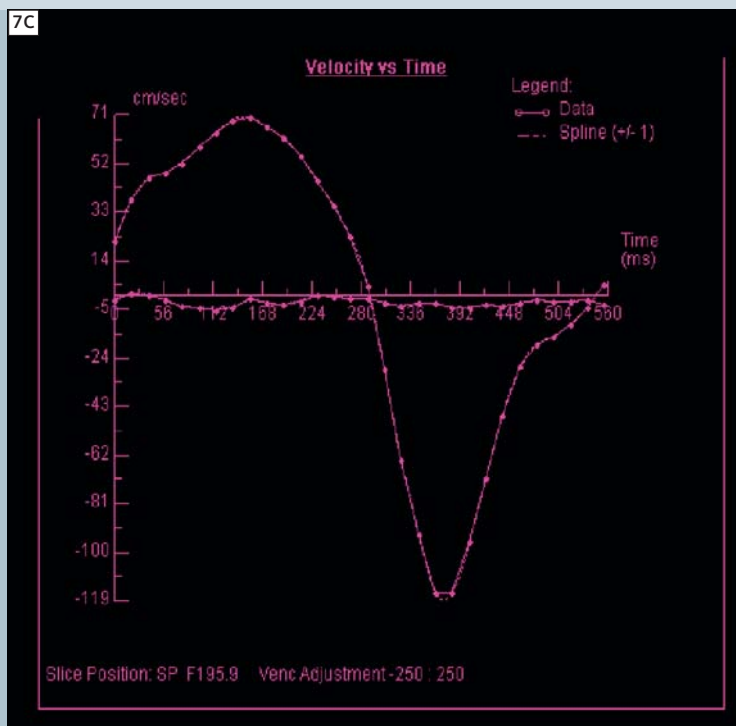


6 11-year-old female, Phase-contrast flow images acquired in short axis view demonstrates flow through mitral valve (6B) and in transverse view demonstrates main, left branch, and right branch pulmonary arteries (6C-6E) with thru-plane and in-plane flow encoding, FOV 360 mm, 192 matrix, 6 mm slice, breath-hold, MAGNETOM Verio. (Courtesy of Children's Mercy Hospital, Kansas City, USA.)

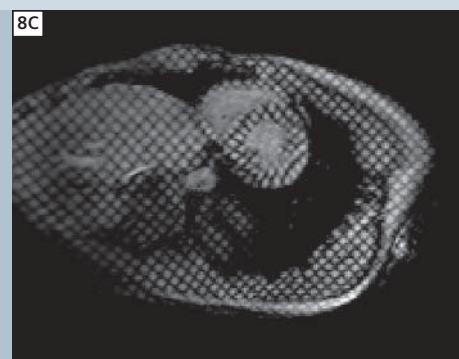
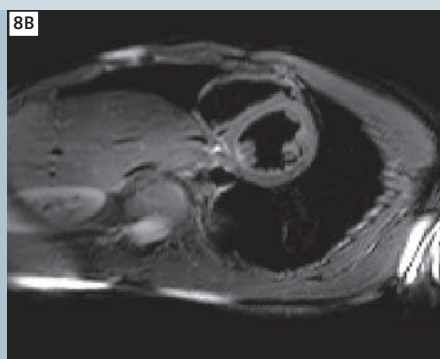
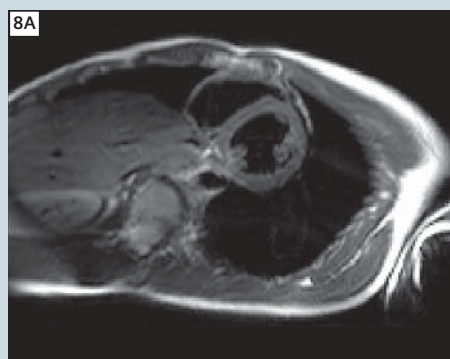
employed in pediatric MR imaging include Dark-Blood Turbo Spin Echo (DBTSE), both with and without fatsat, as well as Grid-Tagged cine. All of these techniques benefit much from the SNR advantage at 3T. Although grid-tagged

techniques have no discernable disadvantages at 3T, it is slightly more difficult to completely null the blood in DBTSE techniques due to the longer T1 recovery rate of blood at 3T compared to 1.5T. Gating to the diastolic segment of

the second heart beat after the trigger pulse and completely skipping over the third heart beat after the trigger pulse may help resolve this issue and improve blood nulling, especially with faster patient heart rates.



7 7-year-old female, Phase-contrast flow images of pulmonary artery regurgitation, forward volume 43 ml, reverse volume 12 ml, FOV 320 mm, 256 matrix, 5 mm slice, 3 averages, free-breathing, MAGNETOM Trio, A Tim System. (Courtesy of Methodist Healthcare System, San Antonio, USA.)

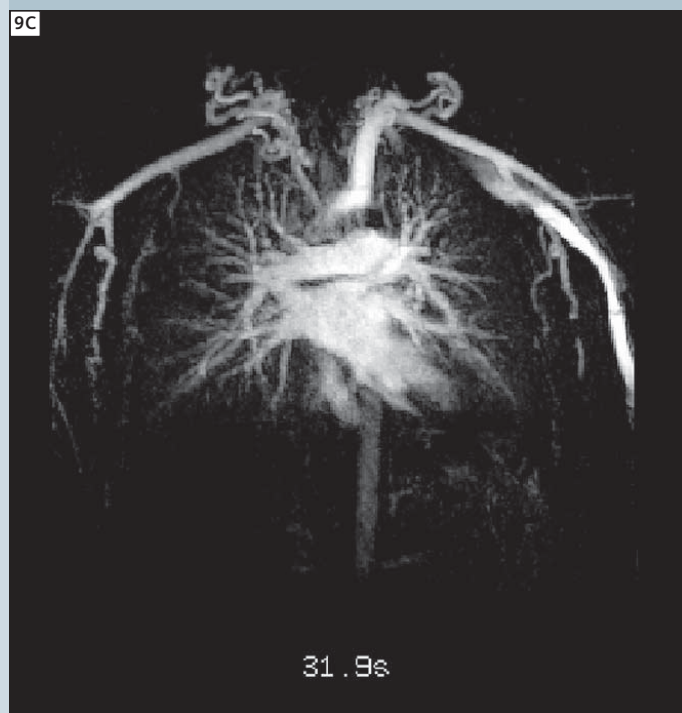
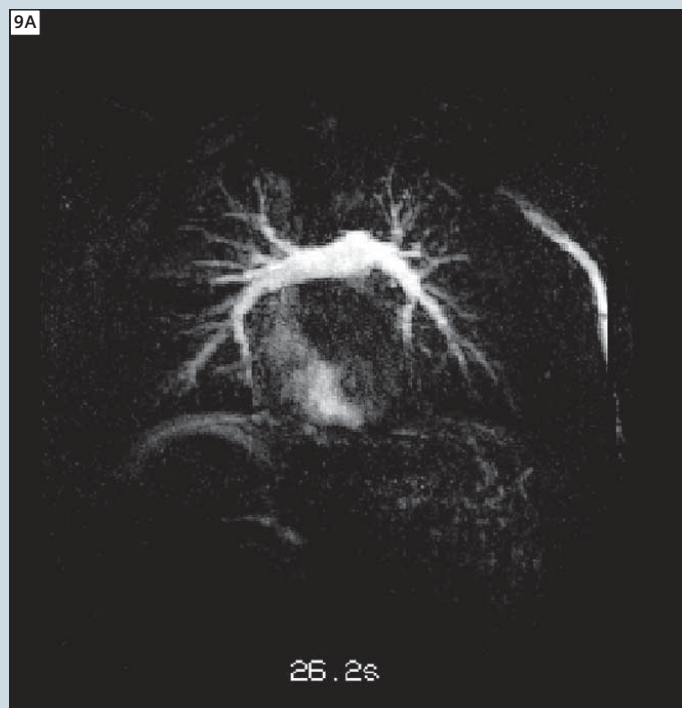


8 17-year-old male, Dark-Blood Turbo Spin Echo without fatsat (left) and with fatsat (middle), both gated to the diastolic segment of the second heart beat and the third heart beat is completely skipped, Grid-Tagged cine (right), FOV 360 mm, 192 matrix, 8 mm slice, breath-hold, MAGNETOM Verio. (Courtesy of Children's Mercy Hospital, Kansas City, USA.)

Easy, robust, time-resolved MR angiography may be performed with the *syngo* TWIST technique. This technique is particularly useful in pediatric patients who are typically free-breathing due to sedation. *syngo* TWIST acquires multiple 3D

measurements (volumes) in a repeated time series during the first-pass of contrast agent through the vascular system. Unlike conventional MR angiographic methods, *syngo* TWIST requires no test bolus to determine optimal injection

timing and dose rates – just inject and scan. The first 3D measurement is always used as an automatic subtraction mask for all remaining measurements, thus it is crucial to allow sufficient scan delay after injection to ensure that no contrast



9 14-year-old male, *syngo* TWIST time-resolved MR angiogram, 3 sec temporal resolution, FOV 420 mm, 320 matrix, 1.4 mm slice, PAT x2, free-breathing, MAGNETOM Verio. (Courtesy of Children's Mercy Hospital, Kansas City, USA.)

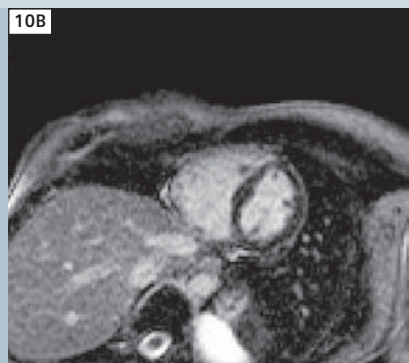
appears within the target vessels during the first measurement. For your convenience, the time duration of the first measurement (whole matrix) and all subsequent measurements (temporal resolution) is displayed within the Acquisition Time (TA) parameter. The first measurement always takes considerably longer to acquire than the remaining measurements. *syngo* TWIST requires only one-half the typical contrast dose of a conventional MR angiogram. This can be used either to substantially reduce the patient's risk or to perform two separate *syngo* TWIST scans with only a single dose.

The increased signal at 3T provides a huge benefit for delayed enhancement imaging of myocardium, especially for pediatric patients where smaller FOV's and thinner slices are used. TrueFISP techniques should be avoided for this application due to extreme sensitivity to susceptibility artifacts and off-resonance artifacts at 3T. Segmented TurboFLASH should be used for patients who can breath-hold, or single-shot TurboFLASH should be used for those who can not breath-hold.

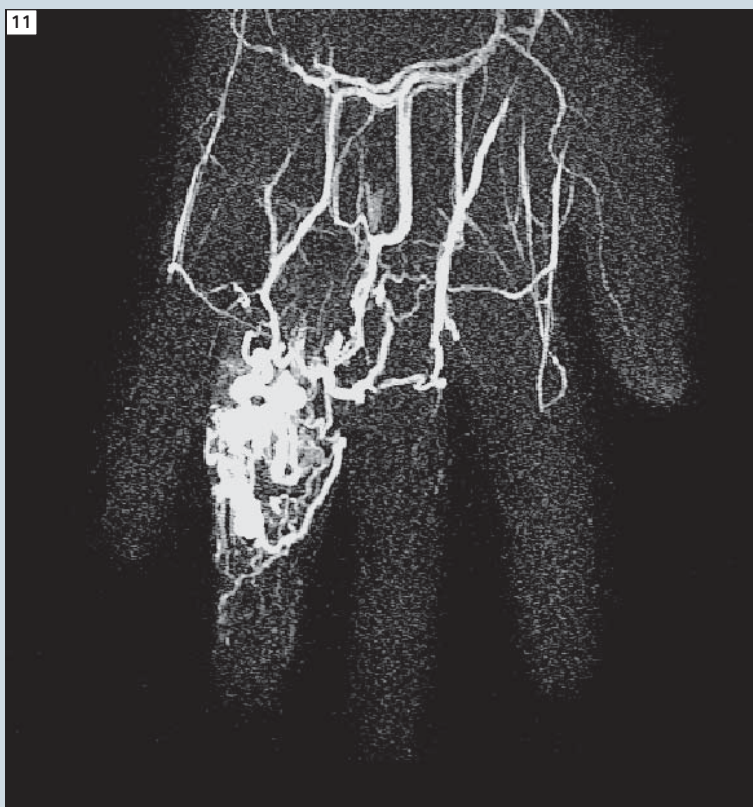
Discussion

One of the challenges encountered when imaging pediatric patients at 1.5T is that the combination of smaller fields-of-view (for improved spatial resolution) and parallel acquisition techniques (for improved temporal resolution) may result in unacceptable loss of signal-to-noise ratio. However, the additional signal provided by the higher field-strength means that this combination is much more feasible at 3T than at 1.5T. Thus it is even more common at 3T to combine higher iPAT factors with smaller FOV's for imaging pediatric patients, especially with vascular MRA techniques.

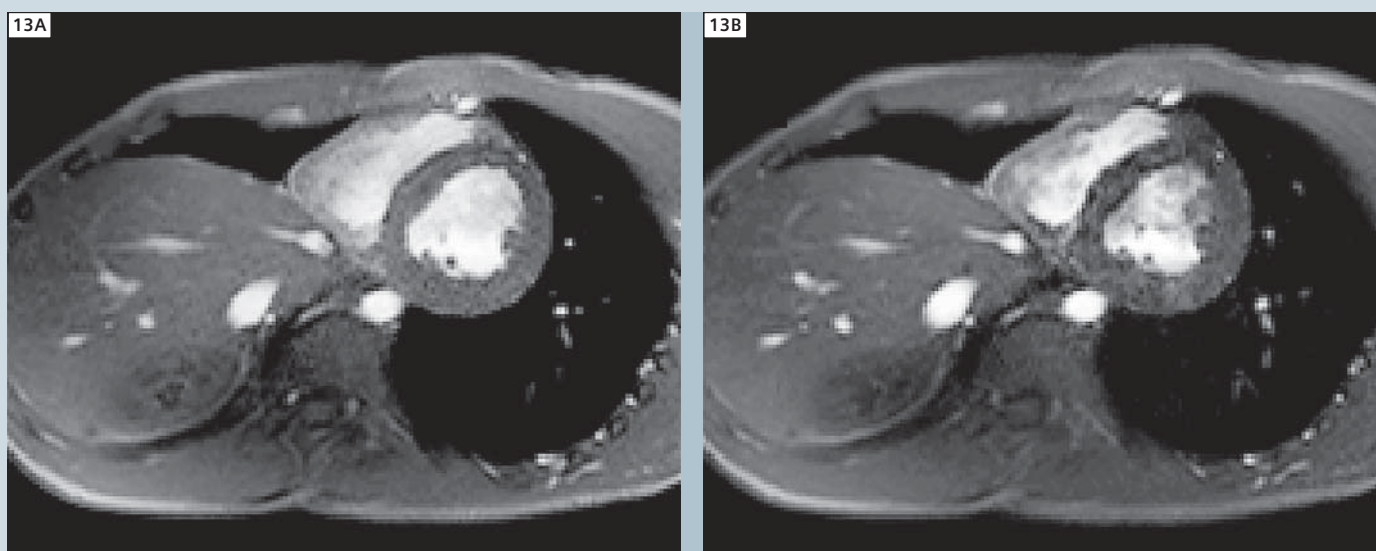
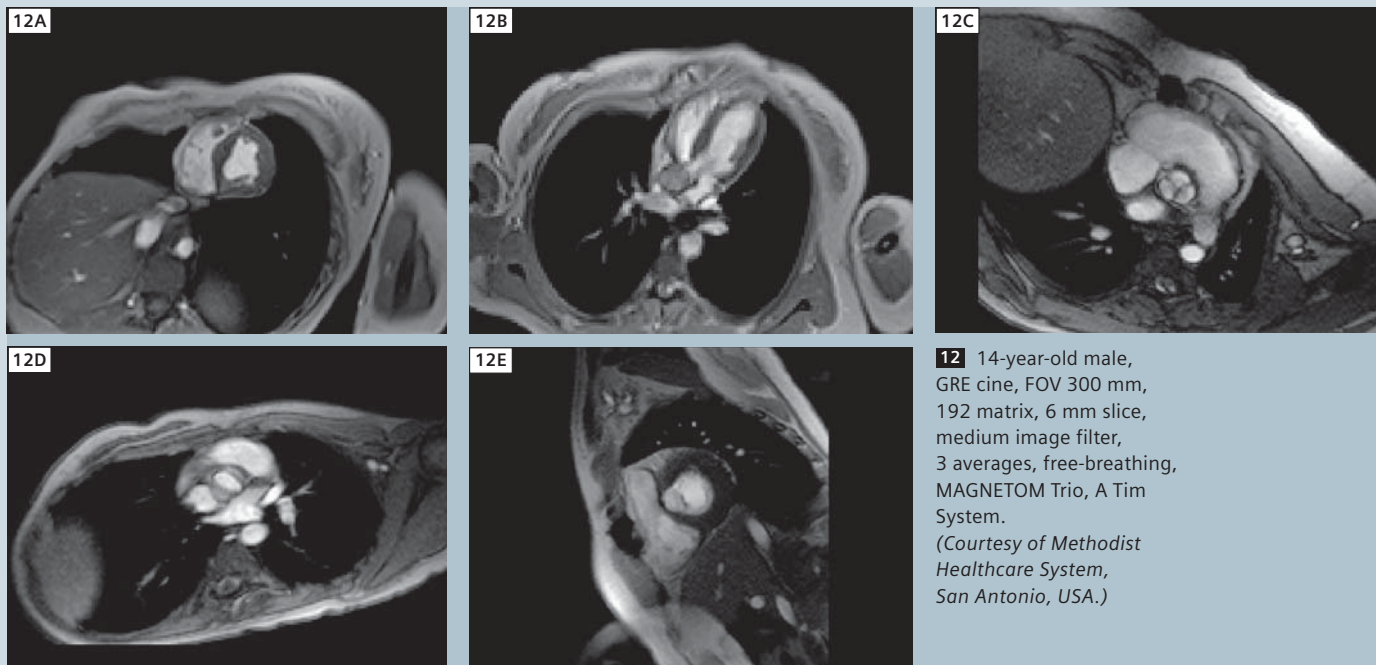
When imaging pediatric patients with smaller FOV's and thinner slices the SNR is always of concern – too often really grainy-looking images result. When this is the case, a simple but effective method to improve image quality is to apply the optional image filter to the acquisition protocol. Begin with the default settings (Resolution, Filter, Medium, 3, 3)



10 23-year-old female, single-shot TurboFLASH, FOV 350 mm, 192 matrix, 6 mm slice, free-breathing, MAGNETOM Trio, A Tim System. (Courtesy of Methodist Healthcare System, San Antonio, USA.)



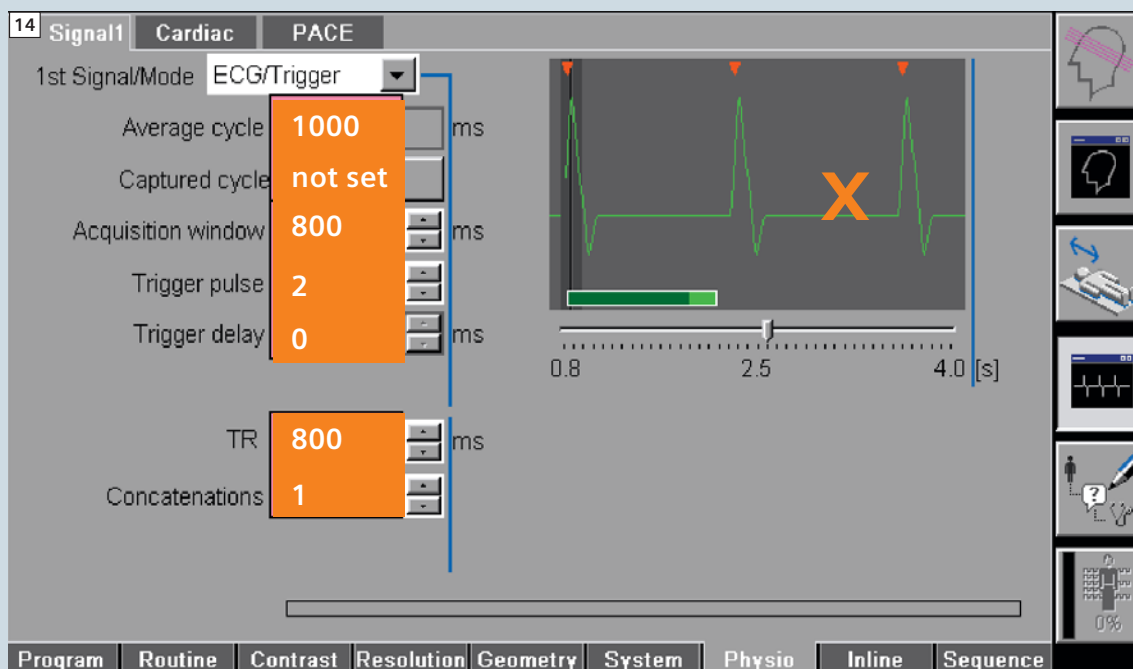
11 15-year-old female, *syngo* TWIST time-resolved MR angiogram, 3 sec temporal resolution, FOV 160 mm, 512 matrix, 1.5 mm slice, PAT x3, free-breathing, MAGNETOM Trio, A Tim System. (Courtesy of Seattle Childrens Hospital, Seattle, USA.)



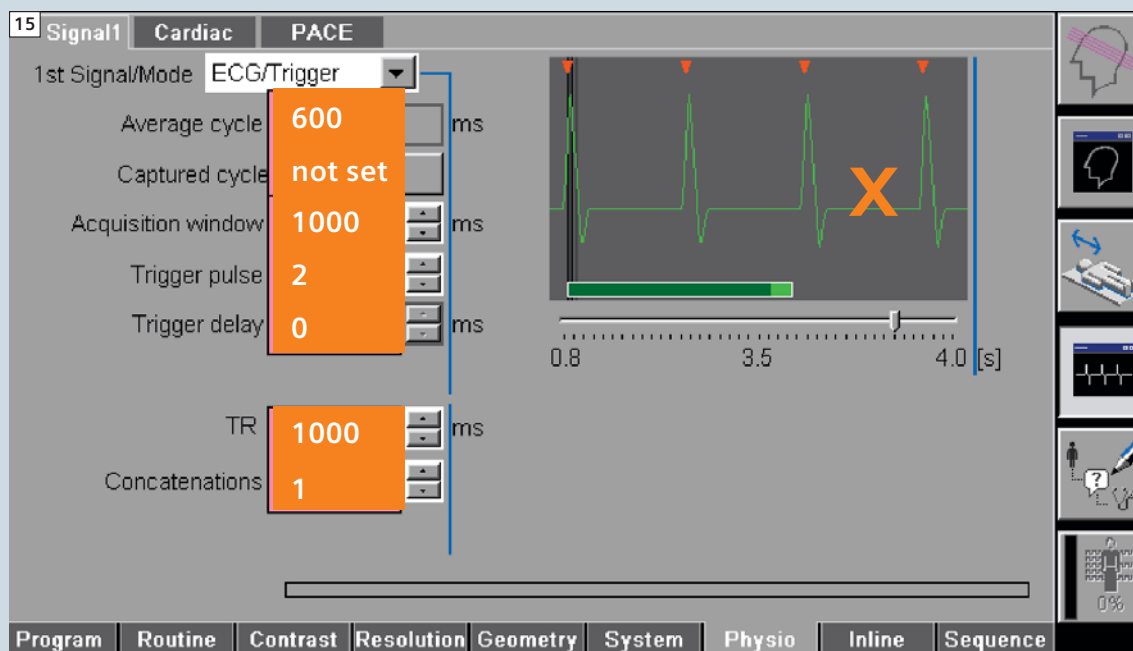
and adjust to your preference if needed. This filter may be used to emphasize edge enhancement, smoothing, or both. It is a common practice at 3T to acquire cine images with gradient-echo (GRE) techniques instead of steady-state-free-precession (TrueFISP) techniques because GRE is less sensitive to susceptibility artifacts, off-resonance artifacts, and heat

deposition. Beware that when using GRE techniques the flip angle must be optimized much differently according to field-strength. At 1.5T the optimal flip angles are about 20°–25° for in-plane flow such as long-axis views of the heart or sagittal-oblique views of the aorta, and about 25°–30° for through-plane flow such as short-axis views of the

heart or transverse views of the aorta. However, at 3T the optimal flip angles are about 12°–13° for in-plane flow, and about 17°–18° for through-plane flow. If you use flip angles too high (for example 30° at 3T) the blood will contain signal voids and extreme flow patterns rather than being homogeneous in appearance, as shown in Fig. 13.



14 Patient heart rate <100 bpm, trigger timing for dark-blood sequence, acquisition window spans nearly 1 complete cardiac cycle, TR adjusted for data acquisition to occur in late diastole of the first heart beat, trigger pulse set to 2 to completely skip the second heart beat.

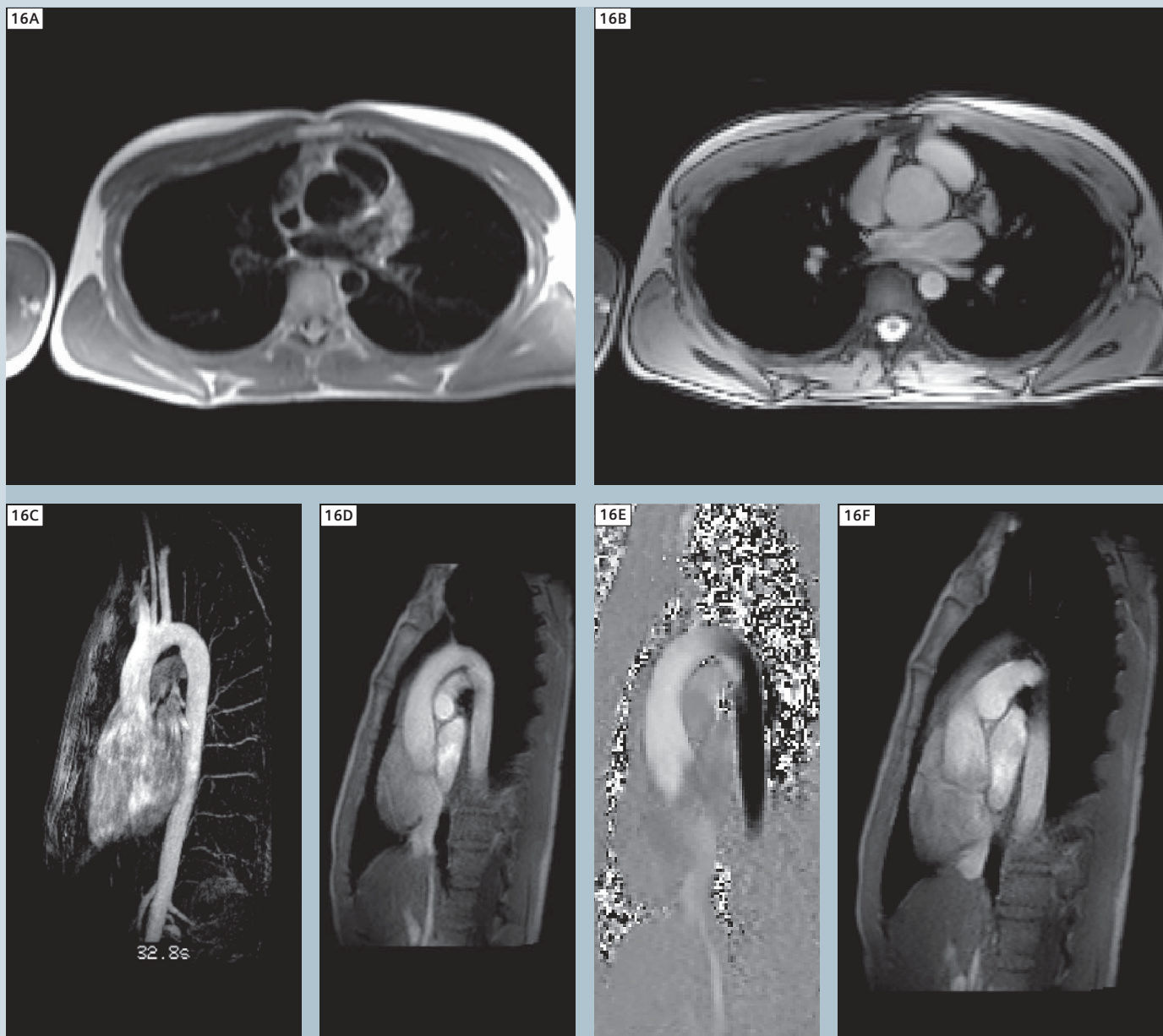


15 Patient heart rate >100 bpm, trigger timing for dark-blood sequence, acquisition window spans nearly 2 complete cardiac cycles, TR adjusted for data acquisition to occur in late diastole of the second heart beat, trigger pulse set to 2 to completely skip the third heart beat.

Very young pediatric patients typically have very fast heart rates (>100 bpm) resulting in very short cardiac cycles (<600 ms). This presents well-known challenges when performing dark-blood imaging, and even more so at 3T due to the longer T1 recovery rates of the tissues at 3T. Thus, it is necessary to slightly modify the trigger timing for heart rates

greater than approximately 100 bpm. The figure immediately below shows trigger timing setup for patient heart rates <100 bpm, and the next figure shows the setup for patient heart rates >100 bpm. For the faster heart rates the acquisition window should be increased to span nearly 2 complete cardiac cycles, the TR should be adjusted for

data acquisition to occur in late diastole of the second heart beat, and the trigger pulse should be set to 2 to cause the third heart beat to be completely skipped. This strategy results in the net repetition period being x3 cardiac cycles duration, and thus helps promote full T1 recovery of the tissues and optimal blood nulling.



16 Marfan syndrome, enlarged aortic root, MAGNETOM Verio. (Courtesy of Children's Mercy Hospital, Kansas City, USA.)

Clinical Case 1

Patient

- 17-year-old male

MR Indication

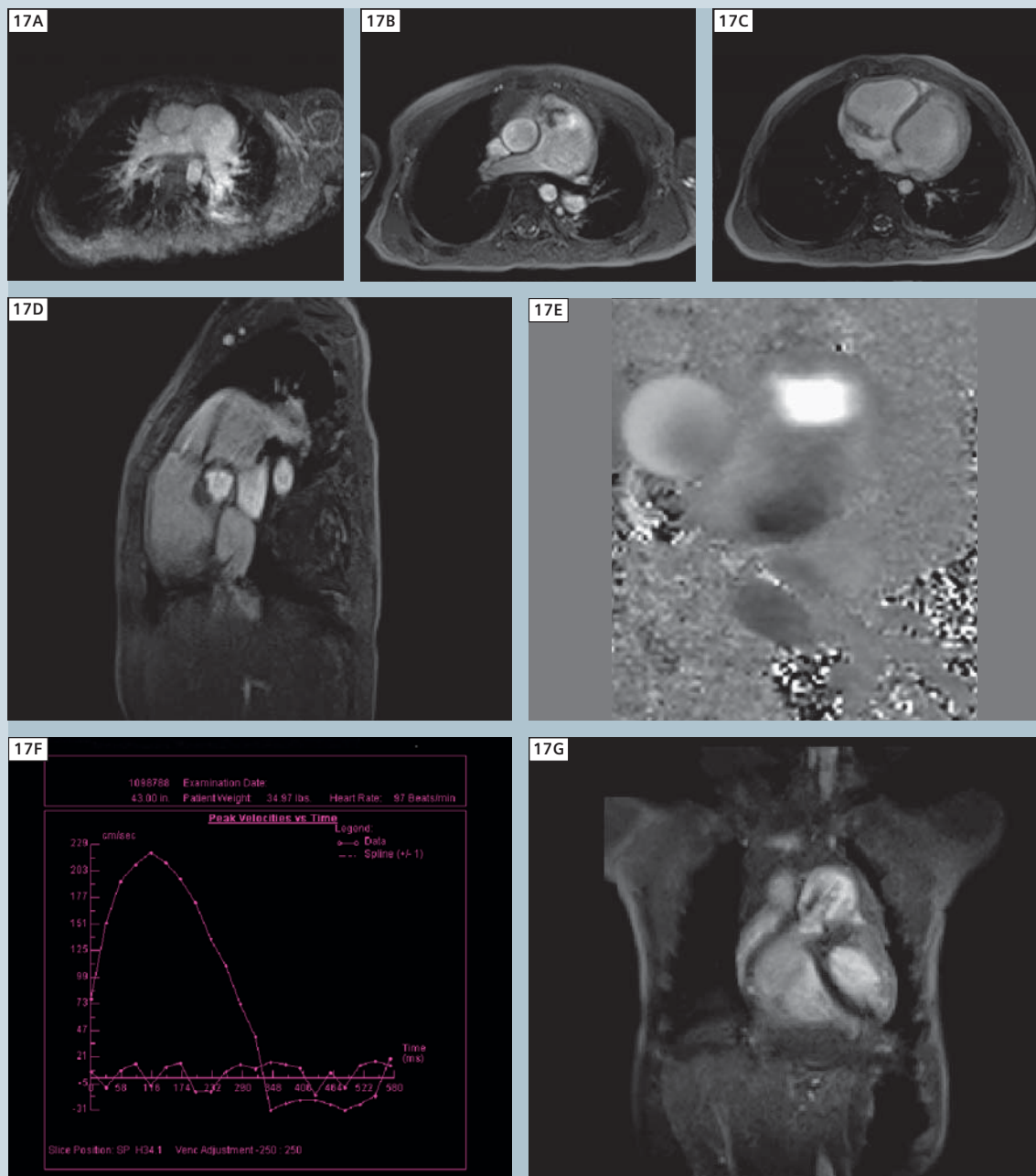
- Marfan syndrome

MR Techniques

- Dark-blood HASTE in transverse view
- Bright-blood single-shot TrueFISP in transverse view
- GRE cine in sagittal oblique view
- Phase-contrast flow in sagittal oblique view
- syngo* TWIST time-resolved MRA in sagittal view

MR Findings

- Enlarged aortic root



17 Dilated pulmonary artery, stenotic and thickened pulmonary valve, MAGNETOM Trio, A Tim System. (Courtesy of Methodist Healthcare System, San Antonio, USA.)

Clinical Case 2

Patient

- 3-year-old male

MR Indication

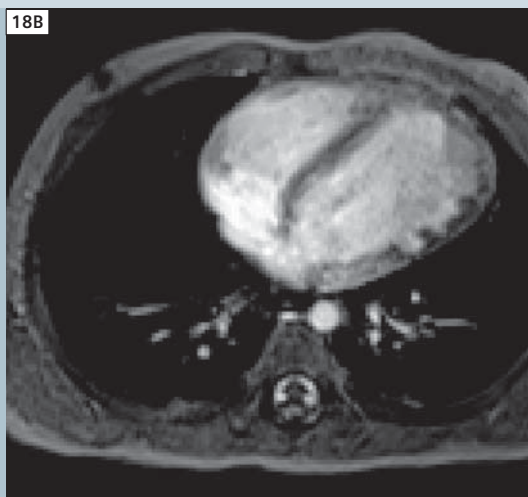
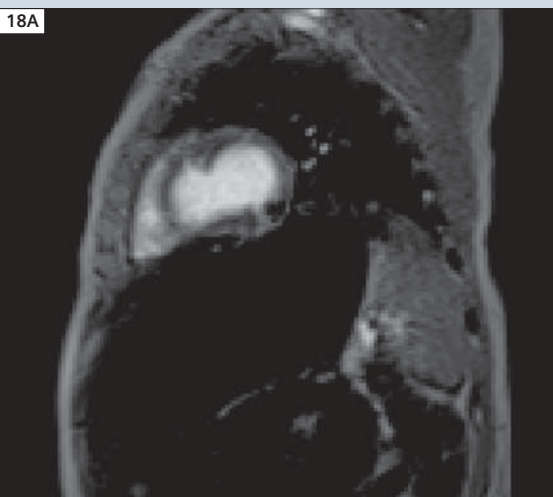
- Pulmonary valve stenosis

MR Techniques

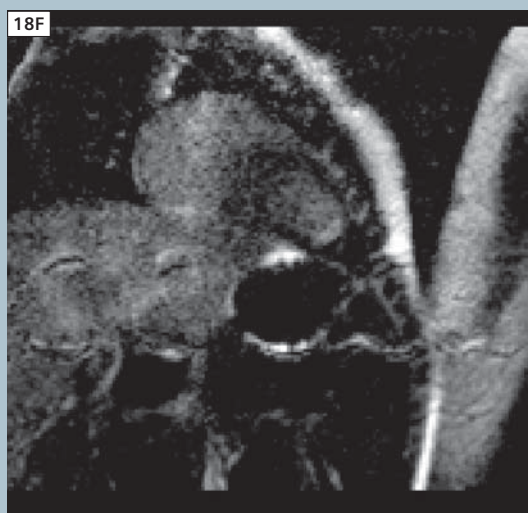
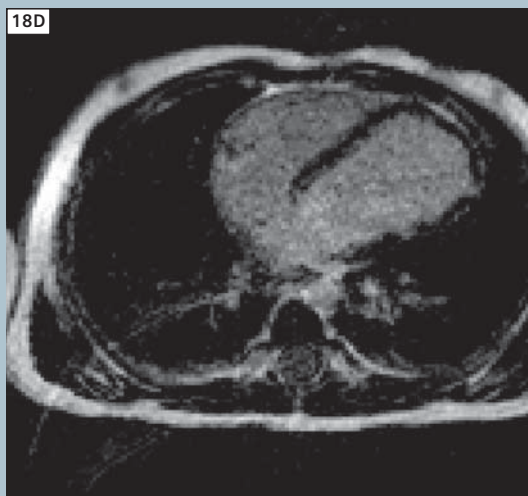
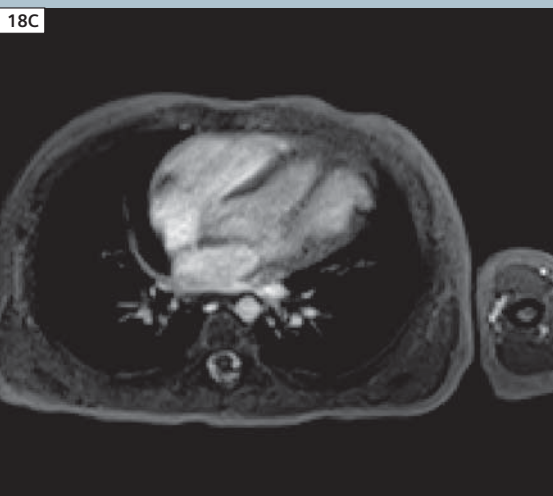
- Contrast MRA in transverse view
- GRE cine in sagittal, coronal, and transverse views
- Phase-contrast flow imaging in transverse view
- Argus flow analysis

MR Findings

- Severe pulmonary artery stenosis
- Dilated pulmonary artery
- Thickened pulmonary valve



18 Small focal scar in lateral apical LV wall, three small aneurysms in LV wall, MAGNETOM Trio, A Tim System. (Courtesy of Methodist Healthcare System, San Antonio, USA.)



Clinical Case 3

Patient

- 2-year-old* female

MR Indication

- Cardiac aneurysm

MR Techniques

- GRE cine in short axis and transverse views
- Segmented TurboFLASH delayed enhancement in short axis, long axis, and transverse views

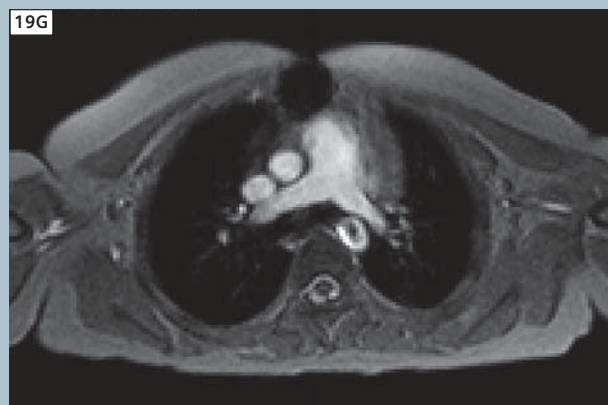
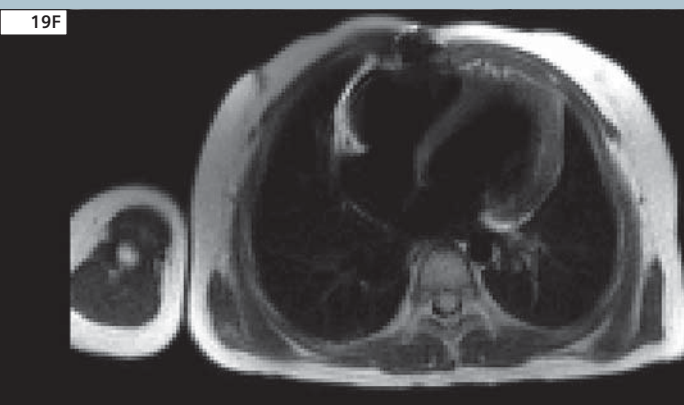
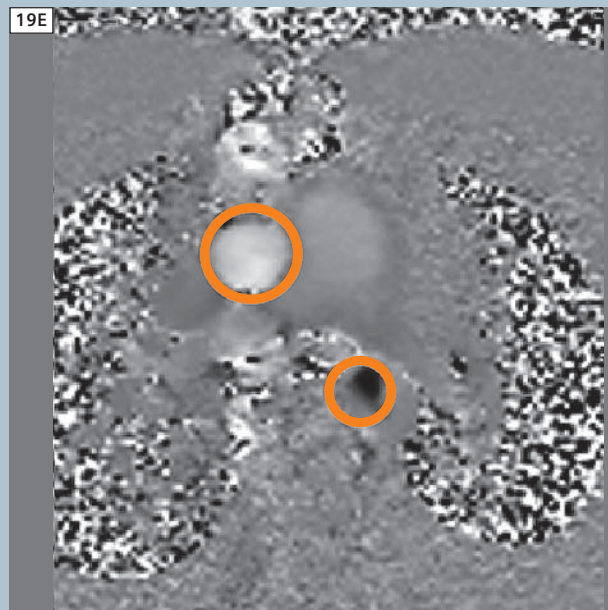
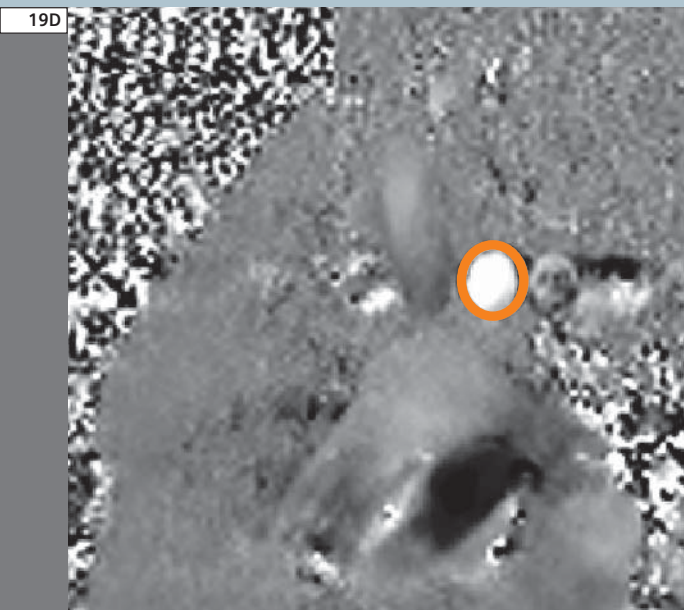
MR Findings

- Small focal scar in lateral apical LV wall
- Three small aneurysms in LV wall

*The safety of imaging fetuses/infants has not been established.



19 High velocities across coarctation of proximal descending aorta, occluded left subclavian artery with vertebral steal, enlarged central pulmonary arteries, MAGNETOM Trio, A Tim System. (Courtesy of Methodist Health-care System, San Antonio, USA.)



Clinical Case 4

Patient

- 4-year-old female

MR Indication

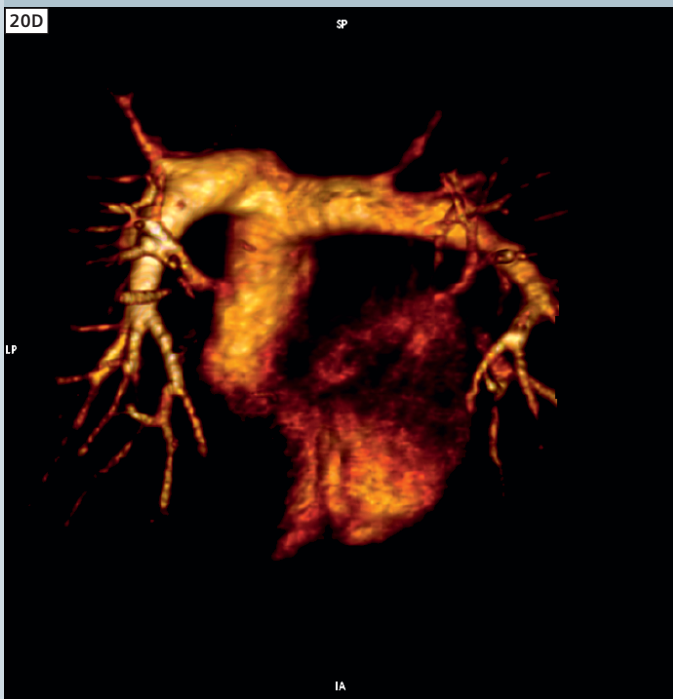
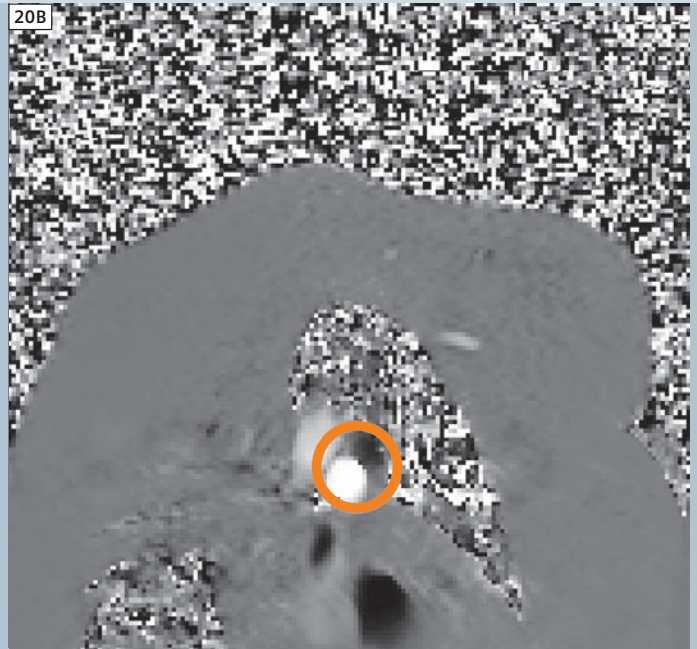
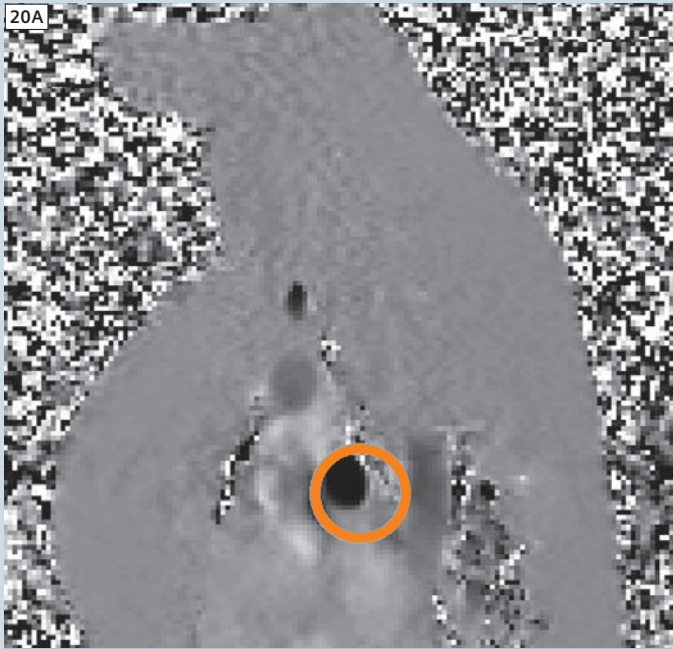
- Aortic Coarctation

MR Techniques

- Dark-blood HASTE in transverse and coronal views
- GRE cine in short axis, transverse, and sagittal oblique views
- Phase-contrast flow imaging in transverse and sagittal oblique views
- Contrast MRA in transverse and coronal views

MR Findings

- High velocities across re-coarctation of proximal descending aorta
- Occluded left subclavian artery with vertebral steal
- Enlarged central pulmonary arteries



20 Anomalous left upper pulmonary vein drains to left innominate vein, no evidence for obstruction or stenosis, MAGNETOM Trio, A Tim System. (Courtesy of Seattle Childrens Hospital, Seattle, USA.)

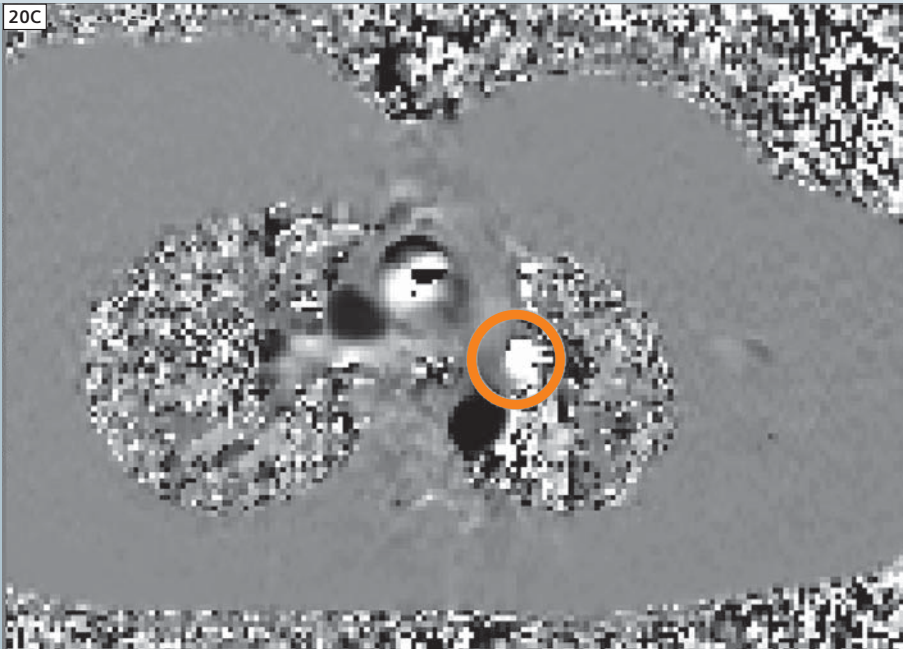


→ Visit
www.siemens.com/magnetom-world
 to download the Cardiovascular
 MR Imaging Smart Guide.

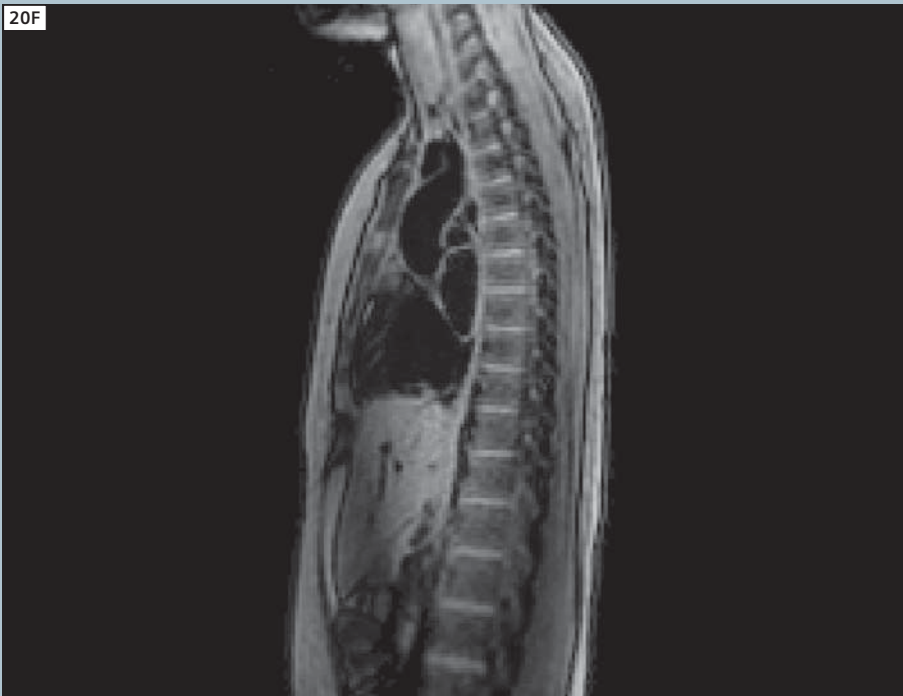


This brochure provides you with information about MR cardiac imaging with syngo MR. As a first step it explains the basics of the individual areas of MR cardiac imaging. This is followed by a practical part that shows parameter settings or descriptive examples of certain steps within the examination.

20C



20F



Clinical Case 5

Patient

- 13-year-old female

MR Indication

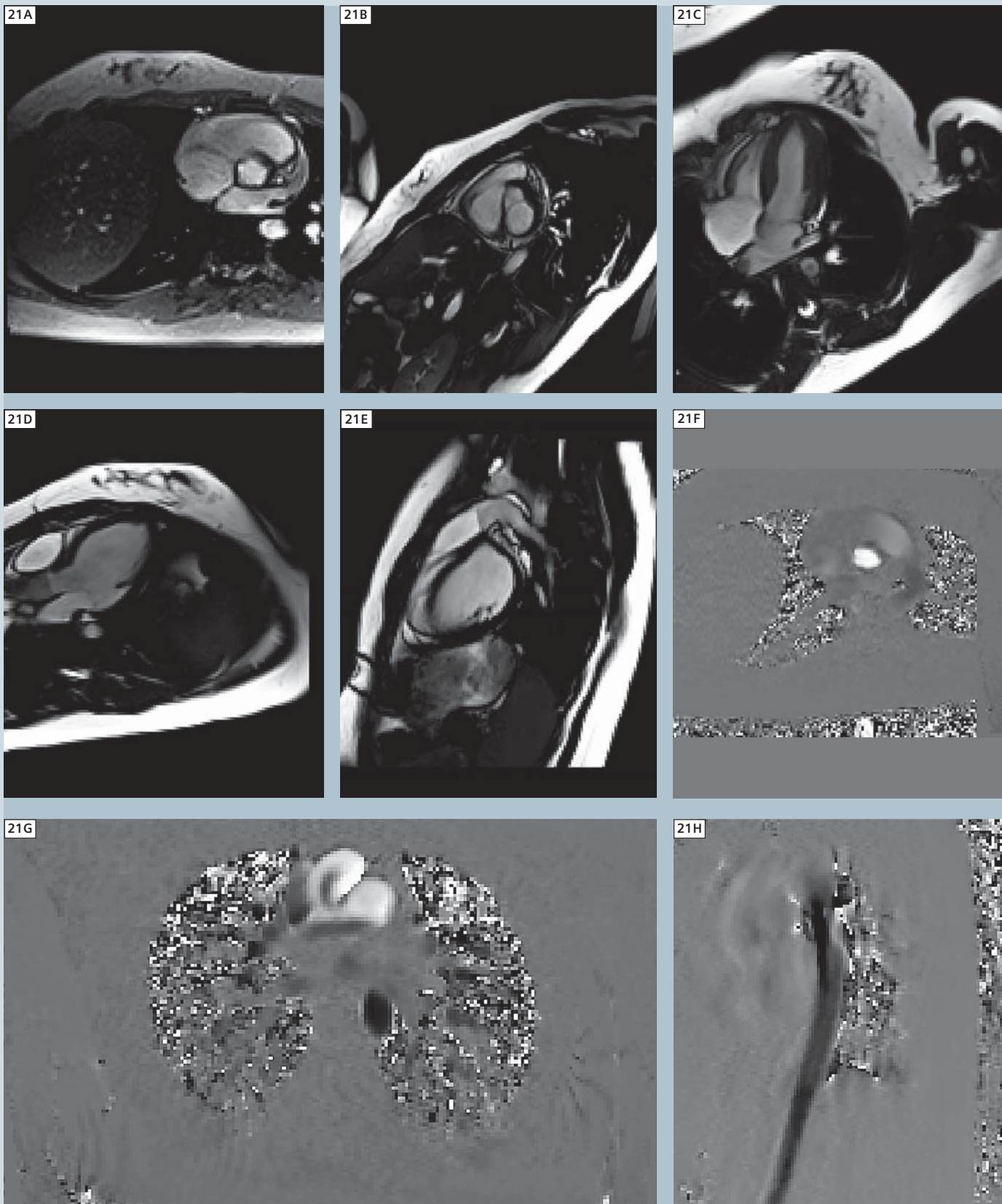
- Followup for congenital aortic stenosis and bicuspid aortic valve

MR Techniques

- Dark-blood TurboFLASH in sagittal, transverse and coronal views
- Phase-contrast flow imaging of pulmonary arteries and veins
- TWIST time-resolved MRA in coronal view

MR Findings

- Anomalous left upper pulmonary vein (LUPV) drains to left innominate vein
- LUPV drains 58% of left pulmonary artery (LPA) flow
- No evidence for obstruction or stenosis

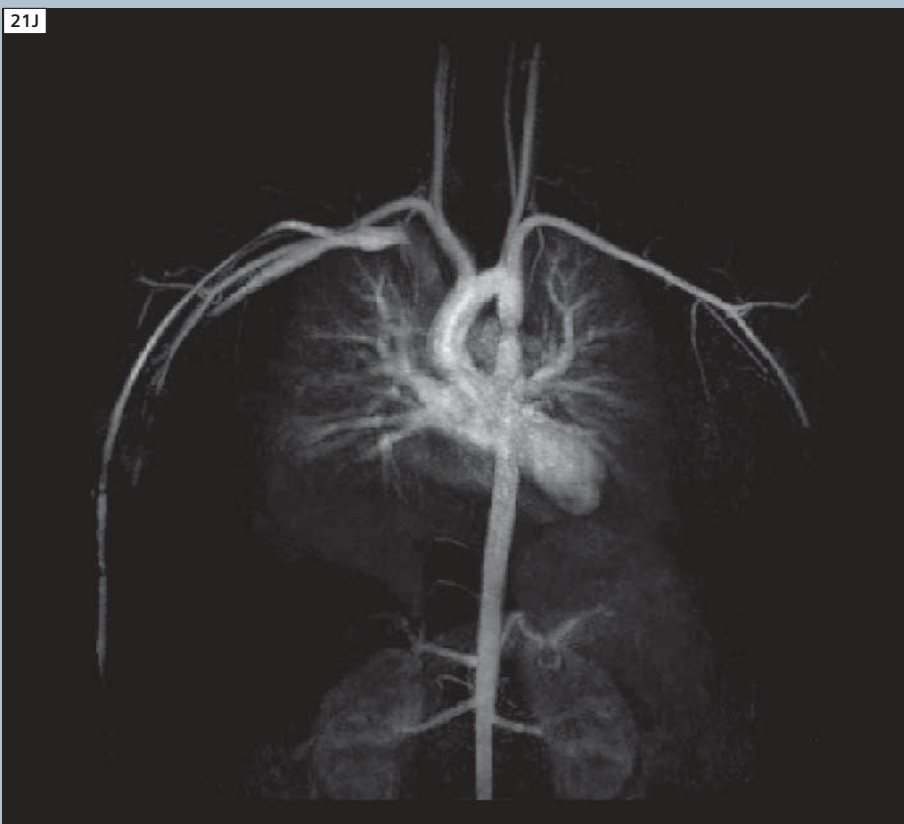


21 Mild stenosis at coarctation, no evidence of collaterals, bicuspid aortic valve, normal LV and RV size and function, MAGNETOM Trio, A Tim System. (Courtesy of Seattle Childrens Hospital, Seattle, USA.)

21I



21J



Clinical Case 6

Patient

- 16-year old female

MR Indication

- Aortic coarctation, aortic valve stenosis and insufficiency

MR Techniques

- GRE cine of aortic valve orifice and leaflets
- TrueFISP cine of LV and RV in all views
- Thru-plane flow imaging of ascending aorta and pulmonary artery
- In-plane flow imaging of coarctation in sagittal oblique view
- syngo TWIST time-resolved MRA in coronal view

MR Findings

- Mild to moderate residual stenosis at level of previous balloon angioplasty
- Peak velocity of 2.9 m/sec just distal to coarctation
- No evidence of collateral formation
- Bicuspid aortic valve with no evidence of significant stenosis or regurgitation
- Normal LV and RV size and function

Contact

Gary McNeal
 Clinical Application Specialist
 Siemens Medical Solutions USA, Inc.
 MR RD Cardiac Collab (NW & UCLA)
 2501 North Barrington Road, Suite 200
 Hoffman Estates, IL 60192-2061
 USA
gary.mcneal@siemens.com

Case Report:

Thoracic Spine Angiogram

Kirralie Lyford; Richard O'Sullivan, M.D.

Primary Health, The Epworth MRI Department, Richmond, Victoria, Australia

Patient history

A 71-year-old male presented to our department with a six month history of progressive myelopathy and also complained of persistent abdominal pain. MRI of the thoracic cord performed elsewhere, demonstrated cord oedema from T5 to T8/9 with prominent adjacent vessels, likely in the subarachnoid space. A CT angiogram had been performed with IV contrast and multiplanar reconstructions. A prominent leash of vessels in the mid and lower thoracic spinal cord extending from T6 to T10 consistent with distended views was reported. CT report stated that dural fistula is fed likely on the left from T6-7. It was reported that this feeding vessel would

better be demonstrated on MRA. With a spinal dural fistula suspected, the patient was referred to us for spinal MRA.

Sequence details

The images have been acquired on our 3T MAGNETOM Verio using software version syngo MR B15.

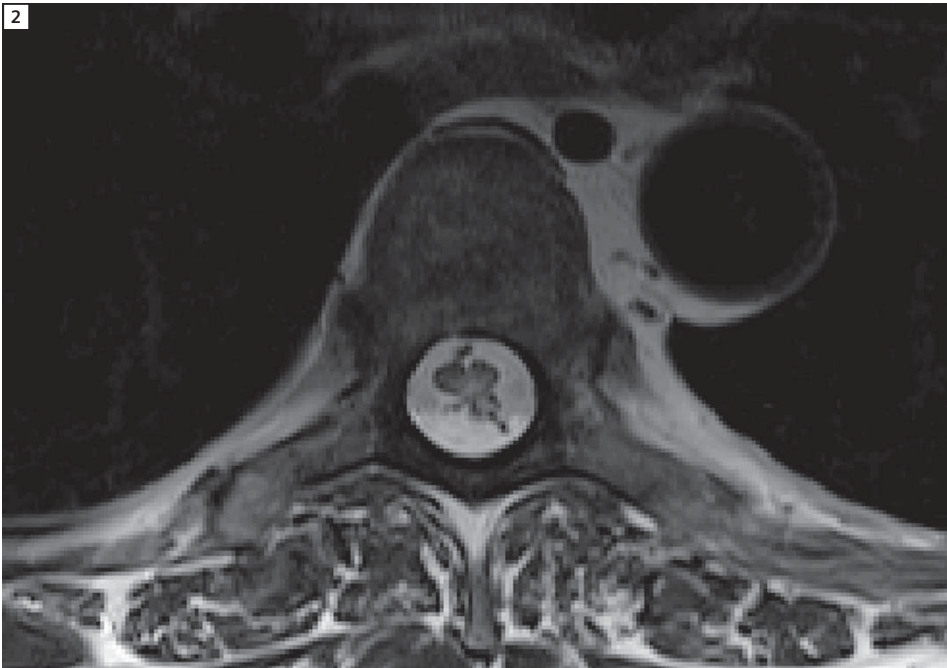
1. Sagittal T2-weighted Turbo Spin Echo (TSE) of the cervical and thoracic spine. This automatically (using Set-n-Go Protocol) inline composed to produce one long field-of-view (FOV) image. TR/TE = 4810/109, FOV of 280 x 2 = 560 mm (FOV phase 100%), 12 slices of 3.3 mm sagittal in the cervical and thoracic spine, distance factor 25%,

PAT factor 2, 1 concatenation, 1 average, base resolution of 512 and 448 respectively (phase resolution 70% for both), BW 238 Hz/pixel, turbo factor 21, echo spacing = 11.9 ms, no fat sat, TA = 2 min and 19 sec + 1 min 20 sec (3.39).

2. Axial T2-weighted TSE with no fat sat. TR/TE = 3210/87, FOV 240 mm (FOV phase 100%), 19 slices of 4 mm, distance factor 30%, PAT factor 0, 2 concatenations, 1 average, base resolution of 448 (phase resolution 70%), BW 248 Hz/pixel, turbo factor 21, echo spacing = 9.67 ms, TA = 2 min 3 sec.
3. Pre contrast-enhanced T1-weighted 3D-FLASH sagittal pulse sequence of the thoracic spine performed, which



1 Sagittal T2-weighted TSE sequence of the thoracic spine. Sagittal T2-weighted TSE of cervical and thoracic spine composed. Note cord oedema from T5 to T8/9 with prominent adjacent oedema.



2 Transverse T2-weighted TSE sequence of the thoracic spine. This confirmed cord oedema without cord expansion. No enhancing lesion was seen on post contrast examination.



3 Post contrast-enhanced MRA of the thoracic spine. T1-weighted 3D FLASH.

would allow subtraction to be performed. We did not find this necessary in this case.

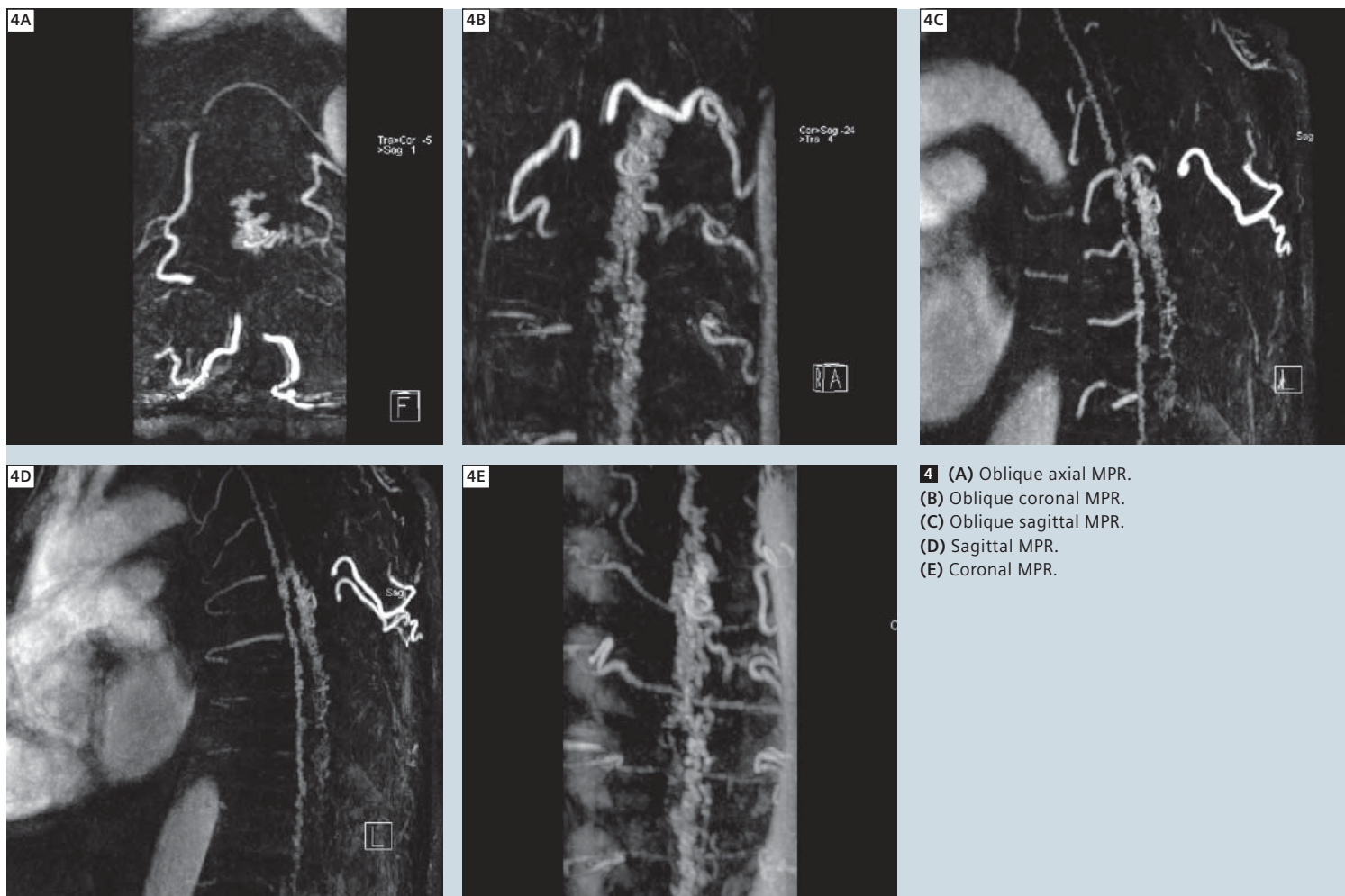
4. Test axial bolus. TR/TE = 62.59/1.63, FOV of 350 mm (FOV phase 100%), 1 slice 2D transverse 18 mm thick, distance factor 20%, PAT factor 0, 1 average, base resolution on 256 (phase resolution 75%), BW 400 Hz/pixel, TA = 1 min 30 sec. The IV bolus was performed as a slow infusion. Viewing this in mean curve application, the exact time of peak enhancement was measured, using time-intensity curve. There are multiple factors that may affect the circulation time, including the hemodynamic situation of the patient. Using the test bolus technique ensures correct timing of the MRA sequence.

5. Post contrast-enhanced (MRA) T1-weighted 3D FLASH sagittal pulse sequence of the thoracic spine. TR/TE = 3.21/1.2 ms, FOV of 250 mm (FOV phase 100%), 88 slices per slab (1 slab), slice thickness 0.9 mm, distance factor 20%, PAT factor 3, flip angle 25 degrees, no fat suppression, 1 average, base resolution of 256 (phase resolution 100%, slice resolution of 60%), phase partial Fourier 7/8, slice partial Fourier 6/8, BW 650 Hz/pixel, voxel size 1 x 1 x 0.9 mm, TA = 17 sec. This sequence can be repeated as many times as thought required. We found the first pass best to visualise the lesion, due to the slower infusion on contrast, and not the usual high concentration bolus technique. The IV bolus was performed as a slow infusion.

Additional Post contrast-enhanced sagittal TSE with fat sat, and axial VIBE scans were performed of the thoracic spine to exclude additional enhancing lesions. Post processing is required to visualise the number and level of the feeding vessels. This is achieved with multiplanar reformats (MPR) and maximum intensity projection (MIP) images.

Results

Diffuse cord oedema is seen extending from T6-T9 secondary to dural fistula supplied via the left T6-7 intervertebral foramen. No mass lesion is seen. There is no enhancement within the cord. This examination was a combination of standard thoracic spine imaging and spinal cord MR angiography to detect and localize arterial feeders of this vascular lesion.



4 (A) Oblique axial MPR.
(B) Oblique coronal MPR.
(C) Oblique sagittal MPR.
(D) Sagittal MPR.
(E) Coronal MPR.

Identification of the vascular supply of both spinal cord and adjacent arteries and veins is difficult. Displaying these small structures, due to their low-to-moderate contrast relative to the surrounding tissue, requires high resolution and correct timing of contrast MRA sequence. Multi-planar reformatting (MPR) and maximum intensity projection (MIP) post processing is essential to display the relevant anatomy. Subtraction pre MRA from post contrast-enhanced sequences may also be required. There is no significant patient preparation requirement to perform this study. The patient was pre cannulated with a 20 gauge needle and connected to the injection pump. He was positioned supine on our standard 24-channel spine

matrix coil, with the anterior half of the 32-channel cardiac coil placed over the abdominal area. The use of the Tim (Total imaging matrix) system allowed us to image the entire spine in a matter of minutes and without limiting us to the thoracic region only.

Conclusion

The contrast enhanced MRA confirmed the level of the fistula and established it was fed only from the left. Post processing visualises both vessels and determines that only the left connects with the fistula with no supply coming from the right. This then allowed the interventional radiologist to perform a much simplified embolisation procedure. Reduction of the complexity of the DSA

procedure is beneficial to the patient, as previously each spinal artery would have had to be individually cannulated and imaged bilaterally. DSA confirmed the MRI findings, and a successful single level super-selective spinal procedure was achieved.

Contact

Kirralie Lyford
3T Supervisor
MRI Department
The Epworth Hospital
89 Bridge Road
Richmond, Victoria 3121
Australia
Tel. + 61 3 92424800
Kirralie.lyford@sybionhealth.com

Case Report:

Multiple Haemangiomas

Noelene Bergen; Nick Ferris, M.D.

Peter MacCallum Cancer Centre, Department of Diagnostic Radiology, Melbourne, Australia

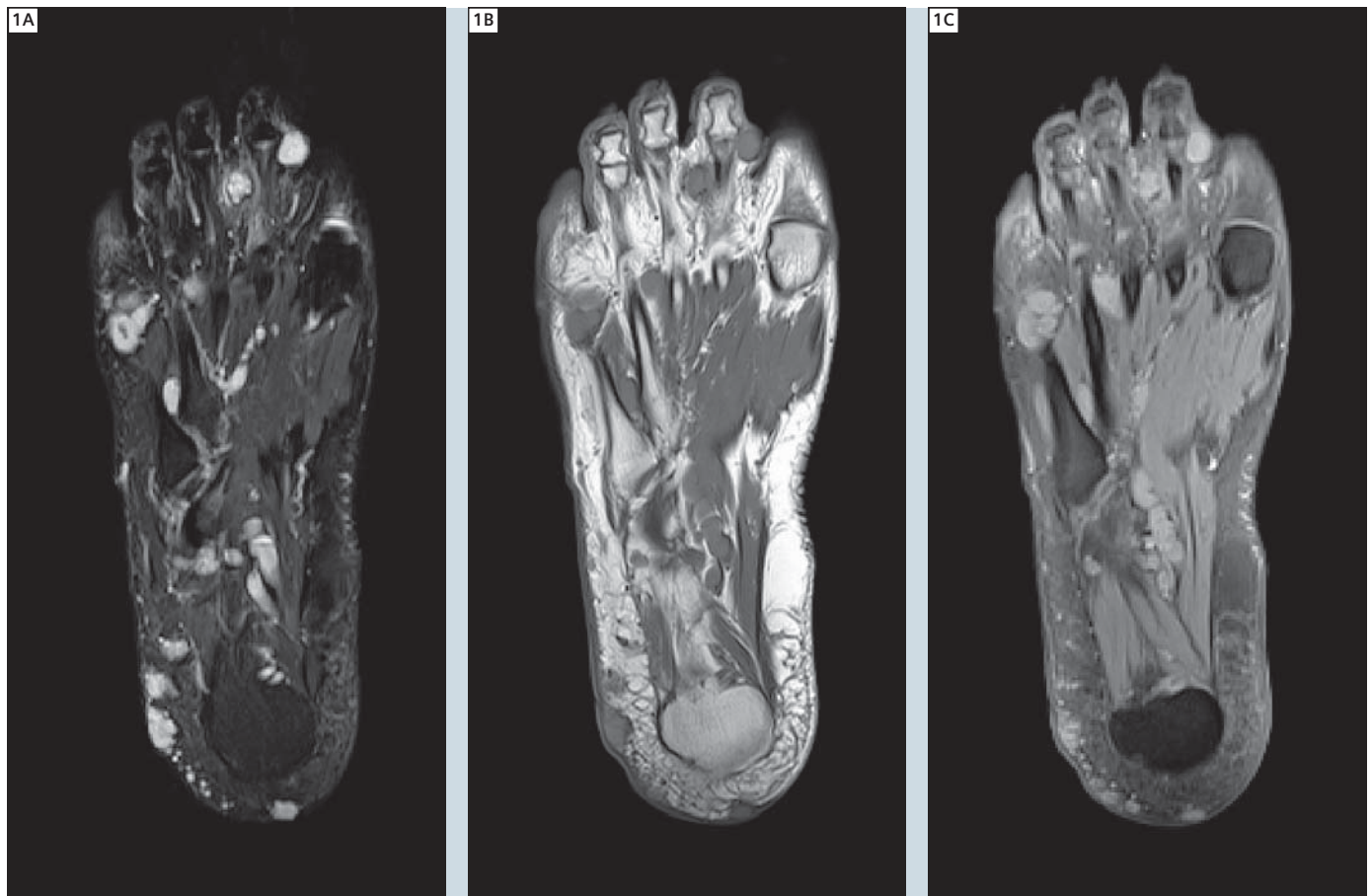
Patient history

A young female presented for follow up scans of her right foot and ankle. This patient has multiple haemangiomas in her right lower limb; these have been monitored clinically for several years. The lesion under her R second toe had become progressively more swollen and painful. The MRI scan was requested to investi-

gate the rate of change of the lesions and assess their relationship to other anatomical structures. The scan will serve as a baseline for later comparisons after radiation or possibly anti-angiogenic drug treatment. There is no guarantee that even with amputation, further lesions will not develop elsewhere in the limb.

Sequence details

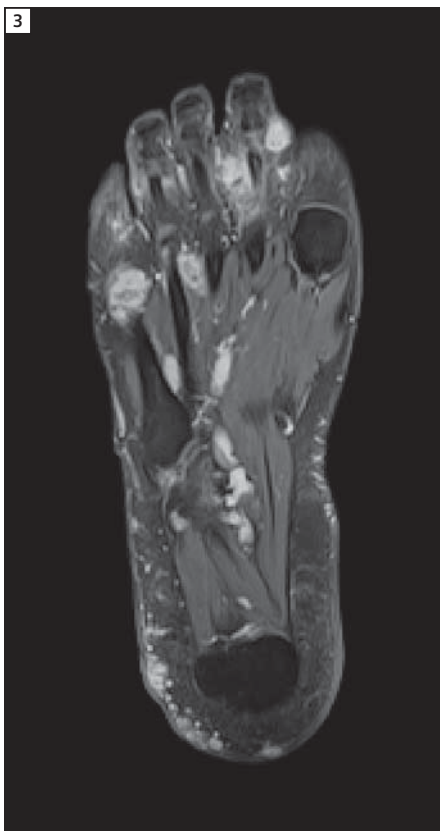
The examination was performed with a Siemens 3T MAGNETOM Trio, A Tim System. Axial STIR, T1, and T1 fat sat were performed on the right foot. The STIR imaging was acquired with a TI of 210, TR 7700 and TE 38. The total time for the acquisition was 2:50 min at a resolution of 384 x 307 and a FOV of 280 x 280.



1 Axial STIR (A), T1-weighted (B) and T1-weighted with fat saturation (C) of the right foot.



2 MIP of post contrast *syngo* TWIST MRA of the right foot; time resolution was 3 seconds. Images acquired (A) 35 s, (B) 44 s and (C) 150 s after start of contrast media administration.



3 Axial contrast-enhanced T1-weighted MRI with fat saturation.

The T1 imaging was acquired with a TR of 695 and TE of 11. The total time was 3:09 min with a resolution of 448 x 358 and FOV of 280 x 280. The fat saturation applied was relatively weak. Post contrast *syngo* TWIST MR Angiography (MRA) of the right foot was performed. Images were taken every 3 seconds to view the temporal enhancement of the lesions. 120 images per acquisition were taken in the sagittal plane with a FOV of 255 x 320 and at a resolution of 320 x 130. Post contrast T1 was performed with the same parameters as the pre-contrast fat sat T1.

Image findings

Structurally, most of the haemangiomata demonstrated no discernible change since the previous MRI. The largest lesions were in the subcutaneous tissue lateral to the calcaneum, just above the distal 5th metatarsal, and immediately below the distal foot metatarsal. There was no evidence of any developing soft tissue mass associated with the haemangiomata to suggest an aggressive component, and there was no focal bony lesion.

On the post-contrast dynamic acquisition MRA, the more prominent subcutaneous lesions along the lateral aspect of the distal/hind foot demonstrated relatively earlier enhancement than the other lesions. This indicates higher blood flow and suggests that these are the more active lesions.

While most of the lesions demonstrated no discernible change since the previous MRI, the lesion along the medial aspect of the second toe did demonstrate moderate enlargement.

Contact

Noelene Bergen
Department of Diagnostic Radiology
Peter MacCallum Cancer Center
St. Andrew's Place
East Melbourne, Victoria 3002
Australia
noelene.bergen@petermac.org

Imaging of the Carotid Atherosclerotic Plaque with 3T MRI Using dedicated 4-Channel Surface Coils

T. Saam, M.D.; M. F. Reiser, M.D.; K. Nikolaou, M.D.

Dept. of Clinical Radiology, University of Munich, Grosshadern Campus, Munich, Germany

Introduction

Complications of cardiovascular disease, including stroke, myocardial infarction and sudden cardiac death, are the most common cause of death in the world [1]. Atherosclerotic disease accounts for approximately 25% of ischemic strokes and for the majority of myocardial infarctions and sudden cardiac deaths. Despite major advances in treatment of atherosclerosis, a larger percentage of victims of the disease who are apparently healthy die without prior symptoms [2]. The challenge for screening modalities and diagnostic methods is to identify high risk patients with lesions that are vulnerable to thrombosis, so called "vulnerable plaques", before the event occurs. To tailor and improve treatment strategies, these screening and diagnostic methods must be able to determine the patient-specific risk of suffering a cardiovascular event. "Vulnerable Plaques" are atherosclerotic plaques which have a high likelihood to cause thrombotic complications, such as myocardial infarction or stroke. Plaques which tend to progress rapidly are also considered to be "vulnerable". Besides luminal stenosis, plaque composition and morphology are key determinants of a plaque's vulnerability to cause cardiovascular events. A classification for clinical as well as pathological evaluation of vulnerable plaques was recently put forward, which proposed 5 major and 5 minor criteria to define vulnerable plaques [3, 4]. These plaque features

were based on studies of coronary arteries and included thin caps with large lipid/necrotic core, active inflammation, fissured plaque, stenosis > 90%, endothelial denudation with or without superficial platelet aggregation and fibrin deposition, endothelial dysfunction, calcified nodules, intraplaque hemorrhage, glistening yellow plaques (on angiography), and outward remodeling.

Magnetic resonance imaging (MRI) has unique potential to identify the key features of the vulnerable plaque [5]. MRI is well suited for this role because it is non-invasive, does not involve ionizing radiation, enables the visualization of the vessel lumen and wall and can be repeated serially to track progression or regression. Furthermore, recent in vivo MRI studies have shown that MRI allows evaluation of compositional and morphological features of atherosclerotic plaques [6–9]. However, most of this carotid MRI studies were done using 1.5T MRI scanners. Disadvantages of previous carotid MRI studies [6, 10, 11] at 1.5T were relatively long scan times of up to 45 minutes and a relatively high number of excluded subjects due to insufficient image quality in 5–20% of the subjects. Furthermore, the spatial resolution of 0.6 x 0.6 mm (0.3 x 0.3 mm² using interpolation techniques) typically used for 1.5T MRI studies might not be able to identify very small features of the atherosclerotic plaque, such as the fibrous cap. This article will give insight into the

hardware requirements and MRI protocols currently used at 3T MRI studies, will provide an overview of the literature of recently published 1.5T carotid MRI studies and will discuss the potential role of 3T MRI in identifying the key features of the vulnerable carotid atherosclerotic plaque.

Carotid Surface Coils

MR phased-array surface coil techniques have been used in all vascular beds and have been proven to be effective in improving the signal-to-noise (SNR) ratio in carotid arteries [12]. The carotid arteries are relatively large, superficial and stationary vessels and therefore well suited for high-resolution MR imaging with a phased-array coil assembly consisting of several adjacent small surface coils that collect data simultaneously. Hayes et al. developed a 1.5T MRI phased-array coil for carotid arteries which has an effective longitudinal coverage of up to 5 cm and which improves SNR 37% when compared to a commercially available 3-inch surface coil [12]. The 3T carotid surface coil used at our institution is a dedicated four-channel surface coil (Machnet, Netherlands) which can be used in combination with head and body coils. This allows us to combine the assessment of carotid plaque morphology and composition with an MR angiography of the supraaortic vessels and / or with a brain MRI.

MRI protocol

Thus far, a variety of MRI protocols have been used to assess the carotid wall. While some of the proposed image acquisition techniques rely on one [13] or two [14–16] MR sequences, others are based on multiple contrast-weighted images [6, 17, 18]. The number and type of sequences used depends upon which plaque characteristics are to be studied. For instance, rapid assessment of overall plaque burden is feasible using one or two MR sequences [19, 20]. However, to evaluate plaque composition and morphology in one imaging session, most studies rely on multiple MR sequences. Black-blood T1-, PD- and T2-weighted images with fat and flow suppression enable the visualization of the full vessel wall and are needed to characterize the major plaque components, such as lipid/necrotic core, calcification and loose fibrous matrix [6]. Bright-blood time-of-

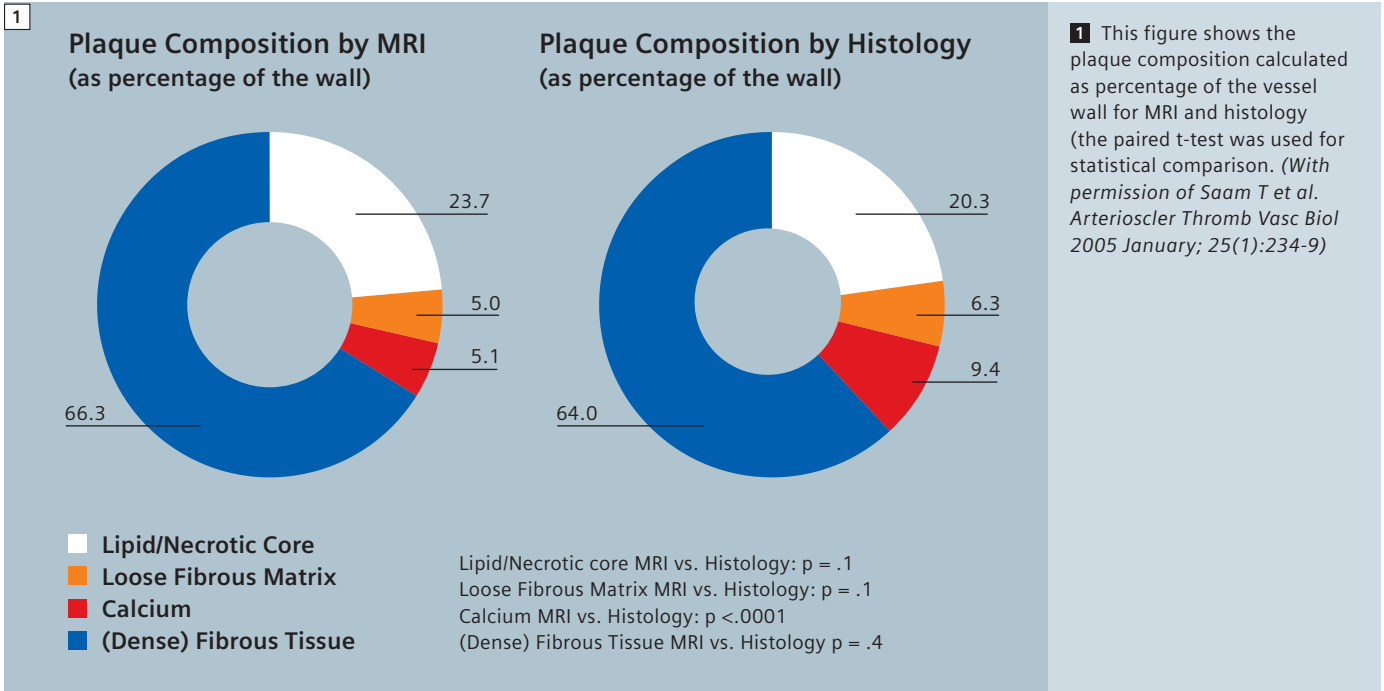
flight (TOF) images are needed to evaluate the status of the fibrous cap [21, 22] and to identify calcified nodules. Other sequences, such as contrast-enhanced (GD-DPTA) T1-weighted images and dynamic contrast-enhanced 2D spoiled-gradient-recalled-echo-weighted images are useful to quantify lipid/necrotic core size and to evaluate plaque inflammation [23–25]. Furthermore, the use of sophisticated contrast agents, such as USPIOs [26], fibrin [27, 28] – and alpha(v)beta3-integrin [29] – targeted nano-particles offers the promise of in vivo targeted imaging of the plaque. We currently use a multi-sequence protocol with dynamic contrast enhanced sequences at our 3T MRI scanner which allows to evaluating plaque composition and morphology and provides perfusion data which can be used to assess plaque inflammation in less than 23 minutes (see Table 1, TOF, pre-contrast T1, PD

and T2, post-contrast T1 and dynamic contrast enhanced sequences (DCES); best-in-plane resolution 0.5 x 0.5 mm² [0.25 x 0.25 mm² interpolated]). Parallel imaging is used for all sequences with an acceleration factor (PAT) of 2 for T1-, TOF-, PD and T2-weighted images and a PAT factor of 4 for DCES images. Imaging time for TOF, T1, PD, T2 and DCES images is 4:11, 4:38, 2:08, 2:08 and 5:00 minutes, respectively, resulting in a total scan time of 22:43 minutes. Fat suppression is used for pre- and post contrast T1W, PDW, and T2W images to reduce signals from subcutaneous and perivascular fat. Each scan covers 30 mm (2 mm thickness x 15 matched images across the 5 sequences). This coverage is usually sufficient to image the complete carotid atherosclerotic plaque.

Table 1: Multi-Sequence 3.0T MRI Protocol

	T1W	PDW	T2W	TOF	DCE*
Sequence	2D-TSE	2D-TSE	2D-TSE	3D-GRE	2D-SR-SGRE
Fat Suppression	Yes	Yes	Yes	Yes	No
TR / ms	800	3000	3000	21	307
TE / ms	12	13	65	3,96	1,72
PAT factor	2	2	2	2	4
ETL	11	13	13	n.a.	n.a.
Flip Angle / °	180	180	180	25	15
Averages	2	2	2	1	3
FOV / mm	160 x 120	160 x 120	160 x 120	160 x 120	160 x 130
Matrix	240 x 320	240 x 320	240 x 320	240 x 320	256 x 208
Number of Slices	15	21	21	52	2
Slice thickness / mm	2	2	2	1	3,5
Pixel size / mm² (Interpolated)	0,5 x 0,5 (0,25 x 0,25)	0,5 x 0,5 (0,25 x 0,25)	0,5 x 0,5 (0,25 x 0,25)	0,5 x 0,5 (0,25 x 0,25)	0,625 x 0,625
Scan Time / min	4:38	2:08	2:08	4:11	5:13
Flow Suppression	DIR	Inflow Suppression (Arteries and Veins)	Inflow Suppression (Arteries and Veins)	Inflow Suppression	None

*TI = 159 ms; D = Dimensional; TSE = Turbo Spin Echo; SR-SGRE = Saturation-Recovery



MRI validation studies

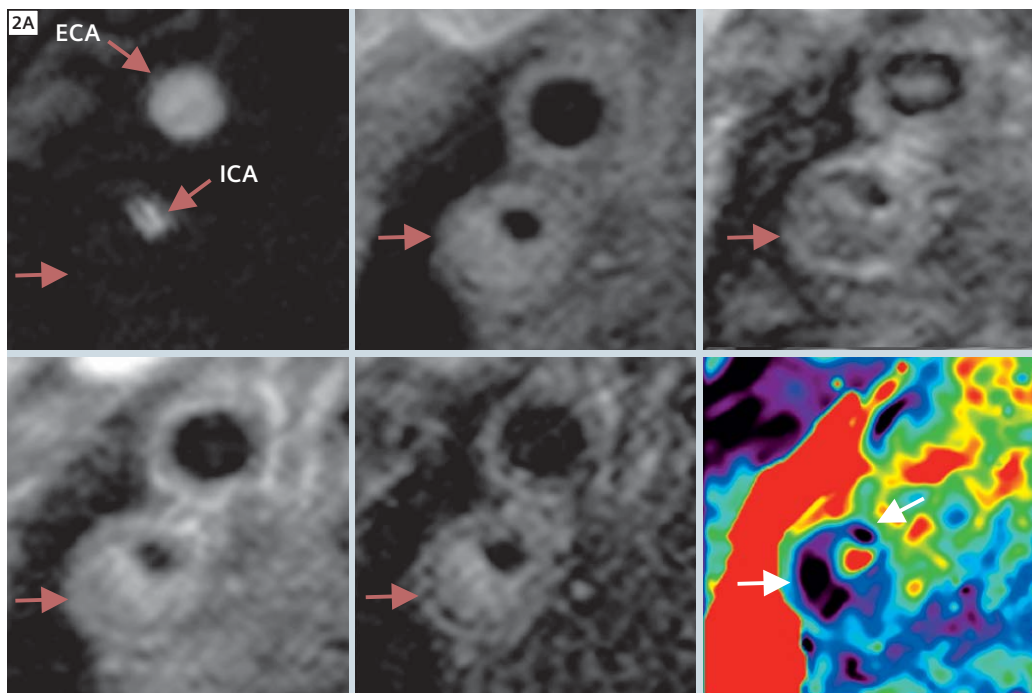
One of the advantages of carotid in vivo MRI studies is the possibility of histopathological validation using carotid endarterectomy specimen. Several groups have proven [7–9, 13, 30], that in vivo carotid MRI is able to depict all major plaque components, including the lipid/necrotic core, through unique combinations of signal intensity of each component in different contrast weightings. Furthermore MRI is able to quantify the major components of carotid atherosclerotic plaques with good correlation to histology [6]. MRI measurements of plaque composition were statistically equivalent to those of histology (Fig. 1) for the lipid-rich/necrotic core (23.7 vs. 20.3%; $p = 0.1$), loose fibrous matrix (5.1 vs. 6.3%; $p = 0.1$) and dense (fibrous) tissue (66.3 vs. 64.0%; $p = 0.4$). Calcification differed significantly when measured as a percentage of wall area (9.4 vs. 5.0%; $p < 0.001$), but not in absolute area (2.7 vs. 3.5 mm²; $p = 0.1$). Other studies have demonstrated that MRI is able to determine the presence, the age and the location of plaque hemorrhages [31–33]. Furthermore, MRI is able to identify the fibrous cap, a layer of con-

nective tissue which is covering the lipid-rich/necrotic core. Lesions with large lipid/necrotic cores and thin, fibrous caps are considered to be most likely to rupture. There are several imaging approaches for MR imaging of the fibrous cap. Hatsukami et al. [21] reported the use of a 3D-TOF bright blood imaging technique (multiple overlapping thin slab angiography, or MOTSA) to identify ruptured fibrous caps in atherosclerotic human carotid arteries in vivo. Trivedi et al. [9] used a short tau inversion-recovery (STIR) to quantify the fibrous cap and lipid/necrotic core of 25 recently symptomatic patients and showed good agreement between MRI and histology. Cai et al. [24] used T1 and contrast-enhanced-T1-weighted images to measure the intact fibrous cap. The authors showed good correlation between carotid MRI and the excised histology specimen for maximal thickness ($r = 0.78$, $p < 0.001$), length ($r = 0.73$, $p < 0.001$) and area ($r = 0.90$, $p < 0.001$) of intact fibrous cap. In our opinion the combination of pre- and post contrast T1, TOF, PD and T2-weighted images has the highest potential to identify the fibrous cap and to differentiate between thick, thin and ruptured fibrous cap. Figures 2A–C

show 3T MR images of an intact fibrous cap that is thick (Fig. 2A), an intact but rather thin fibrous cap (Fig. 2B) and a ruptured fibrous cap (Fig. 2C). The differentiation between intact-thick, intact-thin and ruptured fibrous caps is important, as a prospective 1.5T MR study [34] has shown that the presence of a thin or a ruptured fibrous cap at baseline is associated with an increased risk of suffering an ischemic cerebrovascular event during follow-up (hazard ratio, 9.4; 95% CI, 2.1–42.1; $P < 0.001$). The same study found that plaques with intraplaque hemorrhage (hazard ratio, 4.7; 95% CI, 1.6–14.0; $P = 0.004$), larger maximum % lipid/necrotic core (hazard ratio for 10% increase, 1.4; 95% CI, 1.1–1.9; $P = 0.01$), and maximum wall thickness (hazard ratio for a 1 mm increase, 1.6; 95% CI, 1.1–2.1; $p = 0.007$) were associated with occurrence of cerebrovascular events.

1.5T versus 3T MRI

Most imaging of the vessel wall by MRI has been performed at 1.5T scanners. Recently, 3T scanners and their resulting high resolution images have opened the field of vascular imaging to new potentials. These new scanners increase reso-



2A Figure 2A shows MR images of a 74-year-old asymptomatic patient with a 90% carotid stenosis in his right internal carotid artery (ICA; ECA = external carotid artery). Cross-sectional MR images show a large eccentric plaque in the right ICA with a large necrotic core without intraplaque hemorrhage (arrow), which is covered by a thick layer of dense and loose fibrous tissue, which can be depicted on T1w-, PD- and T2w- images as a compared to the inner of the plaque moderately hyperintense area near the lumen surface. Extraction flow images show an absence of flow within the lipid/necrotic core (dark area, arrow) and an increased extraction flow in the shoulder of the plaque, indicative of an area of loose fibrous tissue.

lution and image quality. A recent study showed that wall SNR and lumen/wall CNR significantly increased ($P < 0.001$) at 3T with a 1.5-fold gain for T1-weighted images and a 1.7/1.8-fold gain for PD-/T2-weighted images compared to 1.5T. Quantitative plaque measurements of lumen and wall areas demonstrated good agreement between 1.5 and 3T MRI with no significant bias ($P = 0.5$), a coefficient of variation (CV) of $< 10\%$, and intraclass correlation coefficient (ICC) of > 0.95 . Another recent study [35] showed signal gains at 3.0T relative to 1.5T for carotid artery wall SNR of 223% and wall-lumen CNR of 255% in all sequences ($P < 0.025$). T1-weighted (T1W) inflow/outflow saturation band (IOSB) and rapid extended coverage double inversion-recovery (REX-DIR) were found to have different levels of SNR and CNR ($P < 0.05$) with IOSB values observed to be larger. While these variations can be resultant of different coil designs, pulse sequences, and contrast weightings, even the most conservative estimates (1.4–1.6 times) provide high potential for improved image resolution and/or shorter scan time. Compared to

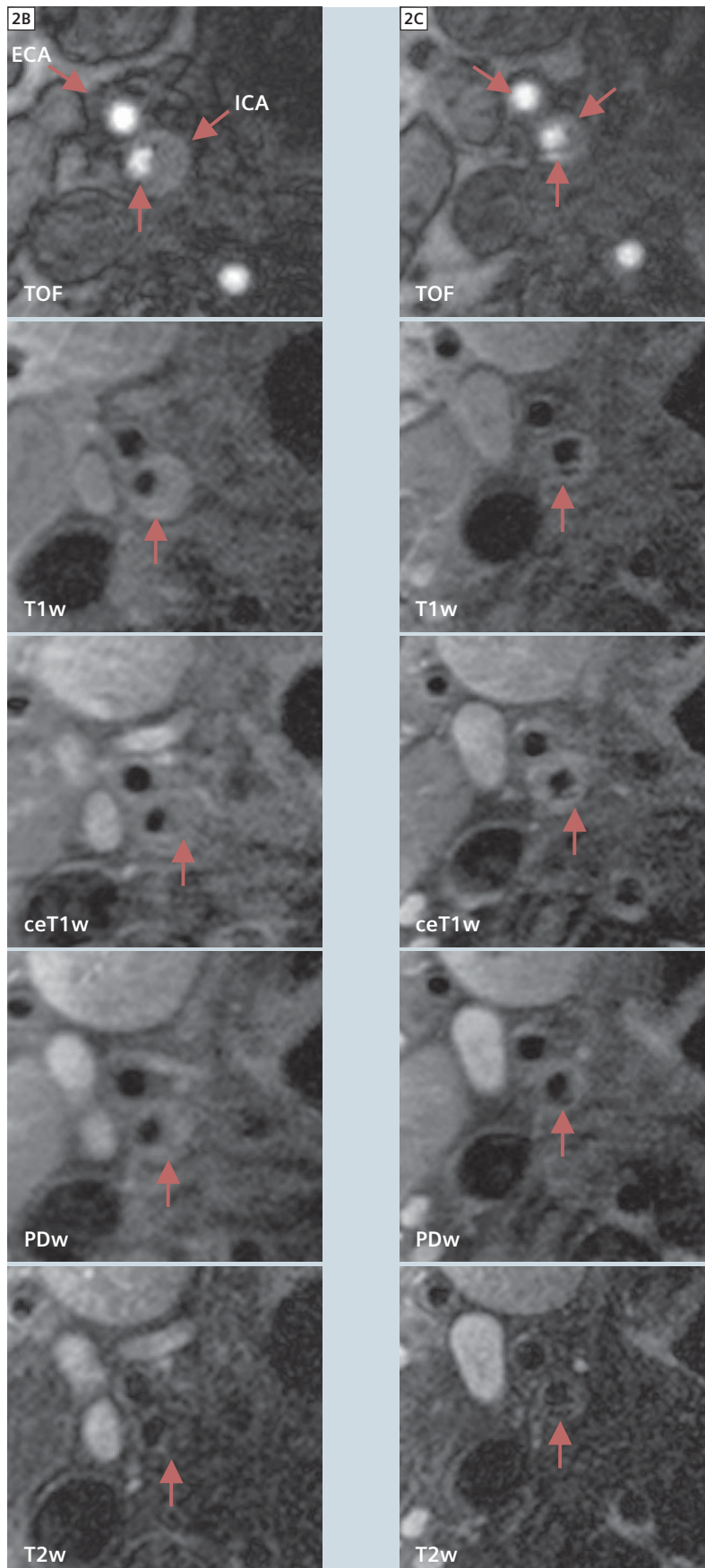
protocols previously used at 1.5T MRI [36] the protocol which we use at our institution has a larger longitudinal coverage (+ 25%), a smaller pixel size (- 31%) and a shorter scan time, which decreased from 28:30 minutes to 22:43 minutes (17:43 minutes without DCE). Currently the percentage of non-diagnostic scans is approximately 2%, which is substantially smaller than the number of excluded scans in previous 1.5T MRI studies [10, 11], where the number of excluded exams ranged from 5–20%.

A study by Underhill et al. [37] compared the interpretation and quantification of carotid vessel wall morphology and plaque composition at 1.5T with those at 3.0T MRI in 20 subjects with 16%–79% carotid stenosis at duplex ultrasonography. There was a strong level of agreement between field strengths for all morphologic variables, with intraclass correlation coefficients ranging from 0.88 to 0.96. Agreement in the identification of presence or absence of plaque components was very good for calcification ($\kappa = 0.72$), lipid/necrotic core ($\kappa = 0.73$), and hemorrhage ($\kappa = 0.66$). However, the visualiza-

tion of hemorrhage was greater at 1.5T than at 3.0T (14.7% vs. 7.8%, $P < .001$) and calcifications measured significantly ($P = .03$) larger at 3.0T. The authors concluded that at higher field strengths, the increased susceptibility of calcification and paramagnetic ferric iron in hemorrhage may alter quantification and/or detection. Nevertheless, imaging criteria at 1.5T for carotid vessel wall interpretation are applicable at 3.0T.

Outlook

Initial experience suggests that imaging of the carotid arterial wall on a 3.0T scanner with dedicated surface coils has a number of advantages, including shorter overall imaging time, higher spatial resolution, larger volume coverage, and improved overall image quality as compared to 1.5T carotid plaque imaging. In our opinion, carotid black-blood multi-echo-sequence 3.0T MRI with parallel imaging is a fast, reproducible and robust method to assess carotid atherosclerotic plaque in vivo. Thus, this method seems to be ready to be used in clinical practice.



2B, C Figures 2B and C show MR images of the right internal carotid artery of a 78-year-old patient with a right-hemispheric stroke ipsilateral to a 60% carotid stenosis 4 days before the MRI scan.

Figure 2B shows a large eccentric plaque in the left internal carotid artery (ICA) with a large lipid/necrotic core with hemorrhage, which has a high signal intensity on TOF- and pre-contrast T1w images and moderate to low signal intensity on PDw and T2w images and does not enhance on the post contrast T1w images (arrow). The surface of the plaque is smooth, suggesting that the fibrous cap is intact. However, the fibrous cap cannot be differentiated from the lipid/necrotic core and is therefore classified as a thin fibrous cap by MRI criteria.

Figure 2C shows MR images of the same patient 4 mm distally in the ICA. At this location the surface of the plaque appears irregular and TOF images show a very bright area posterior to the lumen of the ICA, corresponding to a hypointense area in all other sequences, suggestive of a ruptured fibrous cap. It is tempting to assume that the rupture of the fibrous cap – which is known to cause thrombotic complications – is the reason for the ischemic stroke in this previously asymptomatic patient.

References

- 1 World Health Statistics. 2005. Ref Type: Internet Communication.
- 2 Virmani R, Kolodgie FD, Burke AP, Farb A, Schwartz SM. Lessons from sudden coronary death: a comprehensive morphological classification scheme for atherosclerotic lesions. *Arterioscler Thromb Vasc Biol* 2000; 20:1262–1275.
- 3 Naghavi M, Libby P, Falk E, et al. From vulnerable plaque to vulnerable patient: a call for new definitions and risk assessment strategies: Part I. *Circulation* 2003; 108:1664–1672.
- 4 Naghavi M, Libby P, Falk E, et al. From vulnerable plaque to vulnerable patient: a call for new definitions and risk assessment strategies: Part II. *Circulation* 2003; 108:1772–1778.
- 5 Saam T, Hatsukami TS, Takaya N, et al. The Vulnerable, or High-Risk, Atherosclerotic Plaque: Noninvasive MR Imaging for Characterization and Assessment. *Radiology* 2007; 244:64–77.
- 6 Saam T, Ferguson MS, Yarnykh VL, et al. Quantitative evaluation of carotid plaque composition by in vivo MRI. *Arterioscler Thromb Vasc Biol* 2005; 25:234–239.
- 7 Toussaint JF, LaMuraglia GM, Southern JF, Fuster V, Kantor HL. Magnetic resonance images lipid, fibrous, calcified, hemorrhagic, and thrombotic components of human atherosclerosis in vivo. *Circulation* 1996; 94:932–938.
- 8 Cai JM, Hatsukami TS, Ferguson MS, Small R, Polissar NL, Yuan C. Classification of human carotid atherosclerotic lesions with in vivo multicontrast magnetic resonance imaging. *Circulation* 2002; 106:1368–1373.
- 9 Trivedi RA, King-Im J, Graves MJ, et al. Multisequence in vivo MRI can quantify fibrous cap and lipid core components in human carotid atherosclerotic plaques. *Eur J Vasc Endovasc Surg* 2004; 28:207–213.
- 10 Saam T, Underhill HR, Chu B, et al. Prevalence of American Heart Association type VI carotid atherosclerotic lesions identified by magnetic resonance imaging for different levels of stenosis as measured by duplex ultrasound. *J Am Coll Cardiol* 2008; 51:1014–1021.
- 11 Saam T, Kerwin WS, Chu B, et al. Sample size calculation for clinical trials using magnetic resonance imaging for the quantitative assessment of carotid atherosclerosis. *J Cardiovasc Magn Reson* 2005; 7:799–808.
- 12 Hayes CE, Mathis CM, Yuan C. Surface coil phased arrays for high-resolution imaging of the carotid arteries. *J Magn Reson Imaging* 1996; 6:109–112.
- 13 Serfaty JM, Chaabane L, Tabib A, Chevallier JM, Brigueat A, Douek PC. Atherosclerotic plaques: classification and characterization with T2-weighted high-spatial-resolution MR imaging – an in vitro study. *Radiology* 2001; 219:403–410.
- 14 Corti R, Osende JI, Fayad ZA, et al. In vivo non-invasive detection and age definition of arterial thrombus by MRI. *J Am Coll Cardiol* 2002; 39:1366–1373.
- 15 Kramer CM, Cerilli LA, Hagspiel K, DiMaria JM, Epstein FH, Kern JA. Magnetic resonance imaging identifies the fibrous cap in atherosclerotic abdominal aortic aneurysm. *Circulation* 2004; 109:1016–1021.
- 16 Yonemura A, Momiyama Y, Fayad ZA, et al. Effect of lipid-lowering therapy with atorvastatin on atherosclerotic aortic plaques detected by noninvasive magnetic resonance imaging. *J Am Coll Cardiol* 2005; 45:733–742.
- 17 Cappendijk VC, Cleutjens KB, Kessels AG, et al. Assessment of human atherosclerotic carotid plaque components with multisequence MR imaging: initial experience. *Radiology* 2005; 234:487–492.
- 18 Clarke SE, Hammond RR, Mitchell JR, Rutt BK. Quantitative assessment of carotid plaque composition using multicontrast MRI and registered histology. *Magn Reson Med* 2003; 50:1199–1208.
- 19 Corti R, Fuster V, Fayad ZA, et al. Lipid lowering by simvastatin induces regression of human atherosclerotic lesions: two years' follow-up by high-resolution noninvasive magnetic resonance imaging. *Circulation* 2002; 106:2884–2887.
- 20 Lima JA, Desai MY, Steen H, Warren WP, Gautam S, Lai S. Statin-induced cholesterol lowering and plaque regression after 6 months of magnetic resonance imaging-monitored therapy. *Circulation* 2004; 110:2336–2341.
- 21 Hatsukami TS, Ross R, Polissar NL, Yuan C. Visualization of fibrous cap thickness and rupture in human atherosclerotic carotid plaque in vivo with high-resolution magnetic resonance imaging. *Circulation* 2000; 102:959–964.
- 22 Yuan C, Zhang SX, Polissar NL, et al. Identification of fibrous cap rupture with magnetic resonance imaging is highly associated with recent transient ischemic attack or stroke. *Circulation* 2002; 105:181–185.
- 23 Wasserman BA, Smith WI, Trout HH, III, Cannon RO, III, Balaban RS, Arai AE. Carotid artery atherosclerosis: in vivo morphologic characterization with gadolinium-enhanced double-oblique MR imaging initial results. *Radiology* 2002; 223:566–573.
- 24 Cai J, Hatsukami TS, Ferguson MS, et al. In vivo quantitative measurement of intact fibrous cap and lipid-rich necrotic core size in atherosclerotic carotid plaque: comparison of high-resolution, contrast-enhanced magnetic resonance imaging and histology. *Circulation* 2005; 112:3437–3444.
- 25 Kerwin W, Hooker A, Spilker M, et al. Quantitative magnetic resonance imaging analysis of neovascularity volume in carotid atherosclerotic plaque. *Circulation* 2003; 107:851–856.
- 26 Tang T, Howarth SP, Miller SR, et al. Assessment of inflammatory burden contralateral to the symptomatic carotid stenosis using high-resolution ultrasmall, superparamagnetic iron oxide-enhanced MRI. *Stroke* 2006; 37:2266–2270.
- 27 Flacke S, Fischer S, Scott MJ, et al. Novel MRI contrast agent for molecular imaging of fibrin: implications for detecting vulnerable plaques. *Circulation* 2001; 104:1280–1285.
- 28 Botnar RM, Perez AS, Witte S, et al. In vivo molecular imaging of acute and subacute thrombosis using a fibrin-binding magnetic resonance imaging contrast agent. *Circulation* 2004; 109:2023–2029.
- 29 Winter PM, Morawski AM, Caruthers SD, et al. Molecular imaging of angiogenesis in early-stage atherosclerosis with alpha(v)beta3-integrin-targeted nanoparticles. *Circulation* 2003; 108:2270–2274.
- 30 Shinnar M, Fallon JT, Wehrli S, et al. The diagnostic accuracy of ex vivo MRI for human atherosclerotic plaque characterization. *Arterioscler Thromb Vasc Biol* 1999; 19:2756–2761.
- 31 Chu B, Kampschulte A, Ferguson MS, et al. Hemorrhage in the Atherosclerotic Carotid Plaque: A High-Resolution MRI Study. *Stroke* 2004; 35:1079–1084.
- 32 Kampschulte A, Ferguson MS, Kerwin WS, et al. Differentiation of intraplaque versus juxtaluminal hemorrhage/thrombus in advanced human carotid atherosclerotic lesions by in vivo magnetic resonance imaging. *Circulation* 2004; 110:3239–3244.
- 33 Cappendijk VC, Cleutjens KB, Heeneman S, et al. In vivo detection of hemorrhage in human atherosclerotic plaques with magnetic resonance imaging. *J Magn Reson Imaging* 2004; 20:105–110.
- 34 Takaya N, Yuan C, Chu B, et al. Association Between Carotid Plaque Characteristics and Subsequent Ischemic Cerebrovascular Events: A Prospective Assessment with Magnetic Resonance Imaging – Initial Results. *Stroke* 2006; In Press.
- 35 Koktzoglou I, Chung YC, Mani V, et al. Multislice dark-blood carotid artery wall imaging: a 1.5 T and 3.0 T comparison. *J Magn Reson Imaging* 2006; 23:699–705.
- 36 Saam T, Hatsukami TS, Yarnykh VL, et al. Reader and platform reproducibility for quantitative assessment of carotid atherosclerotic plaque using 1.5T Siemens, Philips, and General Electric scanners. *J Magn Reson Imaging* 2007; 26:344–352.
- 37 Underhill HR, Yarnykh VL, Hatsukami TS, et al. Carotid plaque morphology and composition: initial comparison between 1.5- and 3.0-T magnetic field strengths. *Radiology* 2008; 248:550–560.

Contact

Tobias Saam, M.D.
 Marchioninstr. 15
 81377 Munich
 Germany
 Tel: 0049 (0)89 7095 3520
 Fax: 0049 (0) 89 7095 8832
 Tobias.Saam@med.uni-muenchen.de



How can we reduce exam times by 50% for higher patient comfort?

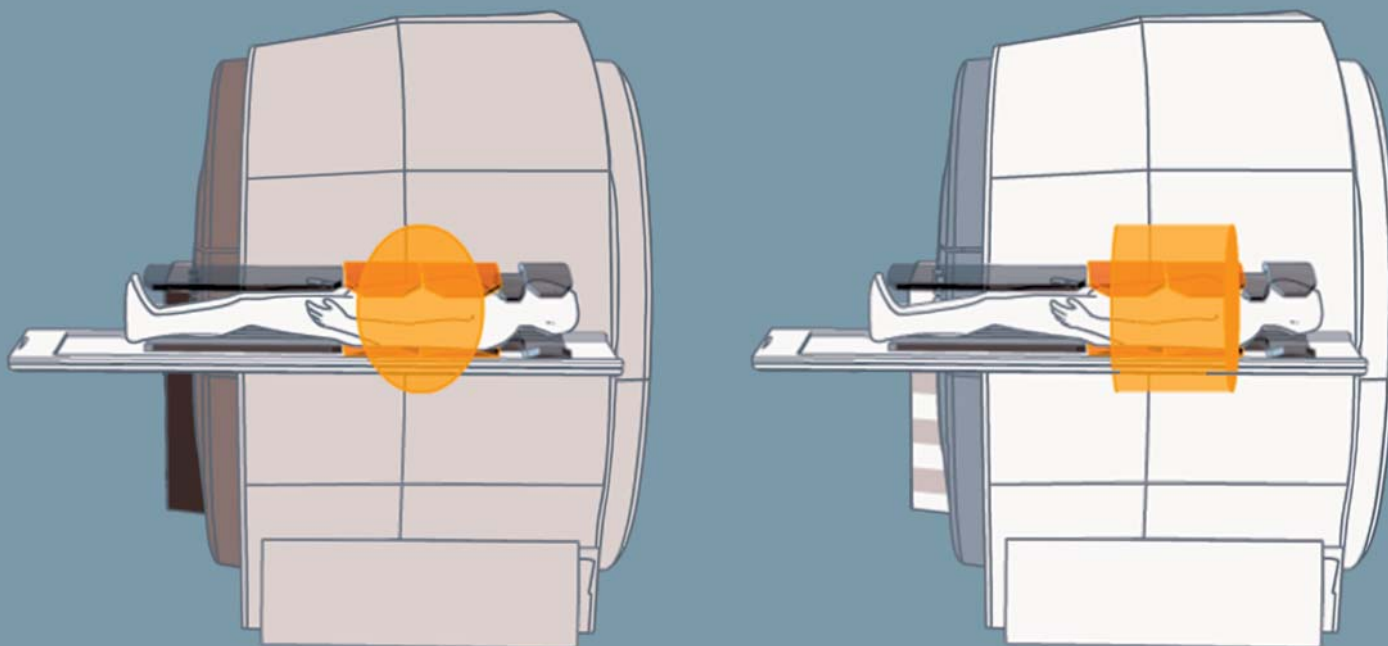


Siemens Tim technology enables multi-organ exams in one single patient setup.

By combining coils in any way, Tim® (Total imaging matrix) technology helps you to reduce your examination times by up to 50%. Around the world, Tim has become a standard in MRI. With its unmatched 32 independent RF channels and up to 102 seamlessly integrated Matrix coil elements, Tim is providing you incredible flexibility, accuracy, and speed for high-quality patient care. www.siemens.com/healthcare +49 69 797 6420

Answers for life.

SIEMENS



1 Comparison of conventional (left) with TrueForm (right) magnet design.

TrueForm™ Technology

Ioannis Panagiotelis; Mathias Blasche

Siemens Healthcare, MR Marketing, Erlangen, Germany

TrueForm is a technological innovation introduced to enable full utilization of the 3T power without the usual limitations and compromises. TrueForm design has been employed in all the field generating hardware units of the system (magnet, gradient, RF) as well as in the operating software (acquisition, processing).

TrueForm magnet and gradient design

TrueForm magnet design is an innovation that produces a cylindrically optimized homogeneity volume instead of the conventional elliptical volume. A cylinder corresponds better to the true form of the human body. TrueForm gradient design also creates a cylindrical

shape for the gradient linearity volume. The two combined result in better image quality by reducing the unusable edges in the images as well as better fat saturation for the whole area covered in a scan. TrueForm reduces the overlap needed between steps for large virtual field-of-view (FOV) exams and thus reduces the number of steps needed for a given scanning range compared to a conventional elliptical design. By modifying the relative diameter, the relative distance, the thickness as well as the density of the windings, a cylindrically optimized homogeneous volume can be achieved (Fig. 1). Cylindrically optimized magnets have a larger homogeneity volume compared to conven-

tional with identical “nominal” specifications – ideally, a cylinder has a 1.5 times larger volume than an ellipsoid with identical dimensions $x/y/z$. Figure 2 shows a schematic representation of the different parameters optimized in order to realize the TrueForm magnet design. The magnet of MAGNETOM Verio consists of 6 coils where the Niobium Titanium superconducting wire is being wound. For MAGNETOM Verio, TrueForm magnet and gradient design provide the ability to use efficiently a large FOV of up to 50 cm x 50 cm x 45 cm for several applications. Clinical examples are shown in Figures 3 and 4.

TrueForm RF Design

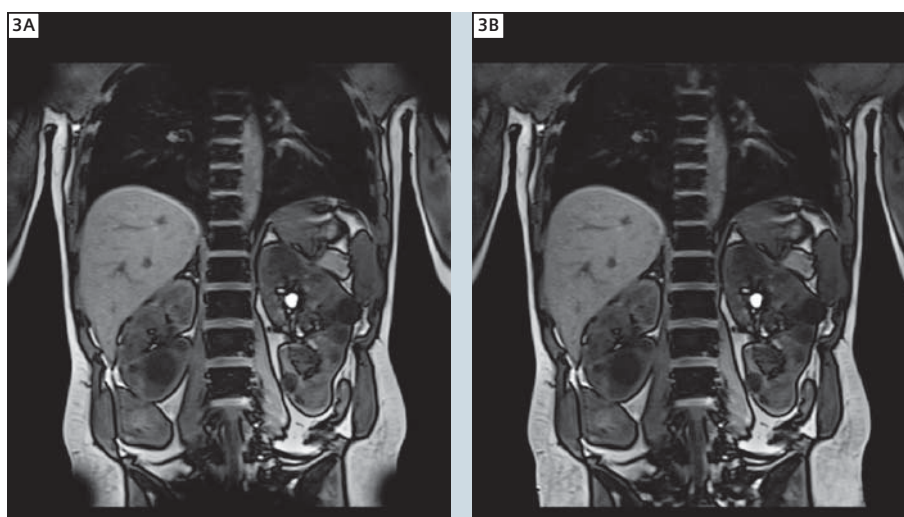
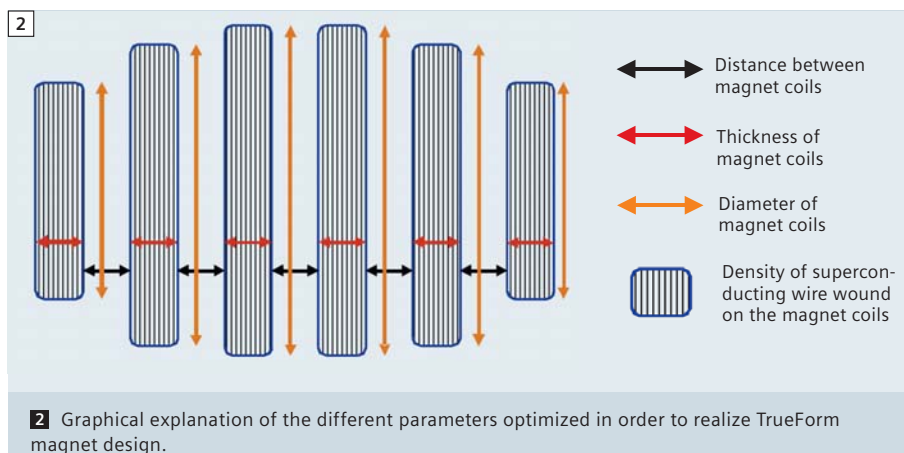
Shading effects in MRI at higher field strength are a common issue. Several techniques and applications have been proposed to solve this problem. Especially for clinical systems it is important to have a solution to improve image quality. Approaches to reduce B1-shading suggested previously involved the use of B1 saturation pads, which were cumbersome and not easy to use for both the patient and the technologist.

TrueForm RF provides an intelligent solution using the standard transmit setup of a clinical 3T scanner. TrueForm RF design includes innovative hardware technology as well as new application and processing features, which ensure uniform RF distribution in all body regions. In particular, TrueForm RF for MAGNETOM Verio consists of:

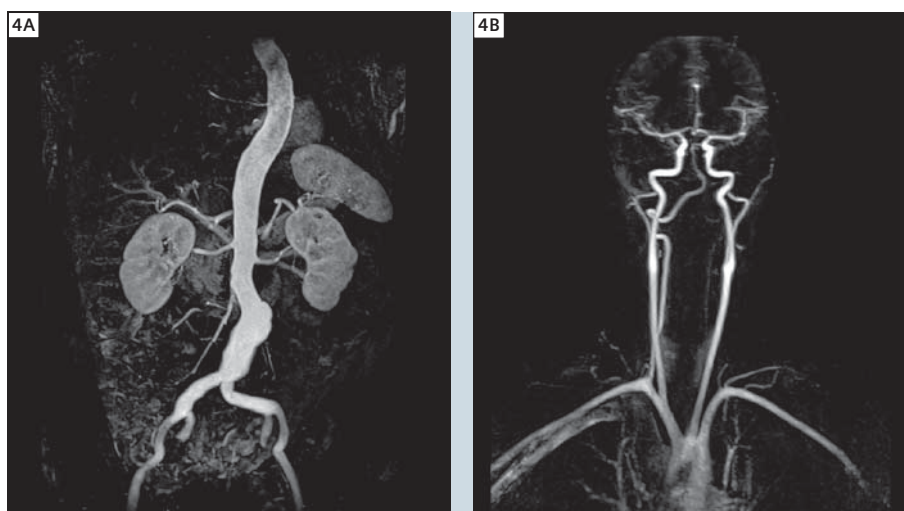
- **TrueForm Excitation**, which uses optimized amplitude and phase transmission settings. TrueForm RF Excitation has the functionality of a 2-channel Transmit Array.
- **α -SPACE** which is a version of the SPACE sequence using composite adiabatic excitation pulses which are insensitive to B1 spatial variations.
- **B1 Filter** which is an adaptive Inline image filter that reduces any remnant B1 effects without affecting image contrast.

TrueForm Excitation

In most scanners the two ports of the body coil are fed with equal amplitude and a 90-degree phase shift to produce a circularly polarized field. At low frequencies, this yields a homogenous field distribution in most cases. But at higher frequencies (3 Tesla and more), the interaction of the fields with the patient could make use of a different feeding approach. Nistler et al. [1] suggested that in several cases there is a better phase difference and amplitude weighting capable of delivering better results than simply using a 90 degree feeding. A 16-rung high-pass birdcage for whole-body imaging was modeled in a simu-



3 Comparison of gradient echo coronal images of the torso without (left) and with (right) TrueForm magnet design. Distortions along the edges of the imaging field are minimized.

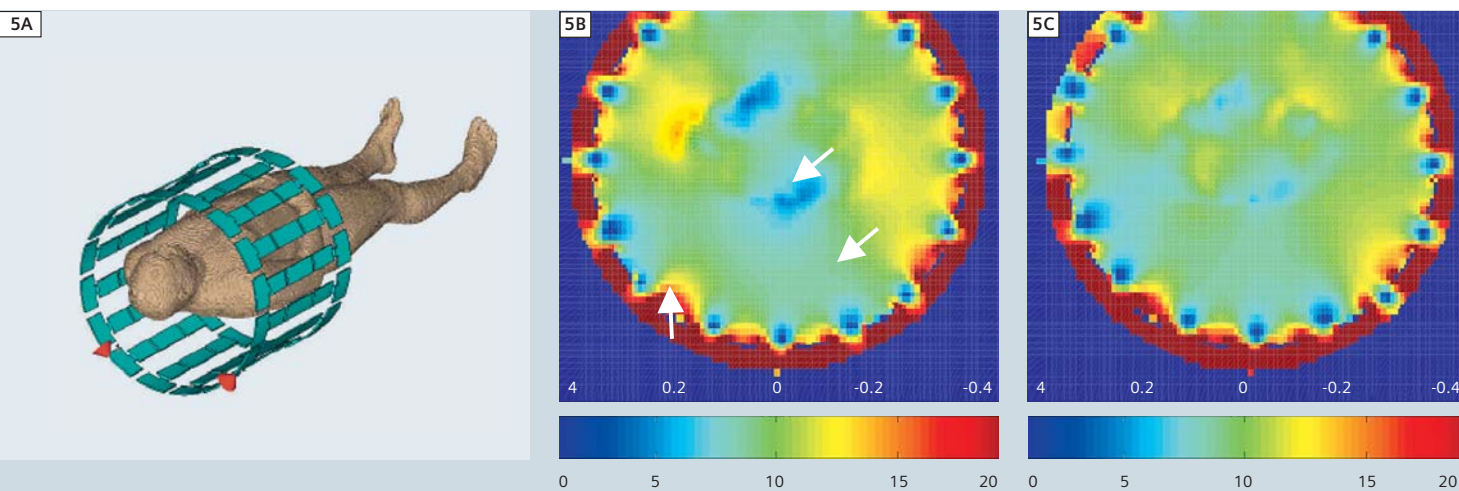


4 MR Angiographies (MRA) with 45 cm FOV in the z-direction acquired in one step with MAGNETOM Verio using 24 Matrix coil elements (left) and 28 Matrix coil elements (right).

lation program. Each of the two ports could be excited separately; the resulting fields were combined and analyzed in the post processing. While this setup produces a homogenous circularly polarized field in the empty coil using the conventional CP feeding (90 degrees / equal amplitude), this is different with human models inside the coil. The results were evaluated using a male and a female human model, both in different positions of the models relative to the coil isocenter. Nistler et al. found that the position of the human model in head-first or feet-first orientation has virtually no influence on the results. Simulations performed by Nistler et al. show that in most cases if you improve

homogeneity also the power deposition in reduced. They also investigated the influence on local SAR hot spots or on the relation of SAR-Local/SAR-whole body (wb) for all model setups. They concluded that if the amplitude and phase settings are varied there are only a very limited number of positions in the human model, where the SAR hot spots arise. The solution they suggested further reduces this possibility. Figure 5 shows the B1 distribution in the human model, when the conventional CP feeding is used. The areas with inaccurate flip angles (lower or higher then the value determined by the sequence) are obvious. Now the phase difference for the feeding ports was

varied between 0 and 360 degree and also the amplitude relation P2/P1 was modified between -21 dB and +21dB. The resulting field distributions were analyzed concerning B1 homogeneity (standard deviation). Additionally, the necessary input power for all combinations was calculated to generate an average field of 11.7 μ T. As a result it could be seen that an improvement in homogeneity is possible and the power deposition into the patient can also be reduced. This is also shown in Table 1. In summary, the results by Nistler et al. show that the field homogeneity and the power deposition in a patient can be optimized by using a conventional birdcage with two feeding ports.



5 (left) Simulation model with a two-port high-pass birdcage coil, with a human male model positioned head first inside the coil. B1 Field Plots for conventional (middle) and TrueForm RF design (right). Arrows show areas of B1 inhomogeneity that is corrected with TrueForm Excitation technology.

Table 1: Abdomen in center of the coil

Excitation scheme	Homogeneity	Power in Patient	Power relation Port 2 / Port 1(dB)	Phase difference Port 2 – Port 1
Symmetric (conventional)	19.3	3639	0	90
Best homogeneity	11,9	3418	6	120

Change in homogeneity (relative standard deviation in %) for possible phase and amplitude weightings, showing a significant improvement in homogeneity change in total power for possible phase and amplitude weightings, showing a power reduction compared to symmetric excitation. Reference power value is for a mean B1 of 11.7 μ T.

Therefore it is necessary to change the weighting for the two ports. In particular, B1 homogeneity can be improved by almost a factor of 2, while the SAR performance (power deposition) can also be improved / reduced by between 5–10%.

This implementation of TrueForm RF Excitation on MAGNETOM Verio has the functionality of a 2-channel Transmit Array system.

It offers a robust and effective method to reduce B1 inhomogeneities.

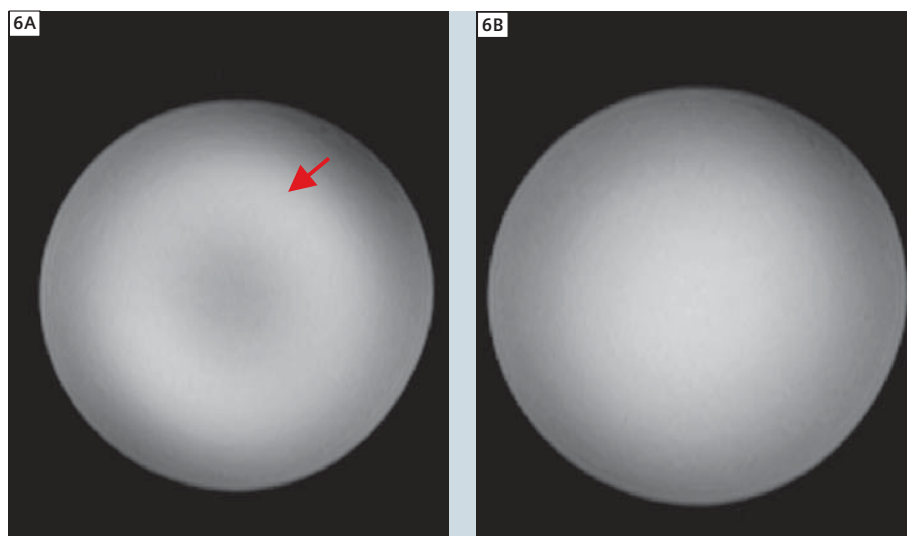
The independent setting of amplitude and phase of the two feeding ports of the RF Body coil is done in an anatomy-specific optimization. No time for patient-specific adjustments is required, saving up to 1 minute per examination. Together with accurate patient- and anatomy-specific SAR calculations, based on the Hugo model, TrueForm RF Excitation increases examination speed and image quality.

a-SPACE

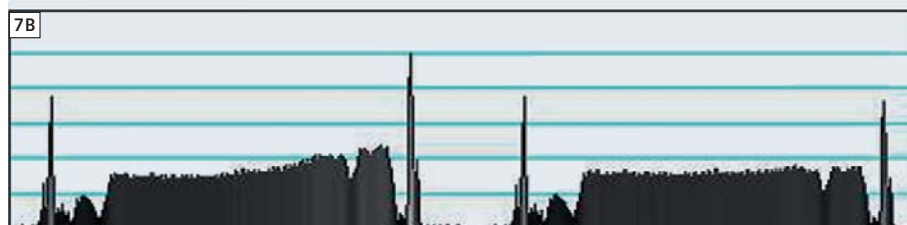
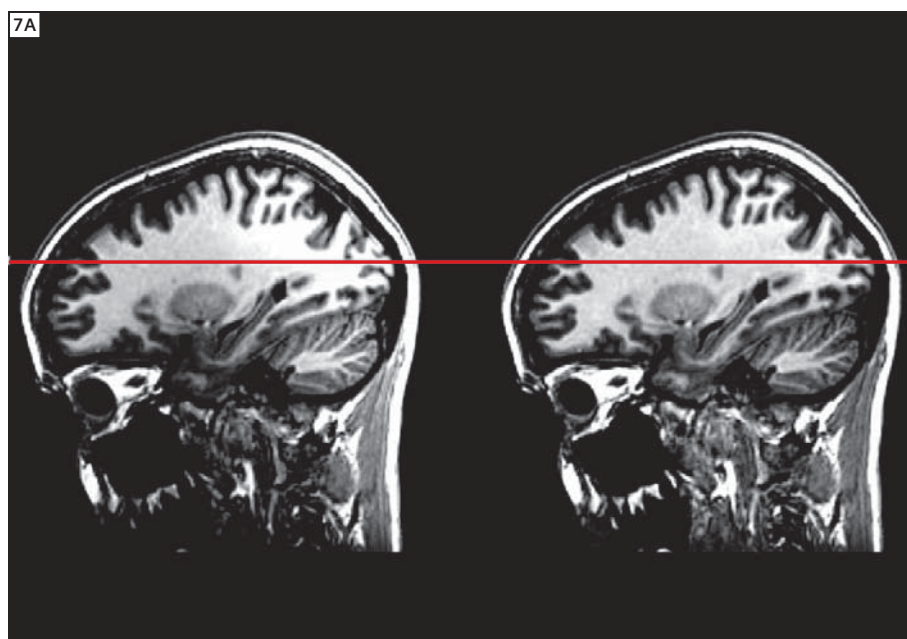
For the case that B1 inhomogeneities are still present in the images, the users have the opportunity to use the a-SPACE sequence with adiabatic instead of conventional pulses. Adiabatic pulses are insensitive to B1 distribution and, as seen in the phantom images below, improve the homogeneity in the images.

B1 Filter

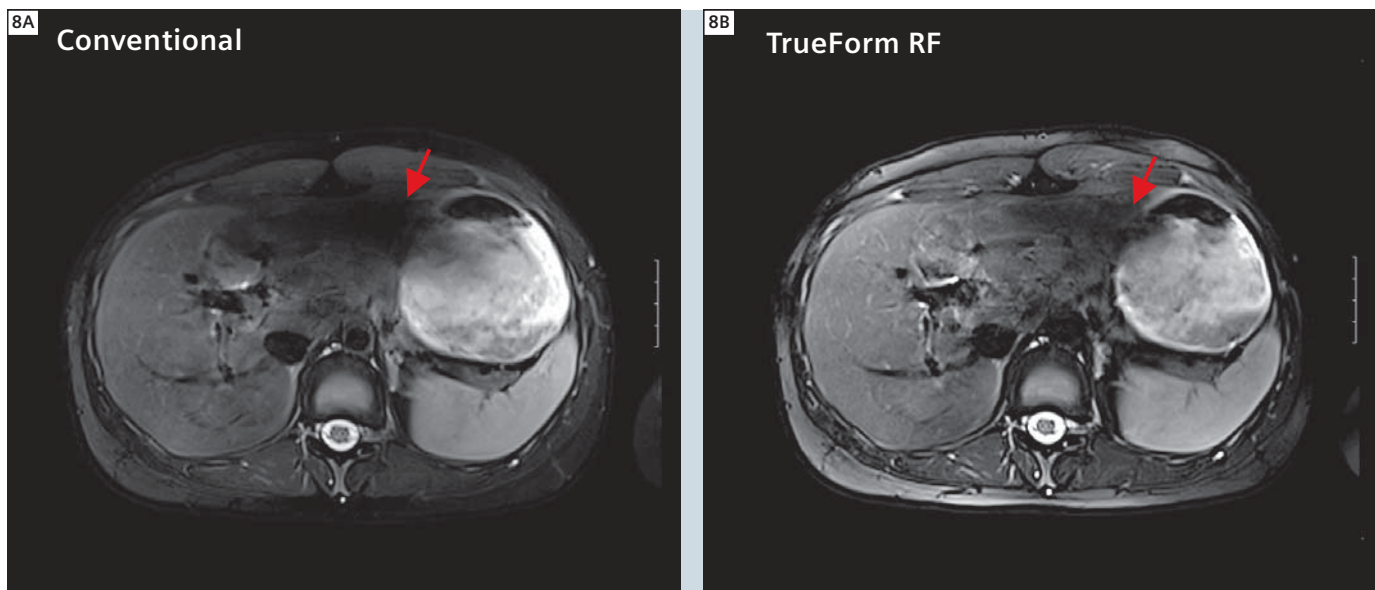
The final measure involved in TrueForm RF Technology is a postprocessing image filter. This filter improves the image intensity profile without affecting the image contrast. Such a filter will not improve the diagnostic value of the images but will enable the radiologists to provide perfect-looking images in their reports to the referring physicians.



6 Phantom image intensity maps acquired with conventional (left) and a-SPACE (right). Part of the TrueForm RF design, a-SPACE significantly improves the homogeneity within the sample.



7 Image Intensity Profile showing the effect of the B1 Filter (right): the signal intensity is much more uniform across the image when using the B1 Filter, part of TrueForm RF design.



8 Images showing uniform image intensity in the abdomen after application of TrueForm RF design.

Clinical Examples

In the clinical examples of the application of TrueForm RF design, one can see elimination or significant reduction of the B1 artifacts that occasionally appear when imaging different body parts at 3T. In particular, Fig. 8 shows how TrueForm recovers the signal in the anterior part of the liver of a very athletic patient. Fig. 10 shows recovery of the uniformity in the image intensity for bilateral breast imaging. Fig. 11 shows elimination of the B1 inhomogeneity in the posterior part of the right leg.

In the abdomen, the existence of B1 inhomogeneities – particularly in patients with ascites or edemas – has been the major obstacle that impeded the spread of 3T MRI in the abdominal and general radiology clinics for some time.

Recently the issue of B1 inhomogeneities has been raised for breast imaging at 3T, where apart from the basic problem of image homogeneity, severe concern was expressed regarding possible misinterpretations of contrast uptake if the actual excitation angle deviates too strongly from the nominal flip angle in gradient echo sequences used for dynamic studies [2]. Geppert et al. compared the application of TrueForm RF in breast imaging. B1 maps were acquired using the body coil in order to have a flat sensitivity pro-

file. The evaluation of the calculated B1 distribution maps was performed by applying several regions of interest (ROI) in areas that exhibited very high or low signal intensities. The maximum and minimum measured flip angles were considered for each breast and normalized to a nominal flip angle of 90 degrees to enable a direct comparison. As a final measure, for each scan the absolute of the maximum deviation from 1.0 was reported.

The last example shows the application of the adiabatic mode with a-SPACE when imaging muscle. When the adiabatic mode is switched on, the signal loss is recovered.

The Next Step: Multi-Channel Tx Array Technology

The use of parallel transmission techniques with multiple Tx channels is a possible solution to the B1 inhomogeneities that may appear at higher field strengths, but it implies costly hardware efforts. This is due to the fact that with the current technology an 8-channel transmit system would necessitate the use of 8 power amplifiers, which are rather expensive. Such a system would also hold the risk of local SAR hot spots

due to the yet-to-be-clarified consequences of the superposition of the multiple RF fields, hence there is still more research necessary to overcome this issue.

The first approach where Tx Array technology could be used is called RF shimming. RF shimming actually refers to a simplified form of parallel transmission where the multiple array elements of a coil are driven with individual amplitudes and phase shifts. Full parallel transmission on the other hand is a more complex approach. It involves in addition the use of separate pulse shapes in each array coil element. Thus, RF shimming utilizes the spatial patterns of the transmit array, but not the encoding ability of the gradient trajectory. As a consequence, the full parallel transmission (pTX) method produces superior B1 mitigation performance and in addition enables additional applications such as organ or arbitrary volume specific excitation.

References

- 1 J. Nistler et al. Homogeneity Improvement Using A 2 Port Birdcage Coil, ISMRM Proceedings 2007.
- 2 C. Kuhl et al. Effect of B1 Inhomogeneity on Breast MR Imaging at 3.0 T, Radiology 2007; 244:929-930.
- 3 Geppert et al. Reduced B1-inhomogeneities in breast MRI using optimized RF excitation, ISMRM Proceedings 2008.

TrueForm Retains the Spectral Integrity on the MAGNETOM Verio

Saadallah Ramadan¹; Peter Stanwell¹; Ravi Seethamraju²; Carolyn Mountford¹

¹ Centre for Clinical Spectroscopy, Department of Radiology, Brigham & Women's Hospital, Boston, MA, USA

² Siemens Medical Solutions, Burlington, MA, USA

Introduction

It is well known that good quality spectra are dependent on the magnetic field homogeneity of the magnet. The field homogeneity, in turn, is dependant on the magnetic field strength, the bore design etc. In the case of the MAGNETOM Verio, a 3T wide and shorter bore scanner, these factors are of concern for the spectroscopy community. The Verio uses an innovative technology known as "TrueForm". In TrueForm the two ports of the CP body coil are unequally fed with a non-orthogonal phase difference which causes an improvement in homogeneity as well as a reduction in power deposition. TrueForm design in the Verio mitigates the homogeneity effects that are normally experienced with both a wide and shorter bore at the magnetic field strength of 3T. This innovation was made possible by innovations in the magnet design, gradients, RF, acquisition and processing protocols. The TrueForm magnet design produces a cylindrically optimized homogeneous volume and a cylindrical shape for the gradient linearity

volume. Here we demonstrate that the Verio, equipped with TrueForm, allows for spectroscopy to be undertaken satisfactorily for brain and breast.

1. Spatial profile with standard spectral RF pulses (sinc and Mao)

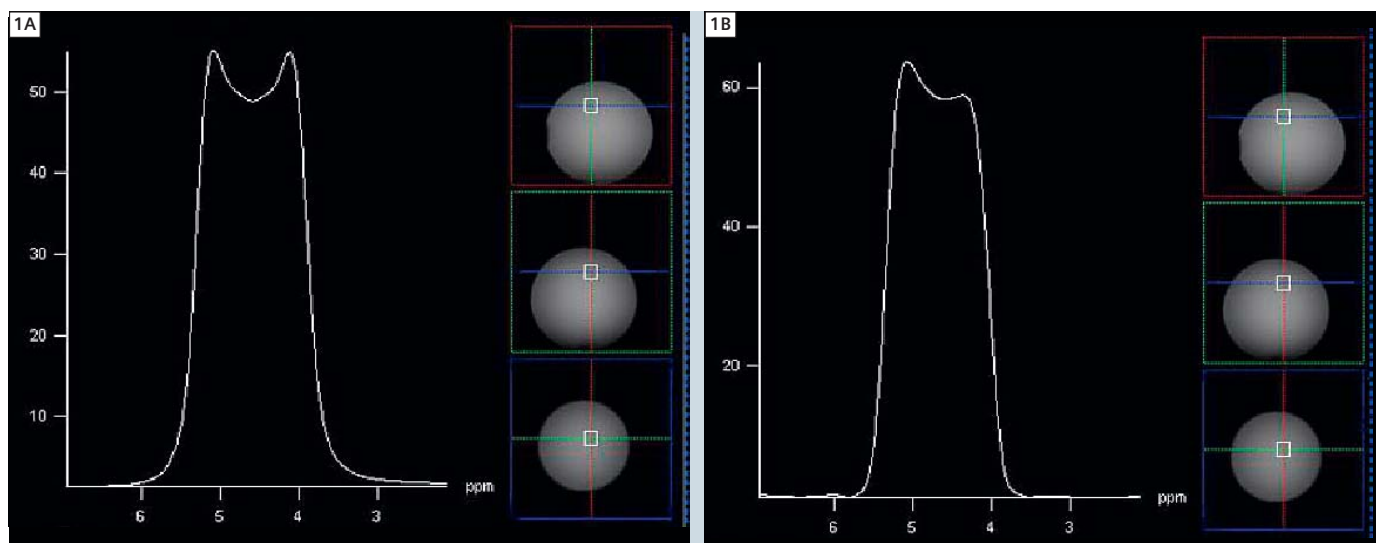
Spatial profile of an RF pulse reports on its system performance (transmitted RF and gradient performance as well as magnetic field homogeneity). In Figure 1 the shape of a 90° (sinc) pulse and an 180° (Mao) pulse is shown. That the gradient linearity and B₁ homogeneity are acceptable is evident in the width of the profile and the near rectangular shape of the profiles.

2. Neuro spectroscopy acquired with a loop coil and a head array coil

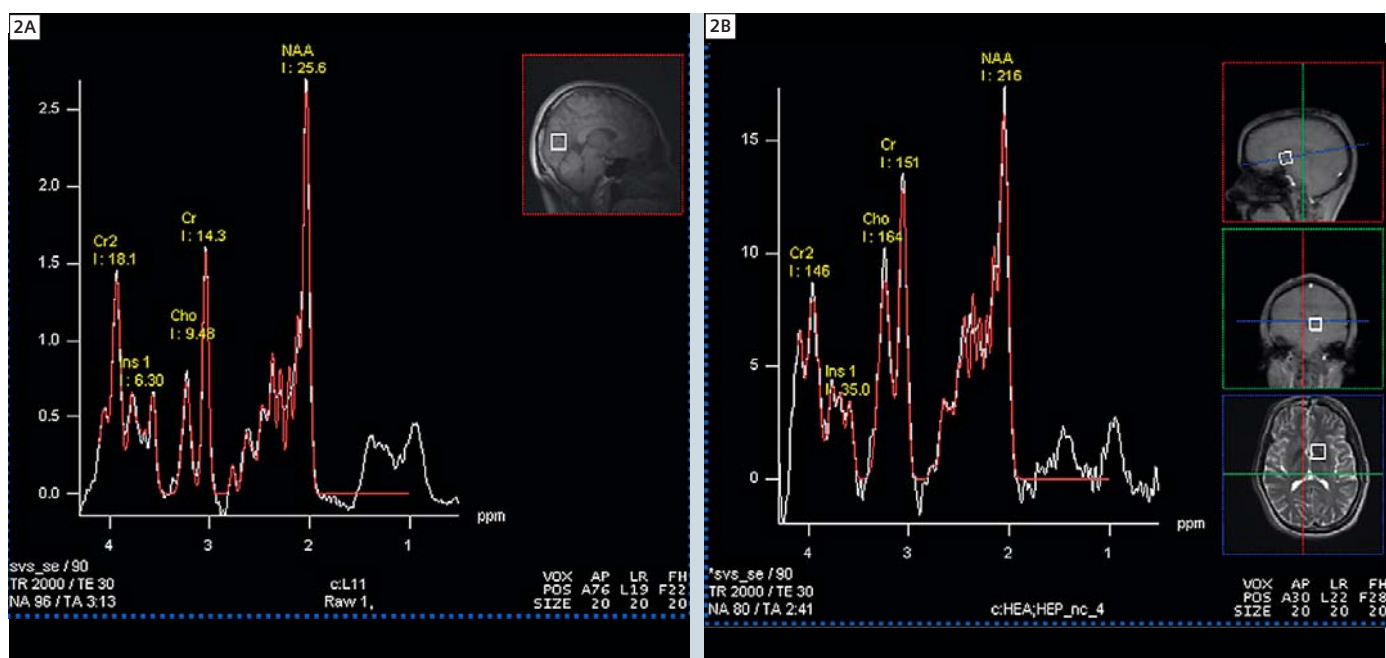
The MAGNETOM Verio performs neuro-spectroscopy well. On the left, in figure 1, is a svs_se (single voxel spectroscopy, spin echo) spectrum acquired with body coil excitation and the 11 cm loop coil for detection. Of note are a narrow line

width at half-height, i. e. spectral resolution, and low lipid contamination especially with the loop coil. Localized shimming, a function of many multiple interacting factors (RF homogeneity, magnet design and gradient design) was achieved very well with a line width at half height of NAA (2 ppm) of 4 Hz. Efficient slice definition, spectral excitation and unwanted signal spoiling are important requirements in order to achieve these results. Utilizing the head array coil spectra could also be acquired from challenging locations within the brain, especially near nasal cavity and sinus (Fig. 1) without compromising the signal-to-noise ratio (SNR) and without lipid contamination.

Spin-echo chemical shift imaging, CSI_SE, was also implemented on a healthy volunteer to test the efficacy of localized shimming and lipid suppression from a wider region of interest (Fig. 3). It would appear that the TrueForm method is able to deliver efficient outer-volume suppression (OVS) pulses.



1 The profile of a 2.6 ms 180° Mao RF pulse (left), and a 2.6 ms 90° sinc RF pulse (right) accrued using a head array coil on the MAGNETOM Verio. The performance of these pulses are evident as seen as the profile width at half-height, which corresponds to 2 cm at the applied read-out gradient.



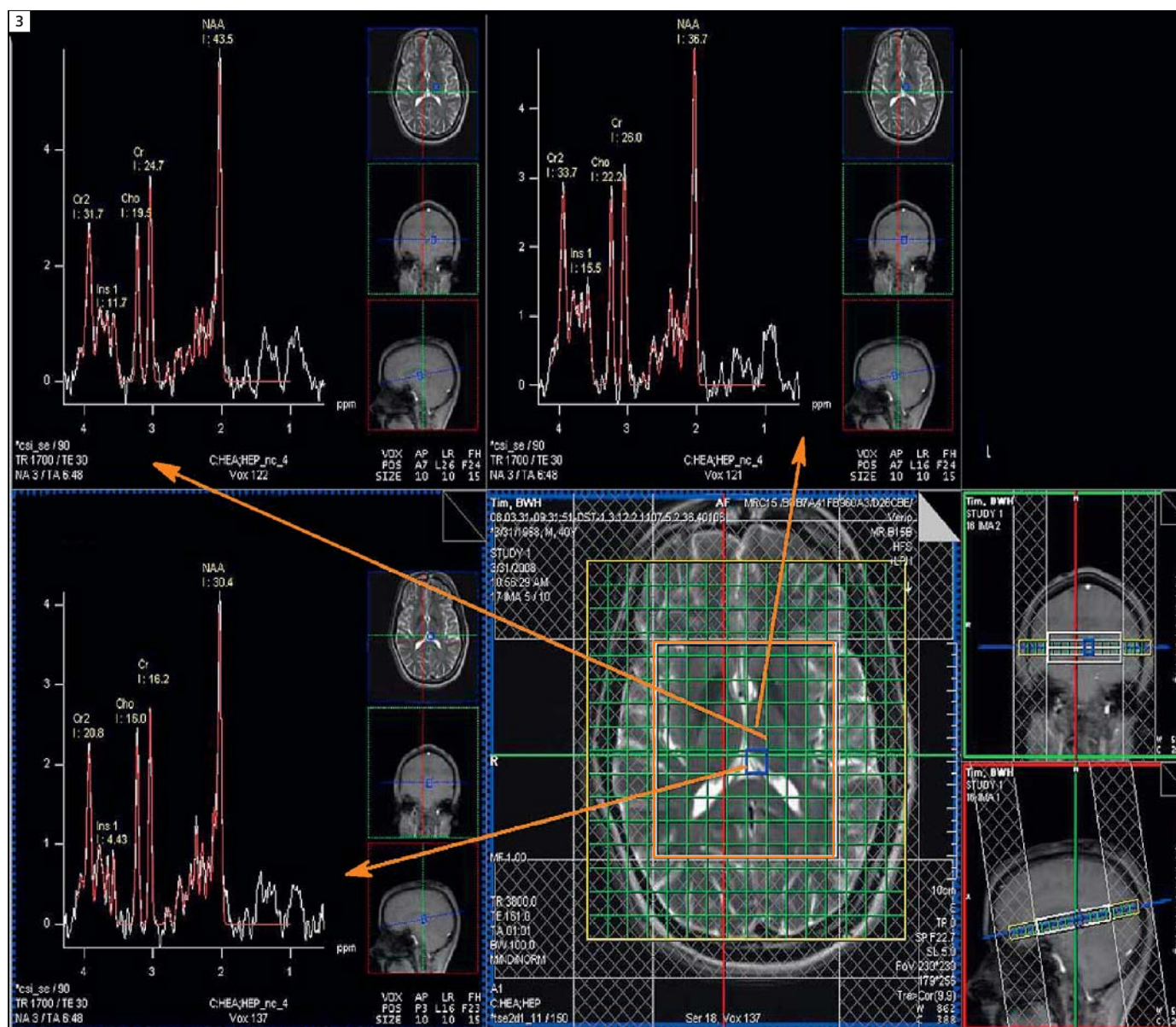
2 Standard, short TE, double-echo (SVS_SE) spectroscopy. (Left) SVS_SE is applied in the occipital lobe region of the brain, using a Siemens single-channel 11 cm loop coil. (Right) Short TE SVS_SE is applied in a challenging region of the brain, near the nasal cavity resulting in a good quality spectrum.

Similar observations to Fig. 2 apply to Fig. 3, where narrow line width, acceptable SNR, high spectral resolution and low lipid contamination were realized. Considering the small voxel size ($1 \times 1 \times 1.5 \text{ cm}^3$) in this particular `csi_se` with 3 averages, the spectral quality is an improvement when compared to the quality obtained with traditional RF waveforms.

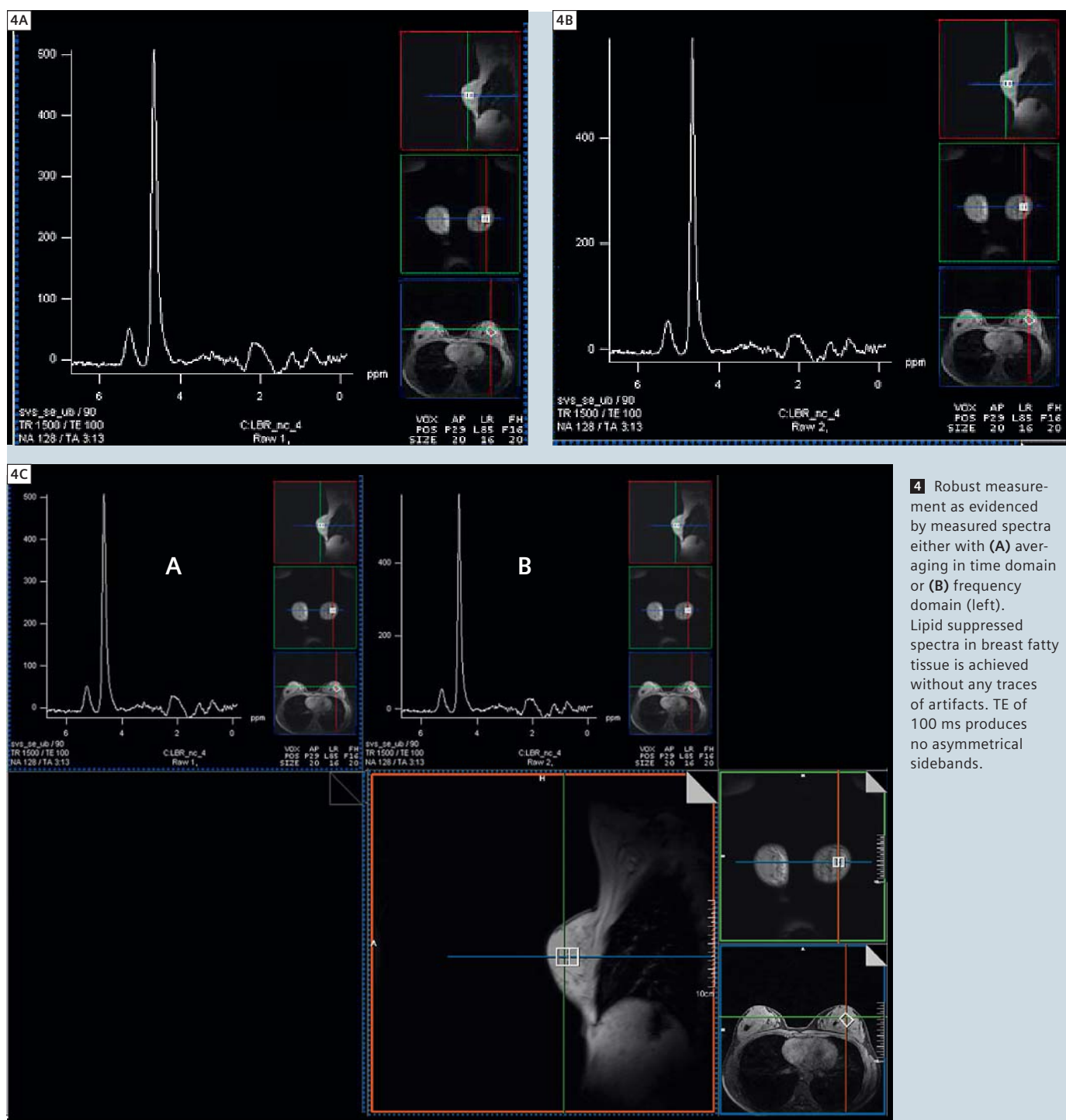
3. Breast spectroscopy

The capacity to collect *in vivo* spectroscopy from the breast using lipid suppression was also tested on the MAGNETOM Verio. The method successfully suppressed the lipid resonance at 1.30 ppm using MEGA pulses [Mescher et al., 1998]. A voxel (20 x 16 x 20 mm³) was prescribed in the breast of a healthy volunteer. The universal body version of SVS_SE (svs_se_ub) was used to check for stability during the acquisition of

the 128 averages. Thus, these averages were averaged in time domain (traditional) and in spectral domain after individual Fourier transforming [Gabr et al., 2006]. In Fig. 4 the same FID is presented using two different types transform, and the difference is nil; a sign of stability. The large lipid peak suppressed without inducing any spectra artifacts (e.g. baseline roll). Anti-symmetric peaks [Bolan et al., 2002] were not observed at a TE of 100 ms.



3 Shimming is integral for successful spectroscopy and this is especially the case for multi-voxel CSI. The quality of 16 x 16 grid 2D CSI data (left) and the resolution of the resonances illustrate good B₀ homogeneity. We conclude that the homogeneity is not compromised by the wider bore or that the TrueForm technology compensates.



References

- 1 Bolan, P. J., Delabarre, L., Baker, E. H., et al. 2002. Eliminating Spurious Lipid Sidebands in 1H MRS of Breast Lesions. *Magn. Reson. Med.*, 48: 215–222.
- 2 Gabr, R. E., Sathyanarayana, S., Schar, M., et al. 2006. On Restoring Motion-Induced Signal Loss in Single-Voxel Magnetic Resonance Spectra. *Magn. Reson. Med.*, 56: 754–760.
- 3 Mescher, M., Merkle, H., Kirsch, J., et al. 1998. Simultaneous in vivo spectral editing and water suppression. *NMR. Biomed.*, 11: 266–272.

Contact

Dr. Saad Ramadan, Ph.D.
Brigham & Women's Hospital
1620 Tremont St.
Boston, MA 02120
USA
sramadan@partners.org

Parallel Transmit Technology for High Field MRI

Lawrence L. Wald^{1, 2, 3}; Elfar Adalsteinsson^{1, 3, 4}

¹Athinoula A. Martinos Center for Biomedical Imaging, Department of Radiology, Massachusetts General Hospital, Boston, MA, USA

²Harvard Medical School, Boston, MA, USA

³Harvard-MIT Division of Health Sciences and Technology, Boston, MA, USA

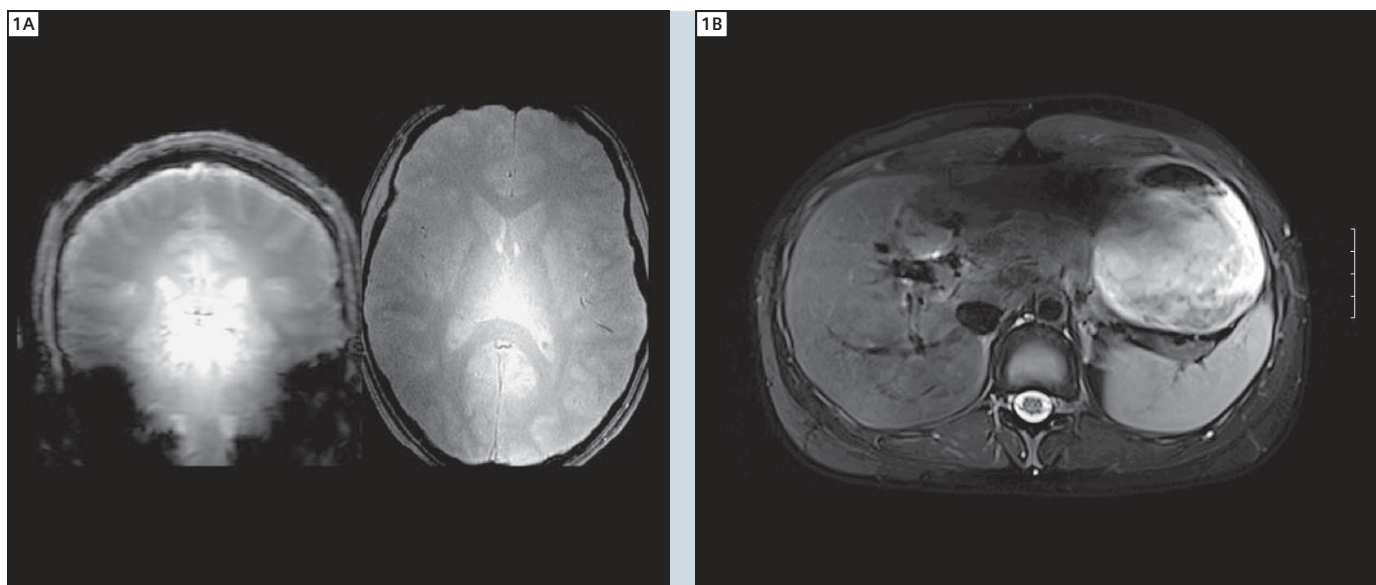
⁴Department of Electrical Engineering and Computer Science, Massachusetts Institute of Technology, Boston, MA, USA

Introduction

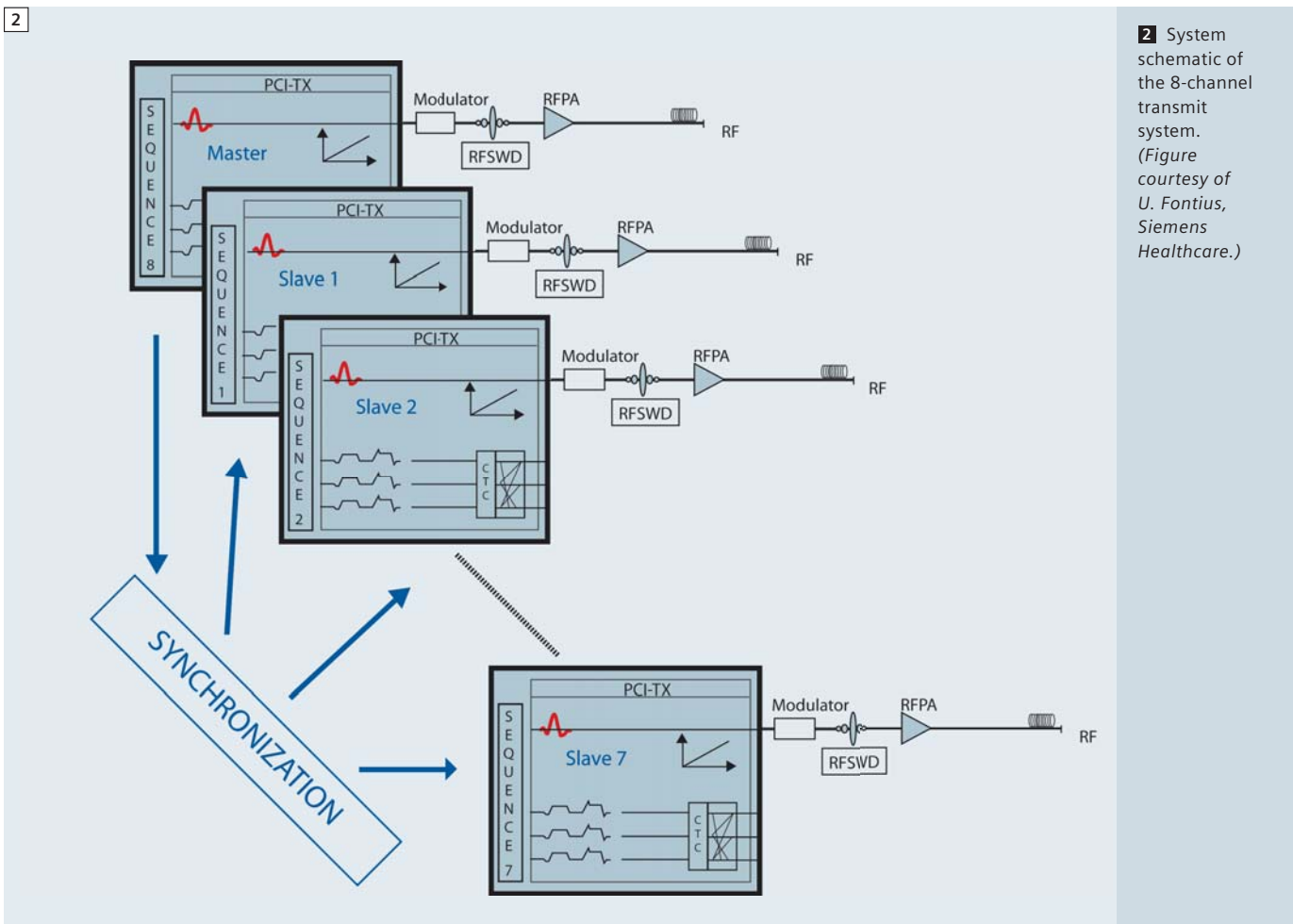
The success of parallel reconstruction methods and their impact on image encoding has sparked a great deal of interest in using the spatial distribution of transmit coils in an analogous fashion. Namely, by breaking down the transmit field into multiple regions each controlled by a separate transmit channel, spatial degrees of freedom are created that allow the spatial information in the array to be exploited in the excitation process. While a homogeneous birdcage-type body-coil driven by a single RF pulse waveform has served the MR com-

munity well, it does not possess spatial degrees of freedom, and subsequently works best for uniform excitations. Parallel excitation arrays and the potential to utilize the spatial information in an array during RF transmission offer the possibility to move beyond the uniform slice-select excitation, and to generate spatially tailored RF pulses; excitation pulses with a carefully controlled spatially varying flip angle or excitation phase that can mitigate artifacts or isolate specific anatomy. While the concept of spatially tailored

excitation pulses has been known for some time, the implementation of such pulses is largely impractical on conventional single-channel excitation systems, and only by introducing the additional spatial degrees of freedom in a transmit array do they achieve practical durations for clinical imaging. An early application of spatially tailored parallel excitation was to mitigate the non-uniform flip angle problem created by RF wavelength effects at high field (Fig. 1). These non-uniformities arise when the wavelength of the RF approaches the dimension of



1 Flip angle inhomogeneity resulting from wavelength effects in the brain at 7T (central brightening) and liver at 3T (drop-out). Spatial variations in the transmit efficiency, and therefore the flip angle, are more problematic than the receive inhomogeneities since they lead not only to image shading, but more importantly, image contrast alterations.



the human head or body and create destructive excitation field interference among sections of a conventional transmit coil. This is most noticeable in the head at 7T where a strong center brightening is a typical feature (perhaps more properly termed peripheral darkening) and in the body at 3T where shading is seen near large regions of non-fatty tissue in the abdomen. Unlike detection inhomogeneity that manifests primarily as image intensity shading, a non-uniform transmit B_1 field results in spatially dependent tissue contrast and therefore reduced diagnostic power, which cannot be recovered with an image normalization scheme. A spatially tailored excitation mitigates this problem by anticipating the flip angle inhomogeneity and compensating for it in the spatial profile of the excitation. Once the technology is in place for spa-

tially tailored RF excitations, the ability to generalize excitation profiles beyond the slice-select pulse offers many exciting opportunities for selective excitations of anatomically tailored volumes. An anatomy-specific excitation could potentially reduce image encoding needs (e.g. for cardiac or shoulder imaging) by reducing the effective field-of-view, it could enable more accurate CSI exams in tissues with many interfaces like in the prostate, and allow selective spin-tagging excitations (potentially allowing vessel territory perfusion imaging), or simply provide clinically useful but non-traditional excitations such as curved saturation bands for the spine or brain. In this article we review some of the progress which has been made with a prototype 8-channel parallel transmit system integrated into a Siemens

MAGNETOM Trio, A Tim System, and a 7 Tesla MAGNETOM system. We discuss some of the recent advances in calculating parallel transmit RF pulses for spatially tailored excitation and show examples of B_1 transmit mitigation at 3T and 7T. Further, we describe some of the recent advances in methodology as well as some of the outstanding issues that must be overcome for routine application.

Experimental Setup

Flexible delivery of independent RF waveforms to each channel of the array is needed to realize the full potential of parallel transmission. Additionally, fast gradient trajectories are required during the RF pulses to modulate the spatial profile of the excitation. Since eddy current compensation is performed during the RF waveform generation using knowledge of the gradient history, each RF channel

needs to be fully integrated into the full waveform generation system of the scanner. To achieve this, a prototype 8-channel transmit system was set up in a master-slave configuration with each channel capable of running an independent pulse sequence, and importantly, independent B_0 eddy current compensation. Finally each channel utilized a separate RF power amplifier (8 kW each in the 3T case and 1 kW each in the 7T case) and fully independent SAR monitoring on each channel.

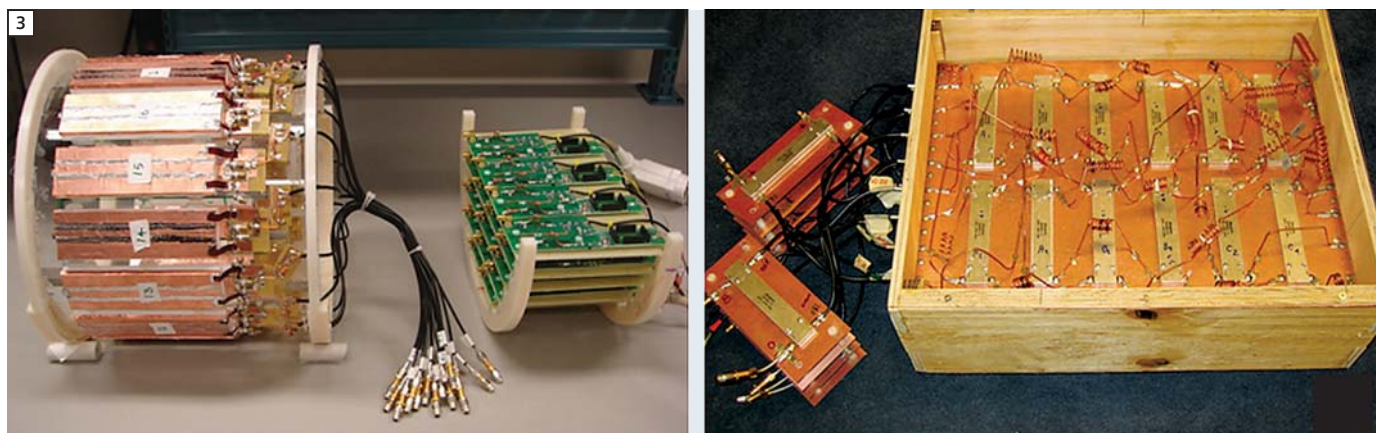
Which RF transmit array configurations capture the maximum ability to capitalize on the parallel nature of the excitation? This question is central to the opti-

mal design of a flexible parallel excitation system and remains an open research problem. Two principles guide our design of the array configuration:

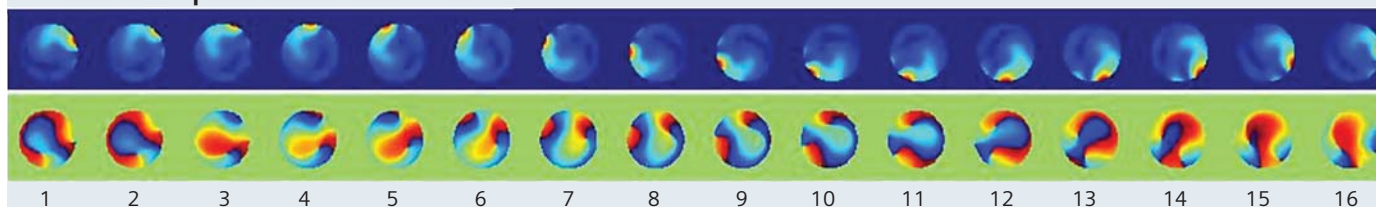
- obtaining the maximum benefit from the limited (expensive) number of excitation channels, and
- retaining the simplicity of birdcage-like excitation in one channel.

These two goals are elegantly achieved when a so-called "Butler matrix" [1] is inserted in the path from the RF amplifiers to the coil elements to drive a ring of excitation coils on a cylindrical former. In contrast to a direct drive of the coil elements by the RF amplifiers, the Butler matrix transforms the phase relationship

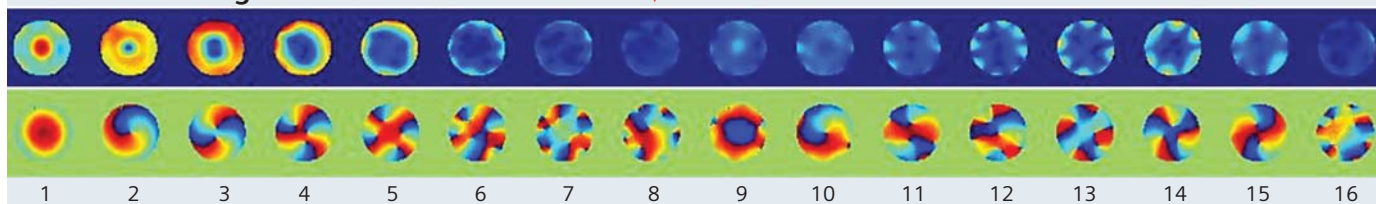
of the array elements so that each RF excitation channel drives not just a single RF element but influences all of them in a specific (and familiar) relationship; namely the spatially orthogonal modes of a birdcage coil. The spatial patterns of these modes and the phase relationships needed to generate them are well known from birdcage theory [2], and when achieved, have several benefits. Firstly, it allows the "master" channel of the array to operate as a uniform birdcage-like excitation coil. Although at high field the so-called uniform birdcage mode generates significant field variation (one of the original motivations for parallel TX technology), it is useful in



16 "strip-line" coil modes



16 "birdcage" coil modes



Butler matrix

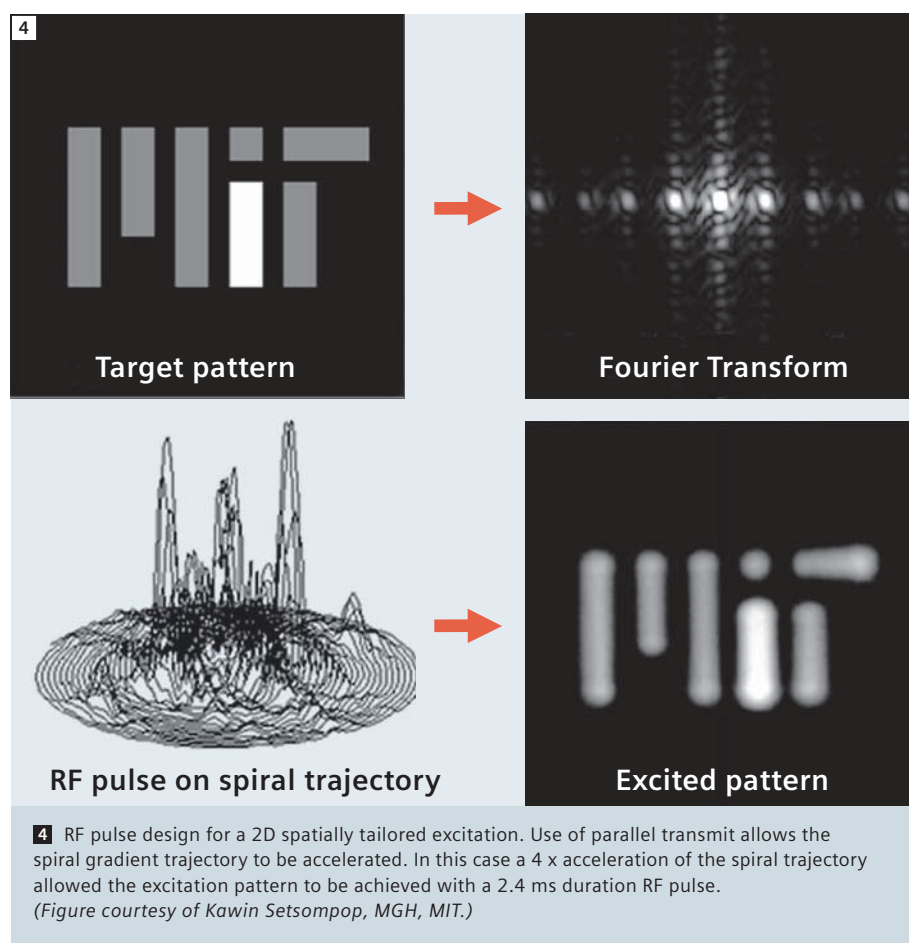
3 A 16-channel 7T strip-line array for the head (upper left) and a 16 x 8 Butler matrix (upper right). Below are the magnitude and phase B_1 maps of each of the 16-channels for both the "strip-line" basis set, and the "birdcage" basis set. While excitation ability is roughly equally divided among the strip-line modes, it is concentrated in a few valuable modes in the birdcage basis set. We can choose which 8 modes to drive based on their performance. (Figure courtesy of Vijay Alagappan, MGH.)

practice to have one of the channels operate from this well established and efficient starting point. The other channels then span progressively higher-order modes of the birdcage coils with their spatially specific amplitude and phase variations.

Since the Butler matrix achieves these modes through simple linear combinations, at first blush it would appear that this “basis set” of excitation patterns would be no better or worse for accelerating spatially tailored excitation than simply driving the array of elements one at a time. The superiority of the Butler matrix driven array becomes apparent when only a subset of the array modes is chosen for excitation. In practice this allows the benefit of a larger array to be captured in a system with fewer transmit channels (i.e. lower cost) by capturing a majority of the transmit efficiency and acceleration capabilities in a valuable subset of the channels (and ignoring the less valuable channels). We explored this “array compression” principle by driving a 16-channel stripline array for 7T head transmit with a 16 x 16 Butler matrix connected to the 8-channel transmit system [3], and demonstrated the theoretically predicted tradeoffs. The excitation configuration that integrates a Butler matrix in this manner allowed us to pick and chose among the modes of a 16-channel array and drive only the best subset of the 16 available modes with our 8 transmit channels. The choice of the optimum 8 birdcage modes compared to 8 strip-line elements allowed a flip-angle inhomogeneity mitigating excitation to achieve a 43% more uniform excitation and 17% lower peak pulse power in a water phantom at 7T [3].

Spatially tailored RF excitation

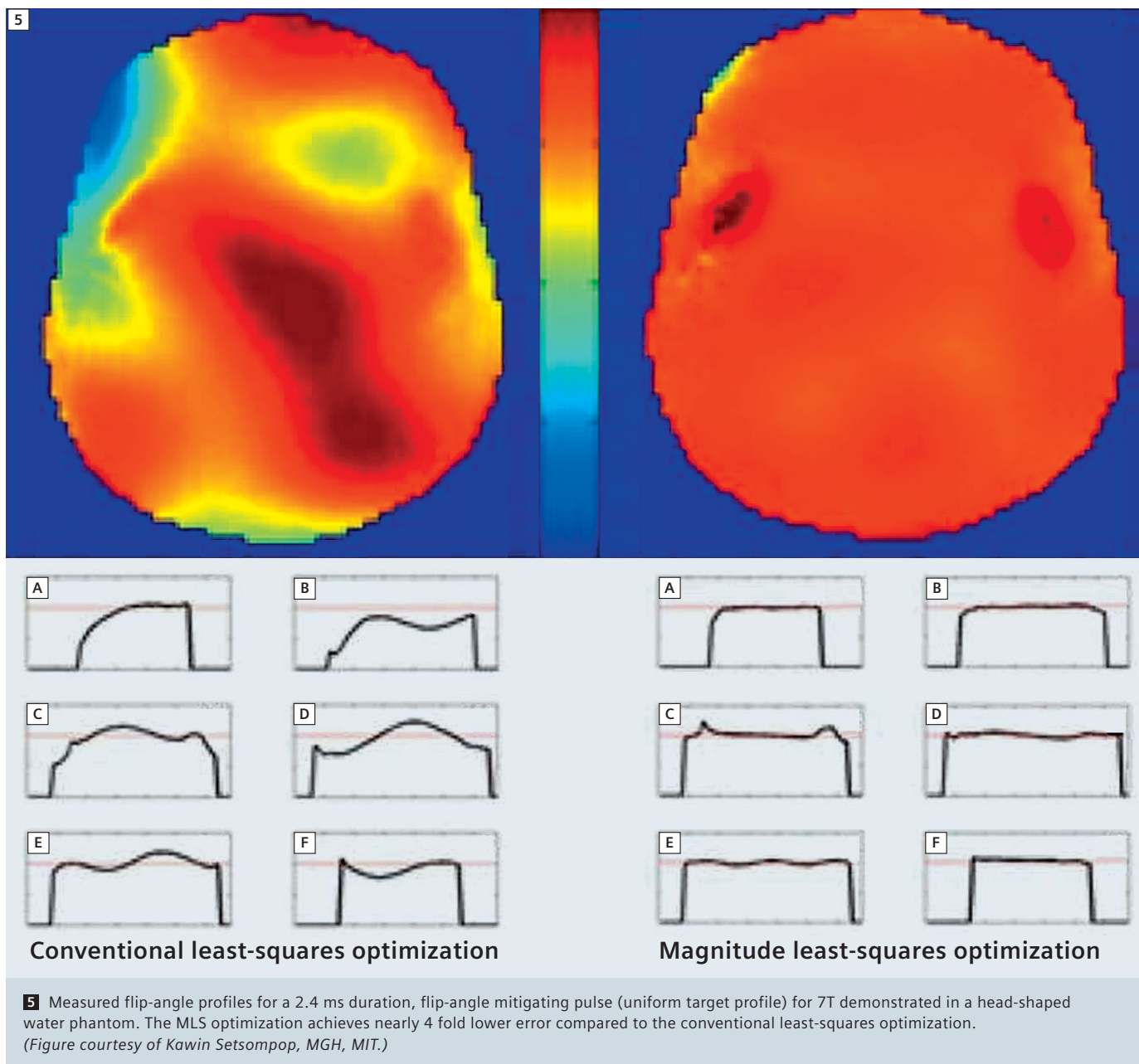
RF excitations appropriately modulated in amplitude and phase during time-varying gradients offer the potential of spatially tailored RF phase and amplitude in the excitation [4]. Although such pulses have been demonstrated for many years, the lengthy encoding period needed duration of these pulses (as long as 50 ms) has precluded their routine use. Parallel transmission addresses



this limitation by accelerating the excitation encoding gradient trajectory analogously to how parallel receive provides unaliased images with an accelerated encoding trajectory [5, 6]. A practical goal is to achieve 3D excitation pulses in less than 5 ms with a spatial profile that can mitigate the observed B_1 pattern in the head or body. This short duration is needed to be useful in common anatomical imaging sequences such as TSE, MPRAGE and FLASH.

Shaping the 2D spatial flip-angle distribution of an RF excitation requires modulated RF amplitude and phase while the gradients trace an excitation k-space trajectory, typically a spiral or echo-planar path. In practice, we first choose a target magnetization map, which is proportional to the flip angle map for small flip angles. For example, the target magnetization map might be a uniform flip-angle distribution or a selected region around

the anatomy of interest (for zoomed imaging). The calculation of the corresponding RF waveform is greatly simplified in the low flip angle case where it can be reduced to a k-space or Fourier analysis [4]. The RF excitation during such a gradient traversal is viewed as a series of short, small flip angle excitations. The phase and amplitude of these small RF pulses is altered so that the deposition of RF energy in the “excitation k-space” matrix is the Fourier transform of the desired spatial flip-angle map. In parallel transmit, the pulse duration is significantly reduced since an accelerated, under-sampled excitation k-space trajectory is used. The missing information is provided by incorporation of the spatial profiles of the multiple transmit array elements in the design process so that an unaliased excitation pattern is achieved.



Regularization of Specific Absorption Rate (SAR) and relaxation of phase constraints

A critical observation about the parallel transmit pulse design problem is that there are many different solutions for the RF pulses that achieve a very similar fidelity to the target excitation pattern. Knowing this, it is beneficial to choose a

solution which produces a “close enough” pattern but minimizes SAR. This can be achieved by explicitly penalizing pulse amplitude when solving for the optimal pulse shapes, thus resulting in a significantly lower global SAR with little loss of excitation pattern fidelity [7]. Another important observation that yields significant payoff in the RF design

is that the vast majority of MR applications ignore the phase in the final image (only magnitude images are viewed). In this case, the excitation can tolerate a slow phase roll across the FOV with no impact on the final image. We have capitalized on the relaxation of the phase restraint by developing a “Magnitude Least Squares” (MLS) algorithm for solv-

ing the parallel transmit pulse design optimization [8]. In this scheme, the algorithm attempts to achieve the target excitation pattern in magnitude, but allows slow phase variations across the FOV. The relaxed constraint allows a higher fidelity in the magnitude pattern or a lower pulse power (i.e. low global SAR). Figure 5 compares the MLS result for a slice-selective excitation with uniform target flip-angle distribution to the conventional Least Squares optimization. A two-fold improvement in target magnitude fidelity was achieved with similar SAR. Conversely, the same target fidelity could be achieved with a ~ 2 fold reduction in SAR.

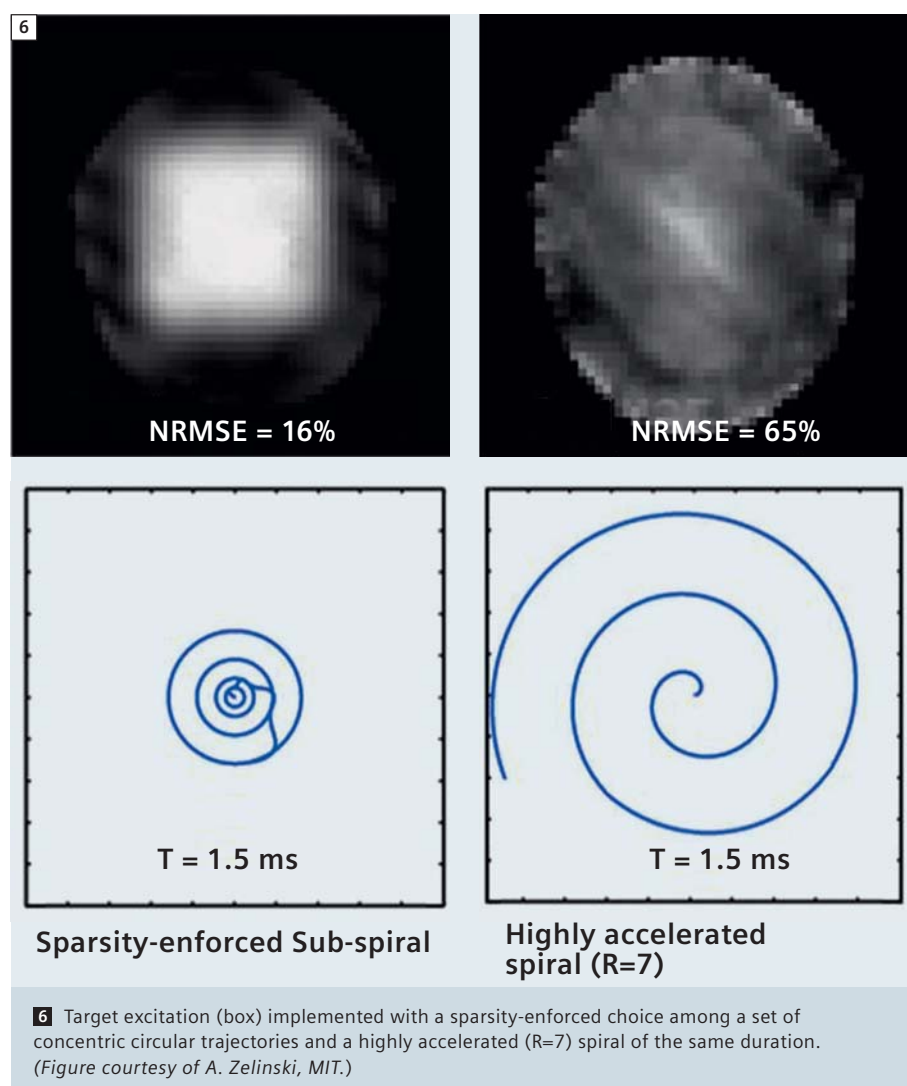
3D shaped excitations

Extending accelerated spatially tailored pulses to general 3D shapes requires covering k-space in 3 directions and is consequently very time consuming. Nonetheless, full 3D excitation is required for many applications, including adding in-plane flip-angle modulation to the traditional slice-selective excitation. We explored the capabilities for these 3D shaped excitations by using a variant of the echo-volume or “spokes” trajectory. This design class of RF excitation pulses can be viewed as multiple slice-selective RF pulses in z that are played out with different amplitude and phase modulations for each (k_x, k_y) -location, providing a conventional slice-selection in z, but with spatial modulations in the image plane, (x, y) . Since the conventional axial slice select gradient can be viewed as a line segment in excitation k-space along k_z , multiple such lines look like a collection of spokes orthogonal to (k_x, k_y) when viewed in k-space. The parallel transmit problem then reduces to determining the number and (k_x, k_y) location of such spokes, as well as the calculation of the phase and amplitude of each transmit channel for each spoke to achieve the desired modulation in the x, y plane.

The excitation trajectory design problem

is guided by our knowledge of the desired target excitation pattern and B_1 profiles of the transmit array elements, and further augmented by a SAR penalty term in the optimization cost-function. Thus, the k-space trajectory and RF pulse can be jointly optimized to produce a higher fidelity excitation pattern while satisfying constraints on overall SAR. When a mode-mixing strategy is employed in the transmit array, we can additionally choose which modes to connect to the transmit channels based on the excitation trajectory. Since the excitation k-space amplitudes and phases

are related to the target pattern by the Fourier transform (for low flip-angle excitations), the k-space trajectory can be limited to regions with the largest magnitude Fourier coefficients. However, this does not take advantage of the “don’t care” regions outside the body but within the FOV. A better strategy is to let a sparsity-enforcing algorithm choose the trajectory from among a discrete set of k-space grid points allowing an explicit trade-off between excitation fidelity and pulse length [9]. The simulation in Figure 6 demonstrates the advantage of choosing a subset of circular trajectories



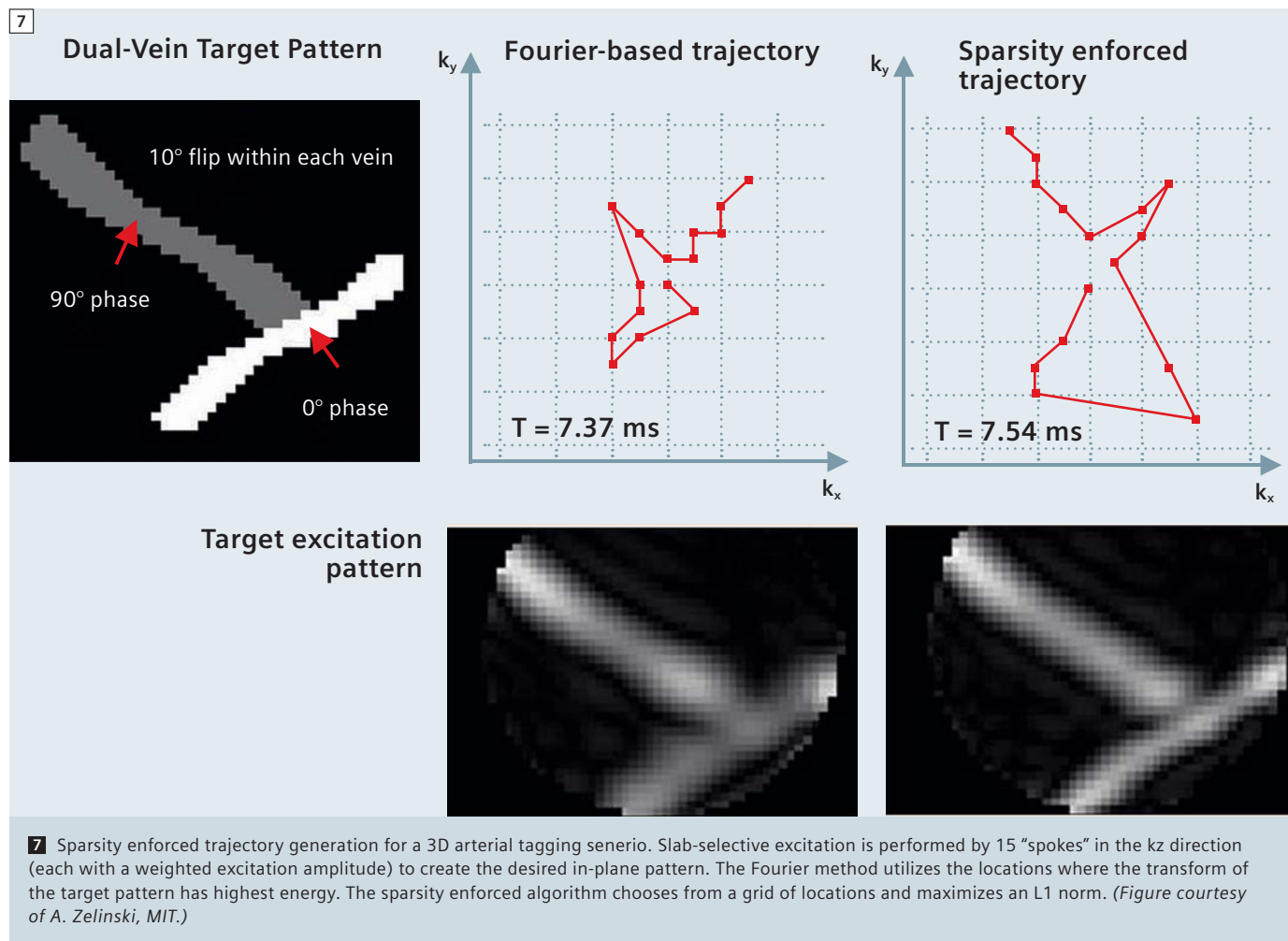
among a candidate set of circles in the k_x, k_y plane compared to a highly accelerated spiral excitation of the same overall duration. Figure 7 shows a similar optimization from among a grid of possible locations in the k_x, k_y plane of the “spokes” trajectory. The target excitation is slab-selective in z , and selectively excites the two simulated arteries in-plane, such as might be used for a vessel-selective arterial spin labeling experiment. In this case the two crossing vessels are tagged with excitations differing in RF excitation phase by 90° , demonstrating tight RF control in both magnitude and phase for a challenging 3D excitation target.

B₁ mitigation at 7T

Parallel excitations were performed on both head-shape water phantom and in

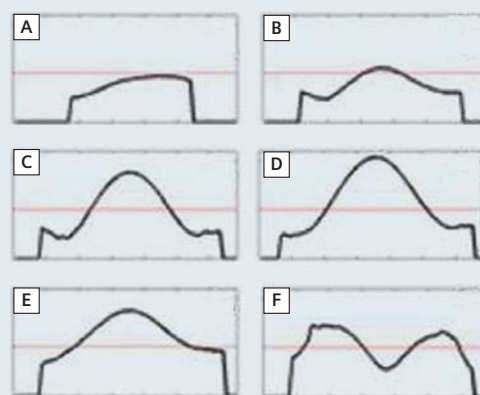
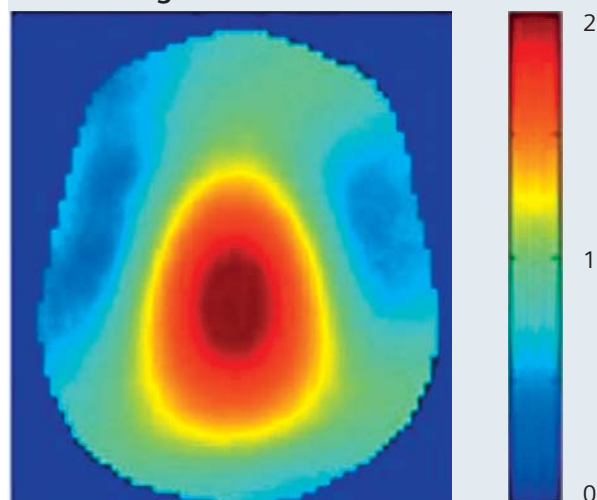
vivo human studies at 7T [10]. Both slice-selective B₁ mitigated excitation and arbitrarily shaped volume excitations were created and validated via a 16-element degenerate strip-line array coil driven with a Butler matrix utilizing the 8 most favorable birdcage modes. RF and gradient excitation waveforms were designed using the MLS optimization, and a spokes’ placement optimization algorithm. With this design method, optimized parallel excitation waveforms for human B₁ mitigation were only ~50% longer than conventional single-channel slice-selective excitation while significantly improving flip-angle homogeneity. We compared the B₁ mitigation performance by parallel transmission to “RF shimming,” which can be viewed as a simplified form of parallel transmit where the array elements are driven

with individual amplitudes and phase shifts but not separate pulse shapes. For the slice-selective excitation, the RF shimming can be viewed as a special case of the “spokes” trajectory where only a single spoke (at the center of (k_x, k_y) -space) is employed. Thus, RF shimming utilizes the spatial patterns of the transmit array, but not the encoding ability of the gradient trajectory. Figure 8 shows the measured B₁ map for the “uniform” birdcage excitation, the RF shimming and pTX with spokes trajectory (all slice selective excitations). The full pTX method clearly demonstrates superior B₁ mitigation performance. The phantom inhomogeneity is similar in shape to that of the head, but exhibits more severe field variations than in the human head; a 3 fold variation in flip angle across the slice. Nevertheless, the



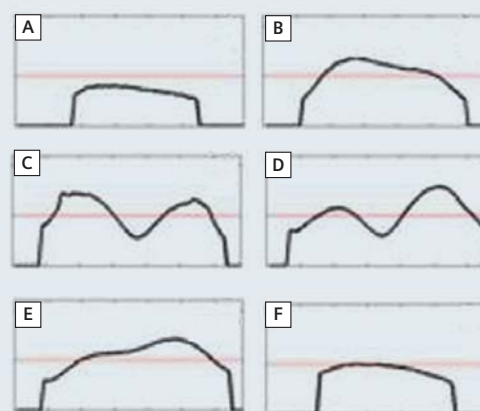
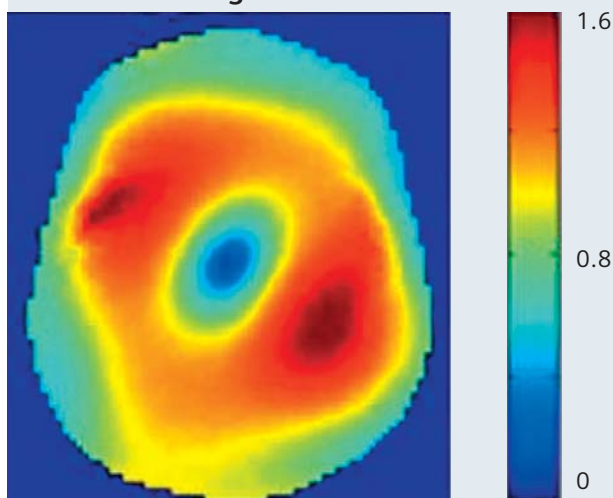
B₁ maps in a head shaped water phantom at 7T.

8A Birdcage mode

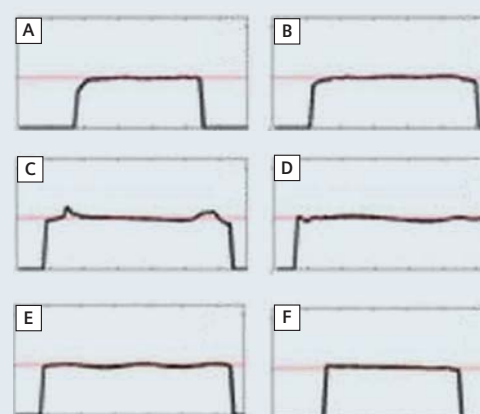
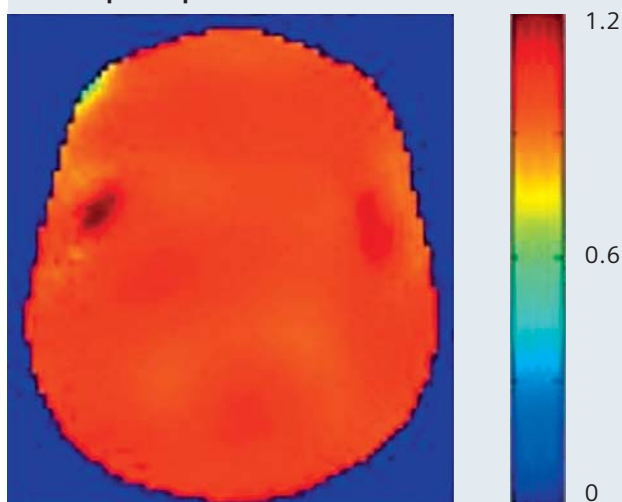


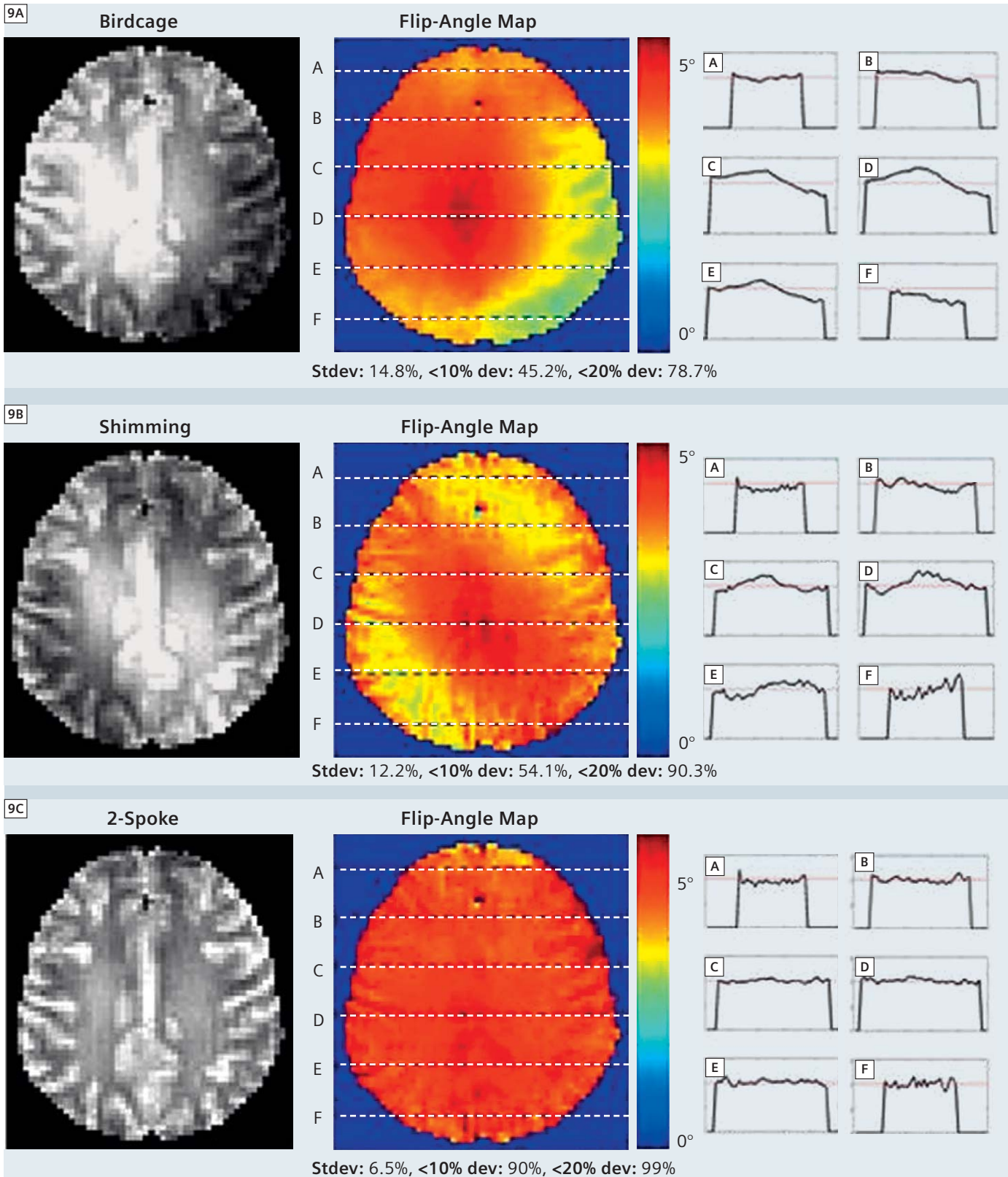
8 Comparison of B₁ inhomogeneity mitigation in slice-selective excitations at 7T (head-shaped phantom) using **A**: conventional birdcage excitation (SD of B₁ across head = 42% of mean), **B**: RF shimming (identification of optimal amplitude and phase excitation settings) with 8-channel transmit array (SD = 29% of mean) and **C**: parallel TX with 3-spoke trajectory (2.4 ms duration) (SD = 5% of mean). (Figure courtesy of K. Setsompop MGH, MIT.)

8B RF shimming



8C 3 spoke pTX

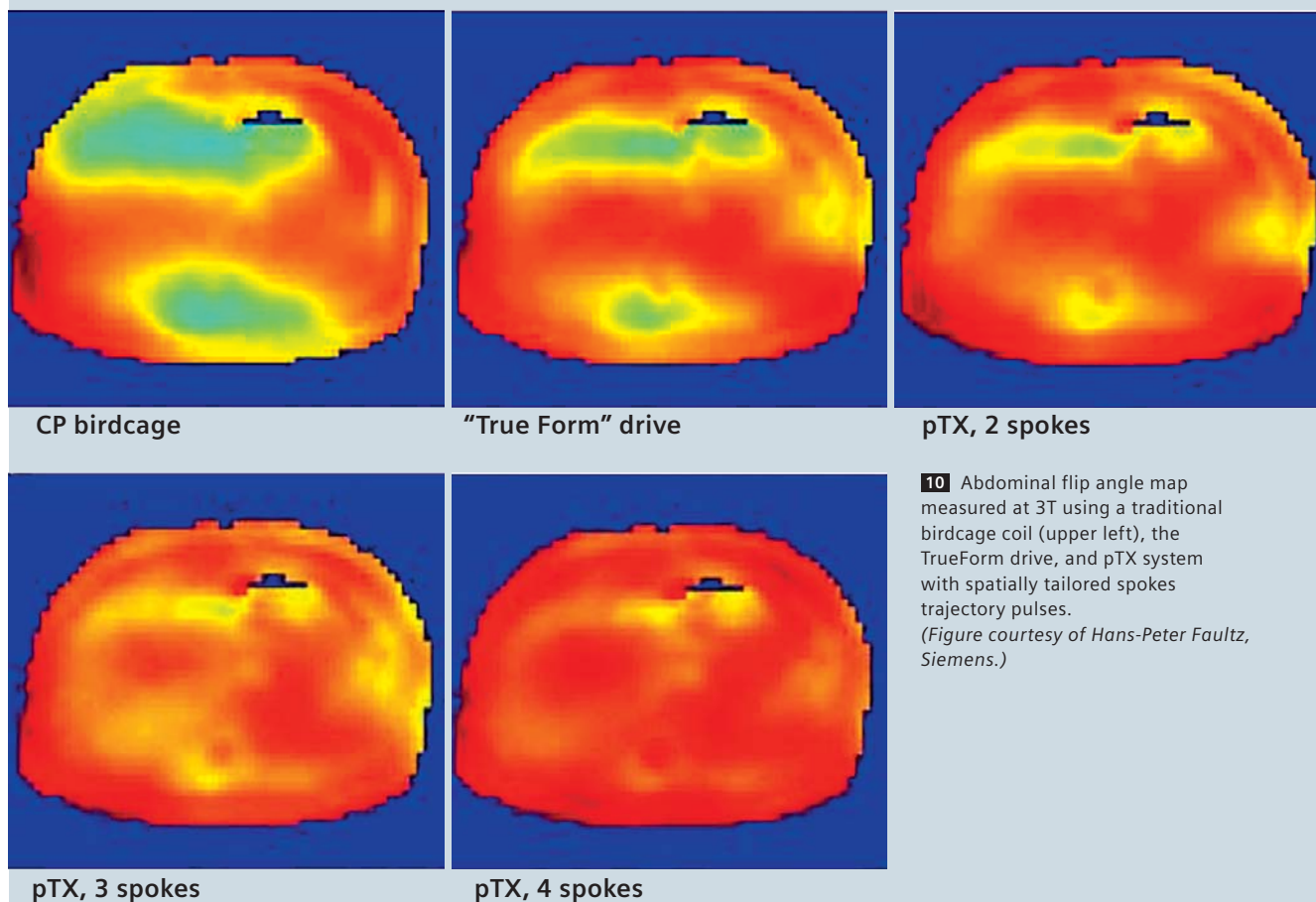




9 Flip-angle inhomogeneity at 7T in the human head using 3 methods (conventional birdcage excitation, RF shimming and pTX with spokes trajectory.) Subject #5 (who displayed the most severe inhomogeneity) is shown. Gray scale images show a proton density-weighted low flip-angle image with the receive profile divided (leaving only variations due to transmit.) Color scale image is a quantitative flip angle map acquired with each of the 3 methods. (Figure courtesy of K. Setsompop MGH, MIT.)

10

3T flip angle maps in abdomen



10 Abdominal flip angle map measured at 3T using a traditional birdcage coil (upper left), the TrueForm drive, and pTX system with spatially tailored spokes trajectory pulses. (Figure courtesy of Hans-Peter Fautz, Siemens.)

3-spoke trajectory and 8-channel array is sufficient to remove the vast majority of the inhomogeneity. Figure 9 shows B_1 maps obtained from one of 6 healthy subjects (studied with institutional approval and informed consent). In this case a 2.3 ms duration 2-spoke slice-selective trajectory was used with the 8-channel system and the MLS design method. The birdcage and RF shimming acquisition used a 1.4 ms sinc-like excitation. While some contamination from anatomy is seen in the B_1 transmit maps, the pTX method significantly reduced the B_1 inhomogeneity (standard deviation (Stdev.) across slice was 8% of the mean compared to 21% for the birdcage excitation and 14% for the RF shim).

Figure 10 shows the parallel transmit method applied to a similar flip-angle inhomogeneity problem; the abdomen at 3T. Here a similar wave-cancellation occurs in body imaging where the size of the body becomes comparable to the wavelength of the RF. The conventional circularly polarized birdcage can be significantly improved upon by optimizing the phase relationship between the drive ports of the coil to produce a more uniform and efficient elliptical polarization tailored to the body. Further gains in uniformity were realized with parallel transmit and the 3D spokes spatially tailored excitation pulses calculated based on knowledge of the B_1 field profiles of the transmit array elements.

SAR considerations

While the results in Figure 8 demonstrate the ability of the parallel transmit method to mitigate the inhomogeneous flip-angle distribution at high field, the spokes pulses used more RF energy to achieve the desired flip angle than the simple birdcage transmit (but less than the RF shim). The total pulse energy for the birdcage, RF shim, and pTX-spokes methods were 10.7 mJ, 24.8 mJ, and 21.8 mJ respectively. This suggests that the parallel methods achieve uniformity only with some degree of self-cancellation among the fields or excited magnetization. A similar effect is seen in the 2D spiral trajectories, where pulse energy significantly increases with acceleration,

even with an explicit B_1 amplitude penalty in the pulse design cost-function and local SAR levels are difficult to predict [11]. An example is shown in Figure 11 where the local SAR is calculated for a series of box-shaped excitations placed at 5 different positions in the head (left to right). The spatially tailored 2D pulses used an 8-channel array and spiral trajectories with accelerations ranging from $R=1$ to $R=8$. The pulse design maintained a constant fidelity to the target pattern by trading off the pulse amplitude constraint and the fidelity constraint. The local SAR was calculated from the E_1 fields in a multi-tissue head model for the array and pulse. The first observation based on these results is the enormous cost in local SAR incurred by keeping the fidelity constant in the face of increasing parallel transmit acceleration (nearly 3 orders of magnitude variation in local SAR!). The second observation is that local SAR varies significantly with the position of the excitation box. For low accelerations the central box positions have the lowest SAR, while the higher accelerations, the peripheral

positions have lower SAR.

For evaluation and monitoring of SAR, the main concern for human imaging is the potential for the E_1 fields from the array elements to constructively superimpose locally, creating a local SAR hot spot. A simple estimate demonstrates how serious the “worst-case” superposition can be. If the E_1 fields from the eight elements superimpose and generate an 8 fold increase compared to a single element, then the local SAR at that location will increase 64 fold. Similarly, electric fields can destructively interfere. This means that if one channel stops transmitting due to equipment failure, the local SAR can actually increase.

Therefore, in addition to monitoring the average power from each channel, a pTX system must make an estimate of local E_1 fields and how they superimpose so that the local SAR limits are not exceeded. As the pulse design becomes increasingly tailored to the individual patient, the local SAR check must also move in this direction. This will require fast local SAR calculation methods based on the field patterns calculated for the array

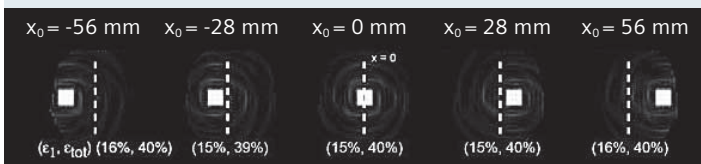
and the specific pulse designed for that subject. Preliminary work has exploited the ability to penalize high-amplitude RF pulses in the pulse design optimization, but significant future development is needed to explicitly include local SAR regularization in the design of the RF pulses and enable a flexible trade-off between RF excitation properties (due to B_1) and local SAR distribution (due to E_1).

Remaining challenges

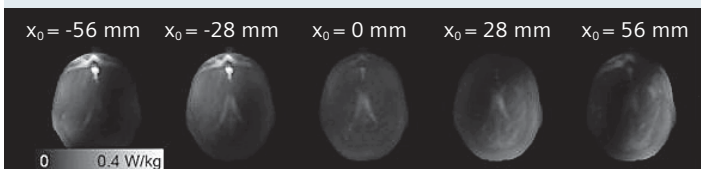
In addition to the SAR estimation and monitoring problem, several other outstanding challenges must be solved before accelerated 2D and 3D spatially tailored excitations can be routinely employed. The method relies on a fast but accurate mapping of the B_1 transmit field in the subject, which is an intense and ongoing area of innovation with several promising methods being proposed in the literature. A second area of innovation is the calculation of high flip-angle spatially tailored RF pulses. Most of the work performed to-date has assumed the small flip angle approximation. While this approximation provides

11

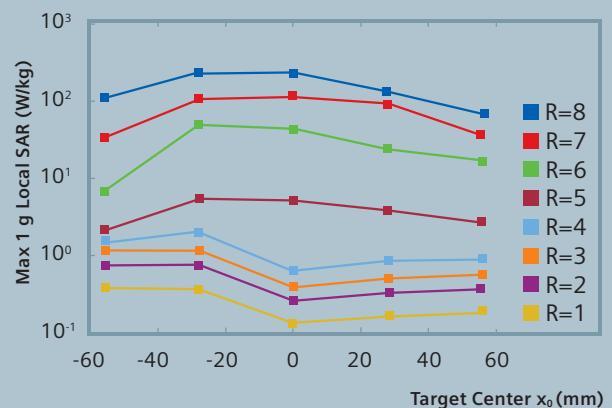
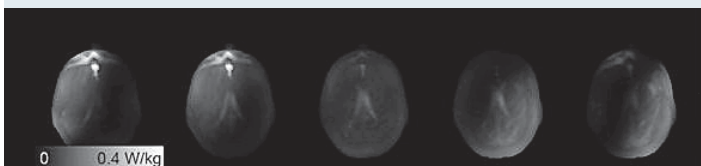
R=4, Excitations



R=1, Max 1g SAR



R=5, Max 1g SAR



11 SAR as a function of acceleration and shift along x (fixed excitation quality). Top row: $R = 4$ excitations. Second and third rows: maximum intensity projections of local 1g SAR maps due to $R = 1$ and $R = 5$ pulses at each spatial box location. Right: maximum 1g SAR as a function box position for each R . (Figure courtesy of A. Zelinski, MIT.)

for elegant and computationally tractable RF designs with familiar tradeoffs based on well known Fourier transform properties, large flip-angle pulses are central to many clinical pulse sequences and the low flip-angle constraint needs to be addressed for general applicability of pTX. This computational problem is now just starting to be addressed.

Conclusions

Theoretical work on parallel RF transmission and recent experimental validations on 8-channel prototype systems at 3T and 7T indicate that parallel excitation has the potential to overcome critical obstacles to robust and routine human scanning at high field strength. As these developments are extended, high-field human imaging will be possible with essentially constant flip angle, and therefore no compromise in signal strength or clinical contrast, across the human head and body with RF pulse durations comparable to current slice selective pulses. While most work has been concentrated on head-sized transmitters at 7T, the methods are readily translatable to body transmit coils at 3T. Of course, intriguing research questions remain open in several areas, including optimal coil array designs that minimize element couplings and maximize spatial orthogonality of individual channels; the estimation of local SAR from a subject-specific spatially tailored RF pulse; and the development of rapid and robust RF pulse designs that extends the current low-flip angle domain to arbitrary excitation angle, such as spin echoes, saturation, and inversions pulses. However, with continued active research in these areas, progress is likely to accelerate, and logical extensions of the architecture of a current clinical scanner readily accommodates the requirements of a general parallel RF excitation system supported by fast, subject and application tailored RF pulse design software capable of extending MR excitation from the simple slice-select to the more generally tailored anatomy- or application-specific RF excitation pattern.

Acknowledgements

The authors would like to acknowledge the many researchers at Siemens, MGH and MIT whose work is summarized here. We especially acknowledge Kawin Setsompop, Vijay Alagappan, and Adam Zelinski whose thesis work was reviewed here. We also thank Ulrich Fontius and Andreas Potthast for their work setting up the 8-channel 3T and 7T systems and Franz Hebrank and Franz Schmitt for their leadership role in the collaboration and Josef Pfeuffer, Axel vom Endt and Hans-Peter Fautz for their on-going support.

We acknowledge grant support from the NIH (P41RR14075, R01EB007942, and R01EB006847) and a research agreement and research support from Siemens Healthcare. One of us (LLW) acknowledges consulting income from Siemens Healthcare.

WIP – Works in Progress. This information about this product is preliminary. The product is under development and not commercially available in the U.S., and its further availability cannot be ensured.

References

- Butler, J. and R. Lowe, Beamforming matrix simplifies design of electronically scanned antennas. *Electron Design*, 1961. 9: p. 170–173.
- Tropp, J., Mutual Inductance in the Bird-Cage Resonator. *J Magn Reson*, 1997. 126(1): p. 9–17.
- Alagappan, V., et al. Mode Compression of Transmit and Receive Arrays for Parallel Imaging at 7T. in *International Society for Magnetic Resonance in Medicine*. 2008. Toronto, Canada.
- Pauly, J., D. Nishimura, and A. Macovski, A k-space analysis of small-tip angle excitation. *J Magn Reson*, 1989. 81: p. 43–56.
- Katscher, U., et al., Transmit SENSE. *Magn Reson Med*, 2003. 49(1): p. 144–50.
- Zhu, Y., Parallel excitation with an array of transmit coils. *Magn Reson Med*, 2004. 51(4): p. 775–84.
- Zelinski, A., et al., Comparison of three algorithms for solving linearized systems of parallel excitation RF waveform design equations: Experiments on an eight-channel system at 3 Tesla. *Concepts in Magnetic Resonance Part B: Magnetic Resonance Engineering*, 2007. 31B: p. 176–190.
- Setsompop, K., et al., Magnitude least squares optimization for parallel radio frequency excitation design demonstrated at 7 Tesla with eight channels. *Magn Reson Med*, 2008. 59(4): p. 908–15.

- Zelinski, A.C., et al., Sparsity-enforced slice-selective MRI RF excitation pulse design. *IEEE Trans Med Imaging*, 2008. 27(9): p. 1213–29.
- Setsompop, K., et al., Slice-selective RF pulses for in vivo B1+ inhomogeneity mitigation at 7 tesla using parallel RF excitation with a 16-element coil. *Magn Reson Med*, 2008. 60(6): p. 1422–32.
- Zelinski, A.C., et al., Specific absorption rate studies of the parallel transmission of inner-volume excitations at 7T. *J Magn Reson Imaging*, 2008. 28(4): p. 1005–18.
- Shinnar, M. and J.S. Leigh, The application of spinors to pulse synthesis and analysis. *Magn Reson Med*, 1989. 12(1): p. 93–8.
- Shinnar, M., et al., The synthesis of pulse sequences yielding arbitrary magnetization vectors. *Magn Reson Med*, 1989. 12(1): p. 74–80.
- Shinnar, M., L. Bolinger, and J.S. Leigh, The use of finite impulse response filters in pulse design. *Magn Reson Med*, 1989. 12(1): p. 81–7.
- Shinnar, M., L. Bolinger, and J.S. Leigh, The synthesis of soft pulses with a specified frequency response. *Magn Reson Med*, 1989. 12(1): p. 88–92.
- Pauly, J., et al., Parameter relations for the Shinnar-Le Roux selective excitation pulse design algorithm. *IEEE Tr Medical Imaging*, 1991. 10(1): p. 53–65.
- Mao, J.M., TH, K. Scott, and E. Andrew, Selective inversion radiofrequency pulses by optimal control. *J Magn Reson*, 1986. 70(2): p. 310–318.
- Conolly, S., D. Nishimura, and A. Macovski, Optimal control solutions to the magnetic resonance selective excitation problem. *IEEE T Med Imaging*, 1986. MI-5(2): p. 106–115.
- Geen, H., S. Wimperis, and R. Freeman, Band-selective pulses without phase distortion. A simulated annealing approach. *J Magn Reson Med*, 1989. 85(3): p. 620–627.

Contact

Lawrence L. Wald
Associate Professor of Radiology
Athinaoula A. Martinos Center for Biomedical Imaging
Department of Radiology
Massachusetts General Hospital
Harvard Medical School and
Harvard-MIT Division of Health Sciences and Technology
wald@nmr.mgh.harvard.edu

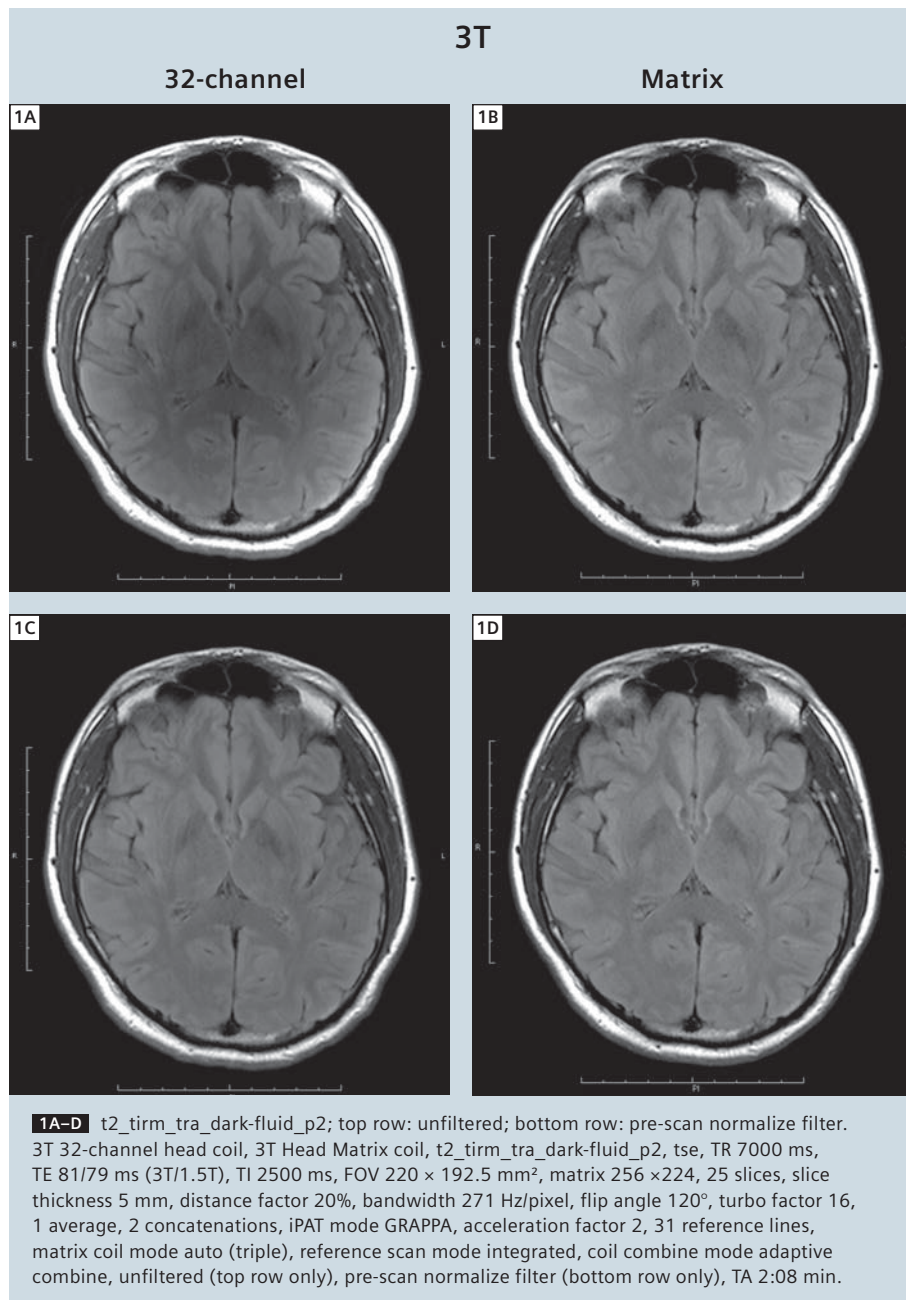
Elfar Adalsteinsson
Associate Professor
Department of Electrical Engineering and Computer Science
Harvard-MIT Health Sciences and Technology
Massachusetts Institute of Technology
elfar@mit.edu

Fast Clinical Protocols at 1.5T and 3T with Matrix and 32-Channel Head Coils

Thomas Benner

Athinoula A. Martinos Center for Biomedical Imaging, Department of Radiology, Massachusetts General Hospital and Harvard Medical School, Boston, MA, USA

In routine clinical MR imaging, short scan times are advantageous for patient compliance, patient throughput and image quality (images are less likely to be affected by motion) but can usually only be achieved at the cost of spatial resolution, coverage or image quality i.e. lower signal-to-noise ratio (SNR). The new 32-channel head coils for 1.5T and 3T provide better SNR and better parallel imaging performance compared to the standard 12-channel Head Matrix Coil [1, 2]. The use of these new coils should therefore allow very short acquisition times at higher acceleration factors at comparable image quality i.e. without loss of SNR and without increase in iPAT (Integrated Parallel Acquisition Technique) related image artifacts. For this report, T1-weighted, T2-weighted, FLAIR, and diffusion tensor imaging (DTI) scans were performed at 1.5T (MAGNETOM Avanto, software version syngo MR B 15A SP2) and 3T (MAGNETOM Trio, A Tim System, software version syngo MR B15A SP2) with the Head Matrix coil and the 32-channel head coil, respectively. While not necessarily achieving optimal contrast at each field strength, the same imaging parameters were used at both field strengths and both head coils for ease of comparison. Echo-planar imaging (EPI) allows ultra-fast image acquisition and may therefore present an alternative to conventional imaging. For comparison, T1-weighted EPI, T2-weighted EPI and FLAIR EPI scans were acquired in addition to the conventional imaging scans.



Altogether, four studies were performed: one study using the Head Matrix coil and one using the 32-channel head coils on each of the two MR scanners. The same healthy appearing volunteer was scanned. AutoAlign was used to ensure closely matching slice positioning between the studies [3–5]. Each study lasted about 25 minutes.

The resulting image data was compared according to

- scan type being used i.e. conventional scans vs. EPI scans,
- acceleration factor being used i.e. PAT 2 vs. PAT 3 vs. PAT 4,
- head coil being used i.e. 32-channel head coil vs. Head Matrix coil, and
- field strength being used i.e. 3T vs. 1.5T.

The performance of the image normalization filter was examined as well.

Signal intensity normalization

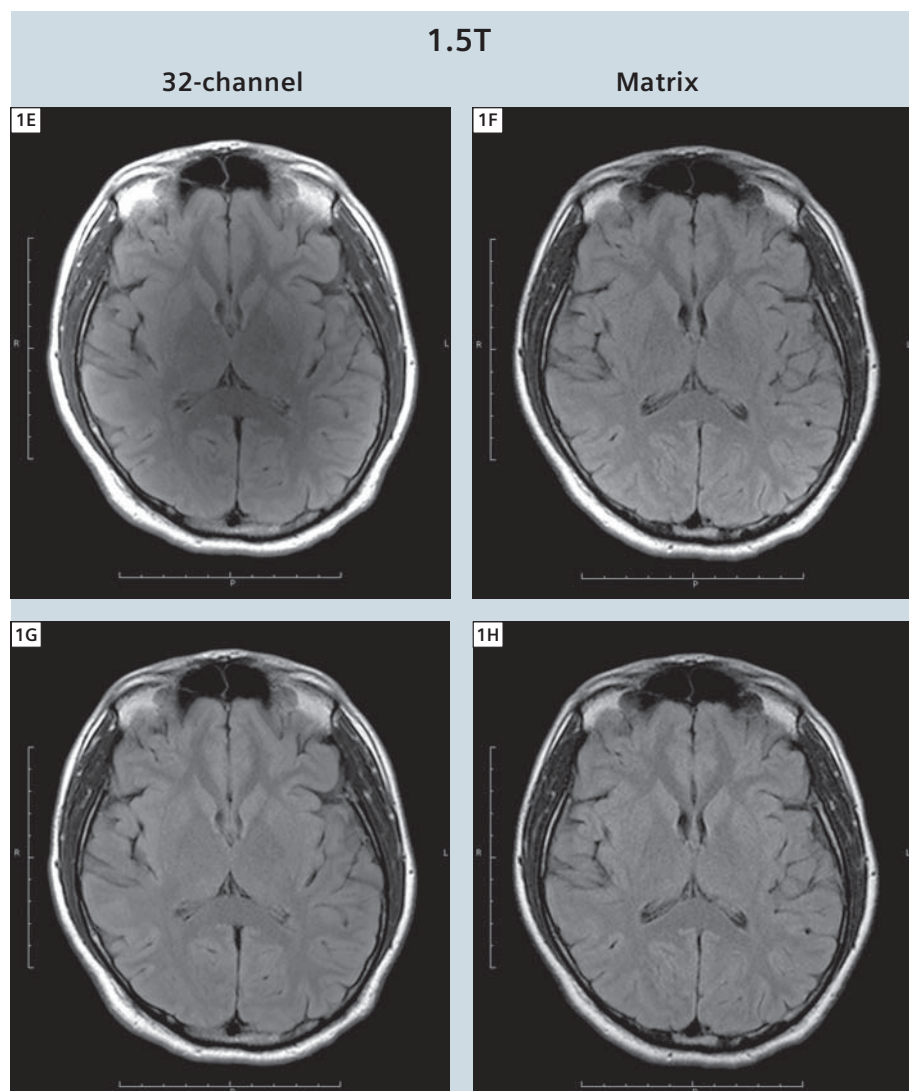
Smaller coil elements coupled with closer proximity of the head to these coil elements causes a more pronounced signal intensity as well as SNR gradient. To reduce the large signal intensity variations from periphery to the center of the brain a signal intensity normalization filter should be used. As expected, the signal intensity variations are larger on images from the 32-channel head coil compared to the more subtle effect on images from the Head Matrix coil (Fig. 1, top row). The signal intensity normalization (pre-scan normalize filter) works well at 1.5T and 3T (Fig. 1, bottom row). This not only applies to the conventional FLAIR scans but also to the T1-weighted, T2-weighted and EPI scans performed.

EPI vs. conventional imaging

Echo-planar imaging allows very fast image acquisition in the order of 10–100's of milliseconds per slice and should therefore allow shorter scan times than conventional imaging.

However, at high spatial resolutions acceleration is essential to achieve short echo times and to reduce susceptibility induced artifacts in EPI. Parallel imaging requires the acquisition of reference

lines at the beginning of the scan, lengthening the scan times by multiple times the repetition time. Thus EPI scans become comparable in duration or even exceed the duration of conventional



1E–H t2_tirm_tra_dark-fluid_p2; top row: unfiltered; bottom row: pre-scan normalize filter. 1.5T 32-channel head coil, 1.5T Head Matrix coil, t2_tirm_tra_dark-fluid_p2, tse, TR 7000 ms, TE 81/79 ms (3T/1.5T), TI 2500 ms, FOV 220 × 192.5 mm², matrix 256 × 224, 25 slices, slice thickness 5 mm, distance factor 20%, bandwidth 271 Hz/pixel, flip angle 120°, turbo factor 16, 1 average, 2 concatenations, iPAT mode GRAPPA, acceleration factor 2, 31 reference lines, matrix coil mode auto (triple), reference scan mode integrated, coil combine mode adaptive combine, unfiltered (top row only), pre-scan normalize filter (bottom row only), TA 2:08 min.

scans. This is also the case if multiple averages or measurements need to be acquired e.g. for increased SNR.

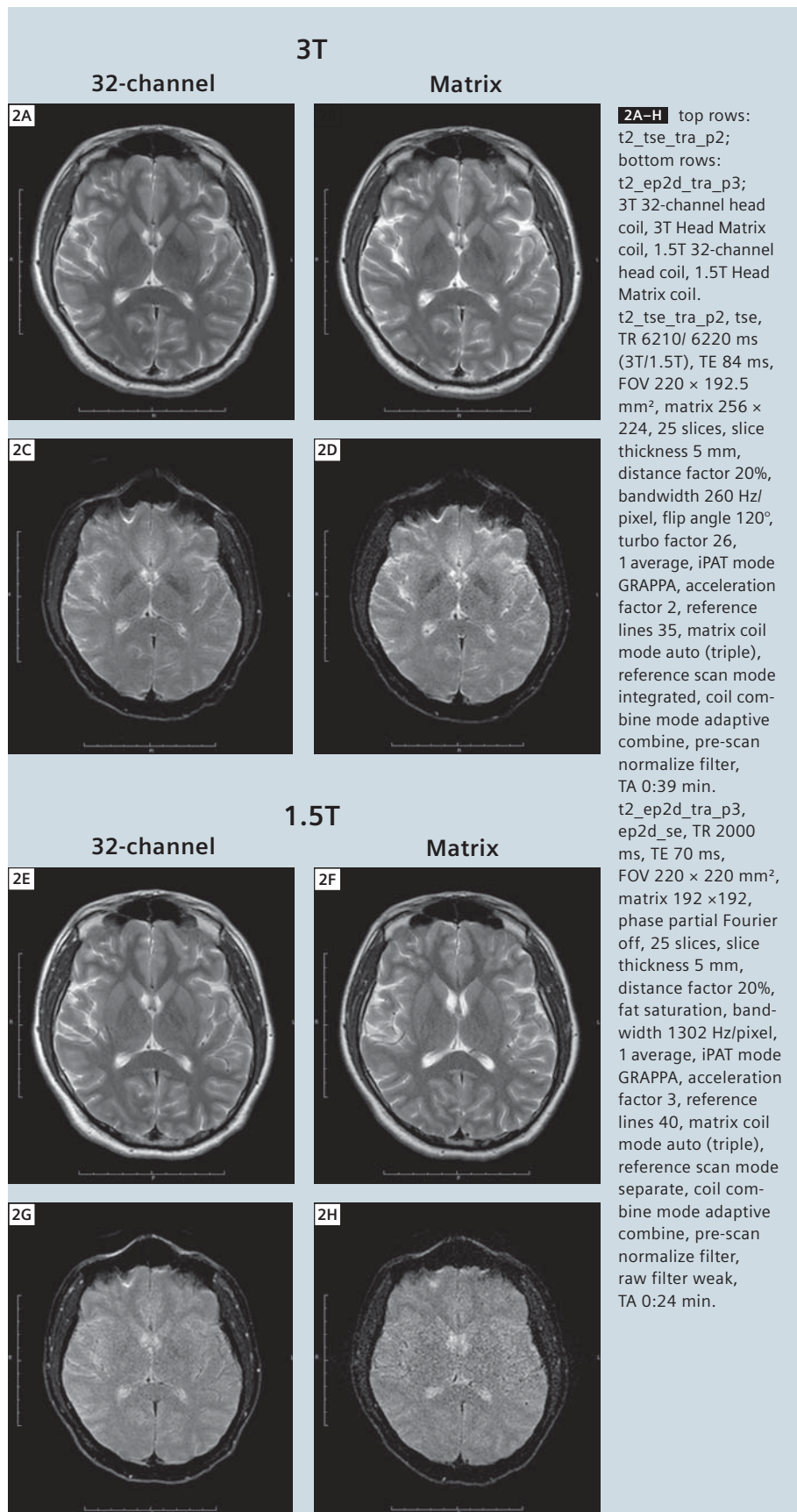
Figure 2 shows T2-weighted images acquired with a conventional TSE scan and an EPI scan. At similar scan times ($t2_tse_tra_p2$, 0:39 min vs. $t2_ep2d_tra_p3$, 0:24 min) the image quality of the TSE data is superior in terms of SNR, contrast, distortions and susceptibility artifacts. The same effect is shown in Figure 3 where images from conventional FLAIR scans are compared to EPI based FLAIR scans ($t2_tirm_tra_dark_fluid_p3$, 1:40 min vs. $t2_ep2d_tra_p3$, 1:47 min). At comparable scan time, the image quality of the conventional scans is superior. The same was found for the T1-weighted scans (images not shown).

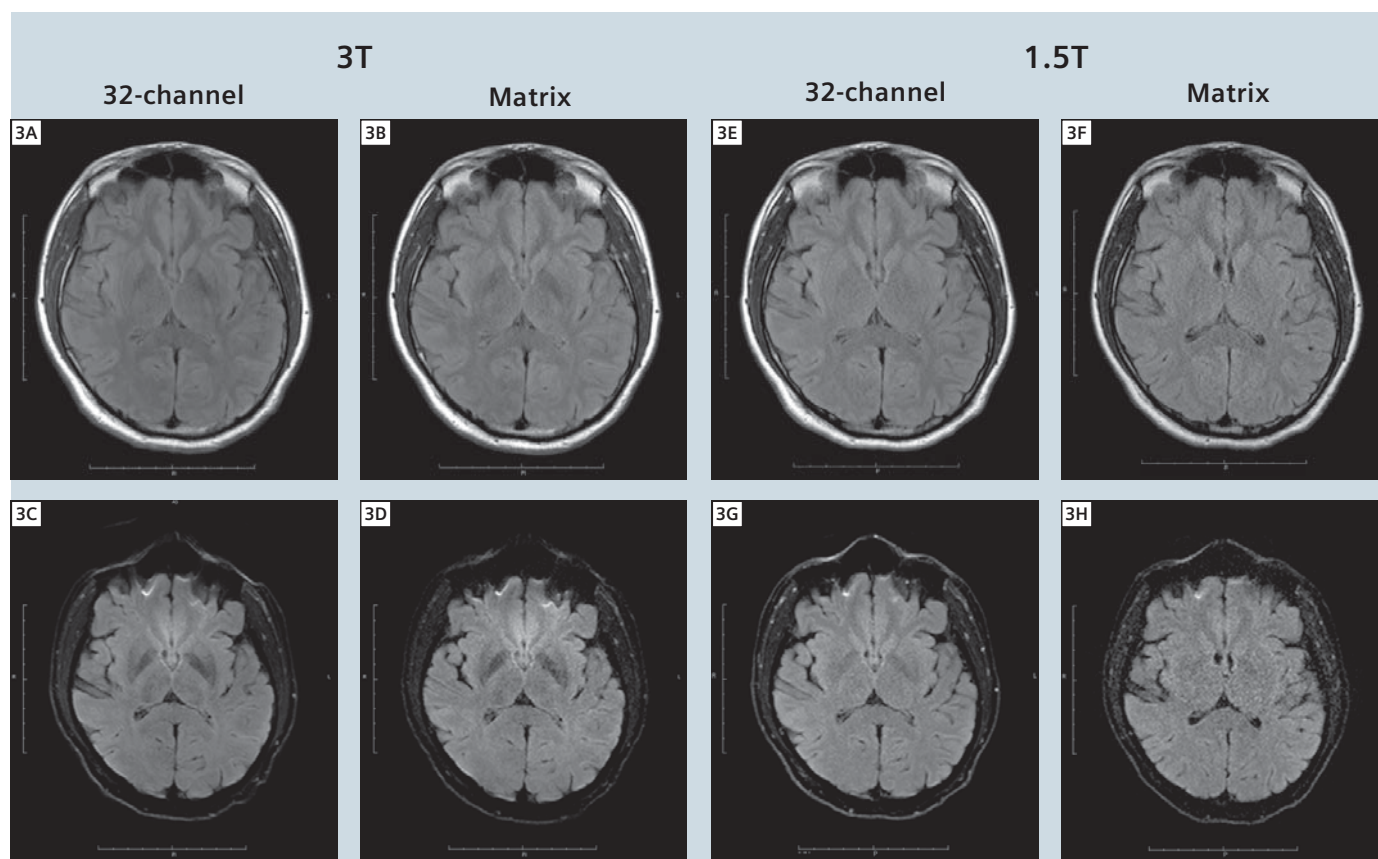
Parallel imaging

A larger number of coil elements usually translates into better acceleration performance (improved g-factor) [2]. This is demonstrated in Figures 4 and 5.

Increasing the PAT factor from 3 to 4 for an EPI FLAIR scan ($ep2d_tra_dark_fluid_p3$ to $ep2d_tra_dark_fluid_p4$) causes little image degradation when using the 32-channel coil at 3T (Fig. 4 A, C). A more pronounced degradation can be found at 3T when using the Head Matrix coil and at 1.5T when using the 32-channel coil (Fig. 4B, D and E, G). An already noisy image at 1.5T with PAT factor 3 is rendered unusable when increasing PAT to a factor of 4 (Fig. 4F, H). The same effect is demonstrated for PAT factor 2 vs. 3 for a conventional T1-weighted scan ($t1_fl2d_tra_p2$ vs. $t1_fl2d_tra_p3$) (Fig. 5). While there is little effect at high field with the 32-channel head coil (Fig. 5A, C), a noticeable increase in noise appears at 3T with the Head Matrix coil and at 1.5T with the 32-channel head coil (Fig. 5B, D and E, G). At 1.5T with the Head Matrix coil, an iPAT related image artifact and noise dominate the picture at a PAT factor of 3 (Fig. 5F, H).

For DTI, increasing the PAT factor from 2 to 3 and to 4 leads to a reduction of distortion artifacts. However, the additional gain is diminishing beyond a PAT factor





3A-H top row: t2_tirm_tra_dark-fluid_p3; bottom row: ep2d_tra_dark-fluid_p3; from left to right: 3T 32-channel head coil, 3T Head Matrix coil, 1.5T 32-channel head coil, 1.5T Head Matrix coil. t2_tirm_tra_dark-fluid_p3, tse, TR 7000 ms, TE 81 ms, TI 2500 ms, FOV 220 × 192.5 mm², matrix 256 × 224, 25 slices, slice thickness 5 mm, distance factor 20%, bandwidth 271 Hz/pixel, flip angle 120°, turbo factor 16, 1 average, 2 concatenations, iPAT mode GRAPPA, acceleration factor PE 3, reference lines PE 32, matrix coil mode auto (triple), reference scan mode integrated, coil combine mode adaptive combine, pre-scan normalize filter, elliptical filter, TA 1:40 min. ep2d_tra_dark-fluid_p3, ep2d_se, TR 15000 ms, TE 83 ms, FOV 220 × 220 mm², matrix 192 × 192, phase partial Fourier off, 25 slices, slice thickness 5 mm, distance factor 20%, fat saturation, bandwidth 1240 Hz/pixel, 2 averages, iPAT mode GRAPPA, acceleration factor 3, reference lines 40, matrix coil mode auto (triple), reference scan mode separate, coil combine mode adaptive combine, pre-scan normalize filter, raw filter weak, TA 1:47 min.

of 2. SNR is decreasing as well as making the images unusable at 1.5T with the Head Matrix coil at a PAT factor of 3. At a PAT factor of 4 only the 32-channel head coil at 3T provides sufficient SNR for interpretable images.

32-channel head coil vs. Head Matrix coil

At both field strengths, 1.5T and 3T, the 32-channel head coil shows improved image quality i.e. higher SNR and better acceleration performance for all scan types performed (Fig. 6). The increased SNR is more dominant at the periphery and less at the center of the brain, which is attributable to the gradient in coil sen-

sitivity with distance from each coil element [1]. Because of the better g-factor of the 32-channel head coil fewer PAT related artifacts are visible even at higher PAT factors.

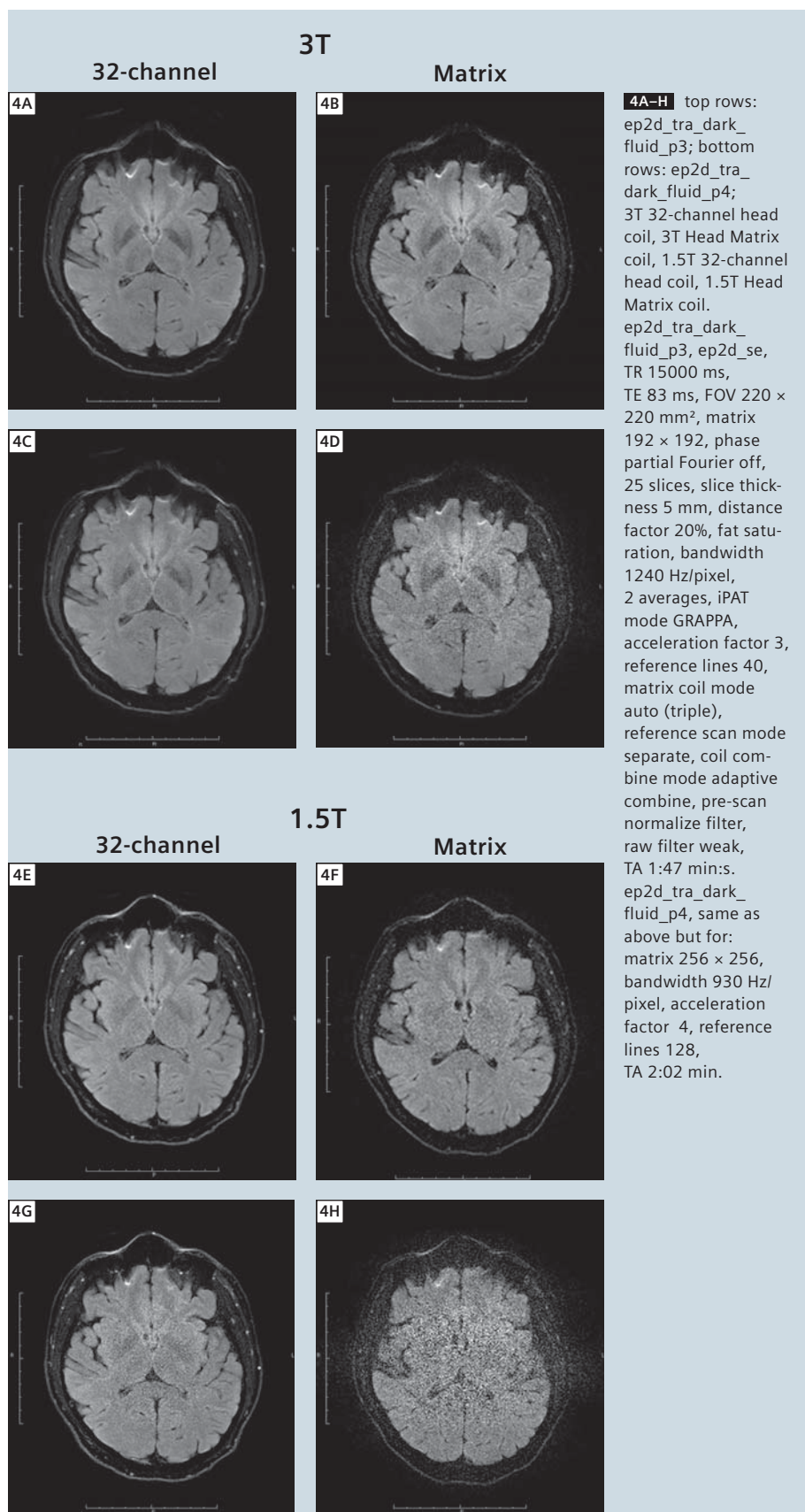
1.5T vs. 3T

A higher field strength (3T vs. 1.5T) translates into increased SNR when using the same head coil i.e. Head Matrix coil at 3T vs. 1.5 (Fig. 6, columns 2 vs. 4) or 32-channel head coil at 3T vs. 1.5T (Fig. 6, columns 1 vs. 3). Interestingly, the image quality (SNR) at 1.5T when using the 32-channel head coil is very comparable to the SNR when using the Head Matrix coil at 3T (Fig. 6, middle

two columns). The most dramatic differences in image quality can be seen between images acquired with the Head Matrix coil at 1.5T compared to those acquired with the 32-channel head coil at 3T (Fig. 6, columns 1 vs. 4).

Conclusions

At both field strengths i.e. 1.5T and 3T, the 32-channel head coils provide image quality that is superior to that from the standard Head Matrix coil. This is mostly due to the increased SNR of the 32-channel head coil compared to the 12-channel Head Matrix coil [1]. Note, though, that the 32-channel head coils exhibit a much larger gradient in SNR

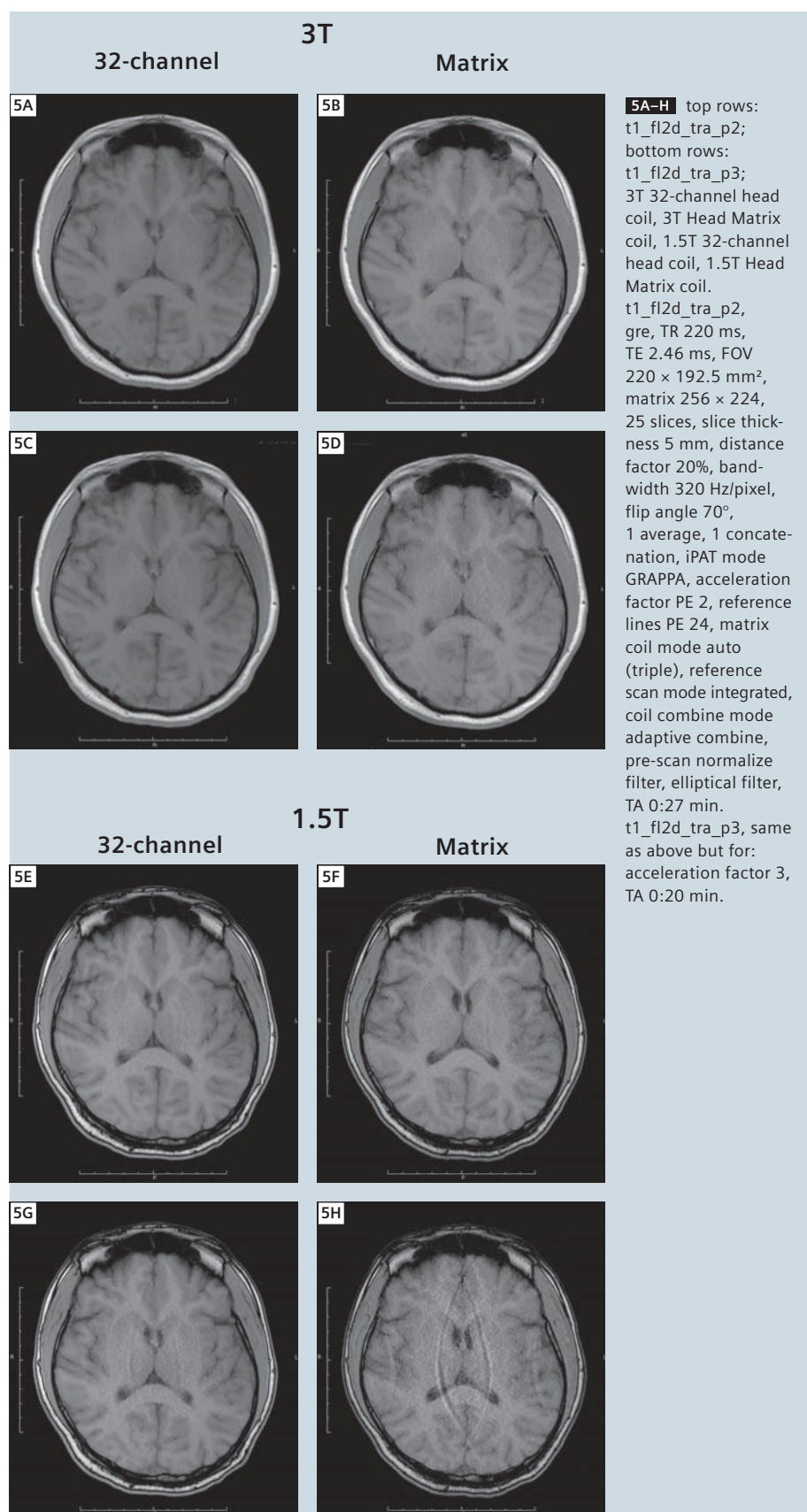


from the periphery to the center of the brain as compared to the Matrix coil, even when the latter is set to triple mode. At the center of the brain, the SNR gain was estimated at 20% compared to >100% at the cortex [1].

It was also shown that the larger number of coil elements allows higher acceleration factors to be used without significantly deteriorating image quality i.e. without causing increase in noise level and PAT related image artifacts. The pre-scan normalize filter works well for all coils at both field strengths to level the signal intensity gradient caused by close proximity to small local coils. No artifacts were seen in any of the scans that may have been caused by the application of this filter.

For fast T1-weighted, T2-weighted and FLAIR clinical protocols, echo-planar imaging is no alternative to conventional imaging with respect to scan times and image quality. However, EPI is unmatched in terms of SNR and acquisition speed for DTI.

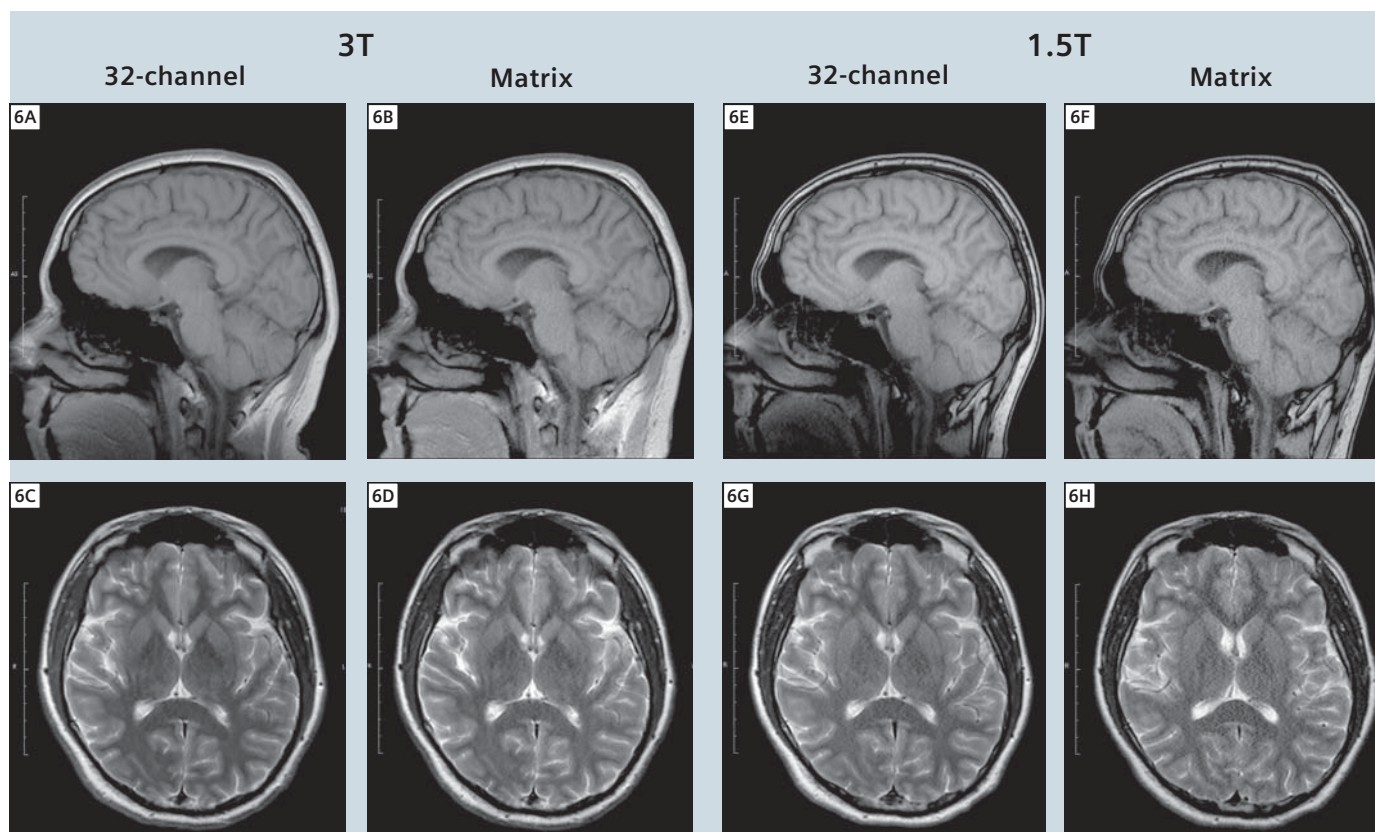
Higher field strength provides the expected boost in SNR as can be appreciated in all scans performed for this study. It must be mentioned that the image quality in terms of SNR of scans performed at 1.5T with the 32-channel head coil are very comparable to the image quality of scans performed at 3T with the Head Matrix coil. In other words: for clinical head imaging the 32-channel head coil may be a worthwhile upgrade to an existing 1.5T MRI scanner. Of course, differences in image contrast between different field strengths e.g. for susceptibility-weighted imaging (SWI) [6] cannot be achieved by using the 32-channel head coil. Table 1 lists a set of recommended protocols that allows the acquisition of T1-weighted, T2-weighted, FLAIR and DTI data in less than 5 minutes while preserving good image quality when using a 32-channel head coil. These protocols apply to both, 1.5T and 3T. However, the image quality (SNR) can be



improved by switching the conventional protocols from a PAT factor of 3 to 2 at the cost of slightly increased scan times. With the use of AutoAlign, these protocols can be set up to allow a “one-click” scan session i.e. after the landmarking of the patient, a single click will load the protocols into the scan queue, perform an automatic slice prescription and acquire the scans. No further user interaction is necessary. As can be seen from the figures, the automatic slice prescription with AutoAlign results in very reproducible slice locations over the course of multiple studies even at different field strength and scanner types. Due to the large number of receive channels, image reconstruction times can be slightly increased when using the 32-channel head coil although this is barely noticeable for the scans performed in this study. A minor disadvantage is the fact that the close fitting 32-channel head coils may not be large enough for some subjects. Finally, the neck array can currently not be used in combination with the 32-channel head coils thereby requiring a coil change when head and neck scans are required. In summary, the 32-channel head coils for 1.5T and 3T provide improved image quality and allow faster image acquisition at comparable image quality when using the Head Matrix coil without significant disadvantages.

Acknowledgements

I would like to thank Michael Hamm for help with data acquisition and acknowledge support from the National Center for Research Resources (P41RR14075).

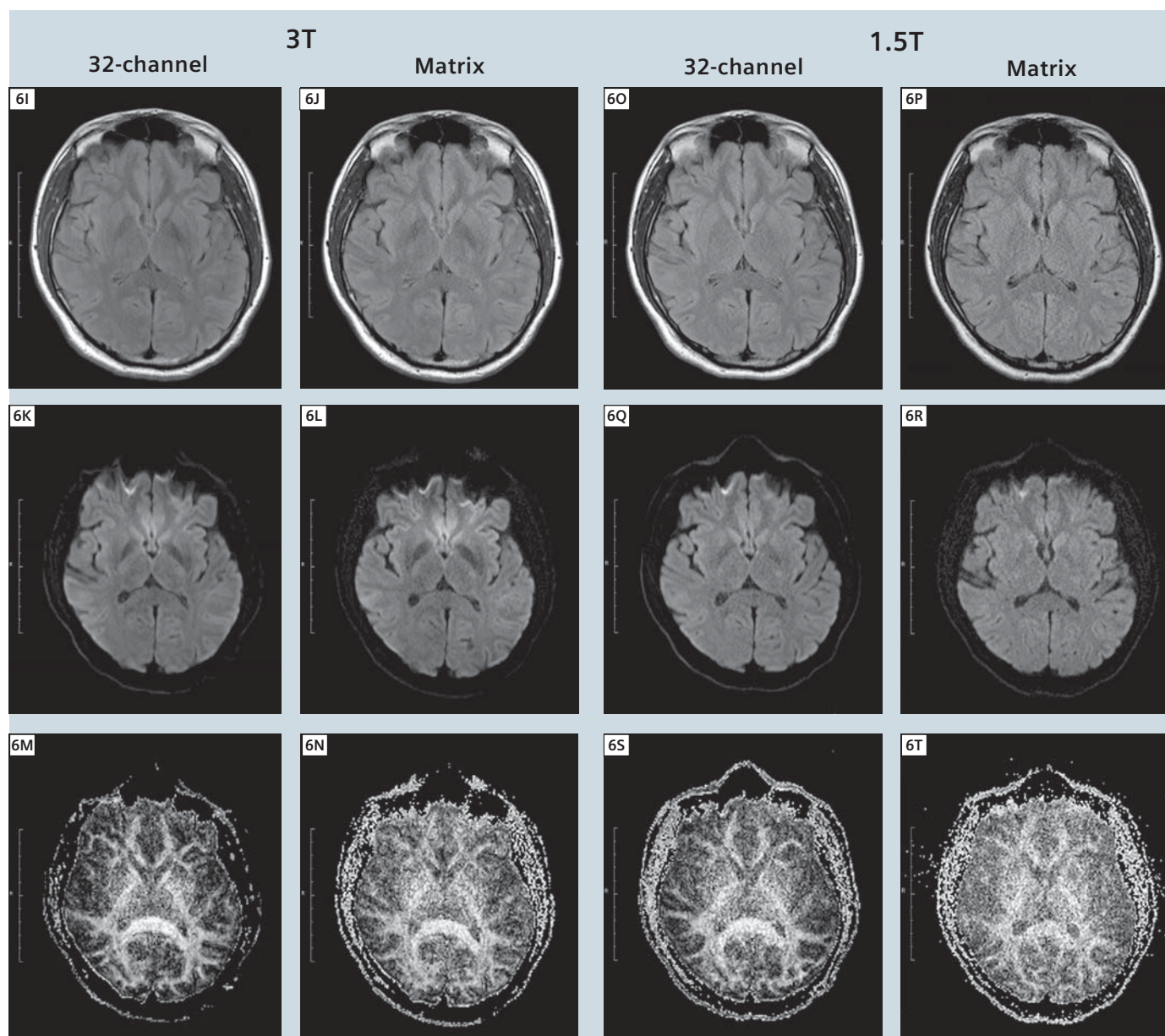


6A-T 6A-F: t1_fl2d_sag_p3, 6C-H: t2_tse_tra_p3, 6I-P: t2_tirm_tra_dark-fluid_p3, 6K-R: ep2d_diff_MDDW_6_p2 trace-weighted, 6M-T: ep2d_diff_MDDW_6_p2 FA; t1_fl2d_sag_p3, gre, TR 280 ms, TE 2.57 ms, FOV 230 × 230 mm², matrix 256 × 256, 25 slices, SL 5 mm, distance factor 20%, BW 270 Hz/pixel, flip angle 70°, 1 average, iPAT mode GRAPPA, acceleration factor 3, reference lines 24, matrix coil mode auto (triple), reference scan mode integrated, coil combine mode adaptive combine, pre-scan normalize filter, elliptical filter, TA 0:28 min.
t2_tse_tra_p3, tse, TR 6210/6220 ms (3T/1.5T), TE 84 ms, FOV 220 × 192.5 mm², matrix 256 × 224, 25 slices, SL 5 mm, distance factor 20%, BW 260 Hz/pixel, flip angle 120°, turbo factor 26, 1 average, iPAT mode GRAPPA, acceleration factor 3, reference lines 44, matrix coil mode auto (triple), reference scan mode integrated, coil combine mode adaptive combine, pre-scan normalize filter, TA 0:33 min.

Table 1: Listing of selected short clinical protocols with scan duration. Protocols correspond to data shown in Figure 6.

Protocol	TR [ms]	TE [ms]	FoV [mm × mm]	Matrix	Bandwidth [Hz/pixel]
localizer					
AAScout					
t1_fl2d_sag_p3	280	2.57	230 × 230	256 × 256	270
t2_tse_tra_p3	6210/6220*	84	220 × 192.5	256 × 224	260
t2_tirm_tra_dark-fluid_p3	7000	81/79*	220 × 192.5	256 × 224	271
ep2d_diff_MDDW_6_p2	3900/4000*	94	220 × 220	192 × 192	1184

Note: total scan duration does not include time needed for scanner adjustments e.g. shimming. (*3T/1.5T)



6A–T t2_tirm_tra_dark-fluid_p3, tse, TR 7000 ms, TE 81/79 ms (3T/1.5T), TI 2500 ms, FOV 220 × 192.5 mm², matrix 256 × 224, 25 slices, SL 5 mm, distance factor 20%, BW 271 Hz/pixel, flip angle 120°, turbo factor 16, 1 average, 2 concatenations, iPAT mode GRAPPA, acceleration factor 3, reference lines 32, matrix coil mode auto (triple), reference scan mode integrated, coil combine mode adaptive combine, pre-scan normalize filter, elliptical filter, TA 1:40 min. ep2d_diff_MDDW_6_p2, ep2d_diff, TR 3900/4000 ms (3T/1.5T), TE 94 ms, FOV 220 × 220 mm², matrix 192 × 192, phase partial Fourier 6/8, 25 slices, SL 5 mm, distance factor 20%, fat sat, BW 1184 Hz/pixel, 1 average, 2 diffusion weightings, b1 0 s/mm², b2 1000 s/mm², 6 diffusion directions, iPAT mode GRAPPA, acceleration factor 2, reference lines 40, matrix coil mode auto (triple), reference scan mode separate, coil combine mode adaptive combine, pre-scan normalize filter, raw filter, TA 0:41 min.

References

- 1 Stapf J. 32-Channel Phased-Array Head Coil for 1.5T and 3T. MAGNETOM Flash 1/2008, 45.
- 2 Wald LL, Wiggins G. Highly Parallel Detection for MRI. MAGNETOM Flash 1/2008, 34–44.
- 3 van der Kouwe AJ, Benner T, Fischl B, Schmitt F, Salat DH, Harder M, Sorensen AG, Dale AM. Online automatic slice positioning for brain MR imaging. Neuroimage. 2005 Aug 1;27(1):222–230.
- 4 Benner T, Wisco JJ, van der Kouwe AJ, Fischl B, Vangel MG, Hochberg FH, Sorensen AG. Comparison of manual and automatic section positioning of brain MR images. Radiology. 2006 Apr;239(1):246–254.
- 5 Scott KT. Software Compensation for Patient Position Enabling Reproducible Slice Positioning – AutoAlign. MAGNETOM Flash 1/2006, 98–103.
- 6 Haacke EM, Xu Y, Cheng YC, Reichenbach JR. Susceptibility weighted imaging (SWI). Magn Reson Med. 2004 Sep;52(3):612–618.

Contact

Thomas Benner
Athinoula A. Martinos Center
for Biomedical Imaging
Dept. of Radiology
Massachusetts General Hospital
and Harvard Medical School
Boston, MA
USA
benner@nmr.mgh.harvard.edu

Large FOV Imaging at 3T with a 32-Channel Body Array Coil

Yutaka Natsuaki, Ph.D.; Gerhard Laub, Ph.D.

Siemens Medical Solutions, Inc., West Coast Team, MR R&D, Los Angeles, CA, USA

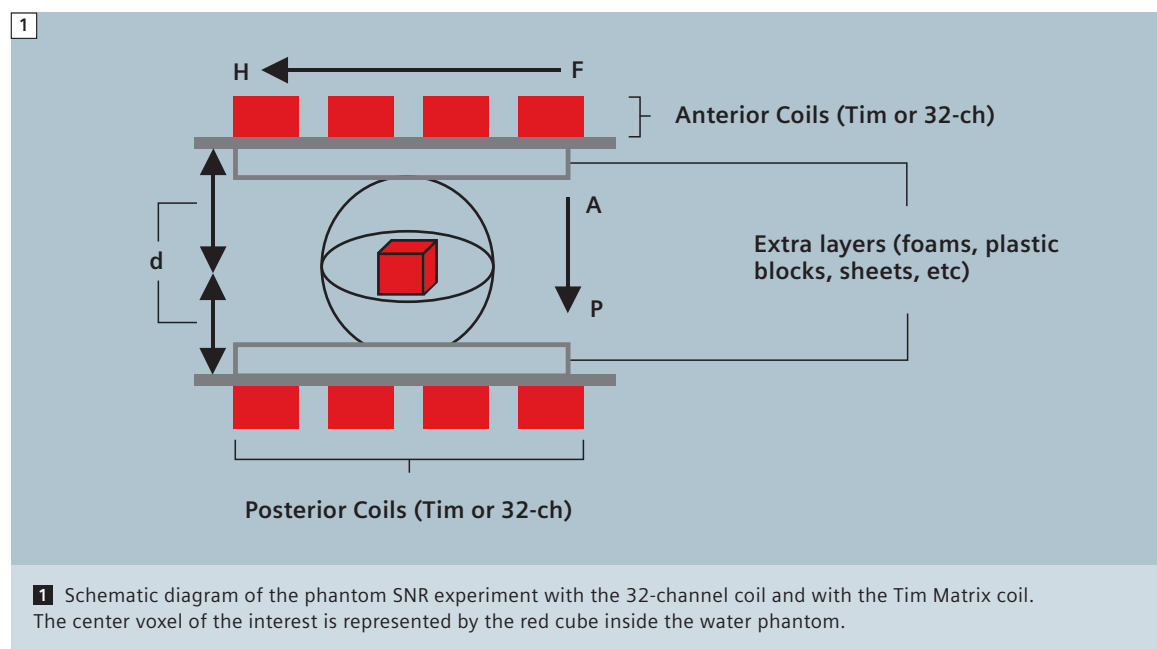
Introduction

Parallel imaging techniques have developed very rapidly, and realization of their full potential has required the development of MR systems with up to 32 receive channels. High-density RF array coils can be connected and utilized in a clinical environment in all Tim (Total imaging matrix) systems. Currently, Siemens offers two 32-channel array coils for brain and body applications, respectively. Both coils are available at 1.5T and 3T. In this article we will show the benefits of the 32-channel body coil for large FOV imaging in the abdomen, and pelvis, including MR Angiography.

Background

The 3T MR system has gained immense popularity among the diagnostic medical imaging community in recent years, largely due to the better image quality (e.g. higher resolution and better contrast) and the shorter scan time when compared to the conventional 1.5T MR system. These advantages in 3T MR system are made only possible by the combination of its inherently high signal-to-noise ratio (SNR) and advancements in parallel imaging, such as GRAPPA. The name "parallel" comes from the fact that each coil element is measuring the signal from the patient's body. The number of

phase encoding steps along the array coil can be reduced according to the acceleration factor, thus reducing the scan time. After the acquisition, the GRAPPA reconstruction estimates the missing k-space data based on information about the coil sensitivity distribution measured in the same object. The SNR in the accelerated scan will be less than that of the fully sampled MRI. The SNR during parallel acquisition, SNR_{PA} , is influenced by both the degree of undersampling, described by the acceleration factor (R), and also by the g-factor (G), which is the local geometry



factor. SNR_{PA} is thus described by the following equation:

$$SNR_{PA} = \frac{SNR_{full}}{\sqrt{R \cdot G}}$$

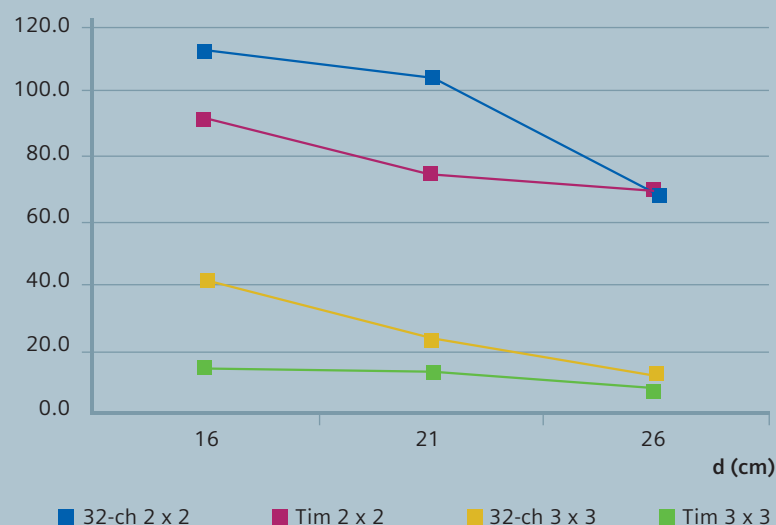
Simulations and experimental data have shown that G can be reduced, for a given acceleration factor and coil geometry, by increasing the field strength B_0 and/or by increasing the number of coil elements in a phased array coil. The use of multi-channel phased array coils with a high number of individual elements thus not only produces higher SNR values near the coil plane, but also decreases the SNR penalty associated with parallel imaging. We will demonstrate in this article how the 32-channel body array coil performs for accelerations of up to 4 in typical imaging techniques which are used for abdominal imaging.

Method

In order to demonstrate the advantages of the 32-channel coil, the following experiments are performed. First, we compare the 32-channel coil performance with the standard Tim Matrix coil. A water phantom is scanned with the 3D FLASH sequence on MAGNETOM Trio, A Tim System using the 32-channel coil and the Tim Matrix coil for the SNR comparisons. The basic measurement is repeated 5 times, and SNR is calculated based on the mean and standard deviation of the same voxel at the center of the spherical water phantom (shown as a red voxel inside the water phantom in Fig. 1). The SNR values are compared for different acceleration factors and for the different coil A/P distance d (i.e. the distance from the coil surface to the center of the water phantom: will be measured at 16, 21, and 26 cm). Note that

2

SNR vs A/P coil distance (axial 3D FLASH)



2 SNR vs. A/P coil distance for 3D FLASH sequence with water phantom. The advantage of the 32-channel coil is decreasing with increasing distance between the anterior and posterior coil elements.

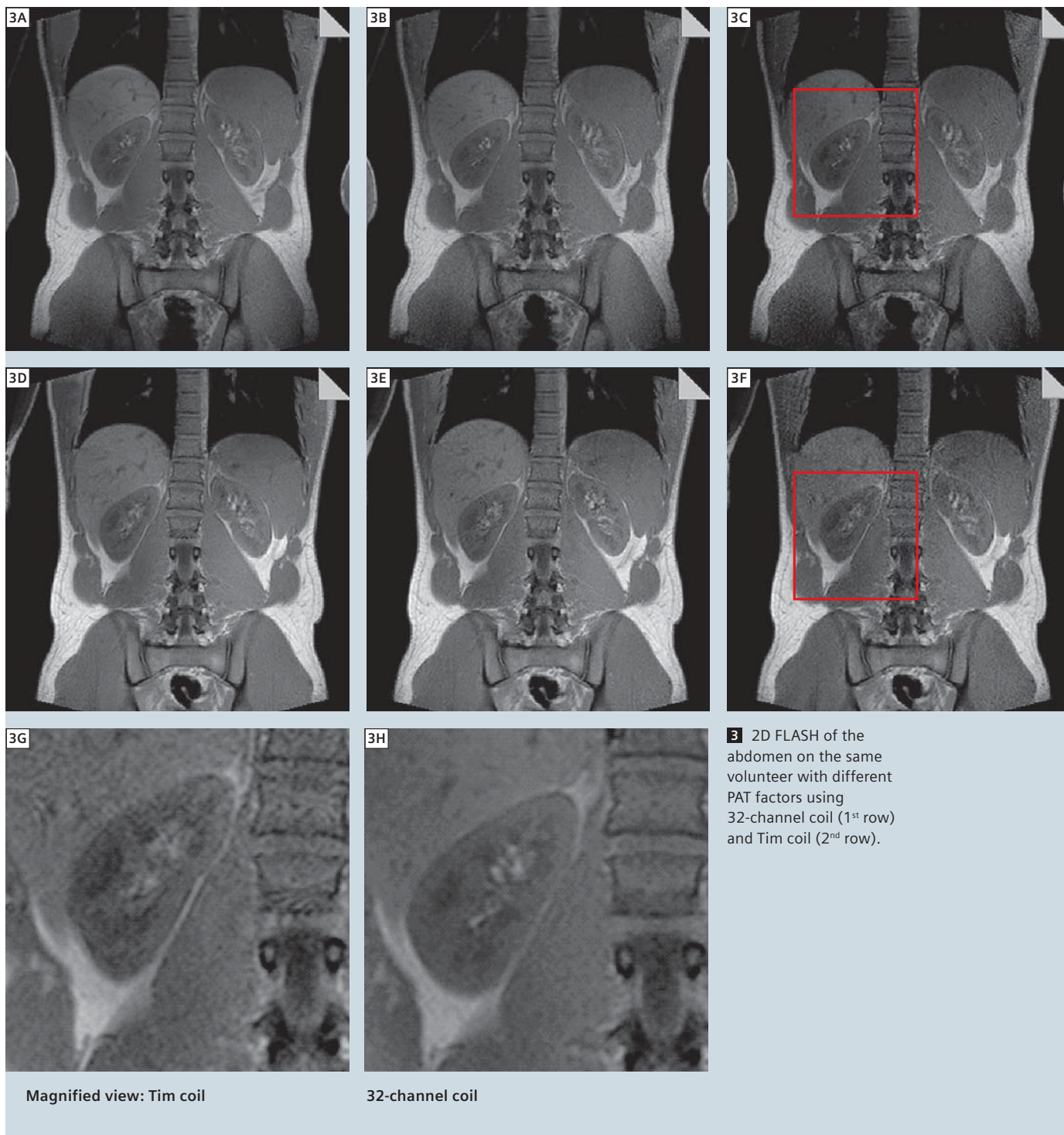
d is set equal distance from both anterior and posterior coils. See Fig.1 for the schematic diagram of the first experiment. Second, 2D FLASH coronal abdomen scans are performed on a volunteer using Tim and 32-channel coils. The 2D FLASH coronal abdomen scans are repeated with the different PAT acceleration factors applied in R/L direction. Finally, the various clinical scans at abdomen/renal and pelvis regions are performed using the 32-channel coil to observe the quality of the images in a clinical situation.

Results

Phantom SNR experiment

Fig. 2 shows the SNR vs. coil A/P distance plots for 32-channel and Tim coils with PAT acceleration factor of 2 x 2 and 3 x 3. In general, the PAT acceleration factor

2 x 2 has the superior SNR than 3 x 3 as expected. Note also, that the SNR drops with an increasing distance between the anterior and posterior coil elements. The 32-channel coil, however, drops faster than the Tim coil which is due to the smaller coil elements in the 32-channel coil. Smaller coil elements will help to improve the SNR for objects closer to the coil, but the signal drops faster when moving away from the coil. Overall, the 32-channel coil shows equal or the better SNR than the Tim coil in all cases, in particular with the cases with smaller d . In practice, however, the advantage of the 32-channel coil becomes more obvious when scanning thinner patients with an A-P distance of less than 25 cm.



Volunteer abdomen study with different PAT acceleration factors

Fig. 3 shows FLASH 2D of the abdomen on the same volunteer with different PAT acceleration factors. In a coronal orientation the phase encoding direction is R/L. In the R/L direction, the Tim coil has

three coil elements, while the 32-channel coil has four. As expected both coils show excellent image quality with acceleration factors of 2 and 3. For the PAT acceleration factor 4, the Tim coil starts to produce noisy images due to the underdetermined reconstruction, and

the PAT related noise becomes apparent (highlighted by the boxes). The 32-channel coil retains the image quality throughout the PAT acceleration factor changes.



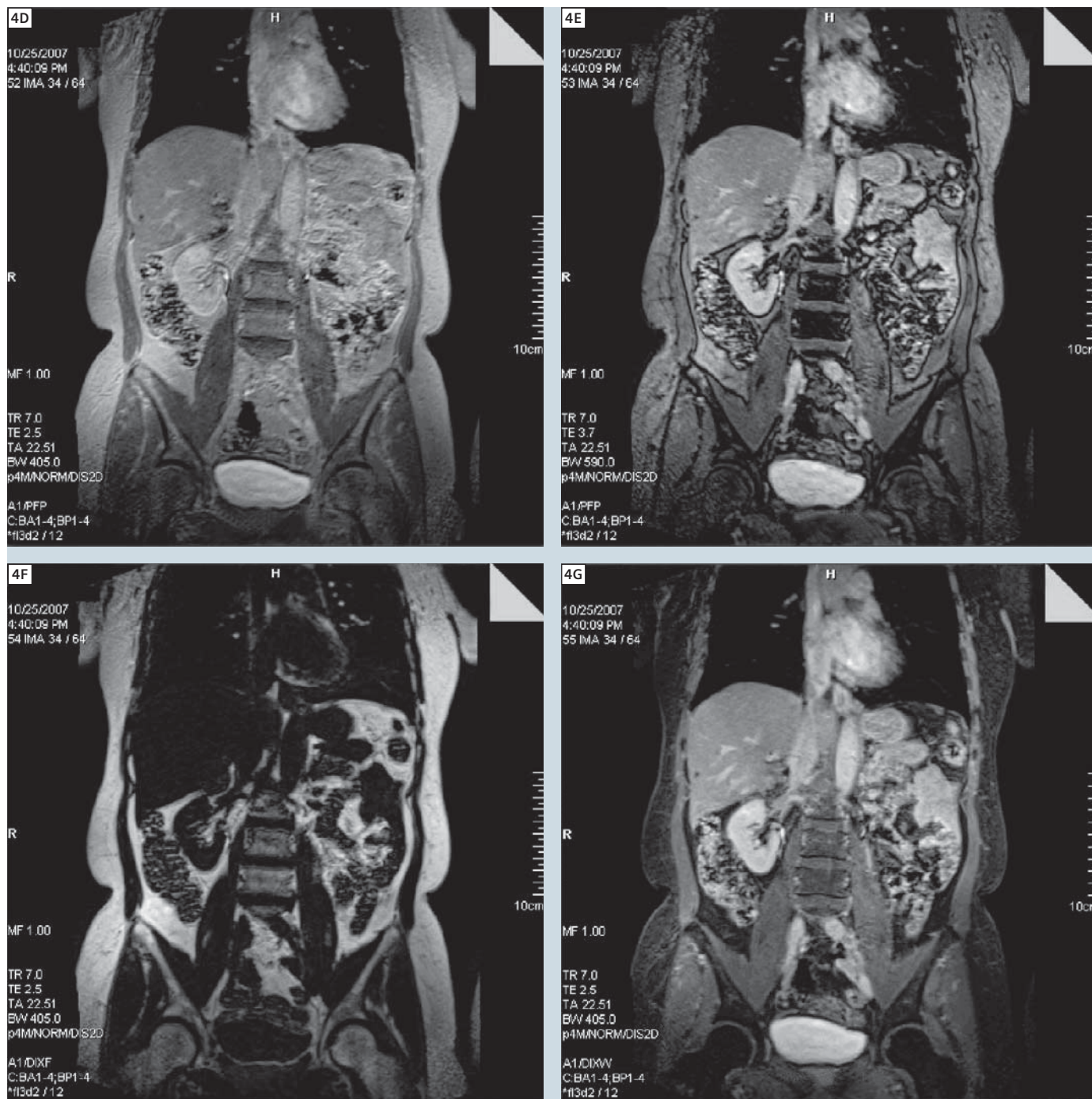
4 Clinical examples of MR images using 32-channel body array coil. The examples include (A) MIP of syngo TWIST dynamic MRA (4 time points with 4 second interval are shown), (B) MIP of high-resolution contrast-enhanced MR angiography (ceMRA) and (C) VRT of high-resolution ceMRA.

Clinical cases with 32-channel coil

Fig. 4 shows various examples of clinical cases using the 32-channel coil. The examples include 6 time points of the coronal dynamic contrast-enhanced MR Angiography (ceMRA - syngo TWIST) on abdomen (Fig. 4A), MIP of high reso-

lution coronal ceMRA on abdomen (Fig. 4B), VRT of the high resolution ceMRA (Fig. 4C), and 4 different image contrasts generated by DIXON method on abdomen (Fig. 4D). Note that for the high-resolution ceMRA shown in Figs. 4B and C, the PAT acceleration

factor 4 is applied in L/R direction, and this allows near-isotropic resolution ($0.92 \text{ PE} \times 0.78 \text{ RO} \times 0.9 \text{ SS mm}^3$) within the single breath hold (22 seconds). For all cases in Fig. 4, the 32-channel coil produces exceptional image quality.



4 Clinical examples of MR images using 32-channel body array coil. (D–G) DIXON of abdomen.

Conclusions

In conclusion, the 32-channel body array coil shows excellent results, with better SNR and with improved image quality for the higher PAT acceleration factors in the left-right direction, particularly for slim patients when the distance

between the anterior and posterior coil elements is less than 25 cm. The 32-channel coil is recommended for those who seek to utilize the maximum potential of MAGNETOM Trio, A Tim System for body MRI applications.

Contact

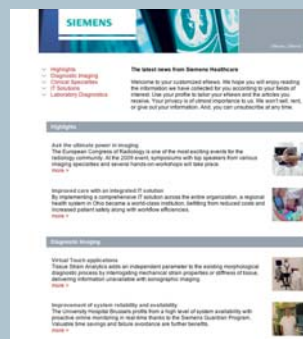
Yutaka Natsuaki, Ph.D.
Siemens Medical Solutions, Inc.
10945 Le Conte Avenue
Suite 3371
Los Angeles, CA, USA
yutaka.natsuaki@siemens.com

Siemens Healthcare – Customer Magazines

Our customer magazine family offers the latest information and background for every healthcare field. From the hospital director to the radiological assistant – here, you can quickly find information relevant to your needs.



Medical Solutions
Innovations and trends in healthcare. The magazine is designed especially for members of hospital management, administration personnel, and heads of medical departments.



eNews
Register for the Siemens Healthcare global eNewsletter at www.siemens.com/healthcare-eNews to receive monthly updates on topics that interest you.



AXIOM Innovations
Everything from the worlds of interventional radiology, cardiology, fluoroscopy, and radiography. This semi-annual magazine is primarily designed for physicians, physicists, researchers, and medical technical personnel.



MAGNETOM Flash
Everything from the world of magnetic resonance imaging. The magazine presents case reports, technology, product news, and how-to articles. It is primarily designed for physicians, physicists, and medical technical personnel.



SOMATOM Sessions
Everything from the world of computed tomography. With its innovations, clinical applications, and visions, this semiannual magazine is primarily designed for physicians, physicists, researchers, and medical technical personnel.



Perspectives
Everything from the world of clinical diagnostics. This semiannual publication provides clinical labs with diagnostic trends, technical innovations, and case studies. It is primarily designed for laboratorians, clinicians, and medical technical personnel.

For current and older issues and to order the magazines, please visit www.siemens.com/healthcare-magazine

Improving High Resolution fMRI at 3T with the 32-Channel Head Array

Christina Triantafyllou^{1,2}; Lawrence L. Wald^{2,3}

¹Athinoula A. Martinos Imaging Center, McGovern Institute for Brain Research, Massachusetts Institute of Technology, Cambridge, MA, USA

²Athinoula A. Martinos Center for Biomedical Imaging, Department of Radiology, Massachusetts General Hospital, Boston, MA, USA

³Harvard-MIT Division of Health Sciences and Technology, Massachusetts Institute of Technology, Cambridge, MA, USA

Introduction

It is well known that BOLD (Blood Oxygenation Level Dependent) effects increase in amplitude at higher field strength, due to the general enhancement of susceptibility contrast resulting in improvements in BOLD sensitivity and specificity. Nevertheless, identifying additive methods of improving BOLD imaging are also worth pursuing. In particular, the new generation of highly parallel brain arrays offers a potential adjuvant approach to high field functional MRI (fMRI). These close-fitting, highly parallel detection arrays allow impressive increases in image signal-to-noise ratio (SNR) in cortical areas and increases in iPAT (integrated Parallel Acquisition Technique) acceleration, helpful for mitigating image distortion in EPI (Fig.1) [1, 2]. It is nonetheless important to closely examine their benefits for fMRI, since the fMRI experiment is limited by physiological fluctuations in the time-series SNR (tSNR) rather than in the image SNR (SNR₀).

In this paper, we review our findings on the benefits of 32-channel receive arrays for the time-series SNR in the fMRI experiment and validate the sensitivity gains in two illustrative fMRI examples; retinotopy of the primary visual system and speech motor region activation. We show that highly parallel detection

offers a powerful adjuvant method to high field fMRI, especially when high resolution brain mapping is desired. The article is organized in two parts. First we characterize the fMRI time-series fluctuations (noise) for different coils and image resolution combinations as a metric for potential improvements in fMRI sensitivity. Second we show results from two real world fMRI experiments.

Physiological noise in fMRI time-series SNR using array coils

Our ability to detect small changes in image intensity associated with subtle brain activation in the fMRI time-series is limited by physiologically induced image intensity modulations (physiological noise). Thus, the noise in fMRI is not the traditional image noise important for anatomical imaging, but arises from the interplay between the imaging and physiological processes which occur during the time-series. The time-series SNR (tSNR) is the most important metric for determining the smallest activation effect which can be seen in a given fMRI experiment. It is defined as a pixel's mean intensity divided by the standard deviation of this intensity over time. In contrast, the image SNR (SNR₀) is defined as the image intensity divided by the noise in that image (traditionally taken as

the standard deviation in the image background area, although this definition is problematic for arrays).

Previous studies of the physiological noise in fMRI time-series have shown that it acts as a modulation of the image intensity with time [3, 4]. Thus, as the signal gets stronger (from higher field scanners or an improved head coil), then the physiological noise grows proportionally, since the noise level is a fixed percentage of the signal level. This is problematic in that at first glance it appears that improving detection sensitivity with array coils will not translate to improved tSNR for fMRI. Namely, gains in image sensitivity are offset by proportional gains in physiological noise. Defining σ_p as the physiological noise standard deviation, and S as the image signal intensity, Krüger and colleagues showed this scaling relationship; $\sigma_p = \lambda S$, where λ is a constant. But, the total time-series noise is the statistical sum of the physiological noise, σ_p , and the conventional image noise, σ_o , thus the potential benefit of improvements in array technology (which improves image SNR) will depend on the relative importance of these two noise sources. For example, as the voxel size is decreased, we expect thermal image noise to dominate and improvements in array technology will translate

to improved fMRI time-series SNR (tSNR). Thus, we sought to examine the benefits of high-N arrays on the tSNR in fMRI experiments of different image resolutions and using a range of head coils. At different image resolutions the time series noise can be expected to derive from varying ratios of physiological to image noise. Furthermore, since many fMRI studies now use iPAT to reduce the image distortion associated with single shot EPI, and since iPAT alters the image noise, we examine the effect of iPAT on fMRI time-series SNR by varying the degree of acceleration for a number of image resolutions commonly used in fMRI.

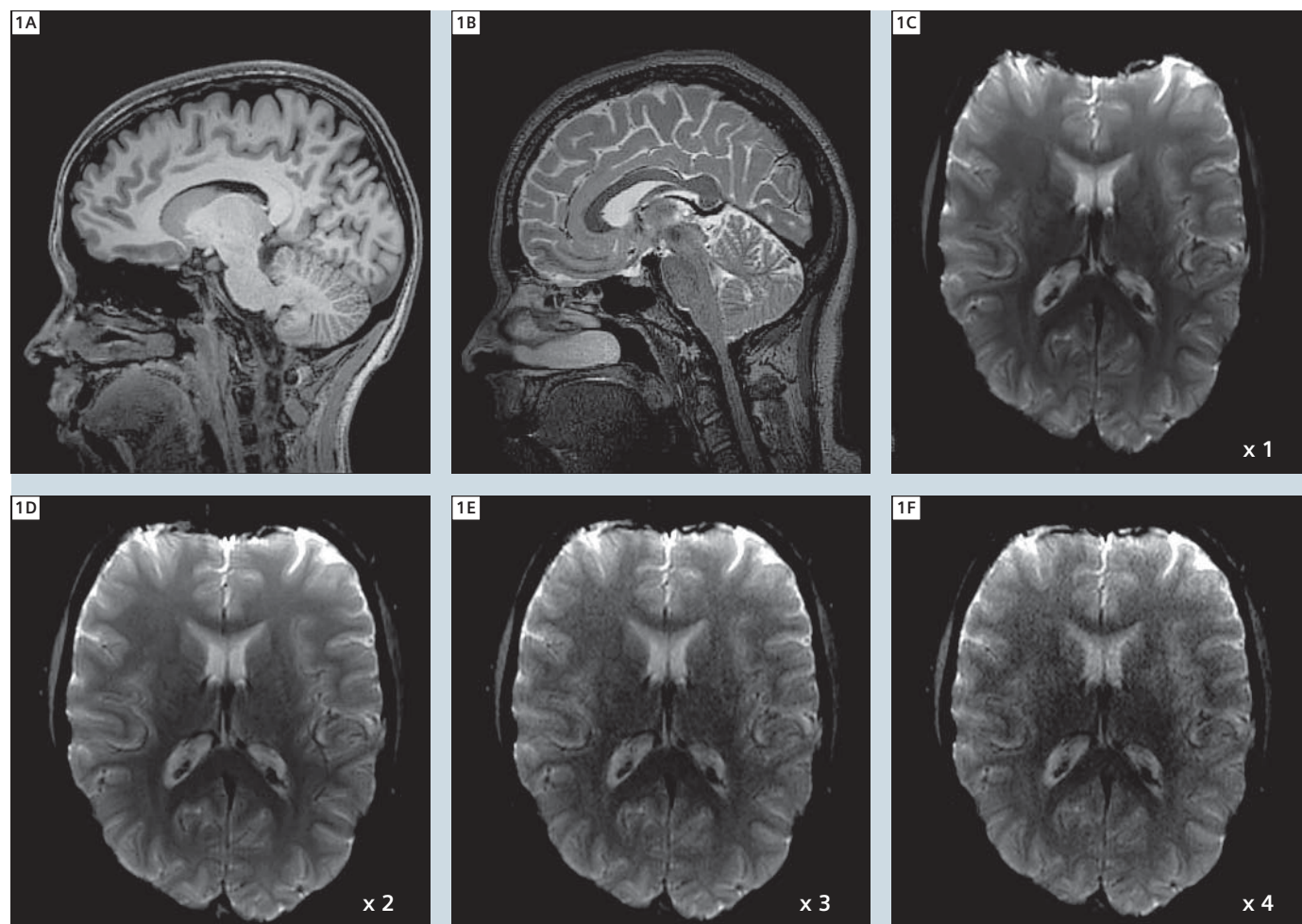
Methods

To evaluate the physiological noise in fMRI, resting state EPI time-series were collected at 3T on a MAGNETOM Trio, A Tim System, using a single-shot gradient echo EPI sequence and three different receive RF coils; a transmit/receive volume head coil (Birdcage), the 12-channel Matrix receive-only head coil, and the 32-channel receive-only phased array head coil. All subjects were asked to relax while in the scanner; no specific stimulus was applied. Written consent was obtained from all the subjects under protocols approved by institutional review. To achieve accurate comparison

between the coils, the same four healthy volunteers were scanned.

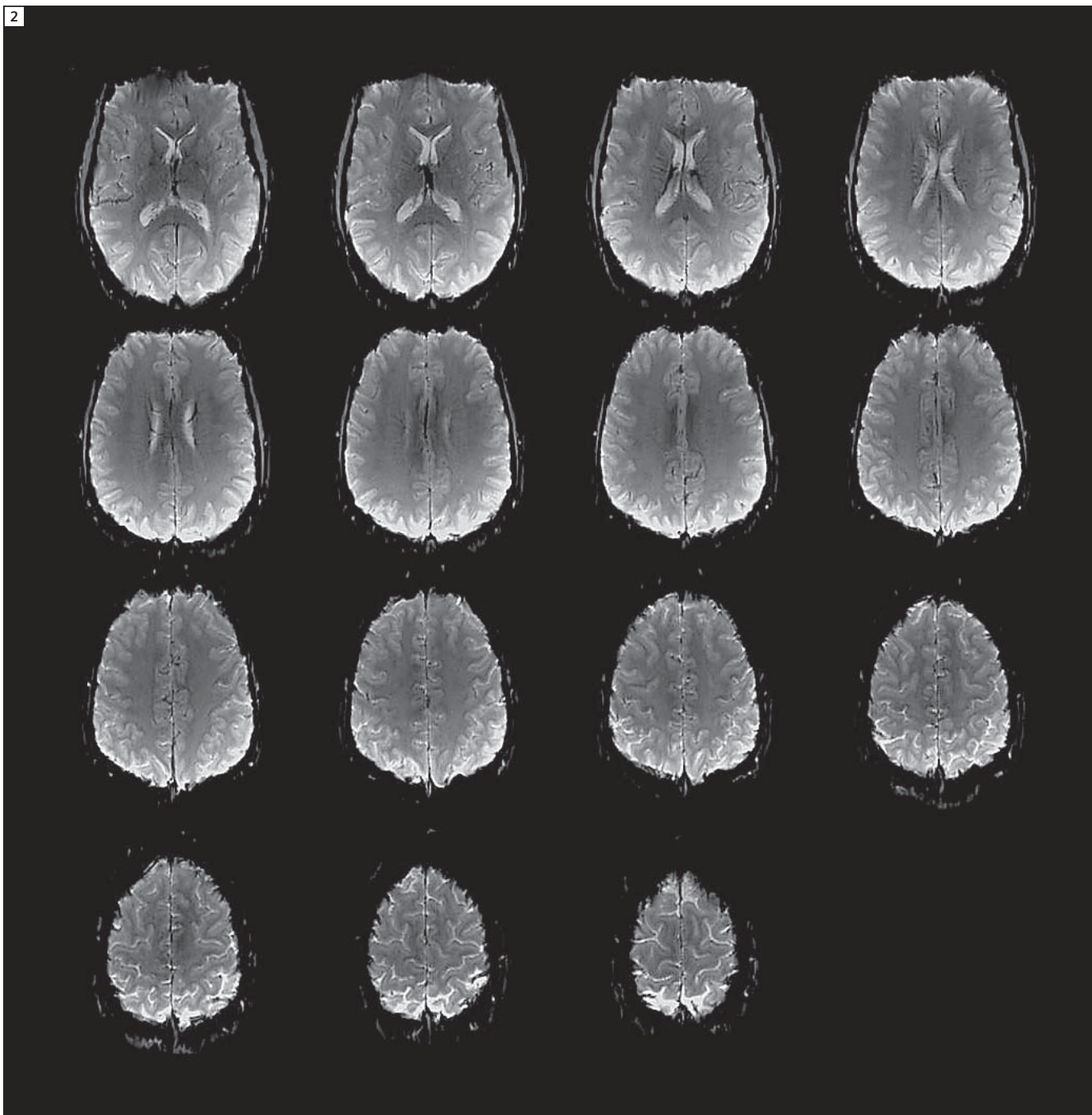
Data were collected parallel to the AC-PC line at six different in-plane resolutions ($1 \times 1 \text{ mm}^2$, $1.5 \times 1.5 \text{ mm}^2$, $2 \times 2 \text{ mm}^2$, $3 \times 3 \text{ mm}^2$, $4 \times 4 \text{ mm}^2$ and $5 \times 5 \text{ mm}^2$). Other imaging parameters were: slice thickness = 3 mm, TR = 5400 ms, TE = 30 ms, 60 time points, flip angle = 90° . Figure 2 shows example images from the $1 \times 1 \text{ mm}^2$ data set acquired with the 32-channel array.

The use of array data requires a more complex analysis to generate SNR_0 in a way that renders it directly comparable to time-series measurements [5]. After



1 High resolution images acquired with the 32-channel coil. **A:** T1-weighted 3D MPRAGE (1 mm isotropic). **B:** T2-weighted 3D-SPACE (0.6 mm isotropic). **C–F:** Single-shot gradient echo EPI images acquired at $1 \times 1 \times 3 \text{ mm}^3$, TE = 30 ms, with GRAPPA acceleration factors of 1–4, respectively (1 = no acceleration).

2



2 Resting state gradient echo 32-channel EPI images acquired at $1 \times 1 \times 3 \text{ mm}^3$ with $TE = 30 \text{ ms}$.

motion correction, time-series SNR maps (tSNR) were estimated as the ratio of the mean pixel intensity across time points to the temporal standard deviation. Measurements of tSNR and SNR_0 were evaluated in a cortical gray matter region-of-interest (ROI) and tSNR was

plotted as a function of SNR_0 for the different in-plane resolutions and receive coils. The data were fit to the model of Krüger et al. [3]. EPI time-series were also collected at three resolutions ($2 \times 2 \times 2 \text{ mm}^3$, $3 \times 3 \times 3 \text{ mm}^3$, $3 \times 3 \times 5 \text{ mm}^3$) using iPAT (*syngo* GRAPPA)

with acceleration factors of 1, 2, 3 and 4 at each resolution.

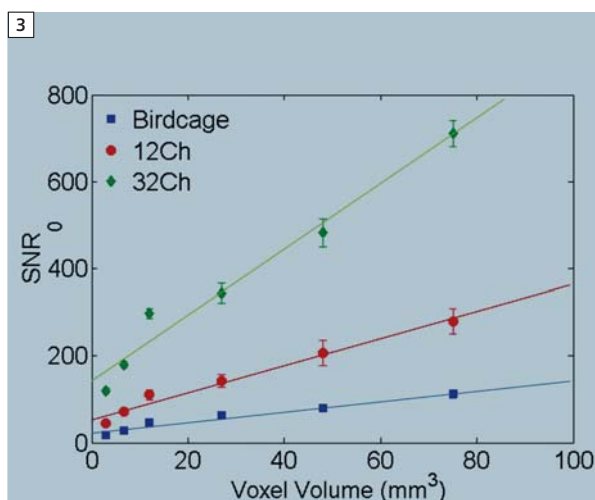
Results

Figure 3 shows SNR_0 as a function of voxel volume for the 3 different coils. As expected, the SNR_0 is nearly linear in

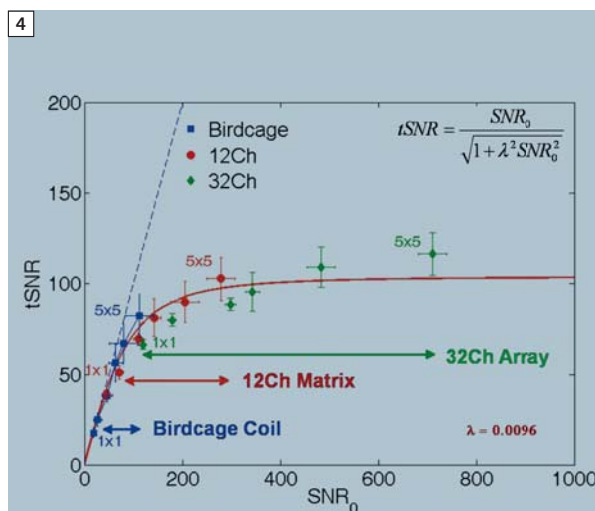
voxel volume and at each resolution the sensitivity is substantially improved in the cortex when the 32-channel array is used. For example, for the isotropic 3 mm voxel, the 32-channel SNR_0 was 1.2 fold higher than that of the 12-channel array. The results shown in Figure 4 suggest that the relationship between tSNR and SNR_0 can be well parameterized by the Krüger model at different resolutions and for array data. Namely, when SNR_0 is modulated by coil performance and image resolution, the physiological noise is well modeled as proportional to the signal. At low values of SNR_0 (small voxels or lower coil performance), the tSNR is dominated by thermal image noise and grows linearly with SNR_0 . As the image SNR increases (above approximately 200), then the curve approaches an asymptote and additional improvement in SNR_0 does not translate to substantial gains in tSNR. Since the highly parallel array coils chiefly increase image SNR, this suggests that their biggest benefits for fMRI (tSNR) will be for higher image resolutions where SNR_0 is below 200. For example, the 32-channel coil increased the tSNR of the $1.5 \times 1.5 \times 3 \text{ mm}^3$ acquisition by 57% compared to the 12-channel coil. At lower resolutions however, (e.g. $5 \times 5 \times 3 \text{ mm}^3$) the increase was only 13%.

Figure 5 shows the tSNR as a function of resolution at acceleration rates $R=1, 2, 3, 4$. The tSNR decreases at higher resolutions as expected, but is also reduced as R increases in all cases.

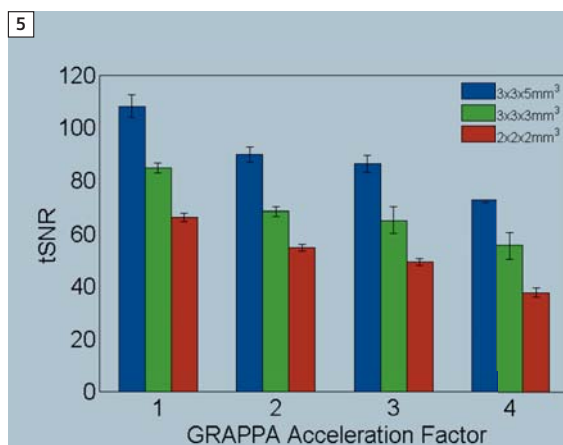
For example, at the lowest resolution used ($3 \times 3 \times 5 \text{ mm}^3$), tSNR decreased by 34% between the $R=1$ and $R=4$ acquisition showing that the improvement in susceptibility distortion afforded by iPAT comes at a cost in time-series SNR. For the higher resolution ($2 \times 2 \times 2 \text{ mm}^3$) the percentage decrease in tSNR between $R=1$ to $R=4$ is the greatest; 43%.



3 Image SNR (SNR_0) as a function of voxel volume. Lines are linear least-squares fit to the data.

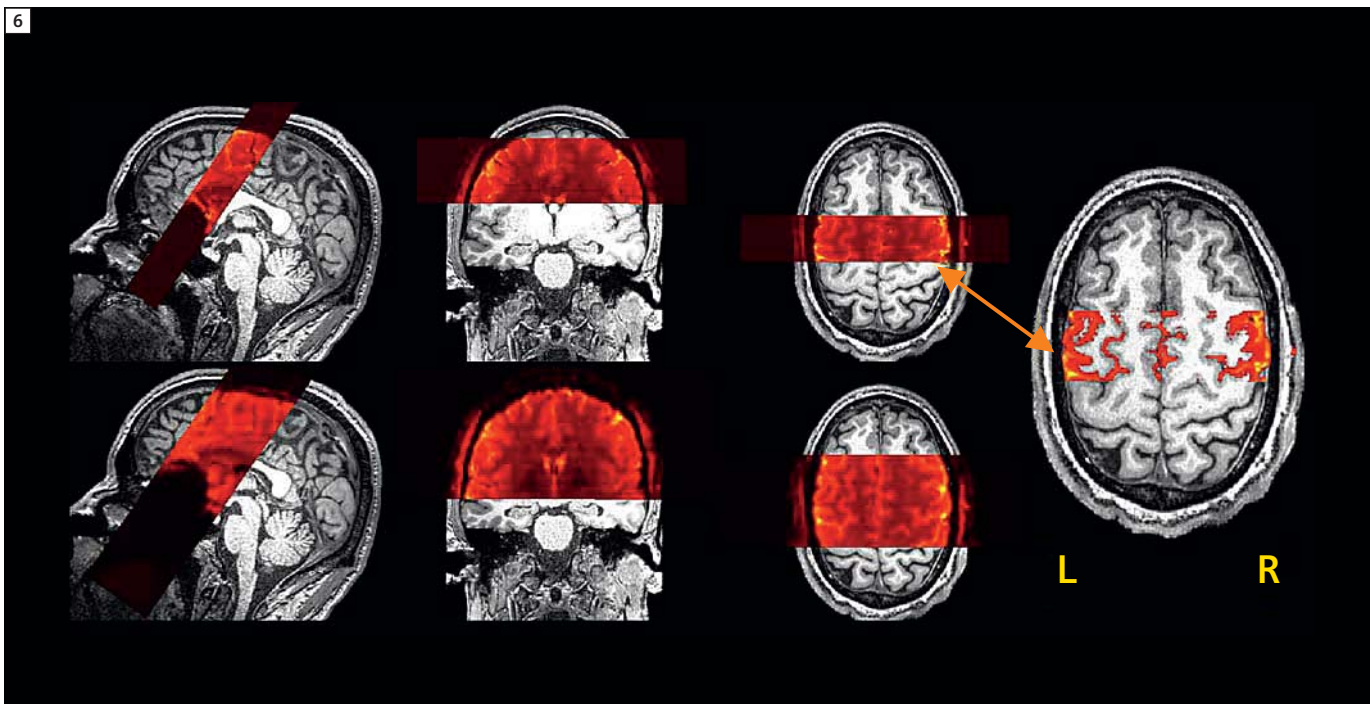


4 SNR in fMRI time-series (tSNR) as a function of image SNR (SNR_0) for different spatial resolutions. Changes in image SNR were produced by varying the voxel volume and coils. Squares, circles and diamonds represent the 3T data for birdcage coil, 12-channel and the 32-channel array coil respectively. Measurements derived from areas of cortical gray matter and are averages over four subjects. The dotted line represents the line of identity ($tSNR = SNR_0$) which should parameterize the data in the absence of physiological noise, and the solid line shows the Krüger noise model fit to all the data points.



5 SNR in fMRI time-series (tSNR) as a function of acceleration factor at different spatial resolutions using the 32-channel coil. Measurements derived from areas of cortical gray matter and are averages over four subjects.

6



6 EPI slice prescription superimposed onto the high resolution 0.6 mm isotropic T1-weighted MPRAGE; top row 1 mm isotropic EPI data, bottom row 2 mm isotropic data, both acquired with 32-channel coil. Image on the right shows a thresholded EPI image and its correspondence to the T1-weighted anatomy. (Figure courtesy of S. Ghosh, MIT.)

Functional MRI applications

a) High-resolution fMRI using a 32-channel coil to identify individual-specific speech motor regions

Previous studies of overt speech sequencing [6] have reported activity in several brain regions such as ventral motor and pre-motor cortex, frontal operculum, posterior inferior frontal gyrus, supplementary motor area (SMA) and the pre-SMA. However, it has been difficult to reliably identify precise locations of activity in individuals because high spatial resolution is needed to resolve the ventral motor regions of the frontal lobe and the activation is weak for experiments limited to an individual. The spatial resolution problem is especially problematic for conventional resolutions ($3 \text{ mm}^2 \times 3 \text{ mm}^2$) and when spatial smoothing is needed in the statistical analysis. In this study, we will utilize the added sensitivity of the 32-channel coil to allow higher spatial resolution at acquisition in conjunction with reduced spatial smoothing

in the analysis, to allow the identification of the ventral motor regions in individual subjects and dissociate the clusters of activity around the frontal operculum and the supplementary motor area.

Methods

High-resolution single-shot gradient echo EPI time-series were acquired using the 32-channel phased array head coil. Written consent was obtained from all the subjects under protocols approved by institutional review. The imaging parameters were: TE = 30 ms, flip angle = 90° , TR = 12 s, TA = 2.5 s, TR delay = 9.5 s, syngo GRAPPA reconstruction with acceleration factor of 2. Twenty five 1 mm thick slices were acquired with a interslice gap of 0.1 mm, and in-plane resolutions of $1 \times 1 \text{ mm}^2$, FOV = 192×192 and matrix size = 192×192 . Slices were positioned so that they cover the SMA passing through the ventral pre-motor cortex (Fig. 6, top row). A second set of images with FOV = 256×256 and matrix size = 128×128 also acquired with in-plane resolution $2 \times 2 \text{ mm}^2$, and

slice thickness of 2 mm, (Fig. 6, bottom row). For comparison, 2 mm isotropic data was also acquired using the 12-channel Head Matrix coil. High resolution T1-weighted structural data was collected using an MPRAGE pulse sequence with isotropic voxel dimensions of 0.6 mm.

Participants were asked to perform a speech task consisting of 3 conditions: **a)** speaking complex sequences of complex syllables (e.g., stra-spli-stru), **b)** speaking simple sequences of simple syllables (e.g., ba-ba-ba), and **c)** passively viewing the letter string (e.g., xxx-xxx-xxx) (baseline).

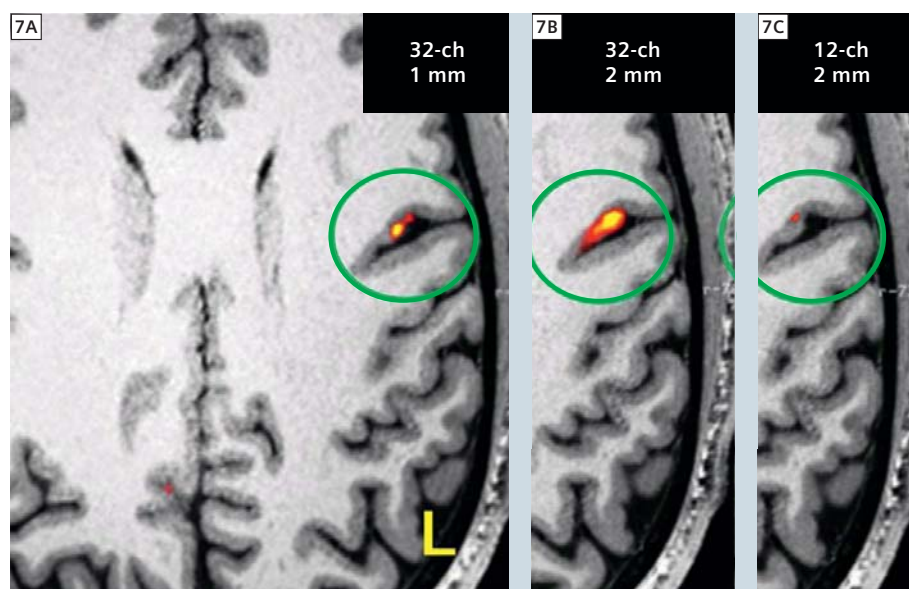
Statistical analysis was performed using SPM5 (Wellcome Department of Cognitive Neurology, London, UK), including motion correction, smoothing and General Linear Model (GLM) fitting. The 1 mm and 2 mm data were smoothed with 2 mm and 4 mm FWHM Gaussian kernels respectively. Two contrasts were evaluated:

- A)** speaking trials compared to baseline trials; and
- B)** complex trials compared to simple trials.

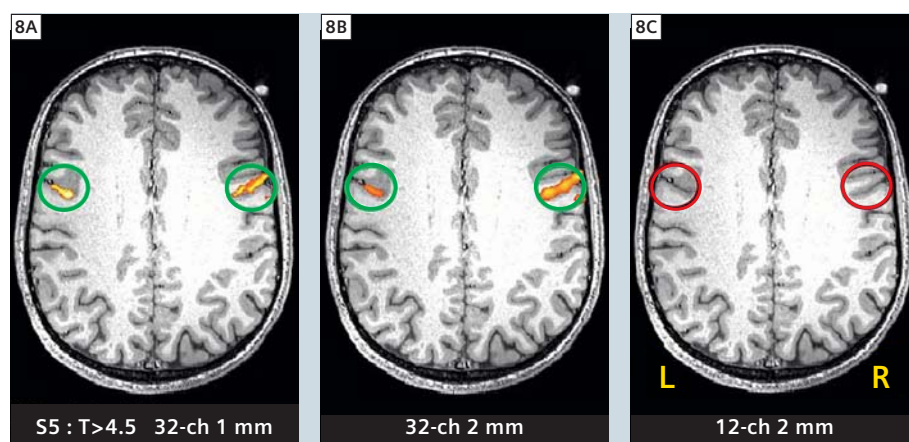
Results

Data from a single subject are shown in Figure 7 illustrating the t-statistics derived from contrast B; complex sequences compared to simple syllables. Activity in the anterior bank of the pre-central sulcus is found in all three acquisitions (1 mm isotropic 32-channels, 2 mm isotropic 32-channels and 2 mm isotropic 12-channels), however the 32-channel coil showed significantly greater sensitivity to the task than the 12-channel Head Matrix coil. Figure 8 demonstrates data from a different individual where activation with 12-channel coil was not detected compared to the 32-channel coil that exhibited activation patterns even at higher resolution (1 mm isotropic).

In this functional MRI study we show that the higher sensitivity of the 32-channel array translates directly into improved detection capability for detecting speech motor activation in individual subjects. Using a high-resolution EPI protocol with the 32-channel coil, we were able to demonstrate sulcal bank specific localization of speech motor activity related to the production of complex sequences of syllables. The amount of required smoothing was limited to the minimum, thus preventing extensive smearing of activity across sulcal banks, bringing the location of the significant voxels to an accurate correspondence with the brain gray matter as identified in the high resolution MPRAGE. This was a significant improvement in localization compared to conventional 3 mm isotropic resolution scans coupled with 6 mm smoothing. In conclusion, our findings demonstrate that employing high-resolution acquisition and highly parallel detection, it is possible to achieve accurate individual-specific mapping of cognitive task related brain networks and enables the examination of individual variability of the structure-function relationship.



7 Activation map (t-statistics) of a single subject overlaid on the 0.6 mm isotropic T1-weighted structural scan. Data acquired with the 12-channel coil are shown at the far right (2 mm isotropic), while 32-channel data are shown at the center (2 mm isotropic) and on the left (1 mm isotropic). Direct comparison of the BOLD activity exhibits higher significance with the 32-channel compared to 12-channel data. Red and yellow indicate lower and higher significance, respectively ($FDR = 0.05$). (Figure courtesy of S. Ghosh, MIT.)



8 Activation map (t-statistics) from another subject, overlaid on the 0.6 mm isotropic T1-weighted structural scan. Activation is present on the 32-channel data, (A) and (B) green circles, while no activation was detected when using the 12-channel coil (C), red circles. (Figure courtesy of S. Ghosh, MIT.)

b) High-resolution fMRI using a 32-channel coil to improve the accuracy of visual field mapping

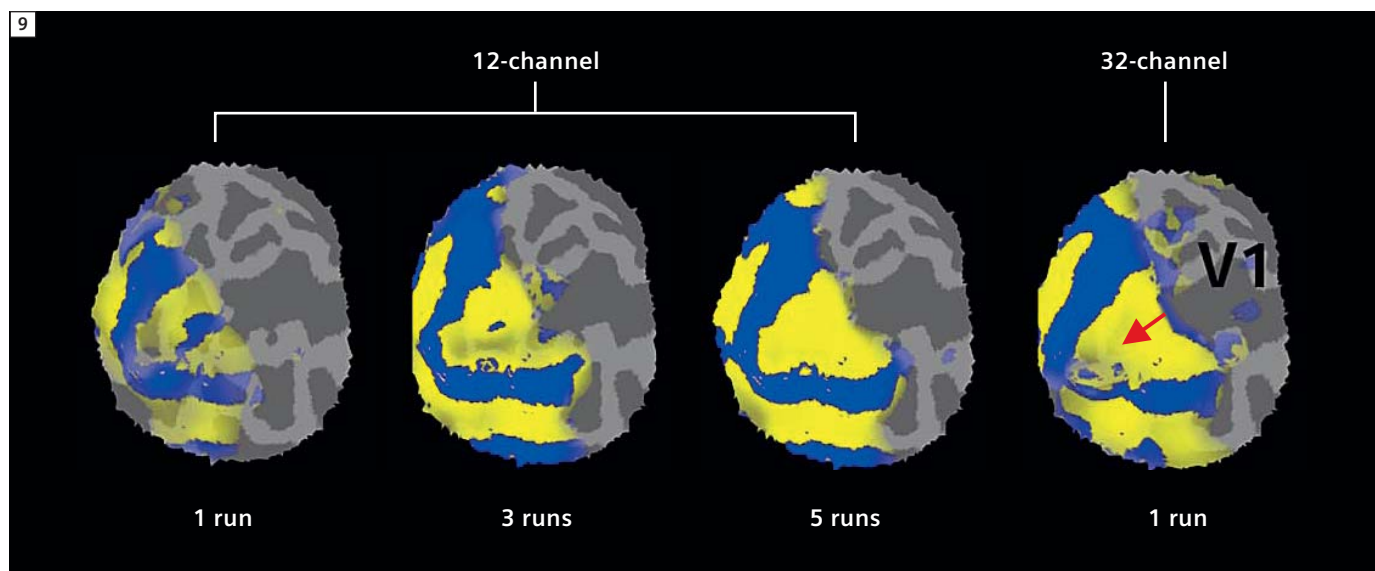
The visual cortex consists of distinct histologically and functionally defined areas arranged topographically based on visual space. Thus, there is a direct topographic mapping of the visual field onto the cortical surface which can be used to identify the boundaries of these areas. This orderly representation is likely to play a critical role in how people process visual information, but it is also often used as a functional marker to locate primary and secondary visual areas in individual subjects as a first step in an fMRI experiment. The mapping of functional boundaries allows a better understanding of the relationships between activation in more complex visual processing experiments. It is important that this initial survey of occipital cortex is robustly and quickly accomplished in each individual subject, so that the bulk of the examination can be devoted to further studies of the workings of the visual system.

In this study we evaluate the potential benefit of highly parallel detectors on the accuracy of fMRI-based mapping of the visual cortex. The visual field mapping benchmark was chosen because the neural organization of primary visual cortex is well understood yet its exact mapping is routinely needed. Furthermore, this benchmark assesses the effect of the array on a more complex fMRI analysis; the quality of boundary estimation is even further dissociated from a simple metric such as image SNR than the more direct measure of activation statistics explored above. Our findings demonstrate that using the 32-channel array provides almost a four-fold decrease in acquisition time needed for a robust estimate of the boundary between visual cortical areas V1 and V2 compared to the 12-channel coil.

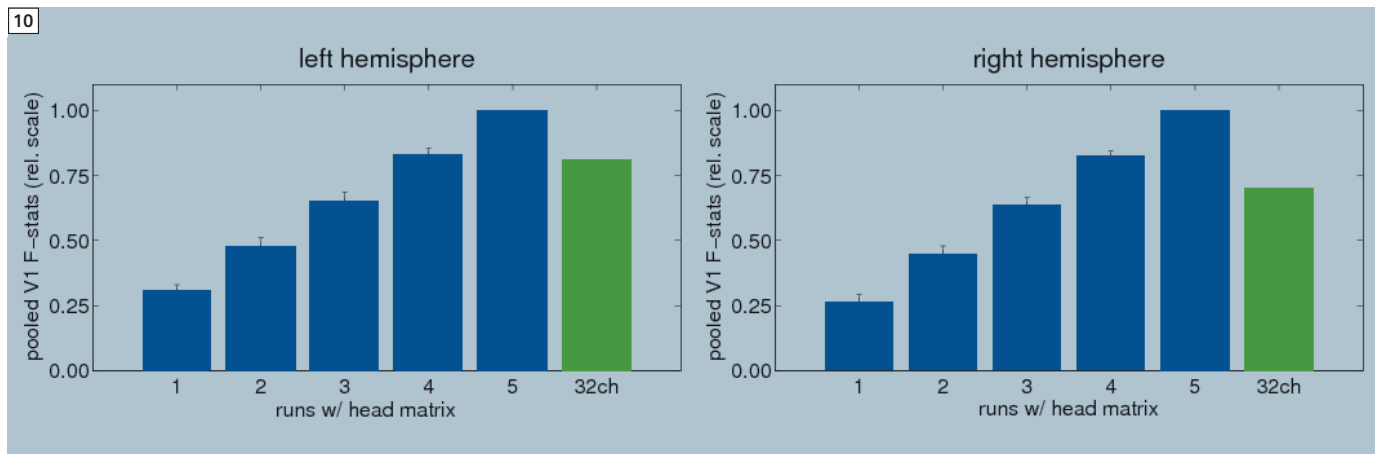
Methods

Data from the two healthy subjects were acquired using the product 12-channel and 32-channel head coils (i.e. each subject was scanned twice). Written consent was obtained from all the sub-

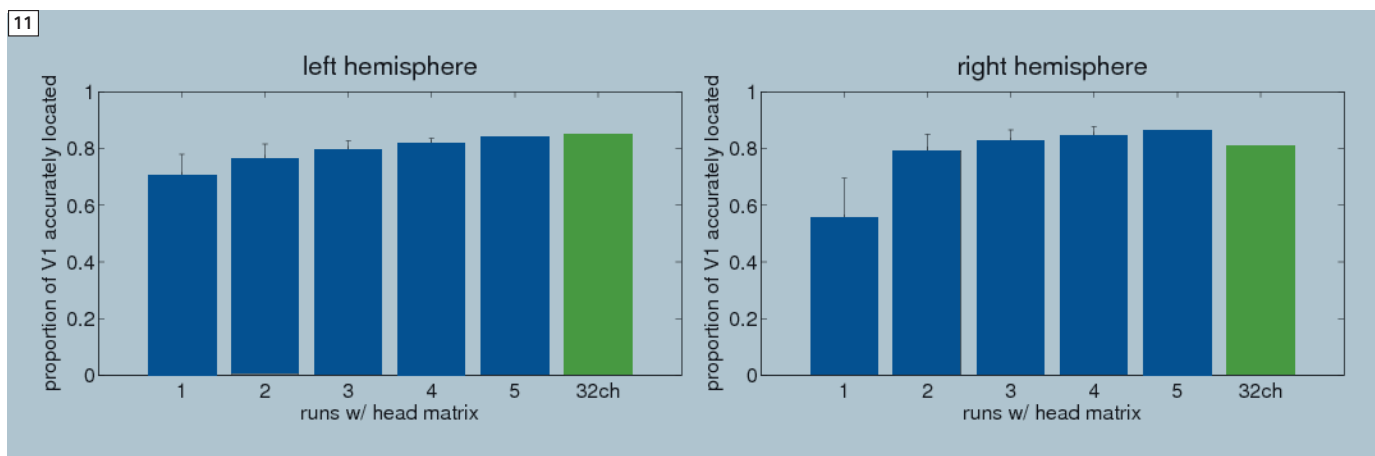
jects under protocols approved by institutional review. Functional MRI data acquired using a single-shot gradient echo EPI sequence. Imaging parameters were: TR = 2000 ms, TE = 30 ms, flip angle = 90°, twenty-eight 2 mm thick slices with inter-slice gap of 0.2 mm and an in-plane resolution of 2 x 2 mm² with FOV = 192 x 192 and matrix = 96 x 96. A high resolution T1-weighted structural scan was acquired using an MPAGE pulse sequence (voxel size of 1 x 1 x 1 mm³, TR/TI/TE/flip angle = 2530 ms / 1100 ms / 3.48 ms / 7°) and used for slice prescription and to generate the cortical surface for flattened representation of the visual activation. The visual field was mapped using a standard fMRI-based phase-encoded retinotopy paradigm consisting of flickering expanding and contracting rings and clockwise and counterclockwise rotating wedges presented in runs lasting 8 minutes each. A single functional run performed with the 32-channel coil was compared to the average of up to five runs acquired with the 12-channel Head Matrix coil. The visual field representation for each



9 Qualitative comparison in the accuracy of visual field mapping for both 32-channel and 12-channel coils. The same flattened patch of the occipital lobe (left hemisphere in an individual subject) is shown with the field-sign computed from different number of scans and different coils. The color (yellow or blue) indicates the handedness of the local coordinate system of the visual field mapping, while the opacity of the color indicates significance of the fit of the measured BOLD signal to the expected response to the visual stimulus. The single acquisition cycle acquired with the 32-channel coil qualitatively shows a similar V1 detection quality to between 3 and 5 acquisitions with the 12-channel Head Matrix coil. (Figure courtesy of O. Hinds, MIT.)



10 Comparison of the accuracy of V1 identification in both hemispheres, using different numbers of runs with the 2 coils (blue = 12-channels, green = 32-channels). The boundary of V1 was traced on the cortical surface based on the field-sign estimate computed from all data. The total number of correct and incorrect field-sign surface vertices within this region was counted to compute the fraction of V1 depicting the correct field-sign (y axis) for all combinations of a given number of runs (x axis) and for the single run collected with the 32-channel coil. (Figure courtesy of O. Hinds, MIT.)



11 Comparison of the significance (F statistic) of the estimate of the visual field mapping experiment within V1 over different numbers of runs with the 2 coils (blue = 12-channels, green = 32-channels). (Figure courtesy of O. Hinds, MIT.)

functional voxel was determined from the preferred phase of the periodic visual stimulus as estimated using the FSFAST software package. The visual field coordinates were then projected onto the cortical surface generated using the FREESURFER software package [8]. The functional areas, such

as primary visual cortex (V1) and secondary visual cortex (V2), are determined by the handedness of the coordinate system required for the mapping between the visual field and the cortex. Because this handedness is opposite in V1 and V2, it can be used to determine the V1/V2 boundary. Thus, mathemati-

cally, the boundary is determined by a change in the sign of the determinant of the Jacobian of the visual field mapping transformation (a measure of the handedness of its coordinate system referred to as a field-sign reversal).

Results

Figure 9 shows representative field-sign estimates derived from different numbers of runs with the 12-channel coil compared with a single run acquired with the 32-channel coil. V1 is the large yellow region in the center and V2 surrounds V1 in blue. The opacity of the color overlay codes the statistical significance of the result. Qualitatively, a single run with the 32-channel coil has similar accuracy and significance to three runs with the 12-channel array. Figures 10 and 11 show more quantitative results for the accuracy of V1 identification. Figure 10 shows the proportion of cortical surface locations within V1 for which the field-sign was estimated correctly, where "correct" was determined from the average of all the data. The total number of correct and incorrect field-sign locations within this region was counted to compute the fraction of correct assignments for all combinations of runs and coils. Figure 11 shows statistical significance (F-statistic) of the V1 activation for the 2 coils and number of runs. The mean significance of all locations within V1 was computed as a measure of the effective contrast-to-noise ratio of the activation for each coil and given number of runs. This analysis suggests that for retinotopic mapping, a single run with the 32-channel array has the F-statistic significance (proportional to BOLD contrast-to-noise ratio) of between 3 and 4 runs with the 12-channel array.

In this study we compared the 32-channel phased array head coil with the 12-channel Head Matrix coil based on qualitative inspection of the visual field map and quantitative measures of the V1 accuracy and significance of the visual coordinate mapping. Our findings demonstrate that images acquired in a single run using the 32-channel coil provide the same quality retinotopy maps and boundary estimation of V1/V2 areas as three to four acquisitions with the 12-channel coil. A single 8 min stimuli cycle with the 32-channel coil has similar contrast-to-noise ratio within primary visual cortex (V1) as three to four cycles with the 12-channel Head Matrix coil. This is a

greater difference than expected based on the time-series SNR studies above where the tSNR difference at a similar image resolution was about 30%. The greater benefit might result from the difficulty of averaging runs in fMRI; a further inducement to develop technology to achieve the desired activation mapping in as few runs as possible.

Conclusion

Highly parallel detection of functional imaging time-series provides the potential for higher image signal-to-noise ratio (SNR_0) as well as decreased susceptibility distortions in echo-planar imaging. When the time-series is thermal (image) noise dominated, we expect the same general increases in functional contrast-to-noise ratio as seen in imaging comparisons. However, for all but the highest fMRI resolutions, physiological noise becomes increasingly important as SNR_0 is improved, and improvements in image sensitivity from more advanced RF detectors are expected to play a smaller role. Nonetheless, switching to the 32-channel coil improved the tSNR for all of the resolutions and provided clear benefits in the functional experiments.

Acknowledgements

The authors would like to acknowledge Satrajit Ghosh (MIT) and Oliver Hinds (MIT) whose work is included in this manuscript. We thank Steven Shannon and Sheeba Arnold at the A.A. Martinos Imaging Center at MIT, for technical support. We also thank Franz Hebrank, Karsten Jahns, Josef Pfeuffer from Siemens. Special thanks to Michael Hamm for his ongoing support in this collaboration with Siemens.

We acknowledge grant support from the NIDCD (R01 DC01925), NIH (P41RR14075, R01EB007942), and funding from A.A. Martinos Imaging Center at MIT, the McGovern Institute for Brain Research, and Harvard-MIT Health Science and Technology (HST), and a research agreement and research support from Siemens Healthcare. One of us (LLW) acknowledges consulting income from Siemens Healthcare.

References

- 1 Wald LL; Wiggins G. Highly Parallel Detection for MRI. *MAGNETOM Flash* 1/2008, 34–44.
- 2 Wiggins GC, Triantafyllou C, Potthast A, Reykowski A, Nittka M, Wald LL., 32-channel 3 Tesla receive-only phased-array head coil with soccer-ball element geometry (2006). *Magn Reson Med.*, Vol. 56(1):216–23.
- 3 Krüger G, Glover GH., Physiological noise in oxygenation-sensitive magnetic resonance imaging (2001). *Magn Reson Med.*, Vol. 46(4):631–7.
- 4 Triantafyllou C, Hoge RD, Krüger G, Wiggins CJ, Potthast A, Wiggins GC, Wald LL., Comparison of physiological noise at 1.5 T, 3 T and 7 T and optimization of fMRI acquisition parameters (2005). *NeuroImage*, Vol. 26(1):243–50.
- 5 Kellman P, McVeigh ER., Image reconstruction in SNR units: a general method for SNR measurement (2005). *Magn Reson Med.*, Vol. 54(6): 1439–47.
- 6 Bohland, J.W., and Guenther F.H., An fMRI investigation of syllable sequence production (2006). *NeuroImage*, Vol. 32(2):821–41.
- 7 Sereno MI, Dale AM, Reppas JB, Kwong KK, Belliveau JW, Brady TJ, Rosen BR, Tootell RB, Borders of multiple visual areas in humans revealed by functional magnetic resonance imaging (1995). *Science*, Vol. 12;268(5212): 889–93.
- 8 Dale AM, Fischl B, and Sereno MI, Cortical surface-based analysis. I. Segmentation and surface reconstruction (1999). *NeuroImage*, Vol. 9(2):179–194.

Contact

Christina Triantafyllou, Ph. D.
Massachusetts Institute of Technology
77 Massachusetts Avenue
Cambridge, MA 02139-4307
USA
ctranta@mit.edu

Over already?



... I was just getting comfortable!

Experience the new 3T MAGNETOM Verio MRI — now available at ABC Imaging Center

- Comfort:** **A more relaxing experience**
An extra-large opening means it can comfortably accommodate patients of different shapes and sizes and can help reduce anxiety and claustrophobia.
- Speed:** **A quicker exam**
Exclusive Tim™ (Total imaging matrix) technology helps make exams faster.
- Confidence:** **Detailed images for your doctor**
Extraordinary images with exceptional details — your doctors will have the information they need to help make a more confident diagnosis.

Rest easy!

**Now available at ABC Imaging Center
(000) 000-0000**

Market your MAGNETOM system

All the tools necessary to market your facility to patients and referring physicians are waiting for you in the **Your MAGNETOM** section on www.siemens.com/magnetom-world

Here you will find everything you need from patient pamphlets to advertisements, to trailers and press releases, postcards, posters, event checklists, high-resolution images and much more – ready for immediate use.

MAGNETOM Flash – Imprint
© 2009 by Siemens AG, Berlin and Munich,
All Rights Reserved

Publisher:
Siemens AG
Medical Solutions
Business Unit Magnetic Resonance,
Karl-Schall-Straße 6, D-91052 Erlangen,
Germany

Editor-in-Chief: Dr. Matthias Lichy, M.D.
(matthias.lichy@siemens.com)

Associate Editor: Antje Hellwich
(antje.hellwich@siemens.com)

Editorial Board: Dagmar Thomsik-Schröpfer,
Ph.D.; Okan Ekinci, M.D.; Ignacio Vallines, Ph.D.;
Wellesley Were; Milind Dhamankar, M.D.;
Michelle Kessler; Gary McNeal; Sunil Kumar, M.D.

Production: Norbert Moser, Siemens AG,
Medical Solutions

Layout: independent Medien-Design
Widenmayerstrasse 16, D-80538 Munich

Printers: Farbendruck Hofmann, Gewerbestraße 5,
D-90579 Langenzenn, Printed in Germany

**MAGNETOM Flash is also available
on the internet:**
www.siemens.com/magnetom-world

Note in accordance with § 33 Para. 1 of the German Federal Data Protection Law: Despatch is made using an address file which is maintained with the aid of an automated data processing system.

MAGNETOM Flash with a total circulation of 20,000 copies is sent free of charge to Siemens MR customers, qualified physicians, technologists, physicists and radiology departments throughout the world. It includes reports in the English language on magnetic resonance: diagnostic and therapeutic methods and their application as well as results and experience gained with corresponding systems and solutions. It introduces from case to case new principles and procedures and discusses their clinical potential.

The statements and views of the authors in the individual contributions do not necessarily reflect the opinion of the publisher.

The information presented in these articles and case reports is for illustration only and is not intended to be relied upon by the reader for instruction as to the practice of medicine. Any health care practitioner reading this information is reminded that they must use their own learning, training and expertise in dealing with their individual patients. This material does not substitute for that duty and is not intended by Siemens Medical Solutions to be used for any purpose in that regard. The drugs and doses mentioned

herein are consistent with the approval labeling for uses and/or indications of the drug. The treating physician bears the sole responsibility for the diagnosis and treatment of patients, including drugs and doses prescribed in connection with such use. The Operating Instructions must always be strictly followed when operating the MR system. The sources for the technical data are the corresponding data sheets. Results may vary. Partial reproduction in printed form of individual contributions is permitted, provided the customary bibliographical data such as author's name and title of the contribution as well as year, issue number and pages of MAGNETOM Flash are named, but the editors request that two copies be sent to them. The written consent of the authors and publisher is required for the complete reprinting of an article.

We welcome your questions and comments about the editorial content of MAGNETOM Flash. Please contact us at magnetomworld.med@siemens.com. Manuscripts as well as suggestions, proposals and information are always welcome; they are carefully examined and submitted to the editorial board for attention. MAGNETOM Flash is not responsible for loss, damage, or any other injury to unsolicited manuscripts or other materials. We reserve the right to edit for clarity, accuracy, and space. Include your name, address, and phone number and send to the editors, address above.

MAGNETOM Flash

The Magazine of MR

Issue Number 1/2009
ISMRM Edition

SIEMENS

Clinical

Clinical Validation
of syngo ASL
Page 50

MRI in Inflammatory
Arthritis
Page 54

Case Report:
Rectum
Page 62

How-I-do-it

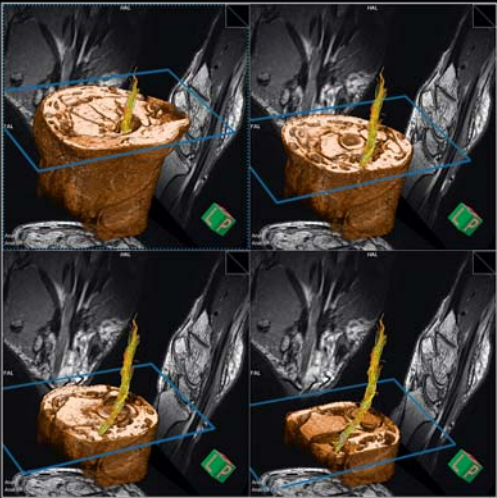
Pediatric Cardiovascular
MRI at 3T
Page 72

Technology

TrueFormTechnology
Page 114

Parallel Transmit
Technology
Page 124

Extent Applications Transfer Edit View Image Tools Scroll Evaluation System Options Help



Waiting for patient registration.

syngo DTI Wrist Postprocessing

Subscription

Please enter your business address

Institution

Department

Function

Title

Name

Street

Postal Code

City

State

Country

MR system used

Please include me in your mailing list for the
following Siemens Healthcare customer magazine(s):

☐ Medical Solutions

☐ MAGNETOM Flash

☐ SOMATOM Sessions

☐ AXIOM Innovations

Stay up to date with the latest information
Register for:

☐ the monthly e-Newsletter

E-mail

Please print clearly!

☐ Yes, I consent to the above information being used
for future contact regarding product updates and other
important news from Siemens.

☐ unsubscribe from info service

MAGNETOM Flash



SUBSCRIBE NOW!

– and get your free copy of future
MAGNETOM Flash! Interesting information from
the world of magnetic resonance – gratis to your
desk. Send us this postcard, or subscribe online at
www.siemens.com/MAGNETOM-World

Siemens AG
Medical Solutions
Magnetic Resonance
Antje Hellwich - Marketing
P.O. Box 32 60
D-91050 Erlangen
Germany

Global Siemens Headquarters

Siemens AG
Wittelsbacherplatz 2
80333 Muenchen
Germany

Global Siemens Healthcare Headquarters

Siemens AG
Healthcare Sector
Henkestr. 127
91052 Erlangen
Germany
Phone: +49 9131 84-0
www.siemens.com/healthcare

www.siemens.com/healthcare-magazine

Order No. A91MR-1000-59C-7600 | Printed in Germany | CC MR 01000 ZS 050920. | © 05.09, Siemens AG

On account of certain regional limitations of sales rights and service availability, we cannot guarantee that all products included in this brochure are available through the Siemens sales organization worldwide. Availability and packaging may vary by country and is subject to change without prior notice. Some/All of the features and products described herein may not be available in the United States.

The information in this document contains general technical descriptions of specifications and options as well as standard and optional features which do not always have to be present in individual cases.

Siemens reserves the right to modify the design, packaging, specifications and options described herein without prior notice. Please contact your local Siemens sales representative for the most current information.

Note: Any technical data contained in this document may vary within defined tolerances. Original images always lose a certain amount of detail when reproduced.

Global Business Unit

Siemens AG
Medical Solutions
Magnetic Resonance
Henkestr. 127
DE-91052 Erlangen
Germany
Phone: +49 9131 84-0
www.siemens.com/healthcare

Local Contact Information

In Asia

Siemens Pte Ltd
The Siemens Center
60 MacPherson Road
Singapore 348615
Phone: +65 6490-8096

In Canada

Siemens Canada Limited
Medical Solutions
2185 Derry Road West
Mississauga ON L5N 7A6
Canada
Phone: +1 905 819-5800

Europe/Africa/Middle East

Siemens AG
Medical Solutions
Henkestr. 127
91052 Erlangen
Germany
Phone: +49 9131 84-0

Latin America

Siemens S.A.
Medical Solutions
Avenida de Pte. Julio A. Roca No 516,
Piso 7
C1067ABN Buenos Aires
Argentina
Phone: +54 11 4340-8400

USA:

Siemens Medical Solutions U.S.A., Inc.
51 Valley Stream Parkway
Malvern, PA 19355-1406
USA
Phone: +1-888-826-9702